Influence of particle and photon fluxes of hydrogen plasmas on the work function of caesiated surfaces

Dissertation

zur Erlangung des akademischen Grades

Dr. rer. nat.

eingereicht an der

Mathematisch-Naturwissenschaftlich-Technischen Fakultät

der Universität Augsburg

von

Adrian Maximilian Heiler

Augsburg, September 2022

Universität
Augsburg
University

Tag der mündlichen Prüfung: 15.12.2022

Erster Gutachter: apl. Prof. Dr.-Ing. U. Fantz

Zweiter Gutachter: Priv.-Doz. Dr. H.-A. Krug von Nidda

Contents

1 Introduction

Sources for the production of negative hydrogen ions have experienced growing interest and active development in recent decades. The extraction of negative hydrogen ions from negative hydrogen ion sources with subsequent acceleration is widely used for charge-exchange injection systems for high energy proton accelerators as well as for neutral beam injection systems for nuclear fusion experiments [FL18a, FL18b]. In negative hydrogen ion sources, the negative ions are produced in a low pressure low temperature hydrogen plasma, and a well known method for the enhancement of the negative ion production is the injection of the alkali metal caesium (Cs) into the source [Dud72, BDD74]. The adsorption of Cs on surfaces significantly lowers their work function, which results in an increase of the conversion yield of impinging hydrogen atoms and positive hydrogen ions into negative ions [BW15].

A milestone toward a commercial fusion power plant is the multinational megaproject ITER [ITE22], which is currently under construction in France and aims to demonstrate the technical feasibility of using the fusion reaction between deuterium and tritium as an abundant and sustainable energy source. The ITER experiment is based on the tokamak principle and two neutral beam injection systems are foreseen to inject fast hydrogen (deuterium) atoms into the fusion plasma for heating and current drive [IAE02]. The neutral beams shall provide a total heating power of 33 MW with beam energies of up to 1 MeV for a duration of up to 3600 s. The neutral beams will be generated by electrostatic extraction and acceleration of negative hydrogen (deuterium) ions with subsequent neutralization in a gas target. The design of the negative ion source is based on plasma generation via inductive radio frequency (RF) coupling and the exploitation of the surface production of negative ions on the extraction electrode, for which Cs will be evaporated into the source. Electrons that are inevitably co-extracted with the negative ions must be removed out of the beam within the extraction system and the co-extracted electron current must not exceed the extracted negative ion current due to technical limitations.

The work function of the caesiated extraction electrode must be low and temporally stable to ensure a reliably good ion source performance, i. e., a high extracted negative ion current and technically manageable co-extracted electron current. This is a challenging task since Cs is effectively sputtered and redistributed within the source during plasma operation. Furthermore, Cs is highly reactive and reactions with residual gases from the background pressure during vacuum phases as well as hydrogen plasma species during plasma phases occur. Experiments at test facilities at the Max Planck Institute for Plasma Physics (IPP) in Garching (Germany) have shown that in particular during long plasma pulses (ranging from minutes up to one hour), a pronounced decrease of the ion source performance is given, which is attributed to an increase of the work function of the extraction electrode [F$^+$21a]. Since the deterioration of the ion source performance is more severe in deuterium than in hydrogen operation, the achievement of the ITER target parameters could not be demonstrated in deuterium so far [W$^+$21d, F$^+$21a]. The reasons behind this isotope effect are not well understood up to now, but aggravated instabilities of the work function of the extraction electrode are expected to play a role. Therefore, a clear understanding of the impact of hydrogen and deuterium plasmas on the work function of caesiated surfaces is indispensable to improve the Cs management and to develop advanced scenarios to meet the ITER requirements.

In order to gain insights into the work function dynamics of caesiated surfaces upon the exposure to particle and photon fluxes being present at ion sources, investigations are carried out at a dedicated laboratory plasma experiment. The experiment is equipped with a finely adjustable Cs oven to caesiate sample surfaces in situ in the plasma chamber. The surface work function is measured via the photoelectric effect and a comprehensive set of diagnostic systems is available for the determination of the fluxes the surface is exposed to in vacuum and plasma phases. While in vacuum phases the residual gases are mainly composed of water vapor, the hydrogen plasma species during plasma phases comprise hydrogen molecules, atoms, positive ions and photons ranging from the infrared to the vacuum ultraviolet region. In previous works, it has been identified that the work function of caesiated surfaces is strongly influenced by the residual gases as well as by the plasma-surface interaction, and the combined influence can reach from a reduction of the work function [FF17] to an increase of the work function due to Cs removal from the surface [CFF20a]. Based on these findings, the aim of the present work is to identify the driving mechanisms that lead to an increase or decrease of the work function during vacuum and plasma phases and to investigate the work function behavior in different operational scenarios for ion sources. Since for these investigations a work function diagnostic with high accuracy is a prerequisite, the photoelectric work function measurement system is upgraded and the detection limit for photocurrents is significantly lowered. With the improved setup, the work function evolution during the caesiation process in vacuum with the influence of impurity gases is extensively studied. By the installation of an additional plasma source, first exploratory investigations on the influence of selected hydrogen plasma species (hydrogen atoms, positive hydrogen ions and energetic vacuum ultraviolet photons) on the work function of caesiated surfaces are carried out. The full plasma impact is investigated by the generation of plasmas in front of the caesiated surface, where particular focus is laid on the identification of possible differences between hydrogen and deuterium operation. These fundamental assessments lay the foundation for the ultimate goal of identifying scenarios with which temporally stable work functions as low as possible can reliably be achieved in an ion source environment.

2 Role of Cs for negative hydrogen ion sources

2.1 Generation of negative hydrogen ions

The electron affinity of atomic hydrogen and deuterium is 0.75 eV [Rum21]. Thus, the binding energy of the extra electron in negative hydrogen (H^-) and deuterium (D^-) ions is relatively low compared to the ionization energy of 13.60 eV for both isotopes [Rum21, LM22]. In negative hydrogen ion sources, the negative ionization can take place both in the plasma volume and on surfaces facing the plasma, which is extensively reviewed in [BW15] and is briefly outlined in the following.

2.1.1 Volume production

The governing process for the formation of negative hydrogen ions in the plasma volume is the dissociative attachment of plasma electrons e^- to hydrogen molecules H_2 in the electronic ground state, following the scheme

$$\mathrm{H_2}(\nu) + \mathrm{e}^- \longrightarrow \mathrm{H_2^-} \longrightarrow \mathrm{H^-} + \mathrm{H}. \tag{2.1}$$

The reaction involves an intermediate resonance state of the H_2^- ion, which is unstable and dissociates into H (typically in the electronic ground state) and H^-. The cross section of the dissociative electron attachment process is given in [JRS03] and increases with increasing vibrational excitation of the H_2 molecule (characterized by the vibrational quantum number ν). Furthermore, the process becomes efficient for low electron temperatures[1] of the order of 1 eV. Therefore, the optimization of the volume production of negative ions must be understood as a two-step process: The first step involves the creation of highly vibrationally excited H_2 molecules, for which high electron temperatures (several eV) and high electron densities are beneficial (excitation processes via electron collisions), and

---

[1] The temperature T is commonly expressed by the energy equivalent $k_\mathrm{B}T$ (with k_B being the Boltzmann constant) and is given in units of eV ($1\,\mathrm{eV} \mathrel{\widehat{=}} 11605\,\mathrm{K}$).

the second step constitutes the dissociative attachment of low energetic electrons to the vibrationally excited molecules. For deuterium, the same process applies, but the cross section for reaction (2.1) is lower compared to hydrogen for the same vibrational quantum number (see [BW20] and references therein).

2.1.2 Surface production

The surface production of negative hydrogen (deuterium) ions represents a single-step process and is based on resonant charge transfer of electrons from the valence band (VB) of a solid to the valence shell of a hydrogen (deuterium) atom:

$$\mathrm{H} + \mathrm{e}^-_{\mathrm{VB}} \longrightarrow \mathrm{H}^-. \tag{2.2}$$

In figure 2.1, the resonant charge transfer process is schematically illustrated for a metal surface. The surface is characterized by the electronic work function χ, which is defined by the energy difference between the vacuum level E_{vac} and the Fermi level E_{F}. For the sake of simplicity, the smearing of the Fermi level at finite temperatures (see chapter 6) is neglected here. When the atom approaches the surface, its electron affinity level E_{a} is lowered due to the induction of a positive image charge within the metal. In case the affinity level is reduced below the Fermi level (for distances $z < z_{\mathrm{c}}$), an electron transfer from the metal to the atom is energetically favored ($z = z_0$ represents the turning point of the atom). According to Fermi's golden rule, the electron transition rate w is given by [RvWL82]

$$w = 2\pi \sum_{\mathrm{deg}} |T_{ki}|^2 \rho_{\mathrm{e}}[E_{\mathrm{a}}(z)], \tag{2.3}$$

where T_{ki} is the transition matrix element between a metallic state k and negative ion state i, ρ_{e} denotes the electron density of states in the metal at the position of the affinity level, and the sum is taken over all degeneracies of the k and i states. The transition rate can be translated into a Heisenberg broadening of the affinity level, which is described by a wave function with a Lorentzian line profile characterized by the full width at half maximum (FWHM) Δ_w. As illustrated in figure 2.1, Δ_w generally increases as the distance between the atom and the surface decreases, which implies that the probability for the electron transfer from the surface to the atom increases.

Within the framework of the so-called amplitude model, the negative ionization probability of the impinging atom is calculated from the time evolution of the wave functions describing the valence band electrons in the metal and the affinity

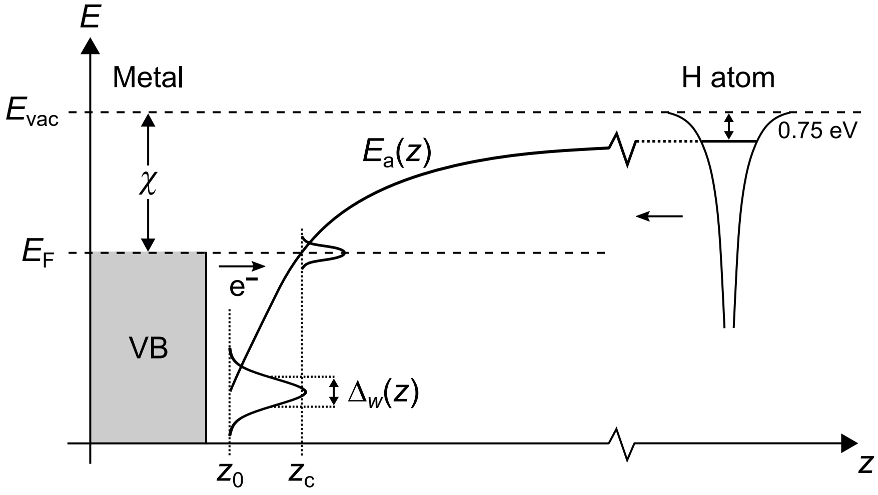

Figure 2.1: *Schematic representation of the shift and broadening of the electron affinity level E_a of a hydrogen atom approaching a metal surface, leading to the transfer of an electron from the metal to the atom for distances $z < z_c$ and thus to the formation of a negative hydrogen ion.*

level of the atom [NL79, BN81, RvWL82]. The result shows that the ionization probability increases by decreasing the work function as well as by increasing the electron density of the surface. For low velocities of the atom, the ionization probability β^- can be approximated by the relation [BNH76]

$$\beta^- \propto \exp\left(-\frac{\chi - E_a}{\alpha v_z}\right), \tag{2.4}$$

where α is the exponential decay constant of the electron transition rate and v_z denotes the velocity component of the outgoing negative ion normal to the surface.

In addition to neutral atoms, positive ions can also be converted into negative ions at metal surfaces. When an H^+ ion approaches the surface, it is neutralized with a high probability via a resonant charge transfer or Auger process [RvWL82], and in the case of molecular ions (H_2^+ and H_3^+), the neutralization process is likely to be accompanied by the dissociation of the molecule [vATG85, IKS92, S$^+$96, T$^+$97]. When the generated neutral atoms capture an additional electron from the surface via the resonant process described above, negative ions are eventually scattered from the surface. Thus, the surface conversion of positive into negative ions can generally be formulated by

$$H_x^+ + 2\,e_{VB}^- \longrightarrow H^- + H_{x-1}, \tag{2.5}$$

where $x = 1, 2, 3$ and H can as well be replaced by D.

2.2 Materials for the surface production of negative hydrogen ions

Modern high-power negative hydrogen ion sources rely predominantly on the surface production of negative hydrogen ions at the aperture(s) of the extraction electrode [BW15, FL18a, FL18b]. Therefore, one of the key issues is the implementation of an extraction electrode surface with a stable and uniform work function as low as possible. Since the surface has to tolerate vacuum conditions of typically $10^{-7} - 10^{-6}$ mbar and has to withstand hydrogen plasma exposure where the surface is bombarded by reactive particles and energetic photons (up to $\approx 15\,\mathrm{eV}$), the achievement of low work function surfaces is a challenging task.

2.2.1 Cs coating on refractory metals

The work function of bulk Cs is $2.0 - 2.1\,\mathrm{eV}$ [Rum21, Mic77], which is the lowest of all stable elements. Therefore, the adsorption of Cs on refractory metals with typical work functions in the range of $4 - 5\,\mathrm{eV}$ leads to a drastic reduction of the work function (described in detail in chapter 4) and consequently to a significant enhancement of the surface production of negative hydrogen ions [BDD74, IKS92, S^{+}96]. In [CFF20a], it has been shown that work function values in the range of $2.1 \pm 0.1\,\mathrm{eV}$ (i. e., those of a virtually pure Cs layer) are achieved in a typical ion source hydrogen plasma environment.

Since Cs is the element with the lowest work function, the negative ionization yield of coatings with other alkali metals such as Rb or K is generally lower [S^{+}81]. However, the alkali earth metal Ba can be as efficient as Cs: Although the work function of Ba is $2.5\,\mathrm{eV}$ [Rum21] and thus considerably higher compared to Cs, comparable negative ionization yields of bariated and caesiated surfaces are reported [vOvAL88, WLK89]. This is attributed to the considerably higher density of conduction electrons in Ba ($3.2 \times 10^{28}\,\mathrm{m}^{-3}$) compared to Cs ($0.9 \times 10^{28}\,\mathrm{m}^{-3}$) [Rum21], leading to an enhancement of the electron transition rate (see equation (2.3)) compensating the higher work function [vOvAL88]. However, Cs is generally more suitable for practical applications as its higher vapor pressure at lower temperatures makes it much easier to evaporate.

An in situ evaporation of Cs is mandatory since the implementation of stable Cs layers is not possible due to the high reactivity of Cs. The Cs evaporation significantly complicates the ion source operation because dedicated Cs ovens are required and additional maintenance issues (e. g., refilling of the Cs ovens and cleaning of contaminated components within the ion source) inevitably occur. Furthermore, the formation of a uniform Cs coverage is generally not easily achieved and in particular challenging in ion sources with large multi-aperture extraction electrodes (e. g., ion sources for nuclear fusion, see section 2.3). Upon plasma exposure, adsorbed Cs on metal surfaces is gradually removed and partially positively ionized within the plasma (Cs^+), leading to complex Cs redistribution dynamics within the ion source. Cs loss can occur by the accumulation of Cs at cold spots and the escape of neutral Cs atoms through the extraction system. Moreover, Cs can form various compounds with the plasma species as well as with impurity gases. Therefore, Cs must be continuously evaporated into the ion source so that the Cs layer is replenished during long periods of operation.

2.2.2 C12A7 electride

To circumvent the drawbacks inherent to volatile Cs coatings, the application of low work function bulk materials is desirable. A material that has attracted attention over the last few years as a potential H^- converter surface is the calcium aluminate electride $[Ca_{24}Al_{28}O_{64}]^{4+}(e^-)_4$ (abbreviated as C12A7:e^-), which has an intrinsic low work function of 2.4 eV [T$^+$07]. It is the first reported electride that is chemically and thermally stable in ambient atmosphere [M$^+$03, Hos04]. The material is mechanically robust and exhibits an electrical conductivity of up to 1500 S/cm at room temperature [K$^+$07c]. The unit cell of the material consists of 12 subnanometer-sized Ca-O-Al cages (internal diameter $\sim$ 4 Å [M$^+$03]) with a total positive charge of +4, which is compensated by four anionic electrons distributed inside the cage structure.

The electride is prepared from the insulating mineral mayenite (abbreviated as C12A7), where two "free" oxygen ions O^{2-} are trapped inside the positively charged $[Ca_{24}Al_{28}O_{64}]^{4+}$ framework. By extracting the oxygen ions in the crystallographic cages via chemical reduction [K$^+$07b, KH12], the insulator is converted into the conducting electride. Since the amount of extracted O^{2-} ions depends on the fabrication process, the C12A7 electride should rather by described by the formula $[Ca_{24}Al_{28}O_{64}]^{4+}(O^{2-})_{2-\delta}(e^-)_{2\delta}$ with $0 \leq \delta \leq 2$ [K$^+$07c, KH12, SR17]. For low anionic electron densities $< 10^{27}\,m^{-3}$, the electrons interact relatively strongly with the cage framework and migration through the crystal is only possible via thermally activated polaronic cage hopping, leading to a semiconducting state. For electron densities $\gtrsim 10^{27}\,m^{-3}$, the material exhibits metallic behavior since band conduction via quantum tunneling through the cage walls is enabled. In case all oxygen ions are replaced by electrons ($\delta = 2$), the density of conduction electrons is $2.33 \times 10^{27}\,\mathrm{m}^{-3}$ [KH12]. The conduction electrons occupy a so-called cage conduction band (CCB), which lies within the wide band gap ($\approx 7.5\,\mathrm{eV}$) of the valence and conduction bands of the lattice framework [S$^+$03, S$^+$07, T$^+$07]. The density of electron carriers determines also the position of the Fermi level in the CCB and thus the work function [KH12, H$^+$15, OHS19].

The electronic surface properties of the C12A7 electride are known to be particularly sensitive to contaminants so that the work function strongly depends on the surface preparation and vacuum conditions [T$^+$07, T$^+$11, KH12]. As a consequence, measured work functions are often higher than 2.4 eV [K$^+$07a, Y$^+$12, K$^+$17, Z$^+$17]. Therefore, the work function performance and stability of the C12A7 electride have been investigated under typical ion source conditions within the scope of this work as well. The investigations were performed at the laboratory experiment ACCesS (see chapter 5) and the obtained results have been published by the author in [H$^+$21]. The tested C12A7 electride material was supplied from the Fraunhofer Institute for Ceramic Technologies and Systems (IKTS) and exhibited an electron carrier density of $1.0 \times 10^{27}\,\mathrm{m}^{-3}$. The investigations have shown that after the sample surface is prepared by vacuum annealing up to about 700 °C, a stable work function plateau of $2.75 \pm 0.10\,\mathrm{eV}$ is reached upon hydrogen plasma exposure on the hour scale, i. e., the achieved work function is about $0.3 - 0.4\,\mathrm{eV}$ higher compared to the reported literature value for chemically pure surfaces. A further enhancement toward 2.4 eV might be achieved by an increase of the electron carrier density beyond $1.0 \times 10^{27}\,\mathrm{m}^{-3}$. Plasma-induced changes of the sample could not be detected by the analysis of the surface with optical, scanning electron and energy-dispersive X-ray (EDX) spectroscopy before and after the experimental campaign, showing that the electride is resilient to long-term hydrogen plasma exposure.

2.2.3 State-of-the-art

In previous works, a number of potential alternative materials to Cs with nominal work functions below 3 eV were investigated in a typical ion source hydrogen plasma environment. In figure 2.2, the achieved work functions of the investigated materials are compiled. As illustrated, the work function values are categorized as high for $\chi > 3.5\,\mathrm{eV}$, medium for $3.5 \geq \chi > 2.5\,\mathrm{eV}$, low for $2.5 \geq \chi > 1.5\,\mathrm{eV}$, and ultra-low for $\chi \leq 1.5\,\mathrm{eV}$ within the present work. Investigations on lanthanated materials such as WLa (La_2O_3 in W, $1 - 2\,\%$ La) and MoLa (La_2O_3 in Mo, 0.7 %

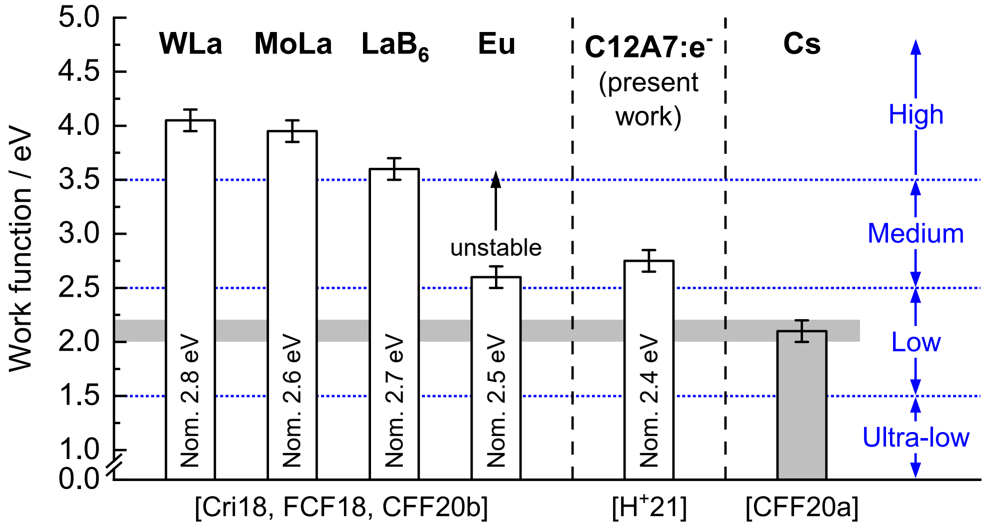

Figure 2.2: *Overview of the measured work functions of potential H^- converter surfaces in a typical ion source hydrogen plasma environment. The nominal work function values are indicated and the reference case of Cs coatings on refractory metals is depicted.*

La) with nominal work functions in the range of 2.6 – 2.8 eV (after activation with temperatures of about 1500 °C) have shown that work functions below 3.9 eV cannot be reached under ion source plasma conditions [Cri18, FCF18]. With lanthanum hexaboride (LaB_6) a slightly lower work function of 3.6 eV is achieved, which is, however, still substantially higher than the nominal value of 2.7 eV [Cri18, FCF18]. The application of an europium (Eu) surface allows to reach work functions of about 2.6 eV (close to the nominal value of 2.5 eV), but the plasma impact leads to a gradual deterioration of the surface accompanied by an increase of the work function to values higher than 3.5 eV [CFF20b].

Since the achieved surface work functions with the tested materials are high upon (long-term) hydrogen plasma exposure, the surface production of negative hydrogen ions is substantially lower compared to Cs coated surfaces [KFF17, F$^+$18] and the materials are thus not considered as a viable alternative to Cs evaporation. The C12A7 electride that has been investigated within the present work shows the most promising performance among the tested Cs-free materials so far and subsequent investigations should thus be performed to check whether the higher work function compared to Cs can be overcompensated by additional H^- production channels [S$^+$18] and/or a reduced complexity of handling.

An approach to use Cs while circumventing in situ evaporation is the implantation of Cs into refractory metals [S$^+$15]. Tests with Cs doped Mo with 6 % Cs surface coverage have been performed, where the expected nominal work function of about 3.9 eV is measured under ion source conditions [FCF18, S+21b]. In order to further reduce the work function, techniques for the implantation of higher Cs concentrations would be required. During plasma operation, however, a gradual increase of the work function above 4 eV is observed, showing that Cs is removed from the surface. Therefore, techniques for an in situ re-implantation of Cs would need to be developed, complicating the ion source operation considerably. In conclusion, the application of Cs evaporation on refractory metals (typically Mo) represents the state-of-the-art technique for the generation of efficient H^- converter surfaces at present-day ion sources [BW15, FL18a].

2.3 Negative hydrogen ion sources for ITER

2.3.1 NNBI system requirements

For the upcoming fusion experiment ITER, two negative ion based neutral beam injection (NNBI) systems are foreseen for heating and current drive, with the option of adding a third one in a later stage.[2] The NNBI systems are based on the electrostatic extraction and acceleration of H^- (D^-) ions from a negative ion source, followed by neutralization in a gas target so that the energetic particles can be injected into the fusion device without being magnetically deflected. The requirements for the ITER NNBI systems are extensively described in [IAE02, H+17b, S+17a, H+17a] and are summarized in table 2.1. During the pre-fusion operation phase at ITER, the NNBI systems will be operated in hydrogen and each beamline shall deliver a heating power of 16.7 MW with particle energies of 870 keV for up to 1000 s. For the subsequent fusion power operation phase, the neutral beam injectors will be operated in deuterium and the same heating power with beam energies of 1 MeV for up to 3600 s must be provided. To guarantee a proper beam transport, the inhomogeneity of the accelerated negative ion beam must be below 10 %. Since significant power losses need to be considered due to the limited neutralization efficiency of negative ions ($\approx 60\,\%$ [BPS75]) as well as due to transmission losses along the beamline, the negative ion beam must have a power of 40 MW, i. e., an H^- current of 46 A and a D^- current of 40 A are required.

The ion current will be extracted from a Cs seeded negative ion source by means of a multi-grid multi-aperture system with an extraction area 0.2 m^2 (details see

---

[2] In addition to the heating neutral beam injectors, a diagnostic neutral beam injector will be applied for charge exchange resonance spectroscopy [C+10].

Table 2.1: *Beam and ion source requirements for the ITER heating neutral beam injectors [IAE02, H+17b, S+17a, H+17a].*

Parameter	Hydrogen	Deuterium
Heating power	16.7 MW	16.7 MW
Beam energy	870 keV	1 MeV
Beam duration	1000 s	3600 s
Beam inhomogeneity	$< 10\,\%$	$< 10\,\%$
Accelerated negative ion current	46 A	40 A
Extracted negative ion current	66 A $\widehat{=}\, 329\,\mathrm{A/m^2}$	57 A $\widehat{=}\, 286\,\mathrm{A/m^2}$
Ratio of co-extracted electron current to extracted negative ion current	< 1	< 1
Ion source filling pressure	$\leq 0.3\,\mathrm{Pa}$	$\leq 0.3\,\mathrm{Pa}$

section 2.3.2). In order to limit the negative ion losses by electron stripping in the accelerator system to about 30 %, the gas pressure in the ion source must not exceed 0.3 Pa [KH06]. Taking 30 % stripping losses into account, an ion current of 66 A must be extracted in hydrogen and 57 A in deuterium operation, corresponding to extracted negative ion current densities of $329\,\mathrm{A/m^2}$ and $286\,\mathrm{A/m^2}$, respectively. Plasma electrons that are inevitably co-extracted with the negative ions must be removed out of the beam, which is done by magnetic deflection onto the second grid of the extraction system prior to full acceleration. To keep the heat load onto this so-called extraction grid on a technically feasible level, the co-extracted electron current density must be kept below the extracted negative ion current density.

2.3.2 Ion source development

Prototype source

The prototype ion source for the ITER NNBI system was developed at IPP [S+06] and is schematically illustrated in figure 2.3. Hydrogen (deuterium) plasmas are generated in the so-called driver, which is done via inductive RF coupling by using a six-turn RF coil operated with a driving frequency of 1 MHz and an RF power of up to 100 kW. The driver represents a cylindrical dielectric vessel (made of aluminum oxide or quartz) with a diameter of 24 cm and a length of 17 cm. In order to suppress capacitive RF coupling and avoid plasma erosion of the dielectric, a Faraday screen is placed inside the driver. The metallic backplate of the driver exhibits cusp magnets for the improvement of the plasma confinement.

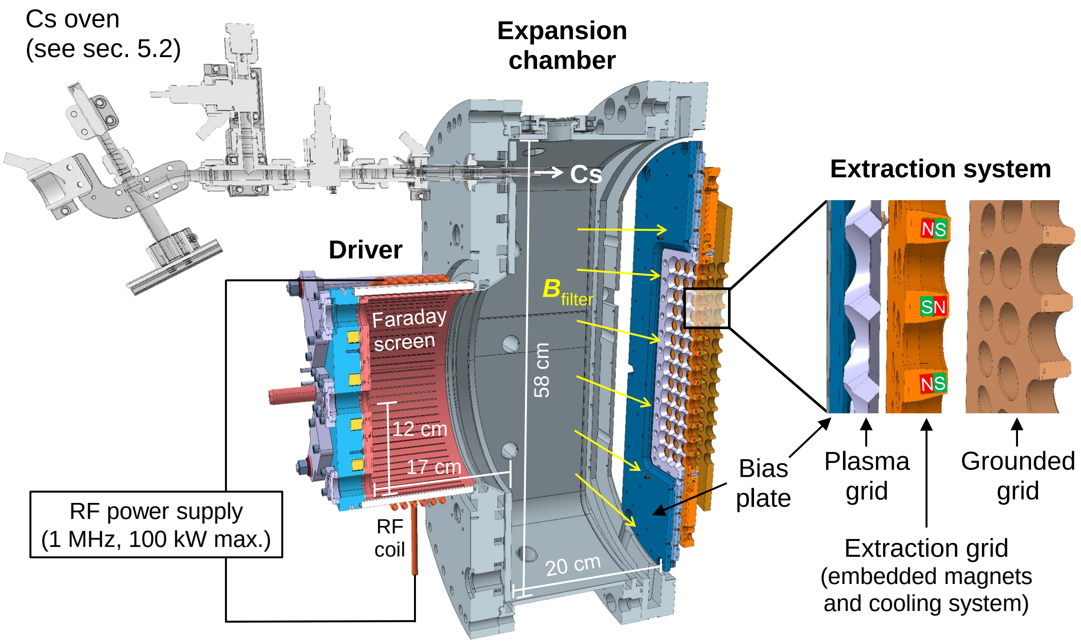

Figure 2.3: *Schematic of the prototype ion source for the ITER NNBI system.*

Within the driver plasma, an electron density of the order of $10^{18}\,\mathrm{m}^{-3}$, an electron temperature of the order of 10 eV, and an atom to molecule ratio of about 0.2 in hydrogen and 0.3 in deuterium are generated [F$^+$21a]. The plasma expands into the expansion chamber, where the first grid of the extraction system is placed at a distance of about 20 cm from the driver exit. This grid is called plasma grid and is made of Mo-coated Cu. It exhibits an array of extraction apertures, each with a diameter of 14 mm in a chamfered geometry. The so-called bias plate surrounds the plasma grid and acts in principle as an extension of the source walls. While the source walls are kept at a temperature of about 40 °C, the plasma grid and bias plate are typically heated to 130 – 150 °C. To exploit the surface production of negative ions on the plasma grid, Cs is introduced into the source by means of a finely adjustable Cs oven, which is described in detail in section 5.2. The Cs evaporation rate is typically set to several mg/h [F$^+$17a], leading to Cs densities in the range of $10^{13} - 10^{14}\,\mathrm{m}^{-3}$ in front of the plasma grid during vacuum phases.

Since the binding energy of the second electron in H^- (D^-) is only 0.75 eV, the negative ions can easily be destroyed by collisional processes within the plasma [JRS03]. In the presence of high electron densities and temperatures, electron detachment processes via electron impact ($\mathrm{e}^- + \mathrm{H}^- \rightarrow \mathrm{H} + 2\,\mathrm{e}^-$) are very efficient. Therefore, a magnetic filter field is applied in front of the plasma grid in order to cool the electron temperature to about 2 eV and to reduce the electron density by about one order of magnitude [F$^+$21a], the latter also reducing the co-extracted electron current. The magnetic field has a strength of a few mT and is generated by a current of the order of kA flowing vertically through the plasma grid (formerly produced by the installation of permanent magnets [S$^+$06, H$^+$17a]). The plasma grid is usually positively biased by several volts with respect to the source body and the bias plate, which contributes to the reduction of the co-extracted electron current [WFN16].

The extraction system of the prototype source consists of the plasma grid, the extraction grid and the grounded grid. The plasma grid (and the source) is set to a maximum potential of $-45\,\mathrm{kV}$ with respect to the grounded grid (at $0\,\mathrm{V}$). The potential of the extraction grid is typically $5 - 10\,\mathrm{kV}$ above the potential of the plasma grid and embedded permanent magnets are used to deflect the co-extracted electrons onto the extraction grid surface. The extraction grid is actively cooled and the created heat load by the co-extracted electrons striking the surface limits their tolerable amount. The caesiation of the plasma grid leads not only to an enhancement of the extracted negative ion current, but also to a significant reduction of the co-extracted electron current. At optimum conditions, the extracted negative ion current is increased by a factor of up to 10 and the co-extracted electron current is decreased by a similar factor compared to Cs-free operation [W$^+$18b]. The reason for this behavior is an evolving ion-ion plasma in front of the plasma grid: The negative ions penetrate into the plasma and push back the electrons to maintain quasi-neutrality, resulting in a negative ion density that is higher than the electron density, i. e., the electrons become the minor negatively charged species.

Size scaling approach

The prototype source, which is currently in operation at the test facility BUG at IPP [F$^+$19a], represents the baseline design for the ITER NNBI ion source. In order to achieve the required negative ion current for the ITER NNBI system (see table 2.1), the prototype source is scaled up in a modular way, i. e., several drivers are mounted on an enlarged expansion chamber [M$^+$11]. As illustrated in figure 2.4, eight RF drivers arranged in groups of two are foreseen for the ITER ion source, resulting in a large source area of roughly $1\,\mathrm{m} \times 2\,\mathrm{m}$. The drivers will be supplied with a total RF power of up to $800\,\mathrm{kW}$ ($100\,\mathrm{kW}$ per driver) at a frequency of $1\,\mathrm{MHz}$. The plasma grid for the ITER ion source provides 1280 extraction apertures, which are arranged in 4×4 aperture groups consisting of arrays of 16×5 apertures ($0.2\,\mathrm{m}^2$ total extraction area). The aperture groups are

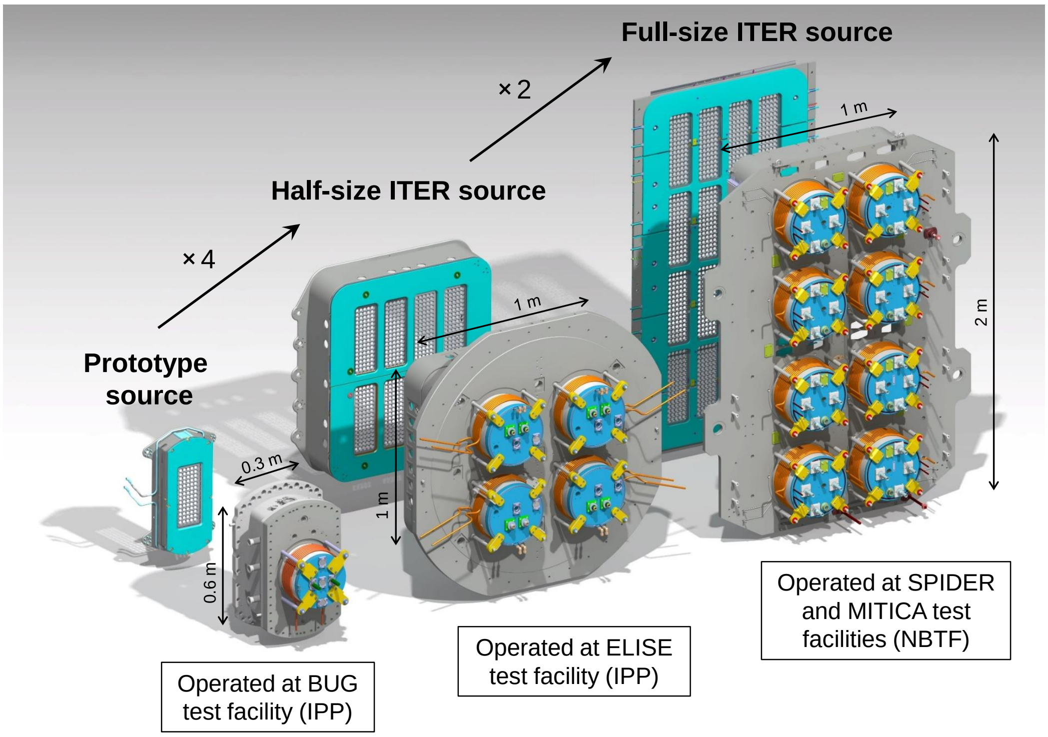

Figure 2.4: *Illustration of the size scaling approach for the development of the ITER NNBI ion source. The driver(s) attached to the expansion chamber as well as the plasma grid surrounded by the bias plate (in cyan) are shown.*

surrounded by the bias plate and three Cs ovens will be installed at the expansion chamber backplate to inject Cs into the source.

To validate the modular concept and to gain early operational experience, a half-size ITER ion source is operated at the ELISE test facility at IPP since 2012 [H+09, H+17a]. As can be seen in figure 2.4, the ELISE ion source is equipped with four RF drivers and a plasma grid consisting of 2×4 aperture groups (640 apertures in total, leading to an extraction area of $0.1\,\mathrm{m}^2$). Cs is evaporated into the source by means of two Cs ovens, which are attached to the side walls of the expansion chamber (left and right) [C+19]. While the plasma can be generated in steady-state mode in the ion source, the extraction and acceleration of negative ions (up to 60 keV) has been limited to about 10 s every 150 s up to now. Currently, the test facility is upgraded for continuous wave extraction [F+22].

The first full-size prototype of the ITER ion source is operated at the test facility SPIDER at the ITER Neutral Beam Test Facility (NBTF) in Padua (Italy) [T+17]. The test facility went into operation in 2018 [S+20, T+21] and first operation with Cs injection was performed in 2021 [S+22]. SPIDER benefits from the experience gained at the IPP test facilities and aims to demonstrate all ITER ion source requirements. The full-scale prototype of the ITER neutral beam injector is currently under construction at the MITICA test facility at the NBTF and is planned to go into operation in 2024 [T+21, B+21].

2.3.3 Present challenges to overcome

The main objective of the IPP and NBTF test facilities is the development of operational scenarios with which the ITER NNBI requirements can be reliably fulfilled. At present, one of the main issues in the ion source development is to keep the co-extracted electron current at a level at which the heat load on the extraction grid does not exceed the technical limitations [F+21a]. In contrast to the extracted negative ion current, the co-extracted electron current is subject to much stronger temporal dynamics and can dramatically increase within a few seconds, i. e., the co-extracted electron current can limit the source performance in particular during long pulse operation on the minute and hour scale. Additionally, pronounced spatial asymmetries can develop. The dynamics of the co-extracted electrons is expected to depend predominantly on the conditions of the Cs layer on the plasma grid. When the provided surface work function is sufficiently low, the electrons are the minor negatively charged species in front of the plasma grid (ion-ion plasma) so that it is assumed that even small changes of the work function and thus of the electron density can drastically affect the co-extracted electron current [F+21a].

At the ELISE test facility, the achievement of the ITER requirements could be demonstrated in hydrogen [W+19a]. For pulse lengths of 1000 s, more than 90 % of the required extracted negative ion current density could be reached, limited only by technical constraints (available RF power and high voltage power supply). During the 1000 s pulses, the co-extracted electron current steadily increased, but could be kept below the technical limit. This was achieved by the installation of additional biased surfaces (potential rods) as well as by sufficiently high amounts of Cs within the source [W+18c].

The operation of the negative ion sources in deuterium is more challenging than in hydrogen because the co-extracted electron current is generally higher and its increase over time is much more pronounced [F+20, W+21d]. This isotope effect was demonstrated in a dedicated campaign at ELISE, where the working gas was switched from hydrogen to deuterium with the operational parameters (i. e., RF power, extraction voltage and magnetic filter field) remaining unchanged [W+19b, F+21a]. While the isotope change lead to a reduction of the extracted negative ion current density by only a few percent, the co-extracted electron current density increased by a factor of up to nine. Moreover, a severe vertical asymmetry of the co-extracted electron current density can develop over the plasma grid area. Experimentally found measures against the increase of the co-extracted electrons are an increase of the magnetic field strength in front of the plasma grid and an enhancement of the Cs evaporation into the source, the latter being limited by the risk of high voltage breakdowns in the extraction system due to the possibility of Cs leakage through the plasma grid [W$^+$21d]. Nevertheless, the dynamics of the co-extracted electron current is still the technological bottleneck and has prevented the demonstration of the ITER target parameters in deuterium so far: Only about 66 % of the required extracted D^- current density with tolerable electron co-extraction could be achieved during one hour pulses [W$^+$19b].

Scope of the present work

The achievement of a temporally stable low work function of the plasma grid surface is one of the decisive knobs for the reduction and stabilization of the co-extracted electron current. However, the ion source environment represents harsh conditions for the formation of stable Cs coatings. During vacuum phases, the background pressure is typically in the range of $10^{-7} - 10^{-6}$ mbar, i. e., the amount of residual gases is not negligible and the formation of Cs compounds is likely due to the high chemical reactivity of Cs [FF17]. During plasma phases, the Cs coating is exposed to fluxes of hydrogen molecules, atoms, ions and photons, and an effective redistribution of (ionized) Cs (compounds) within the source is driven. The resulting impact on the work function can reach from a beneficial reduction (“cleaning effect”) [FF17] to an unfavorable increase (degradation) due to Cs removal from the surface [CFF20a], where in particular the atomic hydrogen radical, positive hydrogen ions and energetic (vacuum) ultraviolet photons are expected to play a crucial role in the plasma-surface interaction. Thus, complex work function dynamics are given under ion source conditions and a detailed understanding of how the hydrogen and deuterium plasma-surface interaction alters the work function of caesiated surfaces is of utmost importance for the optimization of the Cs management in ion sources.

Information on the work function of the caesiated plasma grid is not available up to now because the development of a reliable work function diagnostic is challenging in the harsh ion source environment, and the work function is believed to be about 2.1 eV at optimum source performance (working hypothesis). Therefore, dedicated investigations on the work function of caesiated surfaces are performed at the flexible laboratory experiment ACCesS, which is described in detail in chapter 5 and provides a unique opportunity to monitor the work function under well-controlled vacuum and plasma conditions. For the determination of particle and photon fluxes onto the caesiated surface, a comprehensive set of diagnostic systems is available. The experiment is upgraded within this work by the installation of an additional plasma source (see chapter 5), allowing for a selective exposure of caesiated surfaces to vacuum ultraviolet photons, hydrogen atoms and positive hydrogen ions. Furthermore, the work function measurement system is improved, which is described in chapter 6. By these modifications, the work function of caesiated surfaces is investigated with high accuracy in various scenarios: in the vacuum phase with a background pressure of the order of 10^{-6} mbar (chapter 7), upon the exposure to fluxes of specific hydrogen plasma species (chapter 8), and upon hydrogen and deuterium plasma exposure with plasma parameters comparable to those close to the plasma grid at the NNBI ion sources (chapter 9). The investigations allow to draw valuable conclusions for the Cs management in negative ion sources, which are discussed in chapter 10.

3 Fluxes in low pressure low temperature hydrogen plasmas

The plasma species contained within hydrogen plasmas can be grouped into neutral particles, charged particles and photons (massless particles). The neutral particles are H atoms and H_2 molecules, and the charged particles are H^+, H_2^+, H_3^+, H^- and free electrons [JRS03]. The spectrum of the photons ranges from the infrared to the vacuum ultraviolet region. Deuterium plasmas can be treated equally to hydrogen plasmas with the corresponding particle species based on the heavier isotope D.

The following sections cover fundamental plasma properties and processes as well as a description of the different photon and particles fluxes that are present in a hydrogen plasma environment. The descriptions mainly refer to the protium isotope for the sake of simplicity, implying that the considerations are also valid for the deuterium isotope if not otherwise stated.

3.1 Fundamentals

The hydrogen plasmas considered within this work are generated via inductive RF coupling at low pressures of several Pa. The inductive plasma ignition is achieved by driving an RF current through an antenna located outside the vacuum chamber, leading to an acceleration of electrons by electric fields (transformer principle) to kinetic energies sufficiently high to ionize gas particles.[1] Since produced charged particles recombine again (e. g., at the vessel walls), a dynamic equilibrium with a certain degree of ionization is present in steady-state operation. The densities n of positive and negative charges are equal on a macroscopic scale, which is commonly known as quasi-neutrality. For hydrogen plasmas, the quasi-neutrality condition

---

[1] Detailed information about the plasma generation mechanisms can be found in [LL05, CB11] for instance.

can be formulated by

$$n_{\mathrm{H}^+} + n_{\mathrm{H}_2^+} + n_{\mathrm{H}_3^+} = n_\mathrm{e} + n_{\mathrm{H}^-}, \tag{3.1}$$

where n_e denotes the electron density. In the case the negative ion density is much smaller than the electron density, the total positive ion density $n_{\mathrm{i}+}$ can be approximated by n_e. The density ratio of charged to neutral particles is typically $\lesssim 10^{-4}$ [Fri13, Cri18].

3.1.1 Distribution function and temperature

The different particle species α within the plasma volume are well described by the kinetic theory of gases. Thus, time dependent distribution functions $f_\alpha(\boldsymbol{r}, \boldsymbol{v}, t)$ in the phase space $(\boldsymbol{r}, \boldsymbol{v})$ of particle positions $\boldsymbol{r}$ and velocities $\boldsymbol{v}$ can be readily introduced [LL05, CB11]. The distribution functions are normalized to the particle density, i. e., $\iiint f_\alpha \mathrm{d}^3 v = n_\alpha$. When the ensemble of the particle species is in thermal equilibrium, the distribution function is given by the isotropic Maxwell-Boltzmann (in short: Maxwellian) distribution, which reads

$$f_{\alpha,\mathrm{M}}(v) = 4\pi \left(\frac{m_\alpha}{2\pi k_\mathrm{B} T_\alpha}\right)^{3/2} n_\alpha v^2 \exp\left(-\frac{m_\alpha v^2}{2 k_\mathrm{B} T_\alpha}\right), \tag{3.2}$$

with k_B denoting the Boltzmann constant. As can be seen, the Maxwellian distribution of the particle speed $v = |\boldsymbol{v}|$ is fully determined by the particle mass m_α and the thermodynamic temperature T_α. From $f_{\alpha,\mathrm{M}}$, the thermal or average speed is calculated by

$$\langle v_\alpha \rangle = \frac{1}{n_\alpha} \int\limits_0^\infty v f_{\alpha,\mathrm{M}}(v) \mathrm{d}v = \sqrt{\frac{8 k_\mathrm{B} T_\alpha}{\pi m_\alpha}}. \tag{3.3}$$

When the distribution function is expressed in terms of the kinetic energy $E = m_\alpha v^2/2$, equation (3.2) transforms to

$$f_{\alpha,\mathrm{M}}(E) = \frac{2 n_\alpha}{\pi^{1/2} (k_\mathrm{B} T_\alpha)^{3/2}} E^{1/2} \exp\left(-\frac{E}{k_\mathrm{B} T_\alpha}\right) \tag{3.4}$$

and the thermal or mean kinetic energy is given by

$$\langle E_\alpha \rangle = \frac{1}{n_\alpha} \int\limits_0^\infty E f_{\alpha,\mathrm{M}}(E) \mathrm{d}E = \frac{3}{2} k_\mathrm{B} T_\alpha. \tag{3.5}$$

As mean energies and temperatures are so closely related, it is common practice to express temperatures in the energy equivalent $k_\mathrm{B}T$, where eV is usually used as the energy and therefore temperature unit.

In inductively coupled plasmas (ICPs), the energy is predominantly transferred to the free electrons. For the plasmas applied within this work, the electron energy distribution function (EEDF) can be approximated by a Maxwellian distribution and the corresponding electron temperature T_e is typically in the range of a few eV.[2] The heavy particles (neutrals and ions) are predominantly heated by elastic collisions with the electrons. As the mass difference between the electrons and heavy particles is high, however, the energy transfer to the heavy particles is inefficient. Consequently, high collision frequencies would be needed for the heavy particles to thermalize with the electrons. The thermalization between the electron and heavy particle ensembles is not achieved in the low pressure plasmas applied within this work so that the temperature of the $\mathrm{H_2}$ molecules (called gas temperature), the temperature of the H atoms and the temperature of the ions are far below the electron temperature and typically of the order of $10^{-2} - 10^{-1}\,\mathrm{eV}$ (Maxwellian distribution generally assumed). Therefore, the plasmas are non-thermal plasmas, and due to the given low temperatures they are categorized as low pressure low temperature plasmas.

3.1.2 Reaction rates

Apart from elastic collisions, a multitude of inelastic collisions occur within the plasma, leading to excitation, ionization and dissociation processes for instance. In order to describe the various processes mathematically, reaction rates $\mathcal{R}$ are introduced, which express the occurrence of a specific process per unit volume and unit time. By balancing the reaction rates that act as source terms k and sink terms l for a specific particle or particle state i, the respective density is determined by

$$\frac{\mathrm{d}n_i}{\mathrm{d}t} = \sum_k \mathcal{R}_k - \sum_l \mathcal{R}_l. \tag{3.6}$$

A set of such balance rate equations leads to population density models, which are used to predict the densities of particle species and/or states of particle species in the plasma. Population density models that are applied within this work are so-called collisional radiative models, which are described in section 5.4.3.

---

[2] In the case of a non-Maxwellian distribution (e. g., ν-distribution or bi-Maxwellian distribution [BF94, GMS95, HFF20]), the temperature must be understood as an effective one defined by the mean kinetic energy, i. e., $T^\mathrm{eff} := 2/3k_\mathrm{B}^{-1}\langle E\rangle$.

In low pressure low temperature plasmas, binary collisions between two particle species α and β are dominant and multi-body collisions can be neglected to a good approximation [LL05]. The rate of a binary collisional reaction r is parameterized by the formula

$$\mathcal{R}_r = n_\alpha n_\beta X_r, \tag{3.7}$$

where X_r is the so-called rate coefficient of the reaction. The rate coefficient is given by $\langle \sigma_r v_{\mathrm{rel}} \rangle$, where $\sigma_r(v_{\mathrm{rel}})$ is the cross section of the reaction and v_{rel} is the relative speed between the collision partners. In the case of electron collisions with heavy particles, v_{rel} can be approximated by the speed of the electrons and the corresponding rate coefficient is calculated by [SVY95]

$$X_r = \int\limits_0^\infty \sigma_r(E) \sqrt{\frac{2E}{m_\mathrm{e}}} \frac{f_\mathrm{e}(E)}{n_\mathrm{e}} \mathrm{d}E, \tag{3.8}$$

where the EEDF f_e is a function of the electron temperature.

3.1.3 Plasma processes

The variety of collision processes that can occur in low pressure low temperature hydrogen plasmas are comprehensively reviewed in [JRS03]. The processes include reactions such as excitation, ionization, dissociation, charge transfer and recombination, and the relevance of the different processes depends on the given plasma parameters. In the following, a selection of the most relevant reactions for the hydrogen discharges applied within this work are outlined. As described in detail in section 3.2, the electronic states of the hydrogen atom are characterized by the principal quantum number n (ground state $n = 1$) and the states of the hydrogen molecule are described by the electronic state (ground state $\mathrm{X}\,^1\Sigma_\mathrm{g}^+$) in combination with vibrational (ν) and rotational (N) quantum numbers.

Dissociation The dissociation energy of the hydrogen molecule is 4.52 eV [Rum21]. The predominant channel for the dissociation of H_2 molecules within the plasma is electron impact excitation from the electronic ground state into the anti-bonding $\mathrm{b}\,^3\Sigma_\mathrm{u}^+$ state, leading to the formation of two ground state H atoms:

$$\mathrm{H}_2(\mathrm{X}\,^1\Sigma_\mathrm{g}^+, \nu) + \mathrm{e}^- \longrightarrow \mathrm{H}_2(\mathrm{b}\,^3\Sigma_\mathrm{u}^+) + \mathrm{e}^- \longrightarrow 2\,\mathrm{H}(n = 1) + \mathrm{e}^-. \tag{3.9}$$

The cross section of reaction (3.9) is higher the higher the vibrational quantum number of the H_2 molecule [C$^+$01].

Further dissociative excitation processes include the dissociation via higher electronic states of H_2 resulting in excited hydrogen atoms and the radiative de-excitation from higher electronic H_2 states into the $\mathrm{b}\,^3\Sigma_\mathrm{u}^+$ state. However, the cross sections (and reaction rates) for such processes are much smaller than the ones for reaction (3.9) due to the involvement of higher electronic states of the H_2 molecule [C$^+$01].

Ionization The most relevant process that leads to the formation of positive ions is electron impact ionization:

$$\mathrm{H}, \mathrm{H}_2 + \mathrm{e}^- \longrightarrow \mathrm{H}^+, \mathrm{H}_2^+ + 2\,\mathrm{e}^-. \tag{3.10}$$

The energy thresholds for the ionization out of the ground state are 13.6 eV for the H atom and 15.4 eV for the H_2 molecule [Rum21]. During subsequent collisions of the ions with H_2 molecules, excitation, charge transfer and dissociation processes occur. A governing reaction is

$$\mathrm{H}_2^+ + \mathrm{H}_2 \longrightarrow \mathrm{H}_3^+ + \mathrm{H}, \tag{3.11}$$

where the triatomic ion H_3^+ is produced either via the transfer of a proton or a hydrogen atom. This reaction is exothermic by 1.73 eV and the H_3^+ ion represents a stable ion (in contrast to the H_3 molecule, which is not stable and dissociates into H_2 and H) [JRS03]. The dissociation energy of H_3^+ is comparable to H_2 ($\approx 4.5\,\mathrm{eV}$), which is substantially higher than the one of H_2^+ ($\approx 2.7\,\mathrm{eV}$) [JRS03]. Therefore, the share of H_3^+ ions to the total positive ion density is typically significant. In low temperature plasmas generated at a pressure of several Pa, it has been found experimentally that H_3^+ is even the dominant ion [M$^+$06, NK07]. In consequence, the mean ion mass can be approximated by 3 u in the present work. Since the cross section of reaction (3.11) is comparable for deuterium [CF72], the respective mean ion mass of 6 u can be used.

Excitation and spontaneous emission The excitation of hydrogen atoms and molecules occurs predominantly out of the ground state via collisions with electrons, following the scheme

$$\mathrm{H}, \mathrm{H}_2 + \mathrm{e}^- \longrightarrow \mathrm{H}(i), \mathrm{H}_2(i) + \mathrm{e}^- \tag{3.12}$$

with i denoting the excited states of the particles. The predominant de-excitation channel into lower electronic states is spontaneous photon emission, leading to characteristic emission lines from the H atom and emission bands from the H_2 molecule (see section 3.2).

Additional excitation channels for hydrogen atoms are dissociative excitation processes as mentioned above and ion recombination processes [WF16]. Furthermore, photon self-absorption can play a role, which describes the process of the reabsorption of an emitted photon on its way through the plasma volume (so-called radiation trapping). The consideration of self-absorption is in particular relevant for the resonant emission lines of the H atom, increasing the density of excited states which consequently leads to an influence also on non-resonant transitions [W^+21c].

The dominant loss channel for hydrogen atoms and positive hydrogen ions produced within the bulk plasma is diffusion to the vessel walls [Beh91]. The diffusion is dependent on the amount of collisions the particle undergoes before it reaches the vessel wall, which can be characterized by the mean free path. The mean free path of a particle α between collisions with a particle species β is given by [CB11]

$$\lambda_\alpha = \frac{1}{n_\beta \sigma(v_{\mathrm{rel}})}, \tag{3.13}$$

where σ is the cross section of the collisional process that is dependent on the relative speed between the collision partners. In the plasmas generated at the experiment ACCesS within this work, the mean free path of atoms and ions is determined mainly by elastic collisions with the H_2 molecules and the resulting mean free paths are smaller than the vessel dimensions. Therefore, so-called laminar diffusion is present.

When H atoms diffuse to the vessel walls, they can form strong bonds with the surfaces of the plasma vessel as they are chemically active radicals. In the steady-state condition, a certain coverage of H atoms on the surfaces is present and impinging H atoms can undergo recombination processes. The efficiency of the recombination of H atoms to H_2 molecules is expressed in terms of the so-called recombination coefficient, which is defined as the ratio of H atoms striking the surface with subsequent recombination to the total number of H atoms impinging onto the surface [SL49]. In general, the recombination coefficient for metallic surfaces is orders of magnitude higher than the one for dielectric surfaces. In the present work, stainless steel and quartz vessels are used (see chapter 5), for which typical values for the recombination coefficient are 0.1 [MDZ99, MM71] and $10^{-4} - 10^{-2}$ [G^+59, KB91, WW62], respectively. Consequently, the atomic hydrogen density within the bulk plasma is higher in the quartz vessel than in the stainless steel vessel when the same operational parameters (gas pressure and RF power) are used.

The diffusion of positive ions to the vessel walls is coupled to electrons due to the quasi-neutrality principle (so-called ambipolar diffusion [LL05]). At the vessel walls, the positive ions and electrons recombine to neutrals. As electron impact ionization of neutral particles in the bulk plasma constitutes the main production channel of the ions and diffusion to the vessel walls the main loss channel, the ionization balance can be expressed according to equation (3.6) via

$$0 = n_\mathrm{e} n_0 X_\mathrm{ion}(T_\mathrm{e}) - \frac{n_\mathrm{i+}}{\tau_\mathrm{c,i+}}, \tag{3.14}$$

where the steady-state condition $\mathrm{d}n_\mathrm{i+}/\mathrm{d}t = 0$ is used and for simplicity reasons only one neutral species with density n_0 and one ion species with density $n_\mathrm{i+}$ are considered. While the ionization rate is expressed after equation (3.7) with X_ion denoting the ionization rate coefficient (steep dependence on T_e), the diffusion rate is given by the ratio of the ion density and the average confinement time $\tau_\mathrm{c,i+}$ of the ions. The ion confinement time follows the relation [Möl93]

$$\tau_\mathrm{c,i+} \propto \lambda_\mathrm{i+}^{-1} T_\mathrm{e}^{-1} \sqrt{m_\mathrm{i+} T_\mathrm{gas}}. \tag{3.15}$$

Neglecting the inverse linear T_e-dependence of the confinement time against the steep T_e-dependence of the ionization rate coefficient and using $n_\mathrm{e} = n_\mathrm{i+}$, equations (3.14) and (3.15) yield

$$X_\mathrm{ion}(T_\mathrm{e}) \propto \frac{\lambda_\mathrm{i+}}{n_0 \sqrt{m_\mathrm{i+}}}. \tag{3.16}$$

The correlation (3.16) shows that as the pressure decreases, i. e., the neutral density decreases and the mean free path increases, the ionization rate coefficient and hence the electron temperature increase. The reason is an enhanced ion diffusion to the vessel walls that must be balanced by a higher ionization rate within the bulk plasma. Furthermore, an increase of the ion mass leads to a decrease of the ionization rate coefficient and thus of the electron temperature due to a slower diffusion to the vessel walls.

3.2 Photon fluxes

The energy of a photon resulting from the relaxation of a particle from an excited state i into an energetically lower lying state k is equal to the energy difference between the corresponding energy levels E_i and E_k. The wavelength of the photon is given by

$$\lambda_{ik} = \frac{hc}{E_i - E_k}, \tag{3.17}$$

where h denotes the Planck constant and c the vacuum speed of light. The photon emission is described in terms of the spectral emissivity ε_λ, which is defined as the number of photons emitted per unit wavelength, volume and time into the unit sphere. The spectral emissivity integrated over a distinct wavelength interval yields the emissivity ε in units of $\mathrm{m}^{-3}\mathrm{s}^{-1}$ and constitutes the rate of optical transitions. The emissivity of a distinct transition $i \rightarrow k$ can be expressed by

$$\varepsilon_{ik} = n_i A_{ik}, \tag{3.18}$$

where n_i is the population density of the excited state i and A_{ik} is the spontaneous transition probability, which is called Einstein coefficient for spontaneous emission [TLJ99]. Under the assumption of a homogeneous and isotropic emission over the considered plasma volume V, the average photon flux $\mathit{\Gamma}_{\mathrm{ph},ik}$ onto the plasma surface $S = \partial V$ yields

$$\mathit{\Gamma}_{\mathrm{ph},ik} = \frac{V}{S}\varepsilon_{ik} \tag{3.19}$$

and is given in units of $\mathrm{m}^{-2}\mathrm{s}^{-1}$.

In the subsequent sections, optical transitions of hydrogen atoms and molecules are described in detail. The different spectral regions in which the transitions are located are defined as follows [Kun09]: $380 - 750\,\mathrm{nm}$ is the visible (VIS) range, the adjacent region toward longer wavelengths is the near infrared (near IR) range, $200 - 380\,\mathrm{nm}$ is the ultraviolet (UV) range, and $0.15 - 200\,\mathrm{nm}$ is the vacuum ultraviolet (VUV) range. The range of $0.15 - 105\,\mathrm{nm}$ is sometimes specifically referred to as extreme ultraviolet (EUV or XUV) in the literature, but this distinction is not made within this work.

3.2.1 Emission of atomic hydrogen

The hydrogen atom consists of one proton that is orbited by one electron. Neglecting fine structure and hyperfine structure splitting, the electronic energy levels can be described by the formula

$$E_n = R_\mathrm{H}\left(1 - \frac{1}{n^2}\right), \tag{3.20}$$

where $n \in \mathbb{N}$ is the principal quantum number and $R_{\mathrm{H}} = 13.6\,\mathrm{eV}$ is the Rydberg energy for hydrogen. R_{H} represents the ionization energy of the H atom, which is approached for $n \to \infty$.

Optical transitions are allowed between all energy levels E_n. Prominent emission lines are the Lyman and Balmer series. The Lyman series results from the resonant transitions $n' \geq 2 \to n'' = 1$ and the corresponding emission lines lie in the VUV range (most energetic radiation from the H atom). The Balmer series originates from transitions $n' \geq 3 \to n'' = 2$ and the emission lines lie in the VIS range. Further atomic lines are located in the IR range and are not considered within this work (e. g., Paschen and Brackett series). The wavelengths of the first lines of the Lyman and Balmer series are summarized in table 3.1. The respective lines of the deuterium atom are additionally listed, showing that only slight isotopic differences exist due to the higher mass of the nucleus (slightly different Rydberg energy R_{D}).

Table 3.1: *First five lines of the Lyman series (VUV range) and Balmer series (VIS range) of the hydrogen and deuterium atom [K⁺22].*

			Hydrogen		Deuterium	
Series	n'	n''	Designation	λ_0 / nm	Designation	λ_0 / nm
Lyman	2	1	Ly-H_α	121.6	Ly-D_α	121.5
	3	1	Ly-H_β	102.6	Ly-D_β	102.5
	4	1	Ly-H_γ	97.3	Ly-D_γ	97.2
	5	1	Ly-H_δ	95.0	Ly-D_δ	94.9
	6	1	Ly-H_ϵ	93.8	Ly-D_ϵ	93.8
Balmer	3	2	Ba-H_α	656.3	Ba-D_α	656.1
	4	2	Ba-H_β	486.1	Ba-D_β	486.0
	5	2	Ba-H_γ	434.0	Ba-D_γ	433.9
	6	2	Ba-H_δ	410.2	Ba-D_δ	410.1
	7	2	Ba-H_ϵ	397.0	Ba-D_ϵ	396.9

3.2.2 Emission of molecular hydrogen

The hydrogen molecule is a diatomic homonuclear molecule. Apart from its translational energy, the molecule holds internal energy in form of electronic energy and vibrational and rotational motion. According to the Born-Oppenheimer approximation, the molecular wave function can be separated into an electronic and a nuclear part, which is justified by the much slower motion of the nuclei compared to the electrons due to the mass difference. In a further approximation, also the nuclear wave function can be decoupled into a vibrational and rotational part and the total internal energy E_{int} of the molecule can be expressed by the sum of the independent terms [TLJ99]

$$E_{\mathrm{int}} = E_{\mathrm{el}} + E_{\mathrm{vib}} + E_{\mathrm{rot}}, \tag{3.21}$$

where E_{el}, E_{vib} and E_{rot} are the electronic, vibrational and rotational energy eigenvalues of the respective wave functions.

The electronic states of the H_2 molecule are described in terms of the so-called united atom approximation, where one of the two electrons is considered to remain in the ground state while the other can be excited into a higher orbital. The corresponding spectroscopic notation is given by [Fan06]

$$nl\,^{2S+1}\Lambda^{+/-}_{\mathrm{g/u}}, \tag{3.22}$$

where the excited electron is characterized by the principal quantum number n and orbital angular momentum quantum number l. $2S+1$ is the multiplicity of the total molecular electronic state, where the total spin can take the values $S = 0$ (singlet system) and $S = 1$ (triplet system). Λ is the quantum number of the total orbital angular momentum of the two electrons in the molecule (projected onto the internuclear axis) and its values $0, 1, 2, \ldots$ are designated by Greek capital letters $\Sigma, \Pi, \Delta, \ldots$ The super- and subscripts "+/−" and "g/u" signify the symmetry of the molecular electronic wave function. The notation in (3.22) is usually further simplified by using a Latin letter instead of n and l. For the hydrogen molecule, upper case letters are used for the singlet system and lower case letters for the triplet system. The ground state is denoted as $\mathrm{X}\,^1\Sigma^+_{\mathrm{g}}$. Further details about the electronic states can be found in [Her50, TLJ99] for instance.

The electronic energy eigenvalues E_{el} are dependent on the distance R of the nuclei. Potential curves $E_{\mathrm{el}}(R)$ of selected states of the H_2 molecule are presented in figure 3.1. While the potential curves of stable bonding states exhibit at least one distinct minimum, the curves of anti-bonding states monotonically decrease with increasing R. An anti-bonding state is the $\mathrm{b}\,^3\Sigma^+_{\mathrm{u}}$ state (lowest state in the triplet system), which dissociates into two ground state H atoms (see reaction (3.9)). For a comparison of the energy distances between the electronic states of the H_2 molecule and H atom, the energy levels of the H atom according to equation (3.20) are supplementary depicted on the right of figure 3.1.

The bonding electronic states possess a discrete set of vibrational levels, which is exemplarily indicated for the electronic ground state of the H_2 molecule in

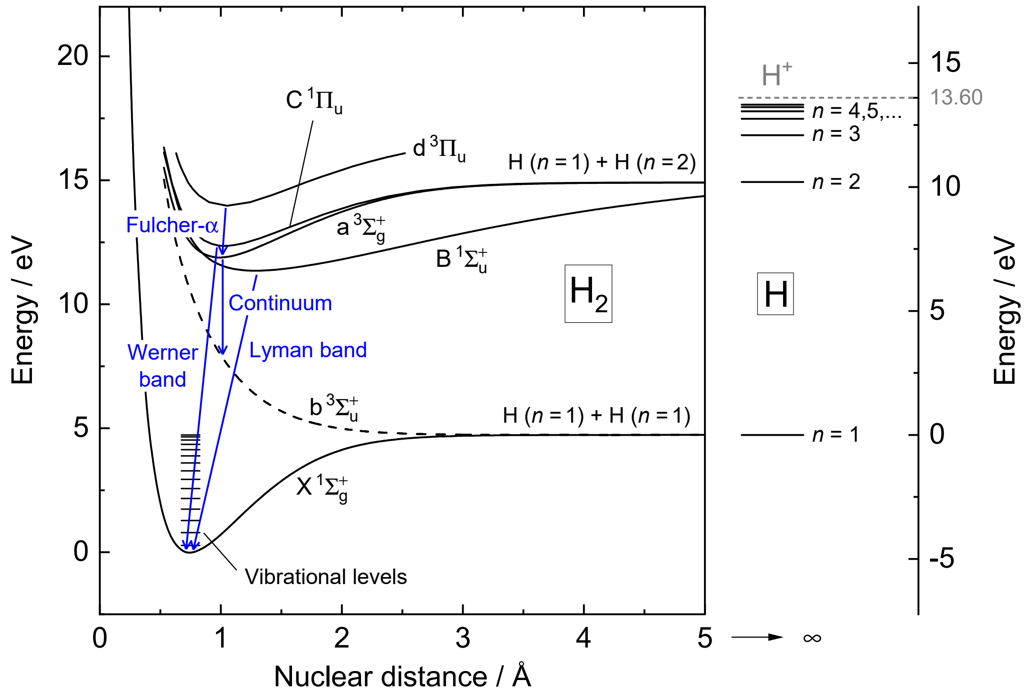

Figure 3.1: *Potential curves of selected electronic states of the H_2 molecule [Sha70, Sha71] with exemplarily indicated vibrational levels of the ground state [FW06]. On the right, electronic energy levels of the H atom according to equation (3.20) are depicted (note the shift of the energy axis to illustrate the correlation with the dissociation products of the hydrogen molecule). Prominent optical transitions of the H_2 molecule are indicated by the blue arrows.*

figure 3.1. Furthermore, each vibrational level has discrete rotational levels (not depicted for the sake of clarity). Thus, a distinct molecular state is described by the electronic state in combination with the vibrational and rotational level (so-called ro-vibronic state). The vibrational levels are characterized by the vibrational quantum number $\nu \in \mathbb{N}_0$ and the rotational levels by the rotational quantum number $N \in \mathbb{N}_0$. The energy difference between vibrational and rotational levels decreases with increasing ν and N, respectively, and the energy differences of the rotational levels are typically orders of magnitude smaller compared to the vibrational levels at comparable quantum number values [Die72, FW06].

Optical transitions between two molecular states of H_2 are subject to a number of quantum mechanical selection rules, which can be summarized as follows [Her50]: $\Delta\Lambda = 0, \pm 1$, $\Delta S = 0$ (i. e., intersystem crossings between singlet and triplet states are forbidden), and $\Delta N = 0, \pm 1$ with $N = 0 \not\leftrightarrow N = 0$. Further, the restriction u ↔ g holds, and for states with $\Lambda = 0$ the rule $\Sigma^{+(-)} \leftrightarrow \Sigma^{+(-)}$ applies. Changes of ν are not restricted. To designate the quantum numbers of the upper and lower electronic states that are involved in the optical transition, single and double prime symbols are used, respectively. The rotational transitions $N' \rightarrow N''$ corresponding to a certain vibrational transition $\nu' \rightarrow \nu''$ are categorized into so-called branches, where $\Delta N = -1$ denotes the P, $\Delta N = 0$ the Q and $\Delta N = +1$ the R branch.

Prominent ro-vibronic transitions of the H_2 molecule are indicated by the blue arrows in figure 3.1. The corresponding wavelength regions of the emission bands are illustrated in figure 3.2, where for the sake of completeness also the emission lines of the first five lines of the Lyman and Balmer series are indicated (see table 3.1). The most intense emission of the H_2 molecule in the VIS spectral region originates from transitions from the $\mathrm{d}\,^3\Pi_\mathrm{u}$ into the $\mathrm{a}\,^3\Sigma_\mathrm{g}^+$ state. The emission lines are distributed over the wavelength range of 520 – 770 nm, with the most intense part lying within 590 – 650 nm. The transition is known as the Fulcher-α transition. In the VUV range, the most intense emission results from the resonant transitions $\mathrm{C}\,^1\Pi_\mathrm{u} \rightarrow \mathrm{X}\,^1\Sigma_\mathrm{g}^+$ and $\mathrm{B}\,^1\Sigma_\mathrm{u}^+ \rightarrow \mathrm{X}\,^1\Sigma_\mathrm{g}^+$, which are named Werner and Lyman band, respectively. While the Werner band emission is most intense in the range of 80 – 130 nm, the emission of the Lyman band is located predominantly between 130 – 170 nm. Furthermore, an overlap with the continuum radiation from the transition $\mathrm{a}\,^3\Sigma_\mathrm{g}^+$ into the anti-bonding state $\mathrm{b}\,^3\Sigma_\mathrm{u}^+$ in the triplet system is given, with the most intense part located in the range of 150 – 280 nm.

The higher nuclear mass of D_2 has a negligible impact on the electronic structure of the molecule. However, it leads to closer lying vibrational and rotational levels [FW06, Die72, FSC85] so that the ro-vibrational emission lines are located closer to each other (e. g., most intense part of D_2 Fulcher-α emission lies in the range of 595 – 635 nm).

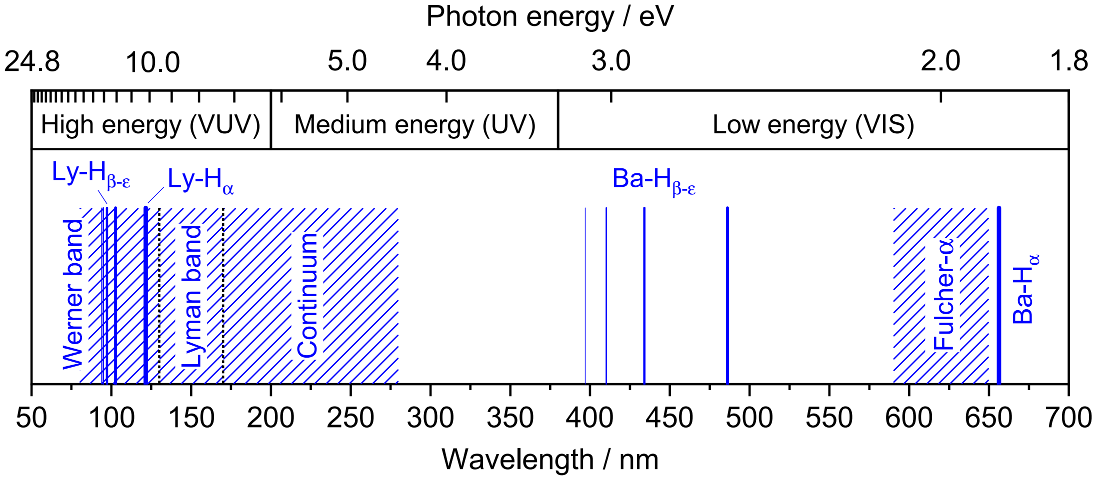

Figure 3.2: *Overview of the dominant molecular emission ranges and atomic emission lines occurring in low pressure low temperature hydrogen discharges.*

The photon emission from the Fulcher-α transition together with the Balmer series in the VIS (low energy) range is diagnostically exploited for the determination of plasma parameters within this work (see section 5.4.3). In contrast, the occurring fluxes in the UV (medium energy) and VUV (high energy) range with photon energies of several eV are of particular relevance in the context of plasma-surface interactions with caesiated surfaces (see section 4.3).

3.3 Particle fluxes

In general, the particle flux $\boldsymbol{\Gamma}_\alpha$ of a particular species α is calculated by the product of the corresponding particle density and velocity, i. e.,

$$\boldsymbol{\Gamma}_\alpha(\boldsymbol{r},t) = n_\alpha(\boldsymbol{r},t)\boldsymbol{v}_\alpha(\boldsymbol{r},t). \tag{3.23}$$

For the determination of the particle fluxes striking a surface within the plasma, neutrals and ions must be treated separately due to the presence of electrostatic fields.

3.3.1 Neutral particles

The average flux of a neutral particle species onto a surface can readily be determined from the respective distribution function f_α within the bulk plasma:

$$\boldsymbol{\Gamma}_\alpha(\boldsymbol{r},t) = n_\alpha(\boldsymbol{r},t)\langle\boldsymbol{v}_\alpha(\boldsymbol{r},t)\rangle = \int \boldsymbol{v} f_\alpha(\boldsymbol{r},\boldsymbol{v},t)\mathrm{d}^3v. \tag{3.24}$$

When the distribution function is given by the isotropic Maxwell-Boltzmann distribution, the average (thermal) particle flux in one spatial direction is calculated from equation (3.24) by [LL05]

$$\Gamma_\alpha = \frac{1}{4}n_\alpha\langle v_\alpha\rangle \overset{(3.3)}{=} \frac{1}{4}n_\alpha\sqrt{\frac{8k_\mathrm{B}T_\alpha}{\pi m_\alpha}}, \tag{3.25}$$

and the respective mean kinetic energy of the particles is given by equation (3.5).

As mentioned in section 3.1.1, the distribution function of the neutral particle species H and H_2 can generally be assumed Maxwellian, and the temperature of the H atoms is to a good approximation equal to the gas temperature T_gas. The total neutral particle density $n_\mathrm{n} = n_\mathrm{H} + n_{\mathrm{H}_2}$ can be approximated from the measured gas pressure p in the vacuum chamber via

$$n_\mathrm{n} = \frac{p}{k_\mathrm{B} T_\mathrm{gas}}, \tag{3.26}$$

and the atomic and molecular hydrogen fluxes can be determined separately when the density ratio $n_\mathrm{H}/n_{\mathrm{H}_2}$ is known (see section 5.4.3).

3.3.2 Positive ions

The positive ion flux striking a metal surface within the plasma cannot be described by the thermal ion flux due to the presence of an electrostatic boundary layer at the plasma-surface interface. The formation of a boundary layer can be understood by the following considerations: An electrically insulated sample surface immersed in the plasma faces a much higher thermal electron than positive ion flux due to $T_\mathrm{e} \gg T_\mathrm{i+}$, $m_\mathrm{e} \ll m_\mathrm{i+}$ and $n_\mathrm{e} \approx n_\mathrm{i+}$ (the density of negative ions is taken as $\ll n_\mathrm{e}$). The different charge fluxes lead to the accumulation of negative space charge at the surface and thus to the buildup of a potential gradient between the surface and the plasma, resulting in an electrostatic repulsion of electrons and attraction of positive ions. In steady-state, the surface is on the so-called floating potential ϕ_fl, which is below the potential of the bulk plasma ϕ_pl that is called plasma potential. The resulting potential difference $\phi_\mathrm{pl} - \phi_\mathrm{fl}$ leads to the balance of the electron and ion fluxes onto the surface.

In figure 3.3, the electron and ion density as well as the electrostatic potential are qualitatively illustrated as a function of the distance x to a floating surface in the steady-state condition. The region $x_\mathrm{s} \leq x \leq x_\mathrm{surf}$ in front of the surface where the potential steeply decreases (typically by several V) is called plasma sheath. At $x = x_\mathrm{s}$ quasi-neutrality is still fulfilled, but the charge density $n(x_\mathrm{s}) = n_\mathrm{s}$ is lower compared to the one within the bulk plasma n_0 and can be approximated by $n_\mathrm{s} = n_0/2$ [CC03]. Within the sheath, the electron density drops below the ion density. The thickness of the sheath in which the quasi-neutrality breaks down is of the order of a few electron Debye lengths λ_De. The electron Debye length constitutes the characteristic screening length within which electrostatic fields introduced in the plasma are effectively shielded and is given by

$$\lambda_\mathrm{De} = \sqrt{\frac{\varepsilon_0 k_\mathrm{B} T_\mathrm{e}}{n_\mathrm{e} e^2}}, \tag{3.27}$$

where ε_0 denotes the vacuum permittivity and e the elementary charge. With typical electron densities of $\sim 10^{16}\,\mathrm{m}^{-3}$ and electron temperatures of a few eV,

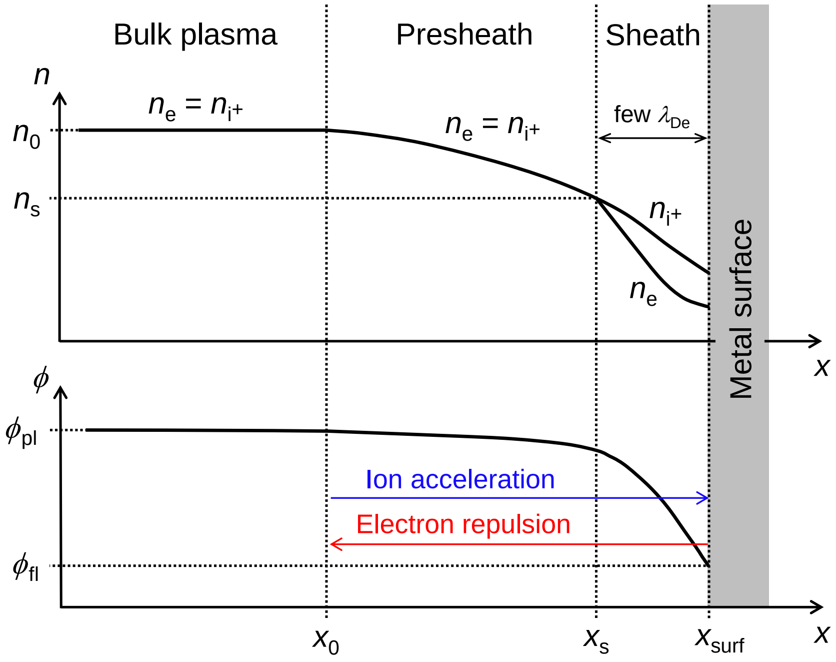

Figure 3.3: *Qualitative illustration of the spatial profiles of the positive ion and electron density (upper diagram) as well as of the electrostatic potential of the plasma (lower diagram) in the vicinity of a floating metal surface. The presence of negative ions is neglected.*

the Debye length is in the range of $10 - 100\,\mu\text{m}$.

The potential drop in front of the surface leads to a directional flux of positive ions toward the surface. Neglecting particle collisions within the sheath, the minimum ion speed at $x = x_s$ that is required to balance the electron and ion fluxes onto the surface can be derived from the principles of conservation of ion energy and continuity of ion flux [LL05]. The result is known as the Bohm sheath criterion and reads

$$v_{i+}(x = x_s) \geq v_{\mathrm{Bohm}} = \sqrt{\frac{k_B T_e}{m_{i+}}}. \tag{3.28}$$

The Bohm speed v_{Bohm} is higher than the average ion speed in the bulk plasma. The acceleration of the ions takes place via a potential drop across the so-called presheath ($x_0 \leq x \leq x_s$), which has a width of typically a few mm. The potential drop can be approximated by $k_B T_e/(2e)$ and is thus of the order of 1 V. Since the ion flux through the sheath remains constant when collisional processes can be neglected, the minimum ion flux (Bohm flux) onto the surface is given by

$$\Gamma_{\mathrm{Bohm}} = n_s v_{\mathrm{Bohm}} = n_s \sqrt{\frac{k_B T_e}{m_{i+}}}. \tag{3.29}$$

The maximum kinetic energy of the ions striking the surface is determined by the potential difference between the plasma and the surface, which is about [LL05]

$$\Delta\phi = \frac{k_\mathrm{B}T_\mathrm{e}}{e}\left(\frac{1}{2} + \ln\sqrt{\frac{m_\mathrm{i^+}}{2\pi m_\mathrm{e}}}\right) \tag{3.30}$$

in case the surface is on the floating potential.

The presence of negative ions within the plasma can lead to changes of the Bohm speed depending on their density and temperature [CB11]. Furthermore, negative ions produced at the surface further complicate the sheath topology, in particular when the H^- ions become the dominant negatively charged species (ion-ion plasma) [M^+19]. At the ACCesS experiment, however, the negative ion density is typically much smaller than the electron density [Cri18] so that the influence of negative ions on the plasma sheath can be neglected.

4 Work function of metal surfaces upon Cs interaction

Caesium is an alkali metal with a melting point of 28.5 °C at atmospheric pressure [Rum21]. The Cs atom has a mass of 132.9 u and possesses 55 electrons with the configuration [Xe] $6s^1$ [Rum21]. The valence electron in the 6s orbital leads to a high electropositivity and to a low ionization energy of 3.89 eV [Rum21]. In consequence, Cs exhibits a high chemical reactivity. The reported work function values for pure bulk Cs are in the range of $\chi_{\mathrm{Cs}} = 1.95 - 2.14\,\mathrm{eV}$ [Rum21, Mic77].

4.1 Pure Cs surface adsorption

The induction of work function changes of metal surfaces upon Cs adsorption is a widely studied topic [Alt86, AM89, C$^+$12, S$^+$21a]. Extensive experimental investigations on the change of the substrate work function χ_{sub} with different Cs coverages θ have been conducted mostly under ultra-high vacuum (UHV) conditions, i. e., with a base pressure $\lesssim 10^{-9}$ mbar. The Cs coverage is defined hereinafter as the ratio of the number of bonded Cs atoms per unit area to the surface density corresponding to a full Cs monolayer (ML). Neglecting surface roughness and crystallographic structures, the surface density of one ML is approximated by 5.6×10^{18} Cs atoms per m^2 (covalent radius of Cs = 2.38 Å [Rum21]). As proposed in [Alt86], the adsorbate-induced work function variation upon θ can be described by the semiempirical formula

$$\chi(\theta) \simeq \chi_{\mathrm{sub}} + \frac{6\Delta\chi_{\mathrm{max}}}{(3-\theta_{\mathrm{min}})\theta_{\mathrm{min}}}\theta - \frac{3\Delta\chi_{\mathrm{max}}(\theta_{\mathrm{min}}+1)}{(3-\theta_{\mathrm{min}})\theta_{\mathrm{min}}^2}\theta^2 + \frac{2\Delta\chi_{\mathrm{max}}}{(3-\theta_{\mathrm{min}})\theta_{\mathrm{min}}^2}\theta^3, \quad (4.1)$$

where $\Delta\chi_{\mathrm{max}} = \chi_{\mathrm{min}} - \chi_{\mathrm{sub}} < 0$ is the maximum work function change of the substrate that is reached for χ_{min} at θ_{min}. In figure 4.1(a), the evolution of the work function according to equation (4.1) is illustrated. With increasing Cs coverage, the work function decreases initially almost linearly. The decrease slows down during the transition from the low to medium coverage regime and the work function

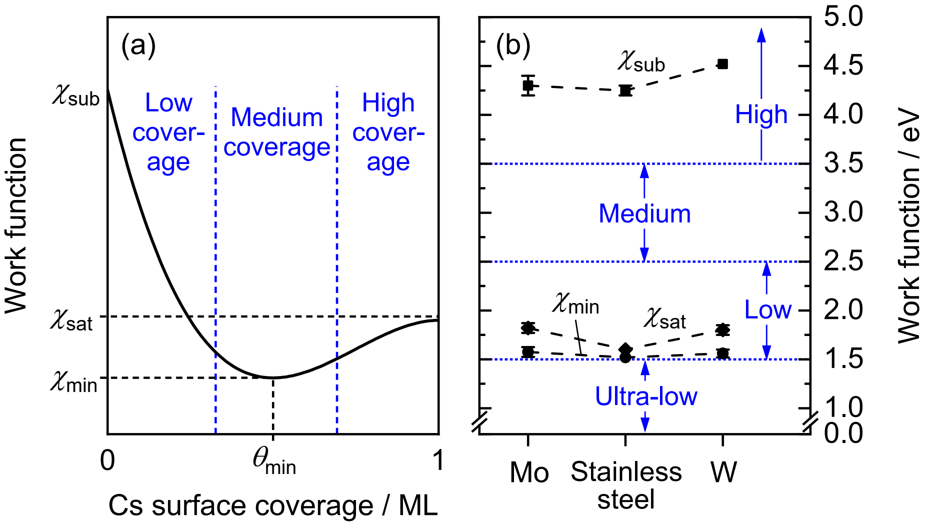

Figure 4.1: *(a) Work function variation of a metal substrate as a function of the relative Cs coverage according to equation (4.1). (b) Corresponding literature values for different polycrystalline metal substrates measured under UHV conditions [Wil66a, Wil66b, SS68]. The high, medium, low and ultra-low work function regimes defined in chapter 2 are indicated.*

reaches a minimum $\chi_{\rm min}$ with $\theta_{\rm min}$ being typically in the range of $0.5 - 0.7\,\mathrm{ML}$. Afterward, the work function slowly increases again and the value of bulk Cs is approached for $\theta \gtrsim 1\,\mathrm{ML}$ ($\chi_{\rm sat} \lesssim \chi_{\rm Cs}$). Since the plasma grid surface at the NNBI ion sources is made of polycrystalline Mo, the corresponding literature values for $\chi_{\rm sub}$, $\chi_{\rm min}$ and $\chi_{\rm sat}$ are depicted in figure 4.1(b). For comparison, literature values are also given for polycrystalline W and stainless steel. While all the substrate work functions are high ($4.3 - 4.5\,\mathrm{eV}$), the minimum and saturation work functions provided via Cs adsorption are in the low work function regime ($1.5 - 2.0\,\mathrm{eV}$).

The work function change of the metal substrate upon Cs adsorption can be understood within the framework of the Langmuir-Gurney model [DM97, SS00]. As illustrated in figure 4.2, the electronic energy level of the valence s electron of the Cs atom is lowered and lifetime-broadened when it approaches the metal surface, allowing electron tunneling from the Cs atom into the valence band (VB) of the metal. The resulting chemisorption bond is characterized by the attractive electrostatic force between the partially positively charged Cs adatom and the corresponding negative screening charge density at the metal surface. The electronic charge transfer induces an electric dipole moment on the metal surface and therefore a reduction of the surface work function. The approximately linear decrease of the work function in the low coverage regime can consequently be explained by the increasing amount of adsorbate-induced dipole moments on

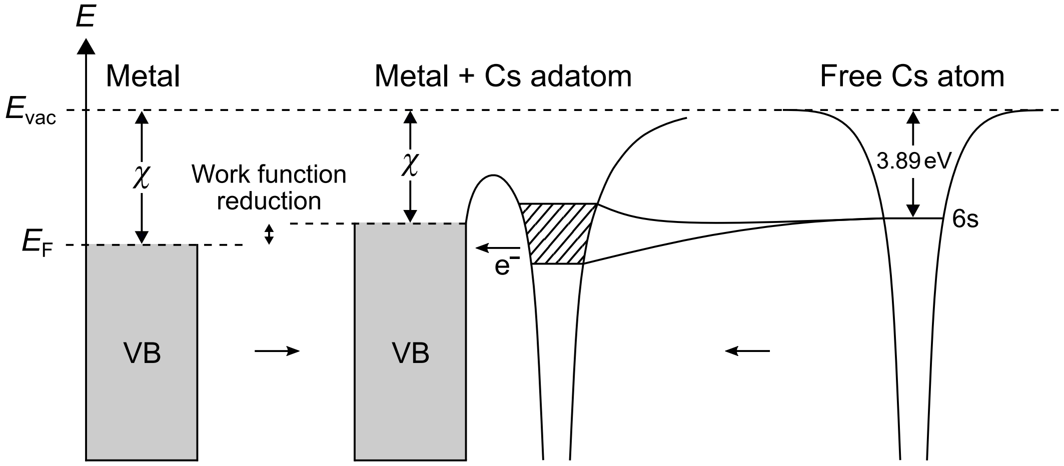

Figure 4.2: *Electronic energy diagram illustrating the work function reduction of a metal surface upon Cs adsorption after the Langmuir-Gurney picture.*

the metal surface. However, the increase of the Cs coverage leads to decreasing interatomic distances between the adatoms and repulsive dipole-dipole interactions arise. This leads to a gradual mutual depolarization, i. e., to a decrease of the net charge transfer to the substrate, and therefore to a work function increase in the medium coverage regime. In the high coverage regime, covalent interactions between the Cs adatoms are dominant and a metallization of the Cs overlayer takes place [FO72, C$^+$12].

Due to the increasing repulsive dipole-dipole interactions with increasing Cs coverage, the surface binding energy of Cs atoms decreases from about 3.3 eV (dependent on the substrate material) to 0.8 eV (sublimation enthalpy of bulk Cs) [K$^+$05]. Already for Cs coverages above one ML, the interaction of the Cs atoms with the metal substrate is significantly reduced and the cohesion of the Cs atoms is mainly determined by Cs-Cs interactions. In this case, the Cs desorption flux can be estimated from the Cs vapor pressure p_{Cs} above the Cs surface. Assuming thermal equilibrium between the Cs surface and the Cs vapor, the Cs desorption flux is determined by the surface temperature T_{surf} and is given via the kinetic theory of gases by

$$\Gamma_{\mathrm{Cs}}^{\mathrm{desorp}}(T_{\mathrm{surf}}) = \frac{p_{\mathrm{Cs}}(T_{\mathrm{surf}})}{\sqrt{2\pi m_{\mathrm{Cs}} k_{\mathrm{B}} T_{\mathrm{surf}}}}. \tag{4.2}$$

In figure 4.3, p_{Cs} and $\Gamma_{\mathrm{Cs}}^{\mathrm{desorp}}$ are plotted as a function of T_{surf}. Using the estimation that 5.6×10^{18} Cs atoms per m^2 correspond to $\theta = 1$, desorption fluxes of 0.4 ML/s and 1 ML/s are given at 25 °C (room temperature) and 33 °C, respectively. At the NNBI ion sources and at ACCesS, typical Cs fluxes toward the surface are in the range of $10^{-4} - 10^{-2}$ ML/s ($\sim 10^{15} - 10^{17}\,\mathrm{m}^{-2}\mathrm{s}^{-1}$) [Mim18, W$^+$18a, CFF20a]

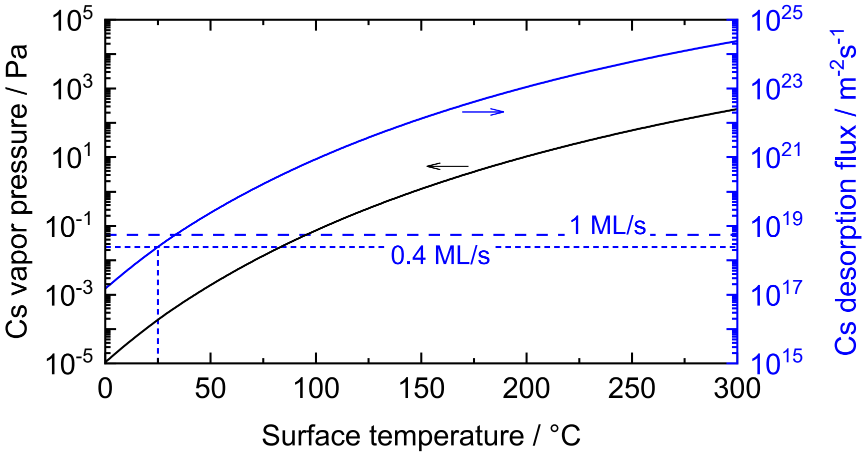

Figure 4.3: *Cs vapor pressure for Cs coverages above one ML as a function of the surface temperature [TL37], together with the corresponding Cs desorption flux. The estimated Cs desorption flux corresponding to 1 ML/s as well as the desorption flux at 25 °C (room temperature) are indicated.*

and the surface temperature is at or above room temperature. In consequence, the growth of pure Cs multilayers would not be possible.

4.2 Influence of coadsorbates on the Cs layer

In contrast to UHV chambers, ion sources operate in a limited vacuum environment and the amount of coadsorbates is thus not negligible. At a typical base pressure of $\sim 10^{-6}$ mbar, the residual gas flux (mainly composed of water vapor and some small amounts of N_2 and O_2) is of the order of $10^{18}\,m^{-2}s^{-1}$ and therefore larger than the typical Cs flux. Furthermore, the surface upon caesiation is exposed to hydrogen species during plasma operation. As Cs exhibits a high chemical reactivity, the formation of Cs compounds is expected [FF17]. Some relevant Cs compounds with regard to the present gas species are summarized in table 4.1, together with the corresponding standard enthalpies of formation $\Delta_f H^0$ and melting points T_{melt} (if available). Whether or not a Cs compound is formed spontaneously depends on the different intermediate steps of the synthesis. However, in each case, the standard enthalpy of formation is negative, i. e., the Cs compound is more stable than its reactants. Under standard conditions, the compounds are solid and crystallize with ionic binding characteristics, and the vapor pressure of the Cs compounds is lower compared to pure Cs.

Under vacuum conditions of 10^{-6} mbar, the mean free path of Cs is much longer than the experimental dimensions at ACCesS and at the ion sources. Therefore,

Table 4.1: *Compilation of Cs compounds with their standard enthalpy of formation $\Delta_\mathrm{f}H^0$ at 298 K and melting point T_melt (if available) [Rum21]. Crystalline and gaseous states are denoted with c and g, respectively.*

Name	Formula	State	$\Delta_\mathrm{f}H^0$ in kJ/mol	in eV/particle	T_melt in °C
Caesium	Cs	c	0.0	0.0	28.5
		g	76.5	0.79	
Caesium hydride	CsH	c	−54.2	−0.56	≈ 170[1]
Caesium hydroxide	CsOH	c	−416.2	−4.31	342
		g	−256.0	−2.65	
Caesium monoxide[2]	Cs_2O	c	−345.8	−3.58	495
Caesium peroxide	Cs_2O_2				594
Caesium sesquioxide	Cs_2O_3				≈ 400
Caesium superoxide	CsO_2	c	−286.2	−2.97	432
Caesium ozonide	CsO_3				
Caesium nitrate	$CsNO_3$	c	−506.0	−5.24	409
Caesium azide	CsN_3				326

[1] Decomposition temperature.
[2] Several suboxides exist, e. g., $Cs_{11}O_3$, Cs_4O or Cs_7O.

the Cs transport can be considered ballistic and the Cs distribution within the vacuum chamber is mainly determined by the Cs oven evaporation profile and the Cs reflection and desorption from the surfaces [M+17]. Interactions of Cs with residual gases are expected to occur predominantly at the surfaces, leading to a different Cs chemistry compared to pure Cs adsorption and thus to an influence on the evolving surface work function. Investigations on the influence of the different gas species on the Cs chemistry and work function have mostly been performed in a controlled manner under UHV conditions [Bon88, DM96], from which some important results are outlined in the following.

Water A major objective in the investigation of water-surface interactions is the question of whether the polar water molecule adsorbs molecularly (associatively) or dissociatively [TM87, Hen02]. In the case of clean metal surfaces, a variety of studies have demonstrated that the adsorption pathway depends on factors such as surface defects, crystallographic orientation and morphology of the surface. Dedicated experimental investigations on the adsorption of H_2O on polycrystalline Mo surfaces are not available. However, simulations by means of density functional theory codes with ab initio molecular dynamics calculations have demonstrated that both the partial dissociation $H_2O \xrightarrow{2\,e^-} OH^- + H^-$ and the full dissociation $H_2O \xrightarrow{4\,e^-} O^{2-} + 2\,H^-$ are energetically favorable, with the electrons donated by the Mo substrate [BČS20]. In consequence, the computed surface work function increases with the number of adsorbing water molecules due to the electron transfer from the Mo substrate to the water molecule and its components.

The presence of Cs adatoms on metal substrates is generally known to promote water adsorption. Water molecules can nucleate around the Cs atoms forming $Cs(H_2O)_n$ complexes [SCČ14], which are stabilized by hydrogen bondings. Furthermore, Cs atoms can enhance the partial and full dissociation of water molecules at the surface [PRB91, SJ94, Hen02]. This can be explained by an electrostatic field-induced effect, meaning that the H_2O dissociation is initiated by the dipole field in the vicinity of the adsorbed Cs atoms [BPR91]. The Cs-induced water dissociation depends on the substrate, temperature and Cs coverage since these parameters determine the strength of the surface dipoles. In the case of partial dissociation, the formation of Cs hydroxide (CsOH) is probable, which is a whitish-yellow crystal, highly hygroscopic and has a melting point of 342 °C. Due to its high thermal stability, thermal decomposition is not possible at temperatures relevant to ion sources. When atomic oxygen is present due to the full dissociation of H_2O, the formation of Cs oxides is likely [VGK14], which is described in more detail in the following paragraph ‘Oxygen’. Moreover, the dissociated H atoms from the H_2O molecule might lead to the formation of Cs hydride (CsH), which is discussed in the paragraph ’Hydrogen’ below. The formation of Cs−OH, Cs−O and Cs−H bonds is generally favored from an energetic point of view because the respective bond dissociation energies are higher than the dissociation energy for Cs and H_2O bonds, as shown in table 4.2.

The exposure of prepared metal surfaces with a Cs submonolayer coverage to water vapor usually induces a work function increase [L^+89, PRB91, VGK14].

Table 4.2: *Dissociation energies of Cs bonds at 298 K [Rum21].*

Bond	Dissociation energy in kJ/mol	Dissociation energy in eV/particle
Cs−OH	373	3.87
Cs−O	293 ± 25	3.04 ± 0.26
Cs−H	175.4	1.82
Cs^+-H_2O	57.3	0.59

This behavior is also known from presumably thick Cs layers under ion source vacuum conditions, where a gradual work function increase over time is observed (Cs layer degradation) [FGW10, FF17]. This is explained by the formation of Cs compounds (in particular CsOH) and an electronic charge transfer to the adsorbing H_2O molecules, whose accumulation results in complexes and clusters over time. However, dedicated investigations on the work function evolution upon Cs adsorption on H_2O covered metal surfaces as well as during continuous codeposition of Cs and H_2O (as it is the case at ion sources) barely exist. Indications of a beneficial impact of H_2O coadsorbates on the work function reduction were reported by Uebbing and James in the context of photocathodes [UJ70]. During the exposure of an Ag substrate alternately to Cs and H_2O in a UHV chamber, the establishment of a Cs compound layer with an ultra-low work function of 1.22 eV was observed, which might be explained by the formation of Cs oxides at the surface (see below).

Oxygen When oxygen is adsorbed on pure metal surfaces, the work function typically increases [Ebe60, DP80]. The reason is the high electronegativity of oxygen, leading to a (partial) electron transfer from the metal to the adsorbate and thus to an increase of the surface potential barrier. With the presence of Cs, however, the situation can significantly change since a whole series of Cs compounds can be formed [Oka10]. The most common oxide of Cs is Cs monoxide (Cs_2O), which is a yellow-orange crystal. Moreover, various suboxides as well as oxygen-rich compounds such as Cs peroxide (containing O_2^{2-}), Cs superoxide (containing O_2^-) and Cs ozonide (containing O_3^-) exist, which are listed in table 4.1. The Cs oxides are strongly hygroscopic and exhibit a high thermal stability so that thermal decomposition is restricted to temperatures that are barely achieved under ion source relevant parameters. The color of Cs_2O is known to change to dark red and eventually to almost black upon heating [Bra78].

The controlled coadsorption of Cs and O_2 in a UHV environment allows the generation of work functions that are lower than that of pure Cs. In the case of Cs submonolayer coverages on metal substrates, the work function minimum can be shifted with small amounts of O_2 down to $1.0-1.2$ eV [SS68, PC73, DP80, Pap82]. Furthermore, comparable low work functions can be generated by the growth of thick adlayers involving Cs-O compounds [UJ70, BS77, Dan81, MS91]. In particular, Cs_2O is usually proposed to provide such low work functions [Dav57, UJ70, Des83], but no clear relationship between the Cs/O ratios and the obtained work functions has been found so far. Therefore, it remains unclear whether the formation of ultra-low work functions can be traced back to one specific oxide or rather to a mixture and interplay of different oxides [G$^+$75, BS77, ES79, YB80, W$^+$87, B$^+$04].

Hydrogen Dedicated investigations on H_2 adsorption on clean and caesiated Mo(110) surfaces in a UHV environment are reported in [EVKP87]. It is found that the adsorption of H_2 on clean Mo results in a work function increase of about 0.2 eV, which is attributed to the higher electronegativity of hydrogen compared to Mo. In contrast, a work function reduction of some 0.1 eV is observed when H_2 is adsorbed on Mo with a Cs submonolayer coverage larger than θ_{min}. The work function reduction is explained by an increased ionicity of the Cs overlayer, resulting from hydrogen atoms going underneath the Cs layer. In [RG65], a similar work function reduction of $0.1 - 0.2$ eV is reported by the exposure of caesiated polycrystalline Mo to H_2, and the formation of Cs hydride (CsH) is speculated.

Cs hydride is a whitish/colorless crystal and has a standard enthalpy of formation of -54.2 kJ/mol [Rum21, Bra78]. Although the standard enthalpy of formation is negative, the formation of CsH in the gas phase is unlikely at a H_2 gas pressure of several Pa because the H_2 molecule must dissociate prior to CsH formation [Bra78]. However, CsH formation is favored at the surfaces, where atomic hydrogen might be present due to dissociated H_2O and/or H_2 molecules [BČS20]. In addition, a significant amount of H atoms is produced in the plasma phase and can enhance the formation of CsH. While the formation is rather unlikely in the plasma volume at the low pressure (a third body must be involved in the collision process to absorb part of the released energy), impinging H atoms onto caesiated surfaces are expected to lead to reactions with Cs atoms (see section 4.3).

Cs hydride has a relatively low decomposition temperature of about 170 °C under standard conditions. Since the solubility of hydrogen in Cs is rather low [SP94], the thermal dissociation of CsH is accompanied by hydrogen desorption under the formation of H_2, i. e., $2\,\mathrm{CsH} \xrightarrow{\mathrm{heat}} 2\,\mathrm{Cs} + \mathrm{H}_2$. Hence, the partial pressure of H_2 above the CsH surface determines the thermal dissociation of CsH and represents the CsH dissociation pressure. In figure 4.4, the CsH dissociation pressure is plotted as a function of the temperature of the surface that is covered with CsH. As can be seen, a temperature of

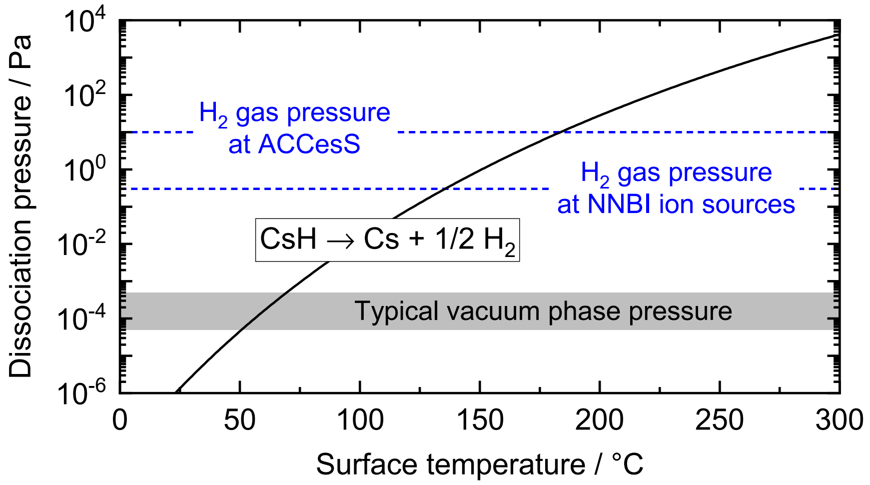

Figure 4.4: *Temperature dependent dissociation pressure of solid CsH [SP94]. Typical vacuum phase pressures and* H_2 *gas pressures for plasma generation at the NNBI ion sources and at the ACCesS experiment are indicated.*

> about 60 °C is sufficient to evaporate H_2 from CsH compounds at a typical ion source background pressure of 10^{-4} Pa. In the case of a H_2 gas pressure of 10 Pa as utilized for plasma operation at the experiment ACCesS (see chapter 5), CsH thermally decomposes at about 185 °C. In consequence, Cs can in principle be retrieved from CsH compounds with temperatures applicable to ion sources, which is not possible for the other Cs compounds that are listed in table 4.1.

From the above descriptions it becomes clear that the chemical surface composition and resulting work function that evolve during a caesiation process in an ion source environment are not easily anticipated. As illustratively summarized in figure 4.5, the formation of Cs compounds with residual water molecules and hydrogen gas is expected to play a decisive role. This is also indicated by measured Cs desorption fluxes that are orders of magnitude lower compared to the ones determined from the vapor pressure of pure Cs [Mim18]. Furthermore, the Cs sticking coefficient, which is defined by

$$S := 1 - \frac{\varGamma_{\mathrm{Cs,refl}}}{\varGamma_{\mathrm{Cs,on}}} \tag{4.3}$$

with $\varGamma_{\mathrm{Cs,on}}$ being the Cs flux impinging onto the surface and $\varGamma_{\mathrm{Cs,refl}}$ the Cs flux reflected from the surface, has been determined experimentally to a value of 0.7 for a Mo surface at room temperature [FGW10], showing that most of the Cs that impinges onto the surface is adsorbed. The high sticking coefficient in combination with the reduced desorption flux allows the formation of multilayers, with the

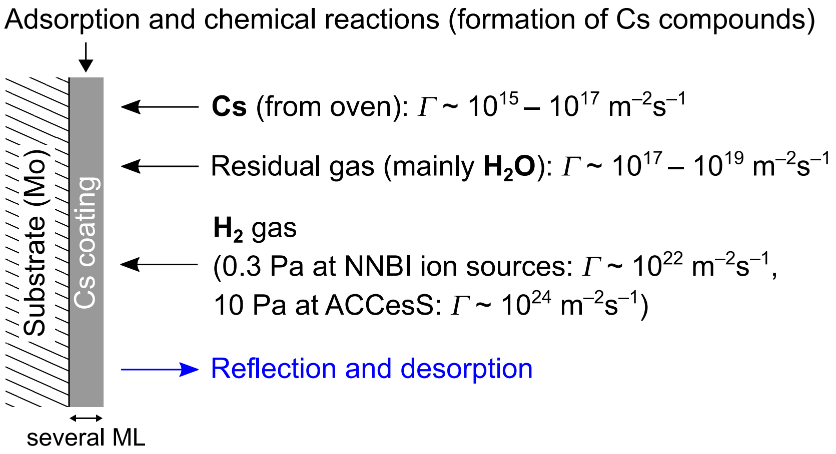

Figure 4.5: *Illustration of the caesiation process under ion source conditions.*

thickness depending on the applied Cs fluence, i. e., the time integrated Cs flux the surface is exposed to.

4.3 Plasma interaction with caesiated surfaces

The Cs coating and thus the surface work function can be heavily affected upon hydrogen plasma exposure due to a multitude of possible reactions with energetic and chemically reactive plasma species. As described in chapter 3, photons with energies up to ≈ 15 eV, atomic hydrogen radicals as well as positive hydrogen ions (H^+, H_2^+, H_3^+) impinge onto the caesiated surface. Depending on the difference between the potential of the surface and the plasma potential, the positive ions can gain kinetic energy while traversing the plasma sheath. Furthermore, Cs atoms and impurities are partially ionized in the plasma phase and can gain energy in the plasma sheath.

Thermal effects The hydrogen plasma leads to an energy flux to the caesiated surface, which results from collisions of the different plasma species with the surface as well as from possible exothermic chemical and physical reactions at the surface. The thermal load that heats the surface is given by the difference of the energy flux to the surface and the energy flux leaving the surface. The energy flux leaving the surface is determined by processes such as radiative and convective cooling, removal of particles from the surface, and endothermic reactions. Dependent on the plasma parameters, the plasma-induced temperature increase can be up to several 100 °C. An elevated surface temperature affects the chemical equilibrium at the surface and thus the chemical composition of the surface layers. Governing processes include thermal decomposition of Cs compounds (e. g., CsH, see figure 4.4), desorption of Cs (compounds) and a variation of the Cs sticking coefficient.

Physical interactions When plasma particles hit the caesiated surface, they can be backscattered or absorbed in the Cs layer. Since a momentum transfer between the incident and target particles takes place, physical sputtering can occur. The threshold energy for this process is given by [Boh80]

$$E_{\mathrm{thr}} = \begin{cases} E_{\mathrm{b}}/[\gamma(1-\gamma)], & m_1 \leq 0.3 m_2, \\ 8 E_{\mathrm{b}} (m_1/m_2)^{2/5}, & m_1 > 0.3 m_2, \end{cases} \tag{4.4}$$

where E_{b} is the surface binding energy of the target particle, m_1 and m_2 are the masses of the projectile and the target particle, and γ is defined as $4m_1m_2/(m_1+m_2)^2$. As mentioned in section 4.1, the surface binding energy of Cs atoms above one ML is about 0.8 eV. Due to the involvement of Cs compounds, however, a somewhat higher binding energy can be assumed. The most energetic particles hitting the caesiated surface are positive ions due to the energy gain in the plasma sheath. By using 0.8 eV as a lower limit for E_{b}, the threshold energy for the sputtering of Cs atoms by incident H^+ ions is 27.8 eV. In the case of D^+ ions, the higher mass leads to a lower threshold energy of 14.5 eV. For the masses of the dominant molecular ions H_3^+ and D_3^+ at the ACCesS experiment (see section 3.1.3), the calculated threshold energies are 10.1 and 5.8 eV, respectively. However, it is expected that these molecules dissociate to a large degree upon hitting the surface, reducing the sputtering capability significantly [vATG85].

The caesiated substrate is usually on the floating potential at ACCesS and the positive ions can gain kinetic energies of about 10 eV in the plasma sheath in maximum. At the BUG and ELISE ion sources, the caesiated plasma grid is biased positively with respect to the source body and the difference between the plasma and plasma grid potential is typically not higher than a few volts. Therefore, physical sputtering of Cs (compounds) by positive hydrogen ions is expected to be ineffective both at ACCesS and at the ion sources.[1] However, self-sputtering of Cs by impinging Cs^+ ions might play a role ($E_{\mathrm{thr}} \overset{(4.4)}{=} 6.4\,\mathrm{eV}$ for $E_{\mathrm{b}} = 0.8\,\mathrm{eV}$) [Wad18]. In addition,

---

[1] Significant physical sputtering of Cs occurs at the backplate of the NNBI ion sources due to backstreaming positive ions with energies of several keV. These ions are created in the extraction system by the interaction of negative ions with the background gas and are accelerated back into the ion source [F$^+$21a].

impurity gases may physisorb on the caesiated surfaces with $E_\mathrm{b} \ll 1\,\mathrm{eV}$ (weak van der Waals forces) and are likely to be physically sputtered.

Chemical interactions Significant modifications of the chemical equilibrium and thus chemical composition and stoichiometry of caesiated surfaces can occur by chemical reactions with the various plasma species. Impinging hydrogen molecules, atoms and positive ions can be absorbed in the Cs layer and form Cs-H compounds [vA+86, Wad18]. Especially the atomic hydrogen radical is chemically very active and can affect the Cs chemistry considerably. Furthermore, chemical bonds of Cs compounds can be broken via impinging VUV/UV photons and ions since the bond dissociation energies are typically below 4 eV (see table 4.2). Once Cs compounds are broken, the fragments might remain at the surface and/or undergo further reactions with particles at the surface. In case the resulting fragments and compounds are more weakly bound to the surface than before, sputtering and/or desorption processes (thermally driven and/or particle/photon stimulated) are enhanced. In consequence, the chemical reactions with incident plasma species can favor the release of Cs from the surface, which is usually subsumed under the term chemical sputtering [WC92].

Figure 4.6 summarizes the interaction of hydrogen plasmas with caesiated surfaces. At the ion sources, the plasma-induced Cs release from the surfaces and walls is generally significant [FW12, W+18a] and is expected to be mainly driven by chemical sputtering. The resulting Cs redistribution within the source is exploited to deposit Cs onto the large plasma grid surface. At the ELISE test facility for instance, the Cs ovens are positioned at the side walls of the expansion

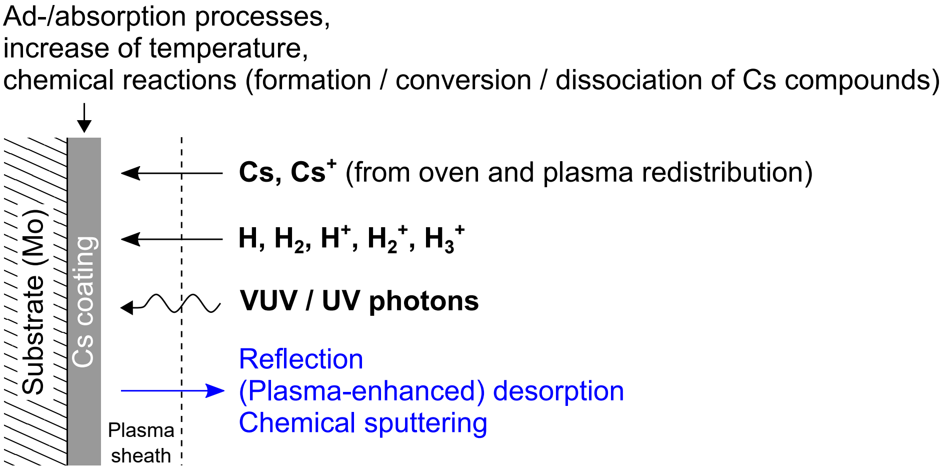

Figure 4.6: *Sketch of the interaction of hydrogen plasmas with caesiated surfaces.*

chamber and the Cs evaporation is directed toward the backplate [C+19]. During a so-called Cs conditioning procedure [W+18b], Cs is continuously evaporated into the source and short plasma pulses of several seconds are repetitively applied to enhance the Cs transport toward the plasma grid [M+17]. The gradual caesiation of the plasma grid leads to a significant improvement of the ion source performance due to the resulting reduction of the surface work function.

During plasma phases from minutes up to hours, the Cs flux toward the plasma grid must be high enough to counterbalance the plasma-induced Cs removal from the plasma grid surface. Furthermore, the Cs layer needs to be re-conditioned after operational breaks due to degradation effects caused by the residual gases, which is typically done by the evaporation of fresh Cs in combination with the application of short repetitive plasma pulses [W+18b]. Since the occurring processes and the resulting chemical composition at the caesiated surfaces depend on the condition of the Cs layer and the plasma exposure time, the plasma impact on the work function can reach from a reduction to an increase, as mentioned in section 2.3.3. Hence, the usage of Cs introduces pronounced temporal dynamics and systematic investigations on the behavior of the surface work function in dedicated scenarios are required to gain insights into the impact of the physico-chemical interactions on the work function of the plasma grid.

5 Experimental setup and determination of fluxes

5.1 The ACCesS experiment

The experimental setup ACCesS (abbreviation for Augsburg Comprehensive Cesium Setup) is schematically illustrated in figure 5.1. It consists of a cylindrical stainless steel vessel with an inner diameter of 15 cm and a height of 10 cm, which is evacuated with a pumping system comprising a turbomolecular and rotary vane pump. The vacuum vessel has an exchangeable bottom plate and is equipped with several ports for the attachment of peripheral components. Cs is introduced into the chamber by means of a Cs oven attached to the bottom plate, which is described in detail in section 5.2. The background pressure is monitored with a cold cathode gauge and is typically in the range of $10^{-6} - 10^{-5}$ mbar (limited by Viton O-ring seals used at the experiment). A gas supply system with calibrated mass flow controllers allows a controlled gas inlet (mostly H_2 and D_2), and the absolute pressure in the vacuum system is measured with a capacitance manometer. An installed angle valve in between the vessel and the turbomolecular pump supports the adjustment of the desired gas pressure (typically in the range of $1 - 10$ Pa) by reducing the effective pump rate.

Since the composition of the background gases in the vacuum system can provide valuable insights into the chemical behavior of Cs and the possibly affected Cs dynamics, a residual gas analyzer (RGA) is applied. The RGA is a compact quadrupole mass spectrometer (Pfeiffer Vacuum PrismaPlus® QMG 220) and is installed at a differentially pumped side arm of the experiment (separate turbomolecular and rotary vane pumps). The side arm is heated to 80 °C to prevent Cs accumulation and is separated from the main chamber by an aperture with 300 µm diameter, which is necessary in order not to exceed the maximum allowed operating pressure of the RGA (10^{-5} mbar) in the side arm during plasma operation. The RGA detector has a distance of about 60 cm to the main chamber and is capable to detect masses in the range of $1 - 200$ u either with a Faraday

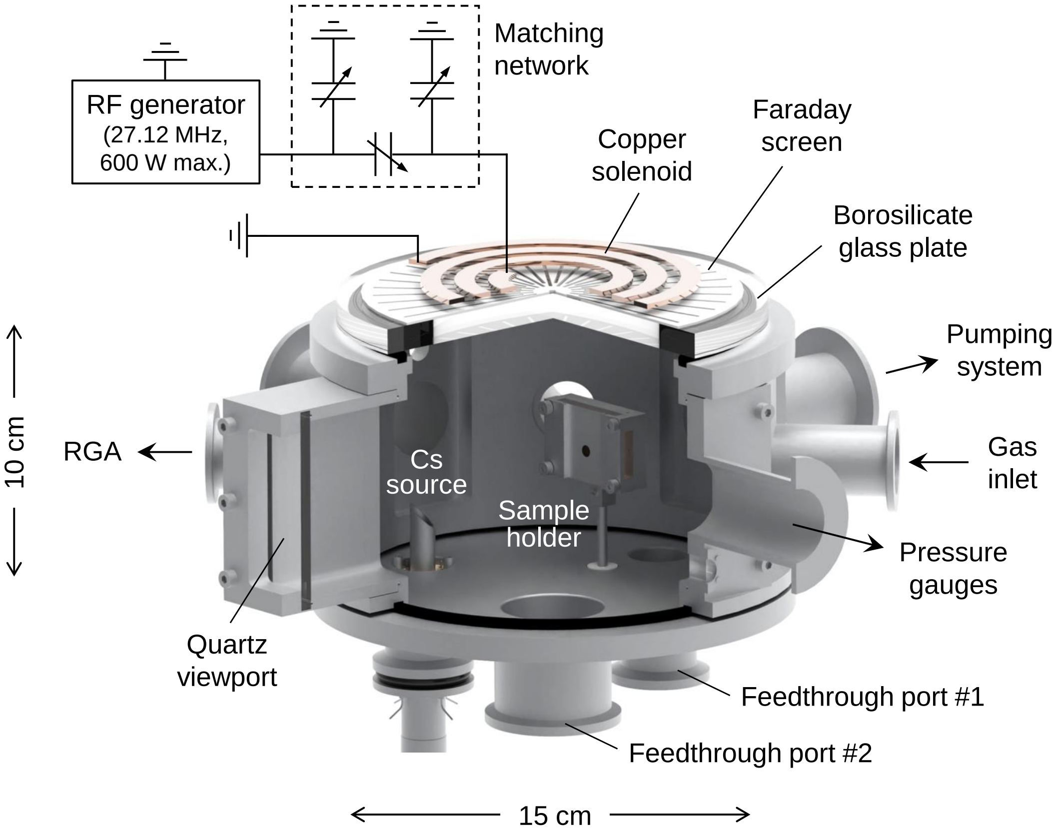

Figure 5.1: *Illustration of the experimental setup ACCesS.*

cup or with a secondary electron multiplier (SEM) for higher sensitivity. However, Cs cannot be detected due to the small diameter of the aperture in combination with the high affinity of Cs to adsorb at the walls. The RGA can be used to record mass spectra as well as time traces of selected masses. A typical mass spectrum of the unbaked vacuum system at ACCesS in the range of $1 - 100\,\mathrm{u}$ is depicted in figure 5.2 (not calibrated for absolute partial pressures in the main vessel). The largest peak in the mass spectrum corresponds to water vapor, and the other smaller peaks can be attributed mostly to atmospheric gases and some cracking products. The RGA is standardly used to monitor the relative behavior of the residual gases over time.

Low pressure low temperature plasmas are generated in the vacuum vessel via inductive RF coupling. This is done by using a planar RF antenna located concentrically above the vessel in atmosphere. The dielectric between the antenna and the vacuum is a Borosilicate glass plate. A Faraday screen is positioned on top of the glass plate and is grounded during plasma operation for the suppression of capacitive coupling components and the associated large electric fields [LL05]. The antenna is a copper solenoid that is connected via an impedance matching network

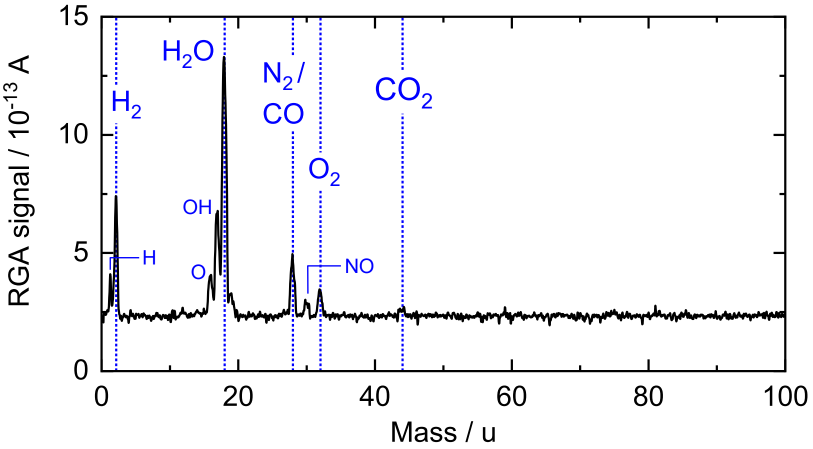

Figure 5.2: *Mass spectrum recorded with the SEM detector of the RGA in the vacuum phase at ACCesS (pressure in the main chamber = 1.1×10^{-5} mbar, pressure in the side arm of the RGA = 2.1×10^{-8} mbar).*

to the RF generator. The RF generator is capable to provide RF powers of up to 600 W at a fixed frequency of 27.12 MHz. The matching network consists of three variable capacitors in a π-type configuration, which is necessary to adjust the impedance Z of the load (consisting of the antenna, Faraday screen, plasma and matching network) to $\mathrm{Re}(Z) = 50\,\Omega$ and $\mathrm{Im}(Z) = 0$ to match the requirements of the generator for achieving maximum power output [LL05]. Standard operational parameters for the generation of H_2 and D_2 plasmas in this work are a gas pressure of 10 Pa and an RF output power of 250 W.

As shown in figure 5.1, a sample holder can be installed close to the center of the vessel. It is mounted with a ceramic block on the bottom plate to ensure electrical and thermal insulation and has a distance of about 2 cm from the cylinder axis of the vessel. Since the previously used sample holder could be heated to a temperature of only $\sim$ 400 °C in maximum (see [Fri13, Cri18]), a new sample holder was designed and manufactured within this work to reach temperatures up to 1000 °C. The new sample holder is presented in figure 5.3(a). It is made of stainless steel and provides a support area of $44 \times 30\,\mathrm{mm}^2$, to which samples can be attached with clamps of various sizes. The sample holder support has a hole with a diameter of 5 mm close to the center in order to provide the possibility for Langmuir probe measurements above the sample surface (provided that the sample is also punched, see section 5.4). The support area can be heated with an embedded heating wire (see photograph in figure 5.3(a)), which is operated with a proportional-integral-derivative controller (maximum heating power $\approx$ 147 W). The controller uses the temperature feedback from a K-type

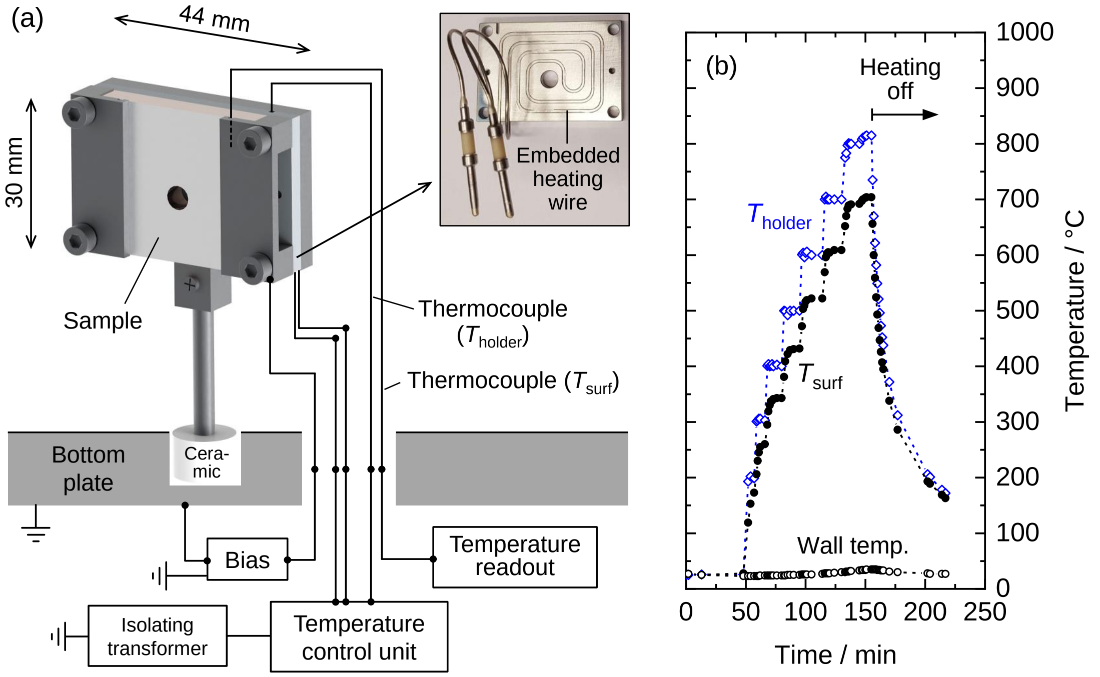

Figure 5.3: *(a) Schematic of the sample holder at ACCesS with installed thermocouples, heating wire and bias against the grounded vessel wall. The photograph shows the embedded heating wire in the sample holder. (b) Exemplary heating of a stainless steel sample.*

thermocouple installed at the sample holder support (T_{holder}) to reach the set temperature via pulse width modulation. The temperature of the sample is monitored with a separate K-type thermocouple (T_{surf}), which is attached to the front surface by using one of the clamps. The temperature response of an installed stainless steel sample ($30 \times 30 \times 2\,\text{mm}^3$) upon heating the sample holder support to 815 °C is exemplarily demonstrated in figure 5.3(b). The sample holder support reaches the set temperature within ~ 1 min and maintains it with fluctuations of only a few degrees. The measured temperature at the sample's front surface follows this temperature increase with a time delay of several minutes and reaches a value of about 87 % from T_{holder}. Since a water cooling system surrounds the vessel walls, thermal radiation from the sample and sample holder leads to an increase of the wall temperature of only a few degrees. After the heating is switched off, the temperatures of the sample and sample holder gradually decrease due to radiative cooling (no active cooling possible).

The heating wire and thermocouples are in coaxial design and the vacuum feedthroughs (realized via port #1, see figure 5.1) ensure electrical insulation of the sample holder against the grounded vessel walls. Furthermore, the temperature control unit is galvanically isolated against the ground potential by the use of an isolation transformer to suppress capacitive coupling to the ground. In consequence, the sample holder and thus also installed samples can be reliably biased against the ground potential, which is necessary for instance for measuring the work function of the sample surface (see chapter 6). For the bias connection either the feedthrough port #2 or a feedthrough from the installed Cs source (see section 5.2) is used.

Within this work, the ACCesS experiment has been equipped with a Siemens SIMATIC programmable logic controller and WinCC software. The customized system controls the mass flow controllers, the RF generator and a switch for the grounding of the Faraday screen. Furthermore, it allows the readout of the pressure gauges and thermocouples. An automatic data acquisition of the set values in the WinCC software and the data from the thermocouples and pressure gauges has been realized with a routine implemented in LabVIEW. The main advantage of the SIMATIC system is the possibility to run the experiment in a pulsed operational mode, i. e., to repetitively apply short plasma pulses of a few seconds.

5.2 Cs source

The applied Cs source is a Cs ampoule oven, which is attached to the bottom plate of the vacuum vessel as shown in figure 5.1. The Cs oven was designed and manufactured at IPP, where it is also applied at the test facilities BUG (see figure 2.3) and ELISE [C+19]. In figure 5.4(a), a schematic drawing of the Cs oven is depicted. The different parts of the oven can be heated by five installed heating sleeves, which are feedback controlled by the use of implemented thermocouples. The electronics for the heating sleeves are controlled by a customized software, which enables automatic data acquisition of all temperatures. As illustrated by the cutaway drawing in the inset, a sealed glass ampoule containing 1 g of pure Cs is installed in a stainless steel tube at the bottom part of the oven. The tube can be pressed from outside to crack the ampoule without breaking the vacuum, and the Cs is collected in the reservoir above the cooling plate (coldest spot of the oven). By gradually heating the reservoir to temperatures in the range of typically $110 - 130\,^\circ\mathrm{C}$, the Cs vapor pressure rises and Cs is transported via a tube made of Ni plated Cu (8 mm inner diameter) to the nozzle of the oven. The other parts of the oven are kept at a temperature of about 280 °C to avoid Cs condensation and to assure a proper Cs transport. The oven nozzle protrudes about 2.5 cm into the vessel and has a 45° edge cut toward the sample holder to enhance the

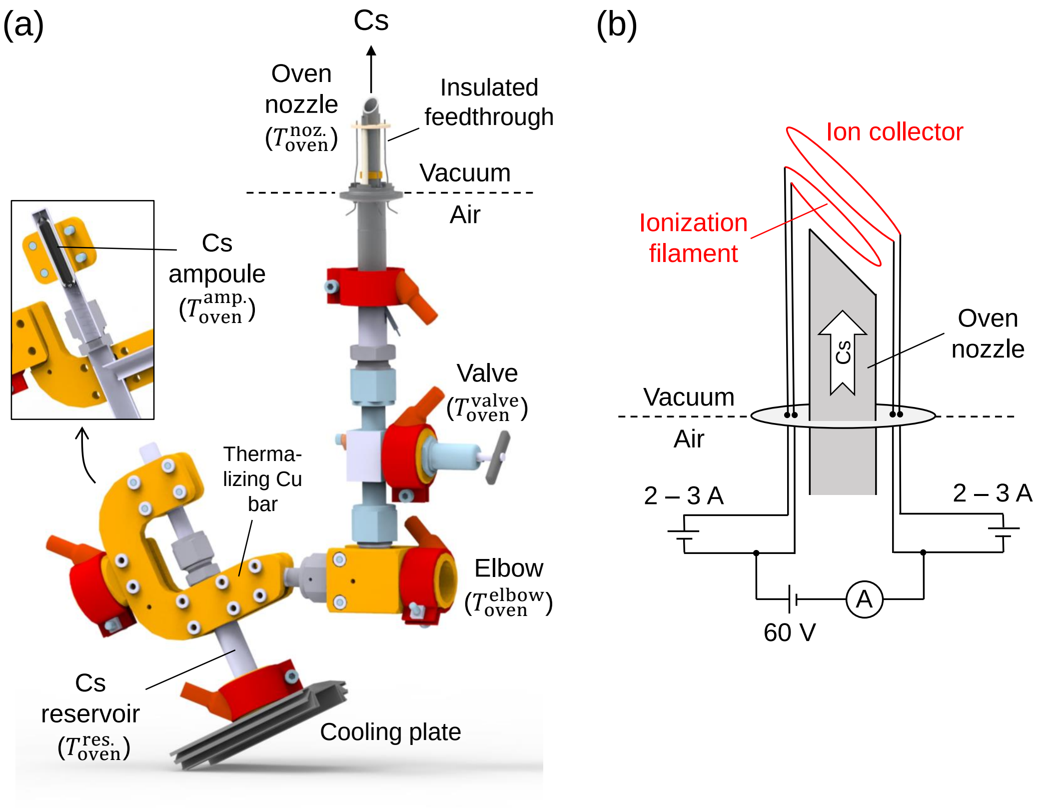

Figure 5.4: *(a) Illustration of the applied Cs ampoule oven at ACCesS. The red components represent the heating sleeves, which are controlled by the use of implemented thermocouples. The cutaway drawing in the inset shows the location of the Cs ampoule. (b) Illustration of the removable oven SID.*

Cs evaporation toward an installed sample surface. A valve at half height of the oven can be closed to quickly stop the evaporation into the vessel. The valve also provides the possibility to aerate the experimental chamber while keeping the Cs reservoir in vacuo, which is necessary to avoid Cs oxidation and contamination.

Four insulated vacuum feedthroughs are available to install a surface ionization detector (SID) directly above the Cs oven nozzle. The SID serves as a monitoring tool for the Cs outflow from the oven. As illustrated in figure 5.4(b), it consists of two tungsten filaments with 300 µm diameter that are biased against each other with about 60 V. By passing a current of $2 - 3$ A through each of the filaments, they are ohmically heated to temperatures $T_{\text{fil}} > 900\,°\text{C}$ to avoid Cs adsorption on them [TL33]. Cs atoms that approach the surface of the first hot filament are positively ionized due to the fact that the value of the work function of tungsten ($\chi_{\text{W}} \approx 4.5\,\text{eV}$) is higher than the ionization energy of Cs ($E_{\text{i,Cs}} = 3.89\,\text{eV}$), leading to the following relationship for the fraction of the positive to neutral Cs flux leaving the filament surface [S⁺00]:

$$\frac{\mathit{\Gamma}_{\mathrm{Cs}^+}}{\mathit{\Gamma}_{\mathrm{Cs}^0}} \propto \exp\left(\frac{\chi_{\mathrm{W}} - E_{\mathrm{i,Cs}}}{k_{\mathrm{B}} T_{\mathrm{fil}}}\right). \tag{5.1}$$

The positive ions are accelerated and collected onto the second filament (ion collector), and the measured current flowing between the two filaments is proportional to the impinging flux of Cs atoms onto the ionization filament. The control and data acquisition of the SID diagnostic is fully implemented in the Cs oven electronics and software. Since the SID at ACCesS is not yet calibrated for the determination of absolute evaporation rates, it can only be used as a tool for the temporal monitoring of the relative Cs outflow from the oven. In general, the SID cannot be used during plasma operation because the bias would draw a high electron current.

The commissioning of the Cs oven at ACCesS is described in [Cri18], where also a stable and reliable Cs evaporation is demonstrated both in vacuum and plasma phases. An exemplary operation of the Cs oven in the vacuum phase is presented in figure 5.5(a). First, the different parts of the oven except the Cs reservoir are gradually heated to 280 °C, monitored by the temperatures $T_{\mathrm{oven}}^{\mathrm{noz.}}$, $T_{\mathrm{oven}}^{\mathrm{valve}}$, $T_{\mathrm{oven}}^{\mathrm{elbow}}$ and $T_{\mathrm{oven}}^{\mathrm{amp.}}$. The temperature $T_{\mathrm{oven}}^{\mathrm{valve}}$ shows a slight oscillation of about ±5 °C around the set value of 280 °C due to a delayed response of the feedback controlled temperature regulation. After the working temperature of the oven is reached, the Cs reservoir temperature $T_{\mathrm{oven}}^{\mathrm{res.}}$ is increased carefully in steps of $5 - 10$ °C. The release of relevant amounts of Cs into the vacuum chamber can be seen by an increase of the SID current, which is given at $T_{\mathrm{oven}}^{\mathrm{res.}} = 110$ °C (typically in the range of $110 - 120$ °C). The further increase of $T_{\mathrm{oven}}^{\mathrm{res.}}$ leads to a further increase of the SID current and after some minutes, Cs can also be detected via tunable diode laser absorption spectroscopy, which is used to measure the neutral Cs density in front of the sample holder (detection limit $\approx 2 \times 10^{13}\,\mathrm{m}^{-3}$, details see section 5.4.1). By keeping $T_{\mathrm{oven}}^{\mathrm{res.}}$ constant at 120 °C for almost 3 h, the measured SID current and Cs density remain at a stable level, confirming that a stable Cs evaporation is provided. The oscillation of $T_{\mathrm{oven}}^{\mathrm{valve}}$ leads to a slight fluctuation of the Cs density, which, however, stays below 10 % and can be neglected. When the Cs oven valve is closed, the Cs evaporation declines strongly on the minute scale. The SID diagnostic shows that the Cs evaporation reaches a certain background level, which is below the detection limit of the laser absorption spectroscopy system. The background evaporation can be attributed to some Cs reservoirs that were built up at the inner surfaces of the nozzle because shorty after the heating of

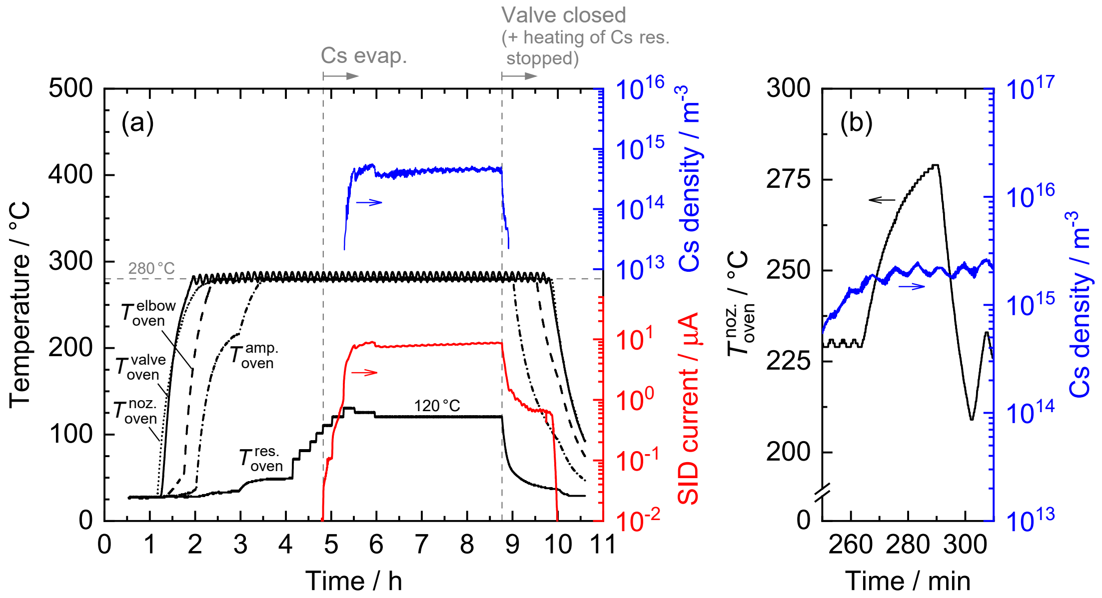

Figure 5.5: *(a) Typical operation of the Cs oven and monitoring of the Cs evaporation with the SID diagnostic as well as via tunable diode laser absorption spectroscopy for the measurement of the neutral Cs density in front of the sample holder. (b) Variation of the temperature of the Cs oven nozzle while monitoring the Cs evaporation via laser absorption spectroscopy.*

the upper parts of the oven is stopped and $T_{\mathrm{oven}}^{\mathrm{valve}}$ and $T_{\mathrm{oven}}^{\mathrm{noz.}}$ start to decrease, the background evaporation vanishes.

Since the inlet of hydrogen gas of several Pa into the vacuum chamber leads to convective cooling of the oven nozzle and thus to a reduction of $T_{\mathrm{oven}}^{\mathrm{noz.}}$ by about $10 - 20$ °C, the influence of a variation of $T_{\mathrm{oven}}^{\mathrm{noz.}}$ on the Cs density in front of the sample holder was tested. In figure 5.5(b), the measured Cs density is plotted for a variation of $T_{\mathrm{oven}}^{\mathrm{noz.}}$ between 210 and 280 °C. As can be seen, no influence on the Cs density can be observed, showing that the Cs evaporation is stable upon a variation of $T_{\mathrm{oven}}^{\mathrm{noz.}}$ by several 10 °C.

5.3 Upgrade by an external plasma source

In order to expose caesiated samples to specific hydrogen plasma species, the ACCesS experiment has been upgraded by an additional RF plasma source within this work. As shown in figure 5.6, the plasma source is attached to a flange (inner diameter of 22 mm) whose cylinder axis forms an angle of 45° to the normal of the sample surface. The plasma is inductively driven by a helical two-turn copper coil wound around a cylindrical quartz glass tube, which has an outer diameter of 50 mm, a wall thickness of 3.5 mm and a length of 200 mm. The

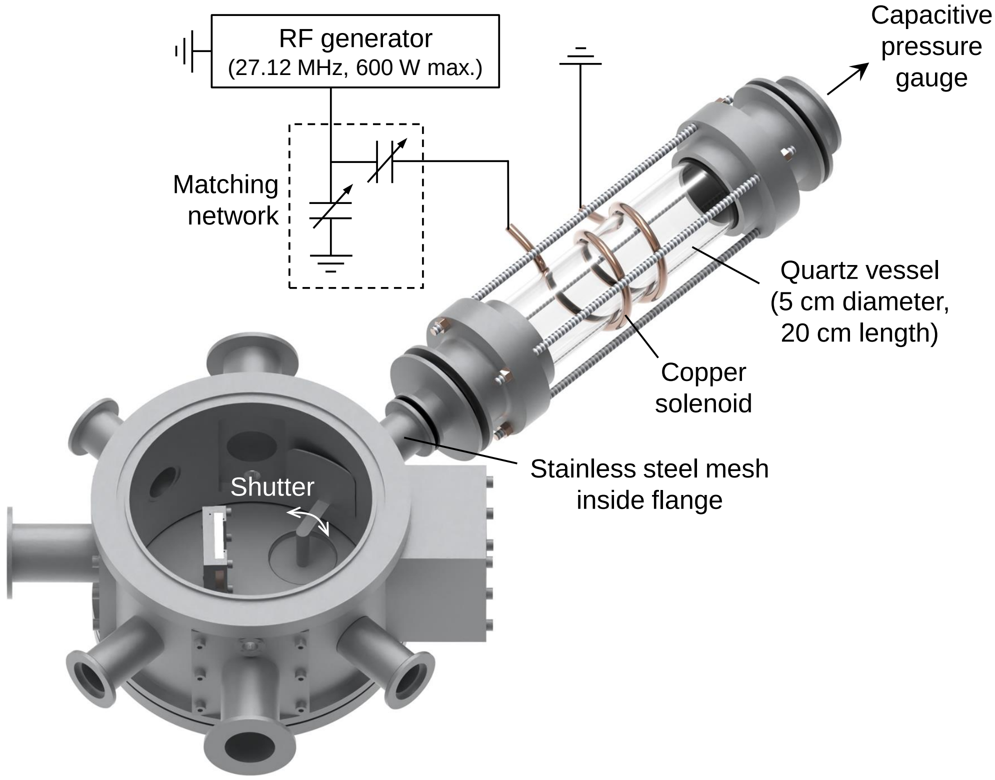

Figure 5.6: *Schematic of the experimental setup ACCesS upgraded by an external ICP source.*

quartz tube is installed with two grounded stainless steel mounts and sealed with the use of O-rings. For the RF power supply, the same RF generator as for the plasma generation in the main vessel is used (27.12 MHz, 600 W max.), i. e., plasma operation is possible either in the main vessel or in the quartz tube. The RF impedance matching network consists of variable capacitors in an L-type configuration. The matching is adjusted with the help of an RF voltage and current probe installed in between the generator and the matching circuit, which allows to measure the phase-resolved RF current and voltage in real time. Since a capacitive pressure gauge at the back end of the plasma source confirms that the filling pressure in the main vessel is maintained in the quartz tube, no separate gas feed system is installed. Inside the flange to which the ICP source is connected, a grounded stainless steel mesh is inserted to prevent capacitive plasma ignition in the main vessel during the operation of the source.

The commissioning of the external ICP source was accompanied by severe RF interference at devices operated at or nearby the experiment. A reduction of induced RF disturbances could be achieved by encaging the quartz tube with a stainless steel mesh and by improving the grounding of the quartz tube mounts.

With this, hydrogen discharges can be generated with RF output powers of up to 600 W in the Pa range. However, it has to be noted that RGA and work function measurements (see chapter 6) cannot be conducted when the source is in operation due to a still too high RF influence on the sensitive current measurement devices. In order to monitor the temperature of the quartz tube, a thermocouple is attached to it in between the coil and the mount at the back end. With the typically applied RF powers in the range of $400 - 600$ W, the temperature increases above 100 °C within a few minutes during plasma operation. To maintain the thermal stability of the elastomer seals of the quartz tube, air cooling systems are installed that limit the temperature increase to about $150 - 200$ °C and allow steady-state operation.

As depicted in figure 5.6, a rotatable shutter is installed in the main vessel via the feedthrough port #2. The shutter enables to cover the flange of the additional ICP source to prevent Cs diffusion into the flange during a caesiation process. The shutter can be rotated from the outside without breaking the vacuum. In order to select the plasma species for the irradiation of caesiated samples, a MgF_2 window can be installed inside the flange and magnets can be attached from the outside (details see chapter 8).

5.4 Particle and photon flux determination

According to the descriptions provided in chapter 3, the particle and photon fluxes onto a sample surface immersed in a plasma are determined as follows: Neutral particle fluxes are calculated via equation (3.25) and hence, the particle densities and temperatures must be known. The positive ion flux onto the surface is given by equation (3.29) and thus, the positive ion density and the electron temperature above the surface are needed. Photon fluxes are obtained via equation (3.19) so that the respective emissivities are required. In order to determine these parameters for the different hydrogen plasma species experimentally, a Langmuir probe, optical emission spectroscopy (OES) and a VUV measurement device (named VUV diode system) [FB22] are applied. Furthermore, the neutral Cs density and temperature (and thus the neutral Cs flux) are measured via tunable diode laser absorption spectroscopy (TDLAS) in the vacuum phase (typically $10^{-6} - 10^{-5}$ mbar), gas phase (typically 10 Pa) and plasma phase. An overview of the applied diagnostics and the respective measured quantities is given in table 5.1 and detailed descriptions are provided in the sections 5.4.1–5.4.4.

Table 5.1: *Overview of the diagnostic systems for the quantification of particle and photon fluxes. The spatial resolution, applicability and quantities that can be evaluated from the diagnostics are listed.*

Diagnostic	**Spatial res.**	**Appl.**	**Evaluated quantities**
Tunable diode laser absorption spectroscopy (TDLAS)	LOS integr.	Vacuum, gas & plasma	• Cs density n_{Cs} • Cs temperature T_{Cs} $\hookrightarrow$ **Cs flux $\boldsymbol{\Gamma}_{\mathbf{Cs}}$**
Langmuir probe	Local	Plasma	• Electron temperature T_{e} • Electron density n_{e} • Positive ion density $n_{\mathrm{i+}}$ $\hookrightarrow$ **Positive ion flux $\boldsymbol{\Gamma}_{\mathbf{i+}}$** • Plasma potential ϕ_{pl} • Floating potential ϕ_{fl} $\hookrightarrow$ Maximum ion energy
Optical emission spectroscopy (OES)	LOS integr.	Plasma	• Electron temperature T_{e} • Electron density n_{e} • H atom density n_{H} • Gas temperature T_{gas} $\hookrightarrow$ **H flux $\boldsymbol{\Gamma}_{\mathbf{H}}$**
VUV diode system	Cone integr.	Plasma	• VUV emissivity $\varepsilon_{\mathrm{VUV}}$ $\hookrightarrow$ **VUV flux $\boldsymbol{\Gamma}_{\mathbf{VUV}}$**

In figure 5.7, the arrangement of the different diagnostics is depicted. As can be seen, the TDLAS measurements are performed along a diagonal line of sight (LOS) through the vacuum vessel, which is in parallel to and at a distance of about 2 cm from the sample holder. To let the applied laser radiation pass the vacuum vessel, small quartz windows are implemented below and above the flanges.

The Langmuir probe can be flexibly used at the experiment and in case it is installed at the port behind the sample holder, it can be fed through the sample holder (provided that the sample is punched as shown in figure 5.7). Thus, measurements can be performed directly above the sample surface from which the positive ion flux onto the surface can be evaluated. Moreover, an upper limit for the energy of the positive ions can be determined by the measurement of electrostatic potentials within the plasma.

Via OES, the plasma emission along a LOS is recorded spectrally resolved from the UV to the near IR. A high resolution spectrometer is applied to determine

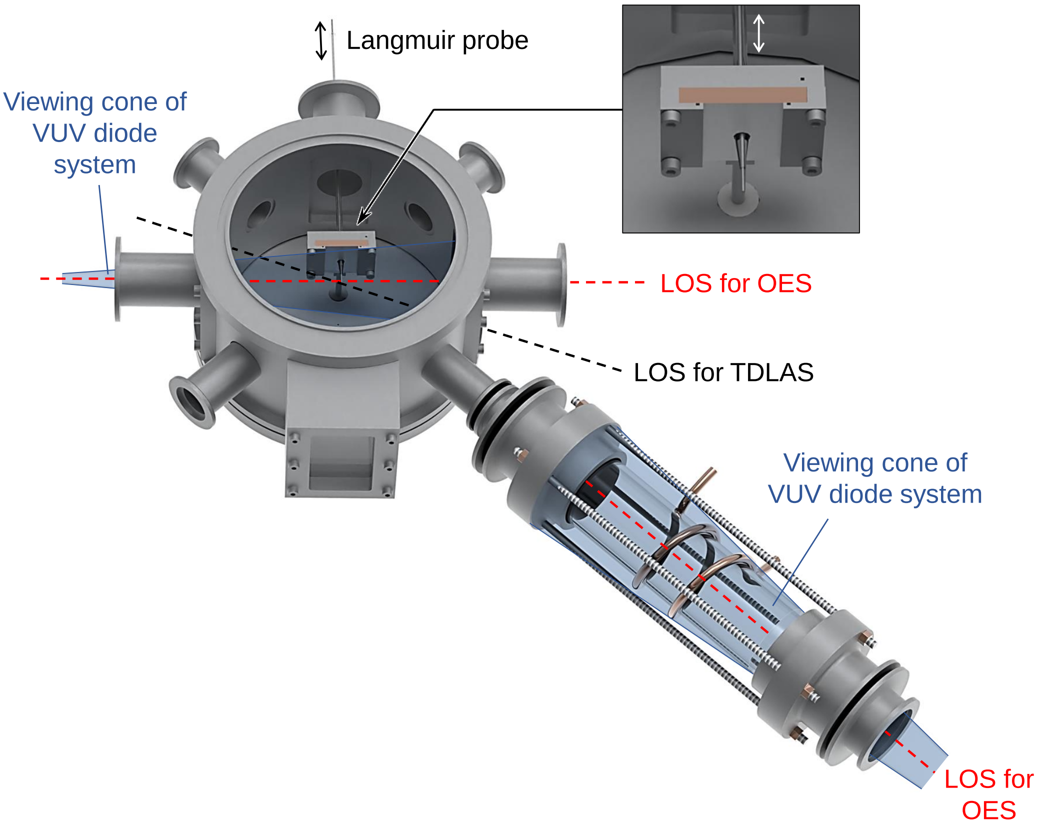

Figure 5.7: *Overview of the arrangement of the applied diagnostic systems for the quantification of particle and photon fluxes at ACCesS.*

absolute emissivities either in the main vessel along a LOS at half height through the vacuum vessel (in parallel to the sample holder) or in the external plasma source along the cylinder axis. Diagnostic access to the plasma emission is provided by the use of quartz glass blind flanges. From the measurement of specific line emissivities, LOS-averaged plasma parameters (typically axisymmetric profiles [S$^+$01, FB22]) can be evaluated, from which in particular the atomic hydrogen flux is determined.

The VUV diode system is a measurement device for the quantification of VUV photon fluxes. It is applied both at the main vessel and at the external plasma source to measure VUV emissivities within a distinct viewing cone.

5.4.1 Tunable diode laser absorption spectroscopy for Cs

TDLAS is a reliable and robust measurement technique for the quantification of the density and temperature of Cs atoms within a Cs gas [FW11]. It is based on the absorption of laser radiation (tuned over characteristic Cs absorption lines) and the measurement of the transmitted laser light intensity.

Fundamentals

When a beam of light with intensity $I(\lambda, x_0)$ travels in x-direction ($x > x_0$) through a homogeneously absorbing medium at the wavelength λ, its intensity is reduced exponentially according to the radiative transfer equation:

$$I(\lambda, x) = I(\lambda, x_0) \exp\left[-\alpha(\lambda)(x - x_0)\right]. \tag{5.2}$$

Here, α denotes the absorption coefficient, and scattering of light and photon emission from excited particles are neglected.[1] From equation (5.2) follows

$$\alpha(\lambda) = \frac{1}{x - x_0} \ln\left[\frac{I(\lambda, x_0)}{I(\lambda, x)}\right]. \tag{5.3}$$

When the absorption is due to the excitation of particles from the state k to the state i, the wavelength-integrated absorption coefficient over the absorption line can be expressed by [TLJ99]

$$\int_{\text{line}} \alpha(\lambda)\mathrm{d}\lambda = n_k \frac{g_i}{g_k} A_{ik} \frac{\lambda_{ki}^4}{8\pi c}, \tag{5.4}$$

where n_k is the LOS-integrated population density of the lower state k, λ_{ki} is the central wavelength of the line (see equation (3.17)), A_{ik} is the Einstein coefficient for spontaneous emission, and g_i and g_k are the statistical weights of the states i and k, respectively. Hence, the density n_k of the absorbing particles can be calculated from equations (5.4) and (5.3) by

$$n_k = \frac{8\pi c g_k}{A_{ik} l \lambda_{ki}^4 g_i} \int_{\text{line}} \ln\left[\frac{I(\lambda, 0)}{I(\lambda, l)}\right] \mathrm{d}\lambda, \tag{5.5}$$

where x_0 is set to 0 and $x = l$ is the absorption length.

For the quantification of the Cs ground state density, the resonant transition from the Cs ground state $k = 6\,^2\mathrm{S}_{1/2}$ ($g_k = 2$) to the excited state $i = 6\,^2\mathrm{P}_{3/2}$ ($g_i = 4$) is exploited ($A_{ik} = 3.279 \times 10^7\,\mathrm{s}^{-1}$ [K+22]). The energy difference between the $6\,^2\mathrm{P}_{3/2}$ and $6\,^2\mathrm{S}_{1/2}$ states is 1.455 eV and corresponds to a wavelength of $\lambda_{ki} = 852.1\,\mathrm{nm}$ (so-called Cs D_2 line). As illustrated in figure 5.8(a), both energy levels underlie a hyperfine splitting due to the coupling of the total electron angular momentum $\boldsymbol{J}$ of the outer electron with the total nuclear angular momentum $\boldsymbol{I}$. The resulting

---

[1] In the plasma phase, radiation resulting from electronically excited Cs atoms is present. However, the laser intensity within this work is several orders of magnitude higher than the plasma-induced radiation so that an emission source term can be neglected here [FW11].

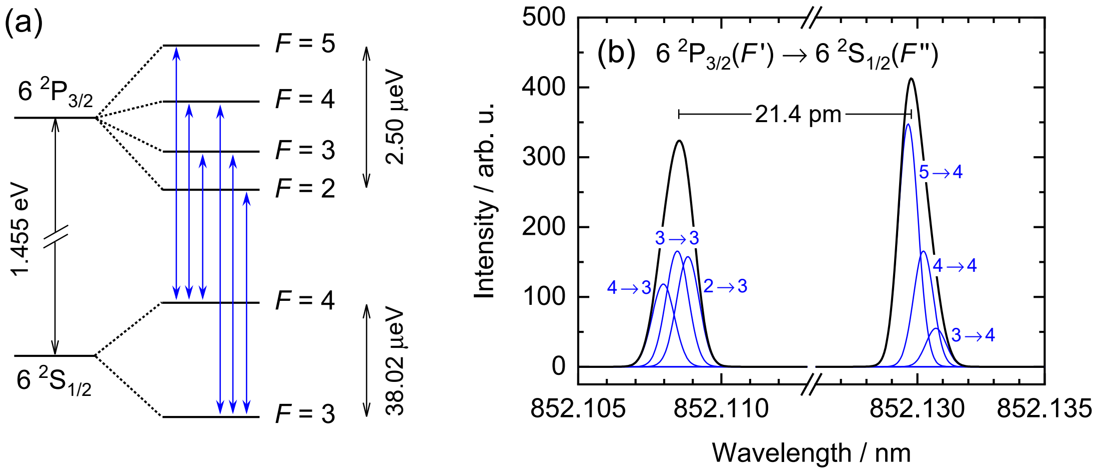

Figure 5.8: *(a) Illustration of the hyperfine splitting of the atomic Cs states 6 $^2S_{1/2}$ (ground state) and 6 $^2P_{3/2}$ [Ste19]. Optically allowed transitions between the hyperfine energy levels are indicated by blue arrows. (b) Simulated spectrum of the Cs D_2 line from the hyperfine lines (labels indicate the transition F'→F"), taking into account natural line broadening and Doppler broadening at 300 K.*

total atomic angular momentum $\boldsymbol{F} = \boldsymbol{J} + \boldsymbol{I}$ exhibits the corresponding quantum numbers $|J - I| \leq F \leq J + I$ with $\Delta F = 1$, where J and $I = 7/2$ [Rum21] are the quantum numbers of $\boldsymbol{J}$ and $\boldsymbol{I}$, respectively. This leads to the possible values of $F = 3$ and 4 for the $6\,^2\mathrm{S}_{1/2}$ state ($J = 1/2$) and $F = 2, 3, 4$ and 5 for the $6\,^2\mathrm{P}_{3/2}$ state ($J = 3/2$), resulting in six lines according to the selection rules for optical transitions ($\Delta F = 0, \pm 1$ and $F = 0 \nleftrightarrow F = 0$). Since the energy splitting of the ground state is much more pronounced than that of the $6\,^2\mathrm{P}_{3/2}$ state, three lines at about 852.11 nm and three lines at about 852.13 nm are generated. The exact central wavelengths λ_0 of the hyperfine lines and their relative intensities can be found in [Ste19] and [WE33], respectively.

The line profile of the hyperfine lines is determined by broadening effects [TLJ99]. The main contribution is the Doppler broadening due to the thermal motion of the Cs atoms, leading to a Gaussian line profile with a FWHM of

$$\Delta\lambda_{\mathrm{Dopp}}(T_{\mathrm{Cs}}) = 2\frac{\lambda_0}{c}\sqrt{\frac{2\ln(2)k_{\mathrm{B}}T_{\mathrm{Cs}}}{m_{\mathrm{Cs}}}}. \tag{5.6}$$

For typical temperatures in the range of 300 − 500 K within this work, $\Delta\lambda_{\mathrm{Dopp}}$ is of the order of 1 pm. Another contribution to the line profile comes from the natural line broadening due to the uncertainty principle for energy and time, leading to a

Lorentzian profile with a FWHM of

$$\Delta\lambda_{\mathrm{nat}} = \frac{\lambda_0^2}{c}\left(\frac{1}{2\pi\tau_k} + \frac{1}{2\pi\tau_i}\right). \tag{5.7}$$

τ_k and τ_i denote the lifetimes of the states involved in the transition. Since the Cs D_2 line is a resonant transition, only the excited state $6\,^2\mathrm{P}_{3/2}$ contributes to the natural line broadening. The lifetime of $\tau_{6\,^2\mathrm{P}_{3/2}} = 30.4\,\mathrm{ns}$ leads to $\Delta\lambda_{\mathrm{nat}} = 0.013\,\mathrm{pm}$, which is two orders of magnitude lower than the Doppler broadening. Further broadening mechanisms have an even smaller contribution to the line profile within the present work and are thus not considered (e. g., pressure broadening with a Lorentzian profile and a FWHM of the order of $10^{-3}\,\mathrm{pm}$ [Fri13]). Figure 5.8(b) shows a simulation of the six hyperfine lines considering their relative intensities and both Doppler and natural line broadening, i. e., the line profile is a convolution of a Gaussian and Lorentzian distribution and is thus a Voigt profile. As can be seen, the three hyperfine lines at 852.11 nm and at 852.13 nm overlap already at room temperature so that the total line profile, which is the sum of all the six lines, shows only two peaks. The peak centers have a distance of 21.4 pm and each peak can reasonably be approximated by a Gaussian profile.

Experimental setup

A schematic block diagram of the TDLAS system applied at ACCesS is shown in figure 5.9(a). The setup basically consists of a laser that crosses the experimental chamber and a photodiode for signal detection. The LOS, which is depicted in figure 5.7, leads to an absorption length of $l = 16\,\mathrm{cm}$. The laser system consists of a laser controller and a laser head. It is a single mode distributed feedback (DFB) diode laser with a tunable wavelength range of $851 - 853\,\mathrm{nm}$, a spectral line width of $\sim 0.01\,\mathrm{pm}$ ($\ll \Delta\lambda_{\mathrm{Dopp}}$), a side mode suppression of 39 dB and a maximum output power of about 45 mW at 852 nm. In operation, the laser wavelength is scanned mode-hop free over the range of the Cs D_2 line by modulating the diode laser current linearly with a sawtooth voltage, while the temperature of the diode is kept constant at 31.80 °C. The laser diode is connected via an optical fiber to a lens head, which generates a parallel laser beam with a diameter of about 8 mm. The laser intensity is reduced with a neutral density filter installed at the optical head (0.07 % transmission at 852 nm) to avoid significant depopulation of the Cs ground state density, which would lead to a severe underestimation of the real particle density [Lin17, FW11]. The photodiode is an amplified Si detector with an active area of $3.6 \times 3.6\,\mathrm{mm}^2$, which converts the received light intensity linearly

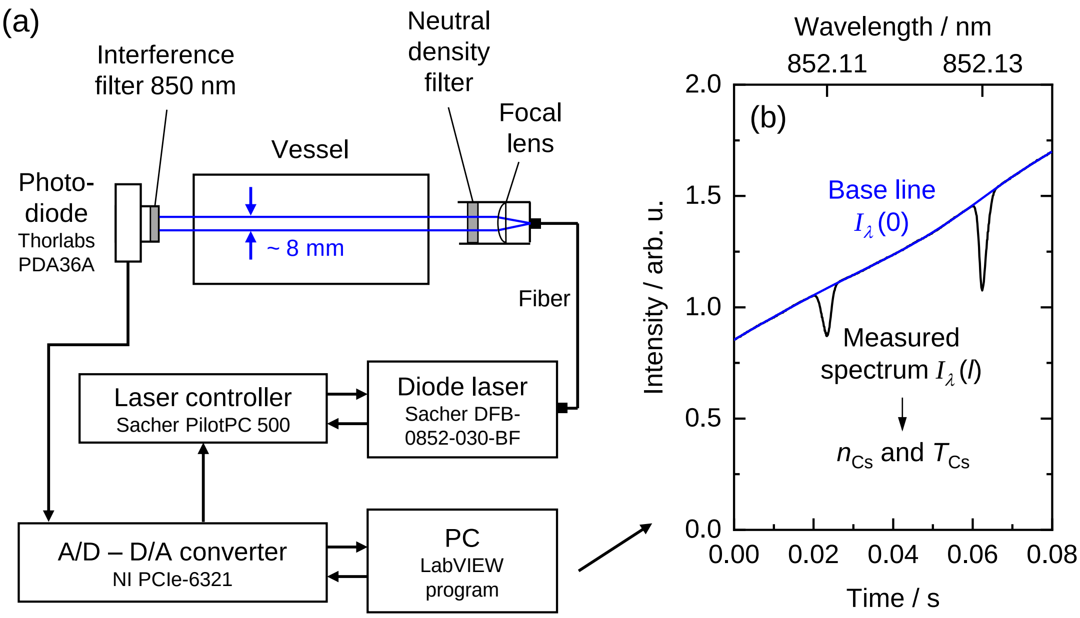

Figure 5.9: *(a) Schematic block diagram of the TDLAS setup for the measurement of the neutral Cs density. (b) Exemplary absorption spectrum with a base line fit for the determination of the intensity of the laser beam before entering the vacuum vessel.*

into a voltage signal (response to a wavelength range of 350 – 1100 nm). An interference filter with a maximum transmission of 70 % at the central wavelength of 850 nm and a FWHM of 10 nm is placed in front of the photodiode to block stray radiation from the plasma for minimizing the signal offset of the photodiode. The photodiode and the laser controller are both connected to a computer via an analog-to-digital (A/D) and digital-to-analog (D/A) converter.

The evaluation of the neutral Cs density is fully automated by a LabVIEW program. The wavelength of the diode laser is tuned with a sawtooth voltage of 10 Hz so that 10 spectra per second are read out from the photodiode with a sampling rate of 10 kHz. An exemplary absorption spectrum measured at ACCesS is depicted in figure 5.9(b). As can be seen, the intensity of the laser increases with the scanned wavelength due to the variation of the diode laser current. Since the such obtained spectral intensity can be subject to slight changes over time due to environmental influences (e. g., vibrations or RF noise), the base line $I_\lambda(0)$ is determined for each measured absorption spectrum $I_\lambda(l)$ specifically. This is done by artificially removing the absorption signal from the spectrum and fitting the remaining signal with a polynomial of ninth order. Since the linear variation of the diode laser current leads to an almost linear variation of the laser wavelength [Lin17], the wavelength calibration of the measured spectrum is done by a linear transformation of the time axis using the known distance of the peak centers (21.4 pm). By fitting the two peaks of the resultant spectrum $\ln[I_\lambda(0)/I_\lambda(l)]$ with a cumulative Gaussian function, the neutral Cs density is obtained by the use of equation (5.5). The determined Cs densities are plotted over time in the LabVIEW program and are written to a text file typically every 5 s. Additionally, recorded spectra can be saved at any time in order to perform a manual evaluation, which is preferred when the signal-to-noise ratio (SNR) is low.

The line profile of the absorption peaks is mainly determined by Doppler broadening and thus by the Cs temperature (see equation (5.6)). In [Lin17], the relationship

$$T_{\mathrm{Cs}} \approx -\frac{1}{4.19 \times 10^{-4}}\,\mathrm{K} \times \ln\left(\frac{3.65 - \Delta\lambda_{\mathrm{FWHM}}^{\mathrm{left}}/\mathrm{pm}}{2.70}\right) \tag{5.8}$$

was found for an estimation of the Cs temperature from the FWHM of the left absorption peak (at about 852.11 nm). Knowing the neutral Cs density and temperature, the neutral Cs flux toward the sample can be calculated after equation (3.25).

Limitations and measurement errors

Since the density of neutral Cs atoms in the ground state is evaluated from the absorption of laser light on its way through the vacuum vessel, the spatial profile of the Cs density within the vacuum vessel is not accessible. The detection limit of the LOS-averaged Cs density is given at the point where the absorption signal can no longer be distinguished from the base line, which is the case at about $2 \times 10^{13}\,\mathrm{m}^{-3}$ at the present setup. The uncertainty of the evaluated Cs density is mainly determined by the SNR, the quality of the base line fit, the assumption of a linear transfer function between the time and wavelength axis and the determination of the absorption length, resulting in a total error of about ±10 %. The error of the Cs temperature is estimated from the standard deviation from several evaluations at the same conditions and is about ±40 K.

In the vacuum and gas phases, the measured Cs density represents the total Cs density. In the plasma phase, however, electronically excited and ionized Cs atoms must be taken into account. While the population density of excited Cs atoms at the considered plasma conditions does not contribute significantly to the total Cs density [FW11], a considerable amount of Cs atoms is ionized by electron impact ionization due to the low ionization energy of 3.89 eV. Simulations for the BUG and ELISE ion sources have shown that up to 70 % of the total Cs density can consist of Cs^+ ions close to the plasma grid [M+18]. In consequence, the determined neutral Cs density in the plasma phase must be understood as a lower limit of the total Cs density.

5.4.2 Langmuir probe

A Langmuir probe is a standard diagnostic tool for the measurement of spatially resolved plasma parameters [MSL26, LL05, CB11]. It represents a small electrode that is inserted into the plasma and biased negatively and positively with respect to the potential of the plasma.

Fundamentals

As illustrated in figure 5.10(a), a cylindrical Langmuir probe is used within this work (probe tip is a thin metal wire) that is biased against the grounded vessel walls (reference electrode). When a voltage ramp is applied and the resulting probe current I_p is measured, a current-voltage ($I-V$) characteristic is obtained. An exemplary $I-V$ characteristic is depicted in figure 5.10(b). In case negatively charged ions can be neglected, the probe current is composed of the electron current I_e and the positive ion current I_{i^+}, where $I_\mathrm{p}(V) := |I_\mathrm{e}(V)| - |I_{\mathrm{i}^+}(V)|$. When the applied voltage is equal to the potential of the plasma ϕ_pl, the probe is to be seen as part of the plasma and the probe current is carried almost exclusively by electrons due to the much higher electron than positive ion flux, as described in section 3.3.2. The plasma potential marks the inflection point of the $I-V$ curve and can thus be found from where the second derivative crosses zero. For $V > \phi_\mathrm{pl}$, electrons are attracted to the probe (electron branch) and the effective collection area for electrons increases with increasing voltage, leading to an increase of the probe current. For $V < \phi_\mathrm{pl}$, the probe current decreases due to a repulsive potential for the electrons (transition regime). When the probe current is zero, the electron and positive ion currents are equal and the probe is on the floating potential ϕ_fl. For voltages sufficiently below ϕ_fl, the probe current is almost exclusively carried by the positive ions (ion branch), and the magnitude of the ion current increases with decreasing voltage due to an increasing effective collection area. The magnitude of the current in the ion branch is much smaller than in the electron branch due to the much higher electron than ion fluxes within the plasma.

The presence of negative ions can influence the shape of the $I-V$ curve. An increasing negative ion density leads to a decreasing electron density to maintain

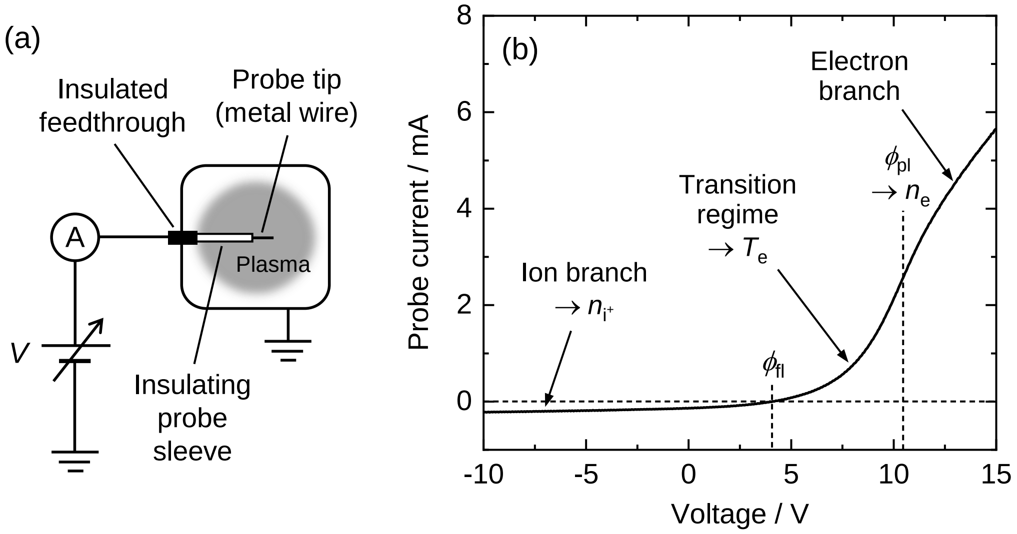

Figure 5.10: *(a) Fundamental electric circuit for a Langmuir probe measurement. (b) Typical current-voltage characteristic of a cylindrical Langmuir probe. The deducible plasma parameters from the different curve regions are indicated.*

quasi-neutrality and thus to a decreasing probe current in the transition regime and electron branch [WPL73]. In hydrogen plasmas with H^- ions being the dominant negatively charged species, the $I-V$ characteristic is consequently symmetrized with respect to the floating potential, which is the case in front of the caesiated plasma grid at negative hydrogen ion sources [MS10, T^+12]. However, the influence of negative ions on the probe characteristic can be neglected within this work because $n_{H^-}/n_e \ll 1$ [Cri18].

From the $I-V$ characteristic the electron temperature as well as the electron and positive ion density can be evaluated. The electron temperature is determined from the current in the transition regime: According to the well-known Druyvesteyn formula, the EEDF f_e is obtained from the electron current for voltages below the plasma potential by [Dru30]

$$f_e(E) = \frac{\sqrt{8m_e}}{e^3 A_p} \sqrt{E} \frac{\partial^2 I_e}{\partial V^2}, \tag{5.9}$$

where A_p denotes the surface area of the probe tip. The electron energy is given by $E = e(\phi_{pl} - V)$ and the second derivative $\partial^2 I_e / \partial V^2$ can reasonably be approximated by $\partial^2 I_p / \partial V^2$, which is described in detail in [GD11]. Since for a Maxwellian EEDF the relation $f_e \propto \sqrt{E} \exp[-E/(k_B T_e)]$ is given (see equation (3.4)), the electron temperature can be determined from the slope of a linear fit to $\ln(\partial^2 I_p / \partial V^2)$ plotted against V. Knowing the electron temperature and using the expression

$$I_\mathrm{e}(\phi_\mathrm{pl}) = eA_\mathrm{p}\Gamma_\mathrm{e} \overset{(3.25)}{=} eA_\mathrm{p}\frac{1}{4}n_\mathrm{e}\langle v_\mathrm{e}\rangle = eA_\mathrm{p}n_\mathrm{e}\sqrt{\frac{k_\mathrm{B}T_\mathrm{e}}{2\pi m_\mathrm{e}}} \tag{5.10}$$

with $I_\mathrm{e}(\phi_\mathrm{pl}) \approx I_\mathrm{p}(\phi_\mathrm{pl})$, the electron density can be calculated from the probe current at the plasma potential via

$$n_\mathrm{e} = \sqrt{\frac{2\pi m_\mathrm{e}}{k_\mathrm{B}T_\mathrm{e}}}\frac{I_\mathrm{p}(\phi_\mathrm{pl})}{eA_\mathrm{p}}. \tag{5.11}$$

The positive ion density is equal to the electron density due to the immanent quasi-neutrality of the plasma. The positive ion density could also be deduced from the ion branch of the $I-V$ characteristic. However, several theories exist for the evaluation of the ion density from the ion branch (see [Che01]) and there is no unanimous opinion on the exact criteria to determine which theory is most appropriate for a particular measurement situation [GD11]. Moreover, for all theories the ion composition within the plasma needs to be known because the mean ion mass is required for the evaluation of the ion density. Consequently, the determination of the ion density from the ion branch is subject to a high uncertainty and the evaluation of the ion density via the electron density is thus preferred in this work.

Experimental setup

Since the Langmuir probe represents an invasive plasma diagnostic, a small probe tip is required to avoid severe plasma disturbance. The dimensions of the electrode should satisfy the condition [GD11]

$$\xi := r_\mathrm{p}\ln\left(\frac{\pi l_\mathrm{p}}{4r_\mathrm{p}}\right) \ll \lambda_\mathrm{e}, \tag{5.12}$$

where r_p and l_p are the radius and length of the electrode and λ_e denotes the mean free path of the plasma electrons. The electron mean free path is estimated by $(n_\mathrm{n}\sigma_\mathrm{e})^{-1}$, where n_n is the neutral particle density and σ_e the energy dependent effective momentum transfer cross section, which can be found in [Phe22]. In order to fulfill inequality (5.12), a thin tungsten wire with a radius of 50 µm and a length of 10 mm is used, leading to a $1-2$ orders of magnitude larger λ_e compared to ξ. The tungsten wire is fed in a stainless steel rod, which is put inside a quartz tube to shield it from the plasma.

The electronics to which the probe is connected allows the application of a voltage ramp in the range of $-60\,\mathrm{V} \leq V \leq +60\,\mathrm{V}$ with respect to ground (ΔV typically $0.05\,\mathrm{V}$) and the measurement of the probe current via an implemented shunt. The electronics is connected to a computer via fiber-optic cables to ensure galvanic insulation. It is controlled by the software PlasmaMeter$^{\mathrm{TM}}$ (version 5.3), which is described in detail in [M$^+$09]. The software also allows an automatic evaluation of plasma parameters from the measured probe data after the procedure described above. The required second derivative of the $I-V$ characteristic is calculated via two-time numerical differentiation and since the measured probe data is inherently noisy, a smoothing technique is implemented to perform the differentiation with noise suppression [M$^+$09].

In order to conduct measurements above an installed sample surface in the main chamber, the probe is moved through the sample as shown in figure 5.7. To avoid adsorbates and in the case of Cs evaporation the accumulation of Cs on the probe tip, $+60\,\mathrm{V}$ are applied regularly for several seconds to heat the tungsten wire to red heat by drawing a high electron current. From the measured electron density and temperature in the direct vicinity of the surface, the positive ion flux onto the surface is calculated via equation (3.29) using the mean ion mass of $3\,\mathrm{u}$ ($6\,\mathrm{u}$) for hydrogen (deuterium) plasmas, as described in section 3.1.3. The maximum kinetic energy of the ions is determined from the difference between the plasma potential and the potential of the floating sample, the latter being measured with the installed bias connection at the sample holder.

Measurement errors

A thorough error analysis for the determination of the plasma potential, electron temperature and electron density was performed within the work of [Cri18]. The main influence on the uncertainty of the plasma parameter evaluation is given by the presence of an inherently oscillating plasma potential at the RF frequency of $27.12\,\mathrm{MHz}$, which is not compensated within the probe system and can thus lead to distortions in the $I-V$ characteristic [F$^+$96]. Moreover, the two-time numerical differentiation of the $I-V$ characteristic with the application of data smoothing is associated with uncertainties. The resulting uncertainty for the plasma potential is found to be $\pm 1.5\,\mathrm{V}$, and the statistical errors for the evaluation of the electron temperature and density are $\pm 0.2\,\mathrm{eV}$ and $\pm 20\,\%$, respectively.

5.4.3 Optical emission spectroscopy

OES is a non-invasive diagnostic that is used to analyze the plasma emission from atomic and molecular transitions spectrally resolved from the UV to the near IR range. The determination of emissivities in combination with population models allows access to a multitude of plasma parameters.

Fundamentals

Population models are used to predict the population densities of excited atomic and molecular states depending on the plasma parameters. From the population densities, emissivities can be calculated by using the respective Einstein coefficients (see equation (3.18)). By matching the calculated emissivities with the experimentally determined ones, plasma parameters (such as the atomic hydrogen density in the ground state) can be identified.

In the present work, zero-dimensional collisional radiative (CR) population models are applied [WF16, W^{+}21a]. The CR models balance all relevant population and depopulation channels of the particle states of interest and are used to predict the emissivities of the Balmer lines of the hydrogen atom (see section 3.2.1) as well as the emissivity of the Fulcher-α system ($\mathrm{d}\,^3\Pi_\mathrm{u} \rightarrow \mathrm{a}\,^3\Sigma_\mathrm{g}^+$) of the hydrogen molecule (see section 3.2.2). The latter is determined experimentally via the diagnostically well accessible emissivities of the first twelve Q branch lines ($N' = 1, ..., 12$, $N'' = N'$) of the first four diagonal vibrational bands ($\nu' = 0, ..., 3$, $\nu'' = \nu'$) of the Fulcher-α transition (single and double primes denote the upper and lower levels that are involved in the optical transition). The corresponding central wavelengths can be found in [Die72] and [FSC85] for hydrogen and deuterium, respectively. It should be noted that the upper Fulcher state is split into the $\mathrm{d}\,^3\Pi_\mathrm{u}^+$ and $\mathrm{d}\,^3\Pi_\mathrm{u}^-$ states, and the Q lines originate solely from the $\mathrm{d}\,^3\Pi_\mathrm{u}^-$ state. The analysis of the distinct Fulcher-α lines includes the evaluation of the gas temperature T_gas, which is required for the determination of the neutral particle density via equation (3.26) and the calculation of particle fluxes.

T_gas and Fulcher-α emission The procedure for the evaluation of the gas temperature is described in detail in [BF20] and is briefly summarized here. The rotational levels of the hydrogen (deuterium) molecule in the electronic ground state ($\mathrm{X}\,^1\Sigma_\mathrm{g}^+$, X in short) are predominantly populated via inelastic heavy particle collisions. In the present case of low pressure low temperature plasmas, the population of the rotational levels is well described by two temperatures: The population of the levels with low rotational quantum numbers ($N \lesssim 5$) is described by the temperature $T_{\mathrm{rot},1} = T_{\mathrm{gas}}$ (typically several 100 K) and the population of the higher rotational levels is characterized by a temperature $T_{\mathrm{rot},2} \gg T_{\mathrm{gas}}$ (in the range of a few 1000 K). The overpopulation of the high-N levels is mainly due to the energy gain of recombinative desorption of hydrogen (deuterium) atoms from the plasma vessel walls [VSE04]. Since the surface recombination of atoms can also lead to vibrational excitation, the population of the vibrational levels in the electronic ground state is also described by a "cold" temperature $T_{\mathrm{vib},1}$ for low vibrational quantum numbers and a "hot" temperature $T_{\mathrm{vib},2}$ for high vibrational quantum numbers. In order to evaluate the gas temperature from the cold rotational population, simulated relative rotational and vibrational populations are compared to the measured ones from the Q lines of the first four diagonal vibrational bands. The vibrational population is simulated by the two-temperature Boltzmann distribution

$$n_{\mathrm{X}}(\nu) = (1-\beta_{\mathrm{vib}}) \frac{n(\nu, T_{\mathrm{vib},1})}{\sum\limits_{\nu} n(\nu, T_{\mathrm{vib},1})} + \beta_{\mathrm{vib}} \frac{n(\nu, T_{\mathrm{vib},2})}{\sum\limits_{\nu} n(\nu, T_{\mathrm{vib},2})} \tag{5.13}$$

with

$$n(\nu, T) = \exp\left[-\frac{E(\nu) - E(\nu = 0)}{k_{\mathrm{B}} T}\right], \tag{5.14}$$

and the rotational population within a vibrational state ν is simulated by

$$n_{\mathrm{X}}^{\nu}(N) = (1-\beta_{\mathrm{rot}}) \frac{n^{\nu}(N, T_{\mathrm{rot},1})}{\sum\limits_{N} n^{\nu}(N, T_{\mathrm{rot},1})} + \beta_{\mathrm{rot}} \frac{n^{\nu}(N, T_{\mathrm{rot},2})}{\sum\limits_{N} n^{\nu}(N, T_{\mathrm{rot},2})} \tag{5.15}$$

with

$$n^{\nu}(N, T) = g(N) \exp\left[-\frac{E(N) - E(N = 1)}{k_{\mathrm{B}} T}\right]. \tag{5.16}$$

The weighting factors β_{vib} and β_{rot} as well as the temperatures $T_{\mathrm{vib},2}$ and $T_{\mathrm{rot},2}$ are set equal, since both the hot vibrational and rotational population originate predominantly from the surface recombination. $E(\nu)$ and $E(N)$ denote the energies of the vibrational and rotational levels, respectively, and $g(N)$ is the statistical weight of the different rotational levels. The distributions are normalized to $\sum_N n_{\mathrm{X}}^{\nu}(N) = n_{\mathrm{X}}(\nu)$ and $\sum_\nu n_{\mathrm{X}}(\nu) = 1$. The projection of the ro-vibrational population out of the ground state into the upper Fulcher state $\mathrm{d}\,^3\Pi_{\mathrm{u}}^-$ is implemented by the usage of vibrationally resolved electron impact excitation rate coefficients (dependent on T_{e}) and radiative decay into the lower Fulcher state $\mathrm{a}\,^3\Sigma_{\mathrm{g}}^+$ is considered via vibrationally resolved Einstein coefficients. In an iterative fitting routine the best match between the measured and simulated rotational and vibrational populations is identified and the rotational and vibrational temperatures of the electronic ground state are determined. The evaluation yields $T_{\mathrm{rot},1} = T_{\mathrm{gas}}$ with a typical error of ±25 K [BF20].

The emissivity of the whole Fulcher-α system (P, Q and R branches) is required for the evaluation of plasma parameters via CR modeling (see below) and is determined from the Q line emissivities and the evaluated ro-vibrational population of the $\mathrm{d}\,^3\Pi_\mathrm{u}^-$ state. As described in detail in [BF20], the measured Q line emissivities are scaled with factors determined by the application of a population model, which considers electron impact excitation from the X into the $\mathrm{d}\,^3\Pi_\mathrm{u}^{+/-}$ states and spontaneous emission into the $\mathrm{a}\,^3\Sigma_\mathrm{g}^+$ state, both vibrationally resolved. As an approximation, the evaluated ro-vibrational parameters for the $\mathrm{d}\,^3\Pi_\mathrm{u}^-$ state are also used for the $\mathrm{d}\,^3\Pi_\mathrm{u}^+$ state.

CR modeling The applied CR models are `Yacora H` and `Yacora H`$_2$ for the hydrogen atom and molecule, respectively. A detailed description of the models is provided in [WF16, W$^+$21a]. The model `Yacora H` comprises excited states up to the principal quantum number 40 including the transition to the ionic continuum. Several population and depopulation channels for the excited states are implemented, where not only H, but also H_2, the positive ions H_x^+ ($x = 1, 2, 3$) and H^- are considered. Examples are electron impact excitation and de-excitation of H, dissociative excitation of H_2, dissociative recombination of H_x^+, and mutual neutralization of H^- and H_x^+. Furthermore, photon re-absorption of the Lyman emission lines is taken into account. The model `Yacora H`$_2$ includes electronic states of the singlet and triplet system up to the principal quantum number 10 without consideration of ro-vibrational levels. For this model, recently improved cross section data for electron impact excitation processes are used [W$^+$21a, W$^+$21c].

For the simulation of emissivities, the densities of the heavy particle species as well as the electron temperature and density are required as input parameters. The neutral particle density $n_\mathrm{n} = n_\mathrm{H} + n_{\mathrm{H}_2}$ is given by equation (3.26) using the evaluated gas temperature from the Q line emissivities of the Fulcher-α transition and is thus a fixed input parameter. Technically, the models are applied iteratively, i. e., the free input parameters are varied until the simulated emissivities match the measured emissivities. In this work, the most relevant excitation channels are electron impact excitation of H and H_2 from the electronic ground state and dissociative excitation of H_2. Processes with ionic species play a subordinate role and can thus be neglected to a good approximation. This reduces the free input parameters to the electron density, electron temperature and the ratio n_H/n_{H_2}, which are iteratively determined by matching the calculated emissivities of the first five Balmer lines and the emissivity of the Fulcher-α system with the measured values.

It should be noted that specific CR models for deuterium are not available up to now. As discussed in detail in [Fri13, Rau18] though, the `Yacora H` and `Yacora` H_2 models can also be applied to deuterium to a reasonable approximation in the case of the plasmas generated within the present work.

Experimental setup

In order to measure the Balmer and Fulcher-α emissivities in the main chamber and in the external plasma source, the LOS that are depicted in figure 5.7 are used. The plasma emission is transmitted through quartz glass ports, is collected by a lens tube and is guided by fiber optics to the entrance slit of a high resolution spectrometer. As illustrated in figure 5.11(a), the lens tube is equipped with an aperture stop and the acceptance volume for plasma light collection can be approximated by a cylinder with a diameter of 10 mm. An edge filter with a cut-on wavelength of 495 nm is inserted into the lens tube to record the spectral range above 500 nm, which is done to suppress higher diffraction orders of lower wavelengths within the spectrometer. The spectrometer is in Czerny-Turner configuration (Princeton Instruments Acton SP2750) and equipped with a grating of 1800 grooves/mm and a CCD camera. Counts are recorded as a function of the scanned wavelength for a set exposure time ($> 200\,\mathrm{ms}$), from which the spectral intensity I_λ is calculated in counts per second. The apparatus profile is of Gaussian shape with a FWHM of about 20 pm. The spectrometer is intensity calibrated in the spectral region of $380 - 900\,\mathrm{nm}$ with an Ulbricht sphere. The emissivity of a distinct wavelength interval $\Delta\lambda$ can thus be obtained by

$$\varepsilon = \frac{1}{l_{\mathrm{pl}}} \int_{\Delta\lambda} I_\lambda K_\lambda \mathrm{d}\lambda, \tag{5.17}$$

where l_{pl} is the length of the LOS in the plasma volume (15 cm in the case of the main vessel and 20 cm in the case of the external plasma source) and K_λ is the wavelength dependent calibration factor. K_λ takes all optical components into account, i. e., the quartz window, the lens tube with the edge filter for $\lambda > 500\,\mathrm{nm}$,

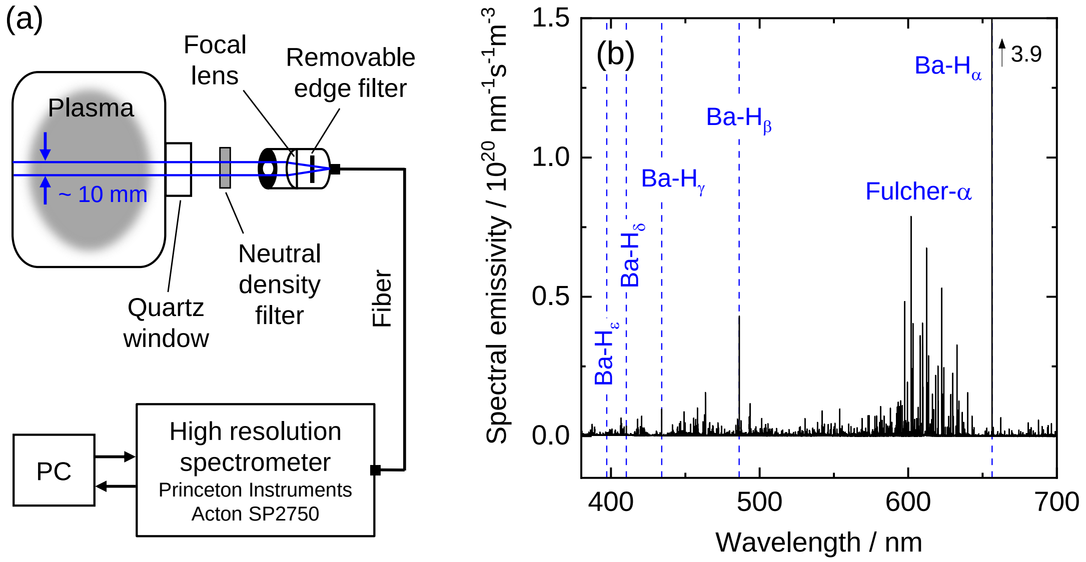

Figure 5.11: *(a) Schematic of the OES setup with the high resolution spectrometer. (b) Exemplary measured emission spectrum of a hydrogen discharge in the main vessel at ACCesS (10 Pa gas pressure, 250 W RF power).*

possibly inserted neutral density filters in the optical path to avoid overexposure of the CCD chip, the optical fiber (600 µm diameter, UV enhanced) and the components of the spectrometer. An exemplary calibrated emission spectrum of a hydrogen discharge in the main vessel at ACCesS is depicted in figure 5.11(b), showing the Balmer and Fulcher-α lines in the range of 380 – 700 nm. For the determination of the emissivity of a single line, a Gaussian fit is used (apparatus profile dominant).

Additionally, a flexible survey spectrometer (Plasus Emicon MC, Gaussian apparatus profile with a FWHM of ≈ 1.5 nm) is applied at the experiment. The survey spectrometer allows to capture the spectral range of 200 – 1100 nm with a single shot. The survey spectrometer is usually used for continuous monitoring of the plasma stability (temporal resolution ≈ 500 ms) and for the detection of plasma impurities.

Limitations and measurement errors

The emissivities and determined plasma parameters represent average values along the LOS in the plasma. A spatial resolution could only be obtained with tomographic techniques by the usage of many LOS, which is, however, not applied in the present work. The uncertainty for the evaluation of absolute emissivities of emission lines is determined mainly by the uncertainty of the calibration factors, the determination of the exact plasma length and the accuracy of the Gaussian fit for the line integral. The total error can be estimated at ±10 % [Fri13].

Plasma parameters are determined by matching CR simulations to measured values. This procedure defines a certain region of uncertainty within which the agreement is given, and typical errors are ±0.5 eV for the electron temperature, ±35 % for the electron density and ±35 % for the atomic hydrogen density.

5.4.4 VUV emission spectroscopy

Radiation in the VUV is strongly attenuated in air due to the absorption by oxygen and nitrogen. Therefore, diagnostic systems for the measurement of VUV radiation must be connected to the vacuum system. Since the installation and absolute calibration of a VUV monochromator is expensive, a flexible and easy-to-use diagnostic tool for the quantification of absolute photon fluxes down to the VUV region has been developed within the work of Fröhler-Bachus [FB22, FFBF22] and is applied here.

Experimental setup

The diagnostic system has a small size of roughly $20 \times 20 \times 20\,\mathrm{cm}^3$ and can be directly attached to the plasma chamber without the requirement of a separate pumping system. It is based on a silicon photodiode and a filter wheel in front of the diode to select the photon energy by optical filters, as depicted in figure 5.12(a). The photodiode has an active area of $10\times10\,\mathrm{mm}^2$ and is sensitive in the wavelength range of $10 - 1100\,\mathrm{nm}$ (responsivity curves can be found in [FB22]). The filter wheel provides five mounts for filters with a diameter of one inch and can be rotated manually by an external actuator without breaking the vacuum. One filter position is permanently occupied by an aluminum cover to block the plasma radiation, which is necessary to measure the dark current and to shield the diode during periods when it is not in use to minimize degradation effects. The output current of the photodiode is amplified and converted into a voltage signal by means of a preamplifier (amplification factor 10^4 V/A). The voltage signal is recorded over time with a digital multimeter, which is controlled and read out by a LabVIEW program.

The standard measurement procedure with the VUV diode system is demonstrated in figure 5.12(b). First, the offset is measured with the aluminum cover in the optical path. Then, measurements with the different filters in the filter wheel are carried out (one after the other). In figure 5.12(b), an exemplary measurement

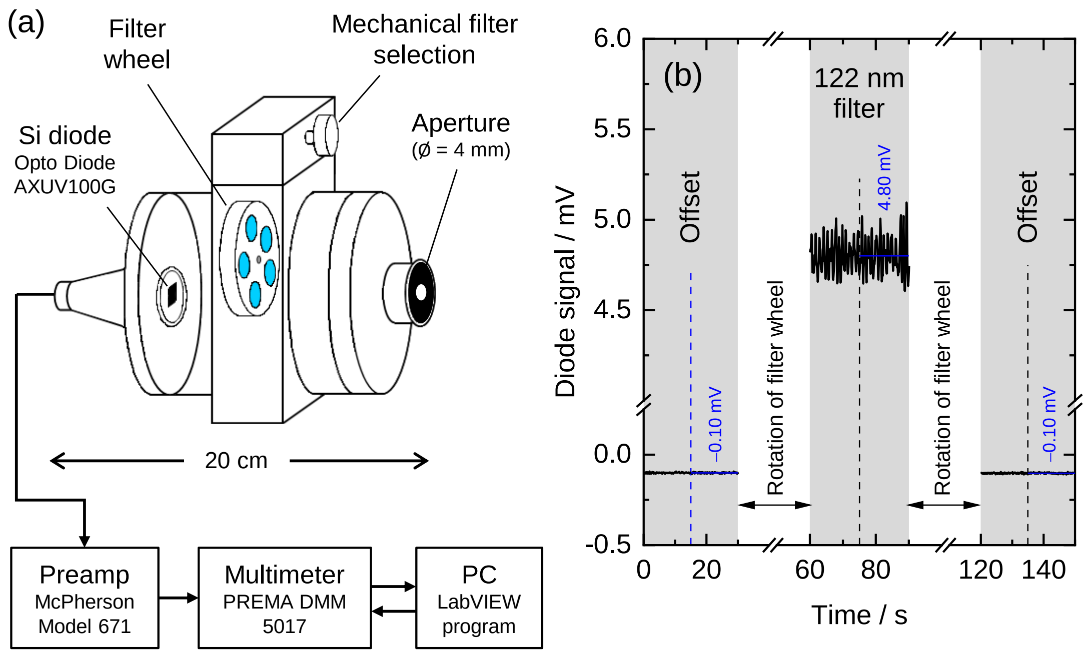

Figure 5.12: *(a) Sketch of the VUV diode system. (b) Demonstration of the standard measurement procedure with the VUV diode system at a hydrogen discharge. The offset is monitored before and after the measurement with the optical filter and the measured voltage signals for a period of 30 s for each filter position are averaged over the last 15 s (average values are depicted).*

with a 122 nm bandpass filter at a hydrogen discharge is shown (details about the applied filters are given below). Afterward, the offset is measured again. The measurement period for each filter position is set to 30 s and the voltage signal is taken as the average of the last 15 s, which is done to avoid fluctuations at the beginning of the measurement period that might occur, as demonstrated in [FB22]. The evaluated offsets before and after the filter measurements are averaged and the result is subtracted from the signals obtained with the respective filters. The offset is determined during each measurement procedure as it can be influenced by thermal effects or RF interferences for instance.

In the present work, interference filters with central wavelengths of 154 nm (30 nm FWHM) and 122 nm (14 nm FWHM) as well as a MgF_2 window are applied. The transmission curves of the interference filters and the MgF_2 window are depicted in figure 5.13, where the typical emission spectrum of a hydrogen plasma in the range of $60 - 190$ nm is supplementary depicted (taken from [FB22]). The transmission interval of the 154 nm filter is determined for a measured transmission $\geq 5\,\%$. This is given for the shaded range of $147 - 187$ nm ($8.4 - 6.6$ eV), where the dominant emission of the Lyman band of the hydrogen molecule is located. Since the transmission curve of the 122 nm filter could not be measured due to a lack of

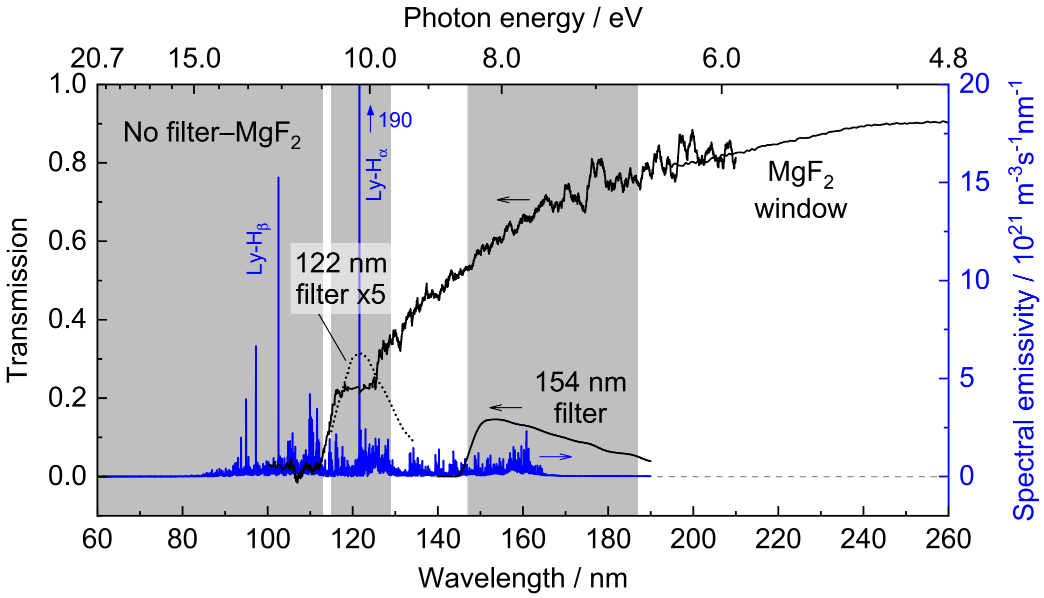

Figure 5.13: *Transmission curves of the interference filters and the MgF_2 window applied in the VUV diode system. The resulting spectral ranges that are accessed with the diode system in the present work are shaded. Additionally, an absolutely calibrated emission spectrum of a hydrogen plasma in the VUV range is depicted.*

radiation sources, only data from the manufacturer are depicted in figure 5.13 as dotted line (scaled by a factor of five). The transmission interval is defined by the FWHM of 14 nm around the central wavelength of 122 nm (10.8 – 9.6 eV) and includes the dominant Lyman-α line of the hydrogen atom at 10.2 eV. The cut-on wavelength of the MgF_2 window is defined at 5 % of the measured transmission and is at 113 nm (11.0 eV). Hence, the conduction of measurements with the MgF_2 window and without any filter gives access to the shaded spectral region above 11.0 eV, where the molecular Werner band and the atomic Lyman series without Lyman-α are located.

Determination of VUV emissivities

In contrast to OES measurements, no collimating optics can be used with the VUV diode system. An aperture stop with a diameter of 4 mm is used between the plasma vessel and the photodiode (blackened on both sides to avoid reflections), leading to a fixed viewing cone with a solid angle of about 0.03 sr. For the determination of absolute emissivities, the VUV diode system is calibrated at a dedicated ICP experiment, which is equipped with an absolutely calibrated VUV spectrometer in the wavelength range of 46 – 300 nm. Details about the experimental setup and the spectrometer can be found in [FB22, FB$^+$21]. By simultaneous measurements with the diode system and the spectrometer, calibration factors K_{filter} for the different interference filters and the $\mathrm{MgF_2}$/no filter combination are determined, which is done by calculating the ratio of the integrated spectral emissivity in the respective wavelength ranges (see figure 5.13) to the measured voltage signals V_{filter} with the diode system ($[K_{\mathrm{filter}}] = \mathrm{m^{-3}s^{-1}V^{-1}}$).

The calibration factors apply only to the geometry of the plasma volume V_{detec} that is detected within the viewing cone at the calibration setup. Therefore, V_{detec} must be quantified and considered when the diode system is transferred to another experiment. This is done by introducing the effective volume of emission V_{eff}. Under the assumption of an isotropic photon emission at each position $\boldsymbol{\rho}$ within V_{detec}, the effective volume is given by [I+20, FB22]

$$V_{\mathrm{eff}} = \int_{V_{\mathrm{detec}}} \frac{\Omega(\boldsymbol{\rho})}{4\pi} \mathrm{d}V, \tag{5.18}$$

where $\Omega(\boldsymbol{\rho})$ is the solid angle subtended by the area of the photodiode A_{d}. Since the square photodiode is illuminated circularly due to the aperture stop, A_{d} is approximated by the circular areas $A_{\mathrm{d},1}$ and $A_{\mathrm{d},2}$, where $A_{\mathrm{d},1}$ has a diameter equal to the side length of the photodiode (10 mm) and $A_{\mathrm{d},2}$ has a diameter equal to the diagonal of the photodiode ($10\sqrt{2}$ mm). Using a cylindrical coordinate system with the z-axis being defined by the normal of the diode as illustrated in figure 5.14, the respective solid angles for the positions $\boldsymbol{\rho}$ within V_{detec} are calculated by $\Omega(\boldsymbol{\rho}) = A_{\mathrm{d},x}\cos(\theta)/\rho^2$ $(x = 1, 2)$, where θ is the angle between $\boldsymbol{\rho}$ and the z-axis. At the calibration setup, the viewing cone lies fully within the plasma volume, which means that V_{detec} represents a truncated cone as depicted in figure 5.14. Under the assumption of a homogeneously emitting plasma, the effective volume is calculated by

$$V_{\mathrm{eff}} = \frac{A_{\mathrm{d},x}}{2}(z_2 - z_1)\left(1 - \frac{1}{\sqrt{1 + (R/z_2)^2}}\right), \tag{5.19}$$

where $z_2 - z_1$ is the length of the truncated cone and R is the radius of the cone at the position z_2. By averaging the effective volumes calculated for $A_{\mathrm{d},1}$ and $A_{\mathrm{d},2}$, the effective volume at the calibration setup is given by $V_{\mathrm{eff,calib}} = 43.70\,\mathrm{mm}^3$.

As depicted in figure 5.7, the VUV diode system is applied at ACCesS both at the main chamber and at the external plasma source. At the main chamber, the viewing cone lies fully within the plasma vessel and the effective volume can thus be calculated after equation (5.19). Since the plasma chamber is identical to the one of the calibration setup, the effective volumes are the same. When the

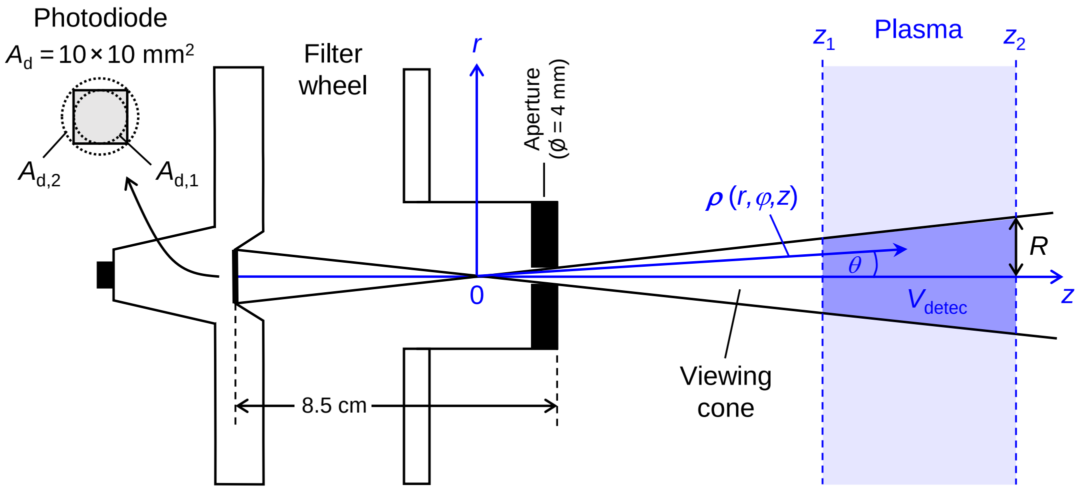

Figure 5.14: *Illustration of the viewing cone of the VUV diode system by the approximation of the square photodiode with circular areas. Positions* $\boldsymbol{\rho}$ *within the plasma volume that is detected by the diode* (V_detec) *are described within a cylindrical coordinate system.*

diode system is attached to the external plasma source, the plasma vessel (quartz tube) lies fully within the viewing cone, i. e., the vessel is the limiting boundary in this case. Thus, the integration in equation (5.18) must be performed over the cylindrical plasma volume within the vessel, which yields

$$V_\mathrm{eff} = \frac{A_{\mathrm{d},x}}{2}\left(z_2 - z_1 + \sqrt{R^2 + z_1^2} - \sqrt{R^2 + z_2^2}\right) \tag{5.20}$$

with $z_2 - z_1$ and R being the length and the radius of the plasma volume. The result is in an effective volume of 26.54 mm^3. By using the determined effective volumes, emissivities can be calculated via

$$\varepsilon = V_\mathrm{filter} K_\mathrm{filter} \frac{V_\mathrm{eff,calib}}{V_\mathrm{eff}}. \tag{5.21}$$

Photon fluxes are determined from the emissivities by the multiplication with the volume to surface ratio of the discharge vessel, which is 0.02 m for the main chamber and 0.01 m for the external plasma source at ACCesS.

Limitations and measurement errors

In [FB22], a reliable application of the VUV diode system has been demonstrated. The accuracy of the evaluated VUV emissivities depends on the errors of the calibration factors for the different filters, which are determined mainly by the uncertainty of the calibration factors for the VUV spectrometer that are used to determine spectral emissivities (see [FB$^+$21]). The resulting uncertainties for the determination of emissivities with the VUV diode system are evaluated in [FB22] and are estimated to ±24 % for the 122 nm filter, ±17 % for the 154 nm filter, and ±60 % for the MgF_2/no filter combination.

Since the diode system collects VUV radiation from a rather large viewing cone (solid angle $\approx 0.03\,\mathrm{sr}$), an integration over possible spatial profiles of the plasma emission is performed. An evaluation of spatial gradients of the spectral VUV emissivities is not possible at ACCesS and thus, a homogeneous plasma emission is assumed in the calculation of the effective volume of emission. In consequence, the uncertainties given above represent lower limits.

6 Diagnostic for the surface work function

The absolute electronic surface work function χ of installed samples at ACCesS is accessed in situ by photoelectron yield spectroscopy (PYS). PYS makes use of the external photoelectric effect: The sample surface under investigation is exposed to electromagnetic radiation with varying photon energies and the photoelectrically extracted electrons are measured [Ish18]. A photoelectric yield curve is obtained by plotting the photoelectric currents per unit incident light intensity as a function of the photon energy. For metals at $T = 0\,\mathrm{K}$, the photoelectric threshold energy is equal to the work function, i. e., only photons with an energy $h\nu \geq \chi$ allow the extraction of electrons into vacuum. For $T > 0\,\mathrm{K}$, thermal excitations lead to an energy dispersion of the order of $k_\mathrm{B}T$ at the Fermi edge and the photoelectric threshold is thus smeared to some extent. This is illustrated in figure 6.1, where the product

$$\mathcal{D}(E_\mathrm{e}) \times f_\mathrm{FD}(E_\mathrm{e}) = \frac{1}{2\pi^2}\left(\frac{2m_\mathrm{e}}{\hbar^2}\right)^{3/2} E_\mathrm{e}^{1/2} \times \frac{1}{\exp\left(\frac{E_\mathrm{e}-\mu}{k_\mathrm{B}T}\right)+1} \tag{6.1}$$

is plotted as a function of the electron energy E_e for $T = 25\,°\mathrm{C}$ (room temperature), $T = 250\,°\mathrm{C}$ and $T = 500\,°\mathrm{C}$. $\mathcal{D}$ represents the 3D density of states of the free electron model and f_FD denotes the Fermi-Dirac distribution. The chemical potential μ in the Fermi-Dirac distribution is set here and in the following equal to the Fermi energy E_F, which is a reasonable approximation for temperatures not higher than a few 100 °C [GM18]. The measurements in this work are typically performed with sample surface temperatures at/near room temperature or with elevated temperatures to $\sim 250\,°\mathrm{C}$ in maximum after plasma operation, which translates to $k_\mathrm{B}T = 0.026\,\mathrm{eV}$ and $k_\mathrm{B}T = 0.045\,\mathrm{eV}$, respectively. The energy smearing at the Fermi level thus remains weak and the photoelectric threshold can be approximated by the work function.

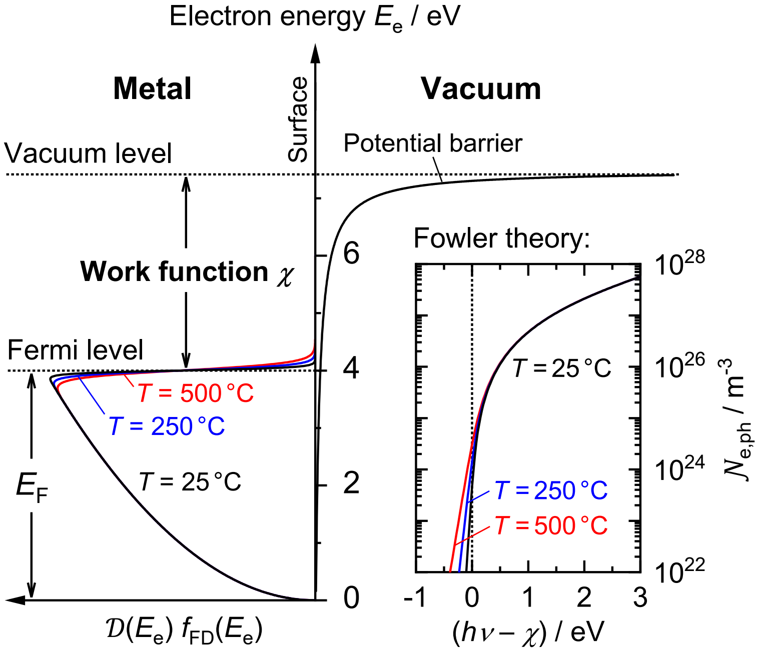

Figure 6.1: *Schematic energy diagram of a metal-vacuum interface. The potential barrier for an electron to escape from the surface is represented by its image potential. The thermal smearing of the occupied electronic states at the Fermi level of the valence band is illustrated for different temperatures (calculated after equation (6.1) with a Fermi energy of 4 eV). The respective photoelectrically releasable electron densities according to the Fowler theory (equation (6.4)) are depicted in the inset graph as a function of the energy difference between the irradiating photon energy and the metal work function.*

6.1 Fowler theory

The evaluation of the work function from photoelectric yield curves is typically done by fitting or extrapolating techniques due to a limited experimental threshold sensitivity, determined mainly by the finite detection limit for photocurrents and often limited available photon energies. To do so, the application of the Fowler theory [Fow31] is common practice, which is a prominent semiclassical approach for the description of photoemission at metal-vacuum interfaces. The Fowler theory is based on Sommerfeld's description of the metal electrons inside the valence band, i. e., the metal electrons are considered as uniformly distributed in momentum space obeying the Fermi-Dirac statistics. Hence, the number of electrons per unit volume with velocities between $\boldsymbol{v}$ and $\boldsymbol{v} + \mathrm{d}\boldsymbol{v}$ ($\boldsymbol{v} = (v_x, v_y, v_z)$) can be expressed by

$$\mathrm{d}^3\mathcal{N}_\mathrm{e} = 2\left(\frac{m_\mathrm{e}}{h}\right)^3 \frac{\mathrm{d}v_x \mathrm{d}v_y \mathrm{d}v_z}{\exp\left[\frac{m_\mathrm{e}(v_x^2+v_y^2+v_z^2)/2-E_\mathrm{F}}{k_\mathrm{B}T}\right]+1}. \tag{6.2}$$

The extractable photocurrent per unit incident light intensity, $I_{\mathrm{ph,u}}$, is assumed to be proportional to the number of electrons in the valence band whose kinetic energy component normal to the surface ($m_\mathrm{e} v_z^2/2$) exceeds the surface potential barrier after the augmentation by $h\nu$. The photon absorption probability is taken to be independent of the photon energy and the initial energy state of the electron. Under these assumptions, the available electron density for photoemission is calculated by [Fow31]

$$\begin{aligned}
\mathcal{N}_{\mathrm{e,ph}} &= 2\left(\frac{m_\mathrm{e}}{h}\right)^3 \int\limits_{\sqrt{\frac{E_\mathrm{F}+\chi-h\nu}{m_\mathrm{e}/2}}}^{\infty} \mathrm{d}v_z \int\limits_0^{2\pi} \mathrm{d}\varphi \int\limits_0^{\infty} \mathrm{d}r \frac{r}{\exp\left[\frac{m_\mathrm{e}(v_z^2+r^2)/2-E_\mathrm{F}}{k_\mathrm{B}T}\right]+1} \\
&= \frac{4\pi k_\mathrm{B} T}{m_\mathrm{e}}\left(\frac{m_\mathrm{e}}{h}\right)^3 \int\limits_{\sqrt{\frac{E_\mathrm{F}+\chi-h\nu}{m_\mathrm{e}/2}}}^{\infty} \ln\left[1+\exp\left(\frac{E_\mathrm{F}-m_\mathrm{e}v_z^2/2}{k_\mathrm{B}T}\right)\right] \mathrm{d}v_z, \qquad (6.3)
\end{aligned}$$

where cylinder coordinates are used for the integration. By introducing the substitution variable $y = m_\mathrm{e} v_z^2/(2k_\mathrm{B}T)$, equation (6.3) transforms to

$$\begin{aligned}
\mathcal{N}_{\mathrm{e,ph}} &= 2\sqrt{2}\pi\left(\frac{k_\mathrm{B} m_\mathrm{e}}{h^2}\right)^{3/2} T^{3/2} \int\limits_{\frac{E_\mathrm{F}+\chi-h\nu}{k_\mathrm{B}T}}^{\infty} \frac{\ln\left[1+\exp\left(\frac{E_\mathrm{F}}{k_\mathrm{B}T}-y\right)\right]}{\sqrt{y}} \mathrm{d}y \\
&= \tilde{C} T^{3/2} \int\limits_0^{\infty} \frac{\ln\left[1+\exp\left(\frac{E_\mathrm{F}}{k_\mathrm{B}T}-y-\frac{E_\mathrm{F}+\chi-h\nu}{k_\mathrm{B}T}\right)\right]}{\sqrt{y+\frac{E_\mathrm{F}+\chi-h\nu}{k_\mathrm{B}T}}} \mathrm{d}y, \qquad (6.4)
\end{aligned}$$

where $\tilde{C} := 2\sqrt{2}\pi(k_\mathrm{B} m_\mathrm{e})^{3/2} h^{-3} \approx 1.36 \times 10^{21}\,\mathrm{m}^{-3}\mathrm{K}^{-3/2}$. By using the variable $\kappa := (h\nu - \chi)/(k_\mathrm{B}T)$, equation (6.4) reads

$$\mathcal{N}_{\mathrm{e,ph}} = \tilde{C} T^{3/2} \int\limits_0^{\infty} \frac{\ln\left[1+\exp\left(-y+\kappa\right)\right]}{\sqrt{y-\kappa+\frac{E_\mathrm{F}}{k_\mathrm{B}T}}} \mathrm{d}y. \qquad (6.5)$$

The inset graph in figure 6.1 shows the numerical solution of equation (6.5) as a function of $h\nu - \chi$ for temperatures in the range of $25 - 500\,^\circ\mathrm{C}$ ($E_\mathrm{F} = 4\,\mathrm{eV}$). It can be seen that for $h\nu \to \chi$ the photoelectrically releasable electron density decreases strongly, which elucidates that a high experimental sensitivity is needed to detect photocurrents close to the work function. Furthermore, the progressions for the different temperatures show that an increase of the photocurrents is expected for increasing temperatures only for photon energies in the close vicinity of the work function: While the increase is $+34\,\%$ at $h\nu - \chi = 0.1\,\mathrm{eV}$ for $T = 25 \to 250\,^\circ\mathrm{C}$, it is only $+2\,\%$ at $h\nu - \chi = 0.5\,\mathrm{eV}$ for instance. For $h\nu \leq \chi$, the decrease of $\mathcal{N}_{\mathrm{e,ph}}$

is very steep: At room temperature, it is two orders of magnitude within 0.1 eV, showing that photoemission from photon energies below the work function need not be considered.

Due to the usually unknown Fermi energy in particular in the context of adsorption processes, equation (6.5) is simplified for the experimental application under the assumption that only photon energies close to the work function are considered. This approximation yields [Fow31]

$$\begin{aligned}\mathcal{N}_{\mathrm{e,ph}} &\approx \frac{\tilde{C}T^{3/2}}{\sqrt{E_{\mathrm{F}}/(k_{\mathrm{B}}T)}} f(\kappa) \\ &= CT^2 f(\kappa), \qquad (6.6)\end{aligned}$$

with $C := \tilde{C} k_{\mathrm{B}}^{1/2} E_{\mathrm{F}}^{-1/2}$ and the function

$$\begin{aligned} f(\kappa) &:= \int_0^\infty \ln\left[1 + \exp(-y+\kappa)\right] \mathrm{d}y \qquad (6.7) \\ &= \begin{cases} \sum\limits_{n=1}^{\infty} (-1)^{n+1} \exp(n\kappa)/n^2, & \kappa \leq 0, \\ \pi^2/6 + \kappa^2/2 + \sum\limits_{n=1}^{\infty} (-1)^n \exp(-n\kappa)/n^2, & \kappa \geq 0. \end{cases} \qquad (6.8) \end{aligned}$$

Consequently, the relation $I_{\mathrm{ph,u}} \propto T^2 f(\kappa)$ can be used to describe the relative progression of the photocurrents independently of the Fermi energy. This approach has proven excellent experimental agreement for $h\nu \gtrapprox \chi$ [Fow31, DuB32, DR32] and its application has become routine for photoelectric work function evaluations. It should be noted that several authors also use the $T = 0\,\mathrm{K}$ approximation of equation (6.6), i. e., [Fow31]

$$\mathcal{N}_{\mathrm{e,ph}}^{T\to 0\,\mathrm{K}} \begin{cases} = 0, & h\nu \leq \chi, \\ \propto (h\nu - \chi)^2, & h\nu > \chi. \end{cases} \qquad (6.9)$$

However, it has been pointed out in [ABZ14] that errors of $\sim k_{\mathrm{B}}T$ might be introduced by this approximation so that equation (6.6) is used within this work. Since the proportionality factor for the relation $I_{\mathrm{ph,u}} \propto T^2 f(\kappa)$ depends on factors such as the Fermi energy and optical properties of the metal surface (e. g., surface reflectance), the level of the photocurrent can vary strongly for different surfaces with the same work function.

6.2 Experimental realization

A tunable light source with a narrow spectral bandwidth is required to record photoelectric yield curves. In this work, a set of several discrete photon energies is provided by the broadband emission of a high pressure mercury arc-discharge lamp (Osram HBO 100W/2) in combination with 20 interference filters with 10 nm nominal FWHM. The mercury lamp is positioned inside a specialized lamphouse and the filters are installed in a motorized filter wheel in front of the lamphouse. The filter wheel can host six filters. As illustrated in figure 6.2, the transmitted light is collimated via two quartz lenses, is guided through the quartz viewport at the main vessel and strikes the sample holder perpendicularly. The illumination spot is located centrally above the hole for the Langmuir probe and is adjusted with the second lens for maximal photocurrent ($\approx$ 15 mm spot diameter as a compromise between the irradiated power density on the surface and the absolute absorbed power). Halos of the illumination spot are suppressed by an aperture in between the two focusing lenses. Emitted photoelectrons are drawn to the grounded vessel walls by applying a bias of -30 V to the sample holder and surface (well above space charge limitation) and the photocurrent is measured with a Keithley 6487 picoammeter. The illumination period is controlled with a shutter

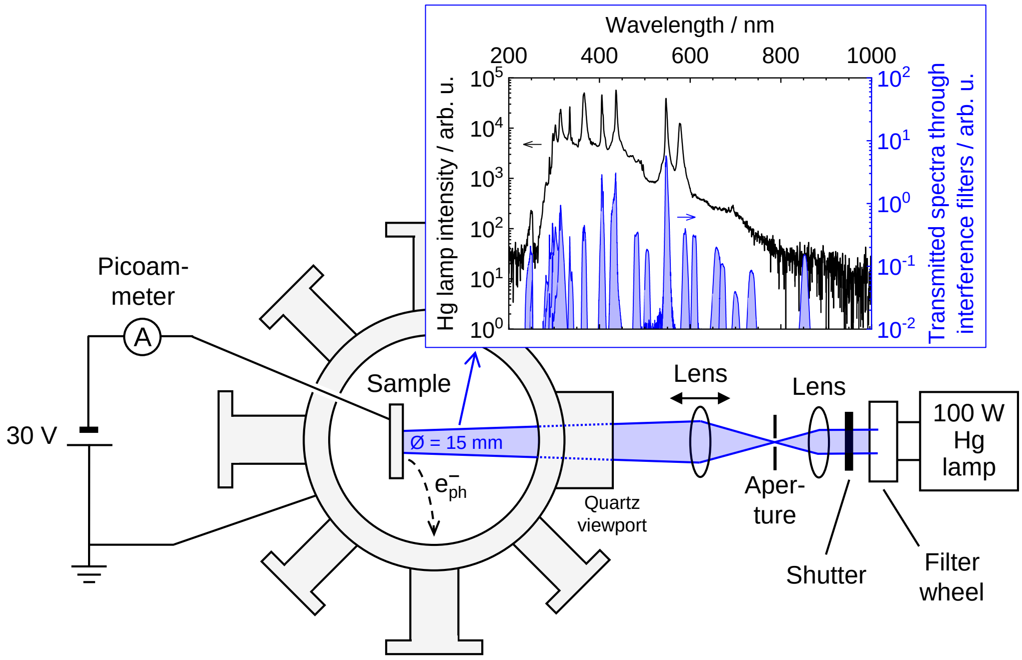

Figure 6.2: *Schematic of the photoelectric work function measurement setup. The emission spectrum of the mercury lamp together with the transmitted spectra through the applied interference filters are shown.*

in the optical path.

The emission spectrum of the mercury lamp and the transmitted spectra through the interference filters are measured behind the quartz window with the survey spectrometer (optical setup separated from the vacuum vessel). As can be seen in the diagram in figure 6.2, the spectrum ranges from the UV to the near IR region and the central wavelengths of the 20 filters are distributed within 239 – 852 nm. The transmitted wavelength and energy ranges of the filters are determined by a cut-off at 5 % of the respective maximum transmissions and are presented in table 6.1. In order to determine the transmitted mean photon energies, the transmitted spectra are calibrated to obtain the spectral emissivities ε_λ and the following formula is used:

$$\langle E_{\mathrm{ph}} \rangle = \frac{\int \varepsilon_\lambda(E_{\mathrm{ph}}) E_{\mathrm{ph}} \mathrm{d}E_{\mathrm{ph}}}{\int \varepsilon_\lambda(E_{\mathrm{ph}}) \mathrm{d}E_{\mathrm{ph}}}. \tag{6.10}$$

Table 6.1: *Wavelength range, energy range, mean energy and radiant power of the light irradiating the sample holder with the interference filters for the work function measurement. The filter label indicates the nominal central wavelength of the filters in nm.*

Filter label	Wavelength range in nm	Energy range in eV	Mean energy in eV	Radiant power in mW
239	235.9 – 253.2	4.90 – 5.26	5.04	0.276
254	244.3 – 253.3	4.89 – 5.08	4.96	0.040
280	274.8 – 303.8	4.08 – 4.51	4.31	0.133
289	284.4 – 306.4	4.05 – 4.36	4.19	0.384
300	292.7 – 320.6	3.87 – 4.24	4.06	0.558
313	307.2 – 324.6	3.82 – 4.04	3.94	0.630
334	330.8 – 342.7	3.62 – 3.75	3.69	0.094
365	360.3 – 372.4	3.33 – 3.44	3.39	0.273
405	400.8 – 411.3	3.01 – 3.09	3.05	0.871
430	424.1 – 439.2	2.82 – 2.92	2.86	1.242
480	474.2 – 490.0	2.53 – 2.61	2.57	0.276
505	497.4 – 513.3	2.42 – 2.49	2.45	0.133
550	543.5 – 554.8	2.23 – 2.28	2.26	2.398
589	580.6 – 597.8	2.07 – 2.14	2.11	0.193
610	601.9 – 616.8	2.01 – 2.06	2.04	0.212
656	644.5 – 675.8	1.83 – 1.92	1.88	0.193
671	662.6 – 680.5	1.82 – 1.87	1.85	0.066
694	687.6 – 714.3	1.74 – 1.80	1.77	0.031
730	721.9 – 749.4	1.65 – 1.72	1.69	0.065
852	839.6 – 865.8	1.43 – 1.48	1.45	0.093

As can be seen from table 6.1, the mean photon energies cover the range of $5.04 - 1.45\,\mathrm{eV}$. The respective radiant powers P_{ph} are measured with a power meter (Newport model 818-UV/DB) and are mostly of the order of $\sim 0.1 - 1\,\mathrm{mW}$. Fluctuations of P_{ph} are less than $5\,\%$ after the mercury lamp has reached thermal equilibrium (after about half an hour), which was tested for a period of up to $10\,\mathrm{h}$.

In order to evaluate the work function, the photocurrents for several photon energies near the work function must be recorded. To do so, a routine for an automated data acquisition and evaluation has been implemented in LabVIEW within this work. A screenshot of the graphical user interface is shown in figure 6.3(a). The LabVIEW program communicates with the Keithley picoammeter, the filter wheel and the shutter in the optical path. Before the program is started, the sample surface temperature T_{surf} (measured with the SIMATIC control system), the installed filters at the six positions in the filter wheel and the position of the filter to be applied first are entered into the respective fields. During one run, the current is continuously recorded and the shutter opens for all the six filters for a certain period of time, as illustrated by the measured raw data in the diagram. The time period the shutter opens for each filter can be freely selected. Usually $6\,\mathrm{s}$ are used as a compromise to obtain a reasonable average value for each filter and to restrict the total measurement time to $\approx 2\,\mathrm{min}$. The time interval for the readout of the current data is typically set to $\Delta t = 1\,\mathrm{s}$, and each current value that is read out is an average of five recorded samples to reduce noise.

For the evaluation of the work function, the recorded raw data is processed as follows: The absolute photocurrents $I_{\mathrm{ph}}(\langle E_{\mathrm{ph}} \rangle)$ are calculated by averaging the current measured during the periods the shutter is open and subtracting the dark current. The dark current is determined separately for each irradiation phase by averaging the currents before and after the shutter is open. With this, temporal changes of the dark current that may occur are taken into account. In case the dark current is highly dynamic during the measurement, a polynomial interpolation and subsequent subtraction of the dark current is performed manually afterward to enhance the accuracy (not implemented in the LabVIEW program). Typically, photocurrents up to $1-2$ orders of magnitude below the dark current are detectable. The photocurrents are then divided by the filter dependent relative intensities F of the irradiated light, which are calculated by converting the radiant powers P_{ph} given in table 6.1 from mW to photons/s. The screenshot in figure 6.3(b) shows that the photoelectric yield data are finally represented in two ways: $(I_{\mathrm{ph}}/F)^{1/2}$ is plotted as a function of $\langle E_{\mathrm{ph}} \rangle$ and $\ln(I_{\mathrm{ph}}/F/T_{\mathrm{surf}}^2)$ is plotted as a function of $\langle E_{\mathrm{ph}} \rangle/(k_{\mathrm{B}} T_{\mathrm{surf}})$. The first representation is chosen to readily approximate

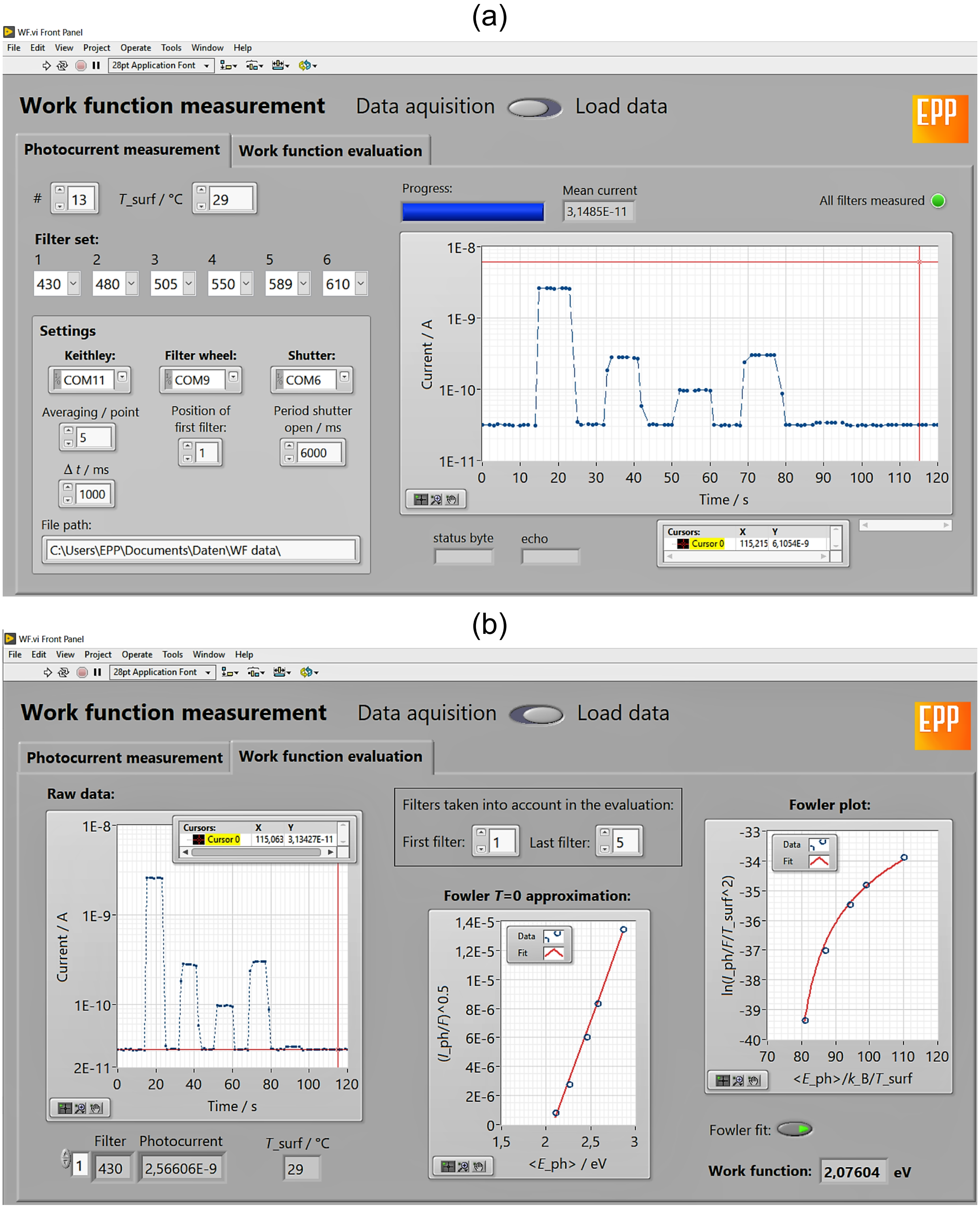

(a)

\# 13 T_surf / °C 29

Filter set:

1	2	3	4	5	6
430	480	505	550	589	610

Settings

Keithley: COM11
Filter wheel: COM9
Shutter: COM6
Averaging / point 5
Position of first filter: 1
Period shutter open / ms 6000
Δ t / ms 1000
File path: C:\Users\EPP\Documents\Daten\WF data\

Mean current 3,1485E-11

Cursors:	X	Y
Cursor 0	115,215	6,1054E-9

(b)

Cursors:	X	Y
Cursor 0	115,063	3,13427E-11

	Filter	Photocurrent	T_surf / °C
1	430	2,56606E-9	29

Filters taken into account in the evaluation:
First filter: 1 Last filter: 5

Work function: 2,07604 eV

Figure 6.3: *Graphical user interface of the work function measurement program developed with LabVIEW. The tabs for the photocurrent measurement and the work function evaluation via the Fowler method are shown in (a) and (b), respectively.*

the work function in a first step: According to the Fowler theory for $T = 0\,\mathrm{K}$ (equation (6.9)), the x-intercept of the implemented linear least-squares regression yields the work function value. The second representation is a classical Fowler plot [Fow31], which is used to evaluate the work function with higher accuracy:

By the application of equation (6.6), the data can be fitted via

$$\ln\left[\frac{I_{\mathrm{ph}}(\langle E_{\mathrm{ph}}\rangle)}{F(\langle E_{\mathrm{ph}}\rangle)T_{\mathrm{surf}}^2}\right] = A + \ln\left[f\left(\frac{\langle E_{\mathrm{ph}}\rangle - \chi}{k_{\mathrm{B}}T_{\mathrm{surf}}}\right)\right], \tag{6.11}$$

with the work function χ and the constant A being fit parameters. The filters to be included in the fits can be selected in the program and the evaluated work function via equation (6.11) is shown. The exemplary evaluation of the work function depicted in figure 6.3(b) corresponds to a caesiated surface and demonstrates that the photoelectric yield data are well described by the Fowler function.

Since not only the work function but also the temporal evolution of photocurrents can provide valuable insight into changes of the surface properties, a separate LabVIEW program is available with which photocurrents can be continuously recorded (not shown here). Photocurrents are usually converted to quantum efficiencies QEs within this work, which are calculated by

$$\mathrm{QE} = \frac{\langle E_{\mathrm{ph}}\rangle I_{\mathrm{ph}}}{eP_{\mathrm{ph}}} \tag{6.12}$$

and give the number of photoemitted electrons per incident photon.

6.3 Enhancement of the photoelectric threshold sensitivity

The evaluation of reliable work function values from photoelectric yield curves depends critically on the experimental sensitivity to the photoelectric behavior close to the threshold. The decisive impact of the photoelectric threshold sensitivity on the work function determination has been described in detail in a recent publication by the author [HFF22] and is briefly discussed here by means of an exemplary caesiation process of a Mo substrate, which is depicted in figure 6.4. The upper diagram of figure 6.4 shows neutral Cs densities monitored with the TDLAS system and measured surface work functions via the Fowler method. The relative evolution of the fit parameter A from the Fowler evaluation (see equation (6.11)) is also represented and is discussed further below. The lower diagram contains the measured dark current I_{dark} and photocurrents obtained with some of the irradiated photon energies. The Mo surface is already caesiated from a preceding campaign (left in vacuum for several days) and exhibits an initial work function of 3.5 eV. By ramping up the Cs evaporation rate, the Cs

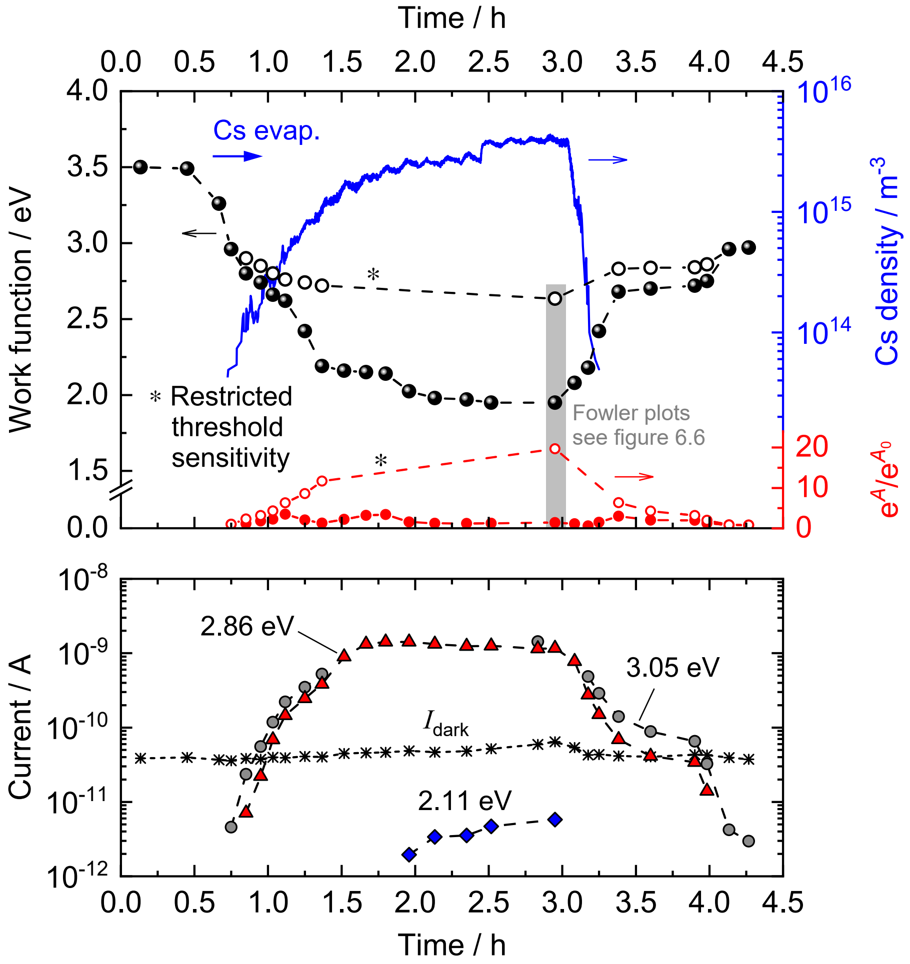

Figure 6.4: *Caesiation of a pre-caesiated Mo surface at room temperature. In the upper diagram, the measured neutral Cs density, the evaluated work function and the evolution of a relative representation of the A-parameter from the Fowler fit are shown. The evaluated work function and the corresponding behavior of the A-parameter in the case of a restricted threshold sensitivity (lack of photocurrents for photon energies below 3 eV) are depicted with the open symbols. In the lower diagram, the evolution of the dark current and photocurrents for some of the irradiating photon energies are shown.*

density rises and the photocurrents increase significantly. The applied photon energies must be gradually adjusted to lower values due to a drastic reduction of the surface work function (plotted by the full symbols). With a reached Cs density of $2.6 \times 10^{15}\,\mathrm{m}^{-3}$ at $t \approx 2.1\,\mathrm{h}$, the lowest photon energy with which photoelectric response is obtained is 2.04 eV, and a work function of slightly below 2 eV is evaluated. The measured work function is comparable to the one of pure bulk Cs, which is remarkable due to the given moderate vacuum conditions (8×10^{-6} mbar) and is discussed in detail in chapter 7. The low work function is sustained as long as the Cs density is kept above $10^{15}\,\mathrm{m}^{-3}$. When the Cs evaporation is reduced and eventually shut down ($t > 3\,\mathrm{h}$), the photocurrents decrease rapidly and the work function increases.

The threshold sensitivity of the work function diagnostic is determined mainly by the available photon energies (number of filters per energy interval and covered energy range) as well as by the detection limit for photocurrents. At ACCesS, first work function measurements were performed with the use of 9 interference filters with $\langle E_{\mathrm{ph}} \rangle = 5.04 - 3.05\,\mathrm{eV}$ [GWF11, Fri16]. This restricted filter set was later extended [Cri18], allowing access to the energy range from the UV to the near IR region with a resolution of mostly $0.1 - 0.3\,\mathrm{eV}$ as shown in table 6.1. The photocurrent detection limit is determined mainly by the radiant power and the dark current in the electric circuit. The radiant power is moderate at the present setup ($\sim 0.1 - 1\,\mathrm{mW}$, see table 6.1) to ensure that the surface under investigation is not affected by strong photon irradiation. To minimize the dark current, ground loops and external noise sources leading to the induction of electrostatic or electromagnetic interference must be avoided. Therefore, unnecessary devices are switched off or are disconnected from the experiment during the conduction of measurements (e. g., heating of the sample holder). With the Keithley 6487 picoameter used in this work, a low dark current of the order of $10^{-11}\,\mathrm{A}$ in minimum is provided.

Depending on the operational scenario, the level of the dark current may increase. As can be seen in figure 6.4, the dark current increases slightly when Cs is evaporated into the vacuum chamber, which might be due to an elevated thermionic electron emission caused by the work function reduction and/or ionized Cs atoms resulting from collisions with electrons due to the applied bias of $30\,\mathrm{V}$. A by far larger impact is given, however, by the operation of the SID diagnostic (see section 5.2). This is demonstrated in figure 6.5, where photocurrent measurements are shown that are taken sequentially with and without the operation of the SID during a similar caesiation process as in figure 6.4. When the SID is in operation, the dark current is of the order of $10^{-7}\,\mathrm{A}$. Such a high dark current can be attributed to thermionic electron emission and/or a substantial fraction of ionized Cs atoms due to the hot tungsten filaments. The lowest photon energy with which photocurrent is detected here is $2.86\,\mathrm{eV}$ (detection limit $\sim 10^{-9}\,\mathrm{A}$). When the SID is switched off, the dark current and hence also the detection limit decrease by about three orders of magnitude, allowing to detect photocurrents for photon energies below $2.86\,\mathrm{eV}$.

The influence of an unfavorable threshold sensitivity, which is given either by restricted photon energies or a high dark current, is demonstrated in figure 6.6. In

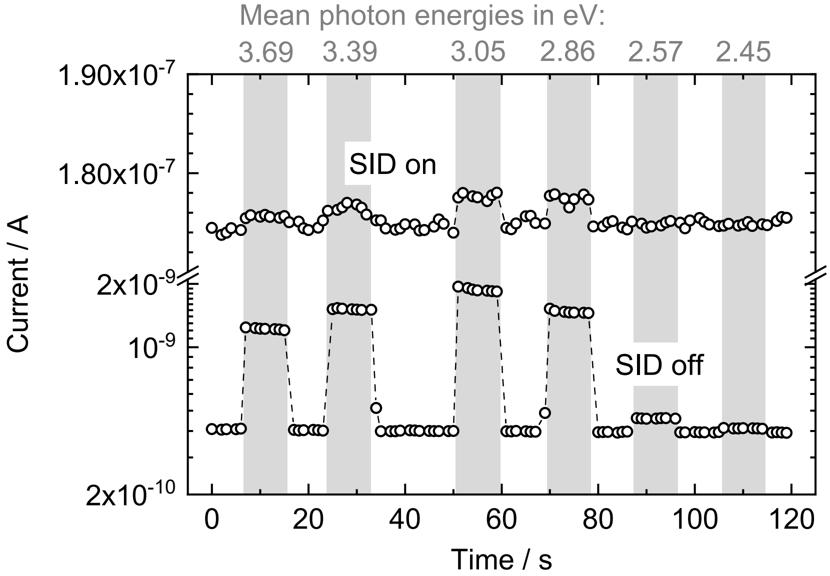

Figure 6.5: *Photocurrent measurements during a caesiation process with the SID diagnostic switched on and off. The gray shaded areas indicate the time when the sample is irradiated with the indicated mean photon energies.*

figure 6.6(a), an exemplary Fowler plot is created from the measured photocurrents for $\langle E_{\mathrm{ph}}\rangle = 2.04 - 5.04\,\mathrm{eV}$ at the time indicated in figure 6.4. With the next lower photon energy of 1.88 eV, no photoelectric response could be detected. The x-error bars result from the transmitted energy range of the filters (see table 6.1). The performed Fowler fit of the first five photocurrents above the threshold ($\langle E_{\mathrm{ph}}\rangle_{\mathrm{min}} = 2.04\,\mathrm{eV}$, $\langle E_{\mathrm{ph}}\rangle_{\mathrm{max}} = 2.57\,\mathrm{eV}$) yields $\chi_{\mathrm{fit}} = 1.95\,\mathrm{eV}$ with a standard error of ±0.01 eV (fitting range #1). The extrapolation of the fitted function to higher photon energies shows that the Fowler theory underestimates the photocurrents for photon energies far above the threshold, with the deviation becoming larger the further the photon energies are above the threshold. It is demonstrated that when $\langle E_{\mathrm{ph}}\rangle_{\mathrm{min}} = 3.05\,\mathrm{eV}$ is used for the fit of five consecutive photocurrents (fitting range #7), the Fowler fit yields a substantially higher value of $\chi_{\mathrm{fit}} = 2.63 \pm 0.02\,\mathrm{eV}$. In figure 6.6(b), the respective evaluations are shown for the Fowler $T = 0\,\mathrm{K}$ approximation and yield virtually the same results. In figure 6.6(c), the evaluated work functions with both methods are plotted as a function of the fitting range, which comprises each time five consecutive photocurrents, i. e., $\langle E_{\mathrm{ph}}\rangle_{\mathrm{max}} - \langle E_{\mathrm{ph}}\rangle_{\mathrm{min}} \lesssim 1\,\mathrm{eV}$ (shown in blue). This illustrates that the work function is gradually overestimated by increasing the distance of $\langle E_{\mathrm{ph}}\rangle_{\mathrm{min}}$ and $\langle E_{\mathrm{ph}}\rangle_{\mathrm{max}}$ to the threshold of 1.95 eV.

One reason for the failure of the Fowler method for photon energies $\gg \chi$ is the near threshold approximations that are performed to derive equation (6.6). These

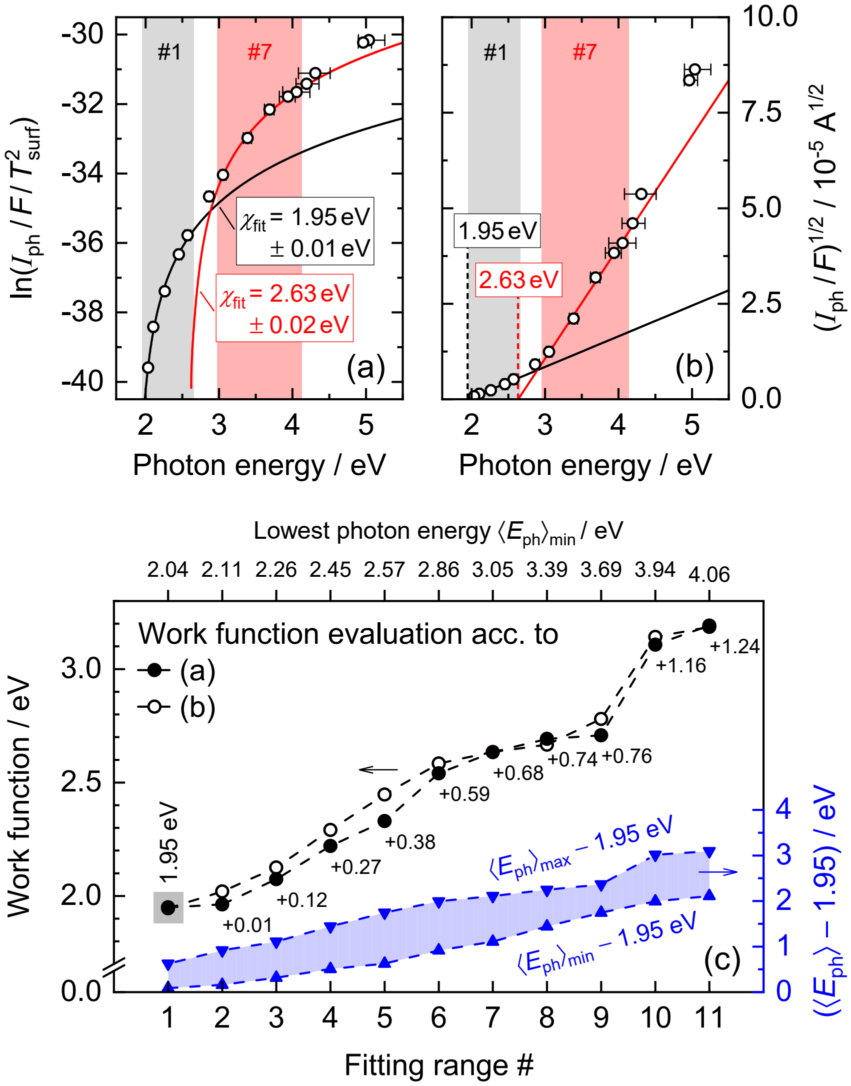

Figure 6.6: *(a) Photoelectric yield curve measured at* $t \approx 3.0$ *h during the caesiation process shown in figure 6.4 (*$T_{\mathrm{surf}} = 33$ °C*). The work function is evaluated via a Fowler fit close to the threshold (fitting range #1: gray shaded area) and for the case that photocurrents for photon energies* < 3 *eV are not measurable (fitting range #7: red shaded area). In (b), the work function evaluation is demonstrated via the Fowler* $T = 0$ *K approximation. In (c), the evaluated work function is shown as a function of the method and fitting range used, and the differences to the threshold of 1.95 eV are labeled. Additionally, the differences between the maximum and minimum photon energies to the threshold of 1.95 eV are plotted for each fitting range.*

approximations lead to an underestimation of the photocurrents for $h\nu \gg \chi$, which is more pronounced the lower the Fermi energy [Fri16]. Furthermore, the Fowler theory is in general not appropriate to predict the photoemission over a wide wavelength range, since wavelength dependent coefficients relevant to the photoemission process are neglected in the calculation of the photoelectrically releasable electron density $\mathcal{N}_{\mathrm{e,ph}}$ and are also not considered in the proportionality factor between I_{ph} and $\mathcal{N}_{\mathrm{e,ph}}$ (taken as constant). Wavelength dependent properties of the surface include the surface reflectance, penetration depth of the photons and escape depth of the photoelectrons. Moreover, the concrete evolution of the density of states and the electronic band structure are generally not considered. In consequence, the Fowler method is only accurate for photon energies in the vicinity of the threshold, which is typically a range of $0.5 - 1.0\,\mathrm{eV}$ above the work function [DuB48, BS64, BS66].

As shown in figure 6.6(a), the overestimation of the work function is not necessarily apparent from the performed Fowler fit. In figure 6.4, the resulting work function evolution by using the restricted filter set (i. e., $\langle E_{\mathrm{ph}}\rangle_{\mathrm{min}} = 3.05\,\mathrm{eV}$) is simulated (open symbols). The overestimation is $0.7\,\mathrm{eV}$ in maximum, resulting from the difference between the evaluated work functions with the fitting ranges #1 and #7 in figure 6.6. When the extended filter set is used but the SID is in operation, the fitting range #6 in figure 6.6(c) applies (see figure 6.5), resulting in an overestimation by $0.6\,\mathrm{eV}$. Unfortunately, the previously performed investigations on the work function dynamics of caesiated surfaces at ACCesS were performed with the restricted filter set and/or the operation of the SID diagnostic. In consequence, the work function values determined in [FGW10, GWF11, Fri13, FF15, Fri16, CFF17, FF17, Cri18, CFF20a, CFF21] can only represent upper limits of the actual work function.

Due to the fact that the accuracy of photoelectric work function measurements depends strongly on the threshold sensitivity, the A-parameter obtained from the Fowler fit is proposed in [Fri16] as a control parameter during the temporal work function monitoring. According to equation (6.11) that is used for the Fowler fit, the measured photocurrent after a work function change from χ_0 to χ_1 is given by

$$I_{\mathrm{ph}}^{\chi_1}(h\nu) = I_{\mathrm{ph}}^{\chi_0}(h\nu)\frac{\mathrm{e}^{A_1}}{\mathrm{e}^{A_0}}\left(\frac{T_{\mathrm{surf,1}}}{T_{\mathrm{surf,0}}}\right)^2 \frac{f(\chi_1, T_{\mathrm{surf,1}})}{f(\chi_0, T_{\mathrm{surf,0}})}. \tag{6.13}$$

The term e^{A} represents the proportionality factor between the photocurrent and $T_{\mathrm{surf}}^2 f(\chi, T_{\mathrm{surf}})$ and should be constant after the Fowler theory. Hence, if at a certain point the determined work function χ_0 and the corresponding A-parameter A_0 are taken as reference values, subsequent changes of A in the evaluation of χ may indicate an erroneous work function determination. In the exemplary caesiation process shown in figure 6.4, the state “0” is defined at $t = 0.75\,\mathrm{h}$. At this point, photoelectric response is obtained for the first time for $\langle E_{\mathrm{ph}}\rangle = 3.05\,\mathrm{eV}$ and hence, the applied five photon energies for the work function evaluation are as close as possible to the expected real work function ($\chi_0 \approx 3.0\,\mathrm{eV}$). The calculated fraction $\mathrm{e}^{A}/\mathrm{e}^{A_0}$ for the subsequent evaluations (full symbols) shows small deviations of the order of 1 from unity. However, in the case of the simulated restricted threshold sensitivity where photocurrents for photon energies below 3.05 eV are not available, $\mathrm{e}^{A}/\mathrm{e}^{A_0}$ increases to close to 20 in maximum (open symbols). Since it is shown that this increase is correlated with an overestimation of the work function by 0.7 eV, it is confirmed that the increased A-parameter indicates that lower photon energies should be used to evaluate the work function with higher accuracy [Fri16]. It must be pointed out, however, that changes of A might also occur due to variations of the surface properties (e. g., optical properties or Fermi energy), which implies that the evolution of the A-parameter can only serve as a tool for a plausibility check.

Limitations and measurement errors

- At the present setup, photocurrents (typically $< 10^{-7}$ A) can only be detected when the dark current does not exceed the photocurrents by more than $1-2$ orders of magnitude. In the vacuum and gas phases, the dark current is usually in the range of $10^{-11} - 10^{-10}$ A and photocurrents down to the pA range can be measured in operando. In the plasma phase, an applied bias of -30 V between the sample holder and the vessel walls would result in a high current masking the photoelectrically emitted electrons. Consequently, work function measurements are performed immediately after the plasma is switched off.

- In order to meet the condition $h\nu \gtrapprox \chi$, the interference filter with the lowest photon energy with which photoelectric response is still obtained must be identified. This may last several minutes due to the required exchange of filters in the filter wheel and can thus limit the temporal resolution of the work function measurement, which must be considered in case the work function changes on the minute scale or even faster.

- The available photon energies allow access to the photoelectric yield from the UV (5.04 eV) to the near IR (1.45 eV). Hence, work functions $\gtrsim 5$ eV cannot be evaluated via the Fowler method and the accuracy of the work function determination for work functions below 1.4 eV is reduced due to a lack of photon energies. In the latter case, the A-parameter is thus used to check whether indications for an erroneous work function evaluation are given.

- The standard error of determined work functions via the Fowler fit is typically below ±0.03 eV. Since the irradiated photon energies have a finite spectral bandwidth, a sensitivity analysis was conducted by simulating the photocurrent after equation (6.6) both for monochromatic light and for different spectral bandwidths by a convolution with a Gaussian function (reasonable approximation for the applied filters). The analysis showed that the narrow bandwidths of the filters have a negligible influence on the Fowler evaluation and thus, this aspect is not taken into account in the fitting routine or the error analysis. However, taking the available photon energy resolution of mostly $0.1 - 0.3$ eV into account, the absolute error of determined work functions is taken as ±0.1 eV.

7 Caesiation under moderate vacuum conditions

Finding scenarios for a reliable reduction of the work function of the extraction electrode surface to a stable value as low as possible during plasma operation is one of the main issues in ion source development. In previous works at ACCesS [GWF11, FF17, Cri18], the minimum achievable work function of Mo and stainless steel substrates upon caesiation under vacuum conditions of the order of 10^{-6} mbar was found to be $\sim 2.7\,\mathrm{eV}$. This work function is substantially higher than that of pure bulk Cs ($1.95 - 2.14\,\mathrm{eV}$) and was attributed to the formation of non-metallic Cs compounds with the background gases. A reduction of the work function to the value of bulk Cs could only be measured after the exposure to hydrogen plasma pulses and was ascribed to a plasma cleaning effect [FF17, Cri18]. However, the presented measurements with the enhanced threshold sensitivity in figure 6.4 reveal that substantially lower work functions than $2.7\,\mathrm{eV}$ can be achieved also in the absence of plasma pulses. This finding opens the window for improving the knowledge about the Cs work function behavior under the given vacuum conditions. Therefore, dedicated investigations on the work function dynamics during the caesiation process under moderate vacuum conditions are conducted with the enhanced sensitivity, with the aim to identify the caesiation scenario providing the lowest possible surface work functions in preparation for plasma operation.

7.1 Formation of ultra-low work function layers

In this section, investigations on the caesiation of polycrystalline Mo and stainless steel substrates are shown. Main parts of the results described here have recently been published in [HFF22].

In order to start the caesiation process from a Cs-free source, the experimental chamber is cleaned with distilled water, acetone and isopropyl alcohol to completely remove Cs and Cs compounds from previous campaigns. After the cleaning of the source, a hydrogen plasma (10 Pa/250 W) is generated in the main vessel for a couple of hours and it is checked whether Cs can be detected in the plasma phase via TDLAS and high resolution OES. In case Cs is detected, the experiment is opened and cleaned again. This procedure is repeated iteratively until no more Cs is detected.

Within this work, a Mo substrate is usually installed at the sample holder. The Mo substrate represents a 3 µm polycrystalline Mo coating on a 5 mm thick Cu material and is the same as that used for the plasma grid at the BUG and ELISE test facilities. After the installation of the substrate and the evacuation of the experiment, a hydrogen plasma (10 Pa/250 W) is applied for a couple of hours to remove adsorbed impurities from ambient air from the substrate surface. The cleaning of the source and the plasma treatment of the substrate are applied every time prior to the first caesiation to ensure reproducibility. The surface work function measured after this procedure lies reproducibly above 4 eV.

In figure 7.1(a), the work function and neutral Cs density measured during the caesiation of the Mo substrate at room temperature are shown, conducted one day after the hydrogen plasma treatment. Prior to the caesiation, the background pressure is 10^{-5} mbar, i. e., considerable adsorption of residual gases (mainly H_2O) is expected on the surface. The measured surface work function is 4.3 ± 0.1 eV. When the Cs oven is activated, the Cs evaporation into the vacuum chamber starts a few minutes before Cs can be detected via TDLAS (see figure 5.5) so that the work function already starts to decrease before the Cs density can be measured. Within the next 45 min, the Cs density is increased to 2.5×10^{14} m^{-3} and the work function decreases to slightly below 2 eV. By maintaining the Cs density for a period of about 40 min, this work function is kept constant.

For $t > 2.8$ h, the Cs density in the vacuum chamber is gradually increased toward 10^{15} m^{-3} and the work function is reduced even further. When the Cs density is slightly above 10^{15} m^{-3}, photoelectric response is obtained for the photon energies in the near IR range. This is demonstrated in figure 7.1(b), where an exemplary photocurrent measurement for photon energies in the range of $2.04 - 1.45$ eV is depicted. The corresponding Fowler evaluation is shown in the inset and yields a work function of 1.25 eV with a low fit error of ± 0.01 eV. Additionally, the evolution of the A-parameter is presented in figure 7.1(a) and shows a reasonably constant progression during the work function reduction to 1.25 eV. In consequence, the trustworthiness of the evaluated work function is rated as very good within the error of ± 0.1 eV. The background pressure is 6.9×10^{-6} mbar when the ultra-low work function is reached. It should be pointed

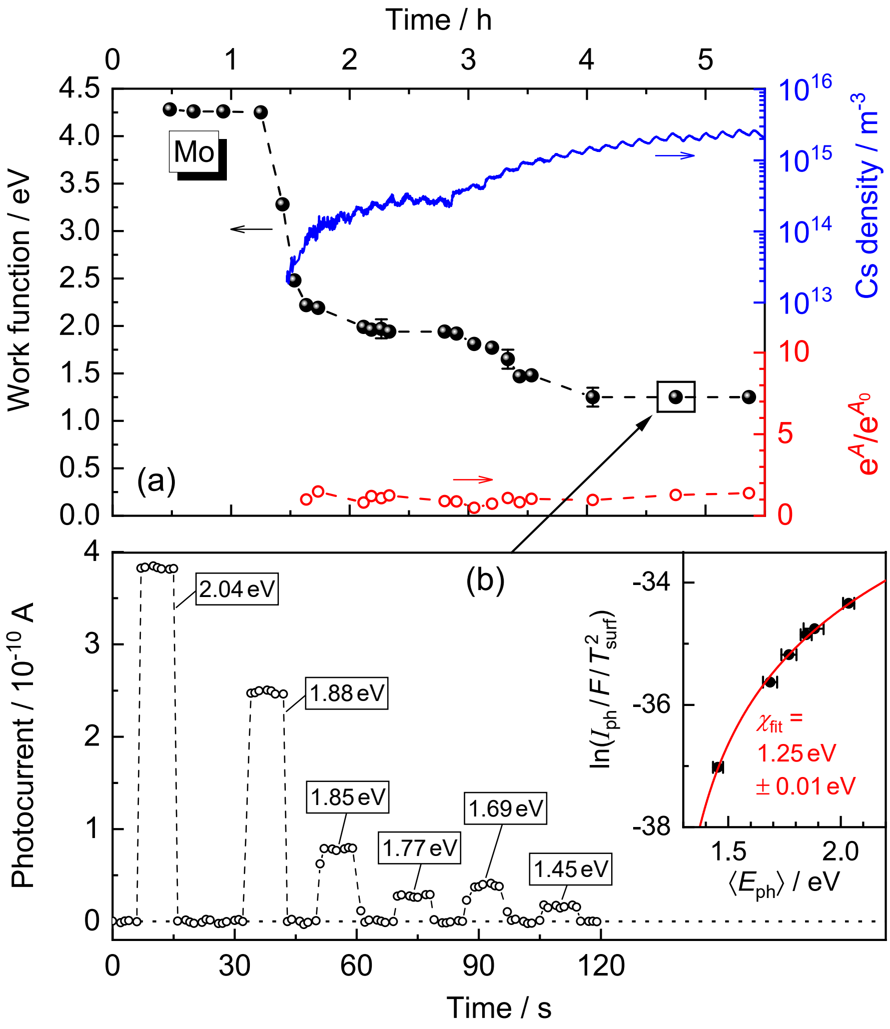

Figure 7.1: *Caesiation of a Mo substrate in the vacuum phase. In (a), the surface work function and neutral Cs density are plotted, and the progression of the A-parameter from the Fowler fit is presented. In (b), an exemplary photocurrent recording is shown for photon energies in the range of 2.04 − 1.45 eV (dark current already subtracted), with the corresponding Fowler fit for the work function evaluation depicted in the inset.*

out that the presented caesiation of the pre-caesiated Mo substrate in figure 6.4 does not lead to such low work functions with Cs densities $> 10^{15}\,\mathrm{m}^{-3}$, which is discussed in more detail in section 7.2.

In previous works at ACCesS, work function measurements were usually conducted with stainless steel substrates due to machinability reasons [Fri13, Cri18]. Therefore, the caesiation process is also applied to a stainless steel substrate (bulk material with 1 mm thickness) to identify possible substrate specific effects. The measurement results are presented in figure 7.2(a), where the measured work functions and Cs densities from figure 7.1(a) are plotted semitransparently for

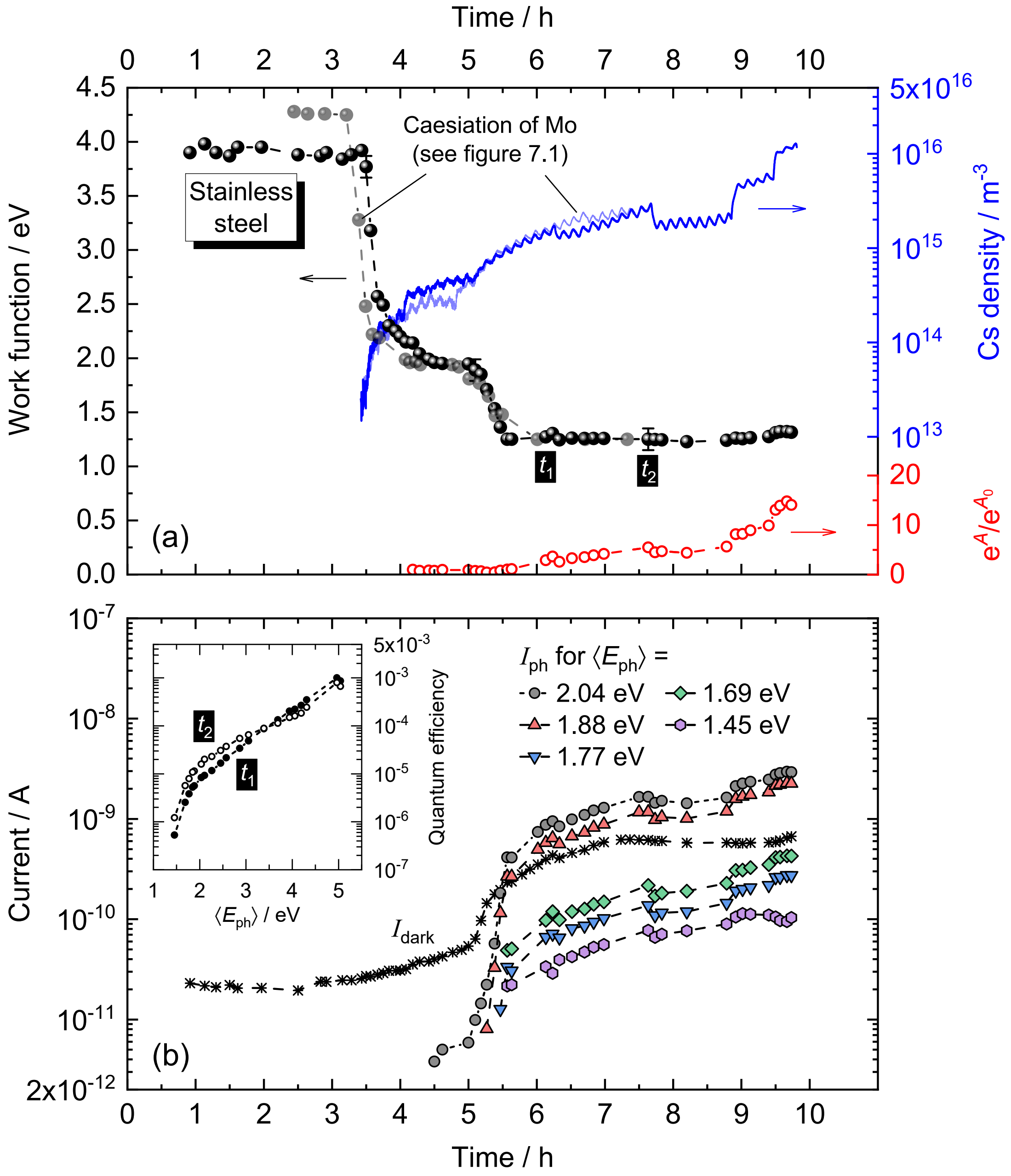

Figure 7.2: *Caesiation of a stainless steel substrate in the vacuum phase. The applied neutral Cs densities and the evolution of the surface work function together with the A-parameter are shown in (a). The Cs densities and work functions from the caesiation of the Mo substrate shown in figure 7.1(a) are plotted semitransparently for comparison. In (b), the dark current and photocurrents for photon energies in the range of 2.04 − 1.45 eV are plotted. Exemplary photoelectric QE curves are depicted in the inset.*

the sake of comparison (time axis shifted with respect to initial Cs detection). The work function of the stainless steel surface is slightly below 4 eV prior to the caesiation. Upon Cs exposure, the work function reduction is comparable to Mo.

At a Cs density of some $10^{14}\,\mathrm{m}^{-3}$, a work function of slightly below 2 eV is obtained. Since Cs densities in this range were usually applied in [Cri18] for the caesiation of stainless steel substrates under the same conditions, it is unambiguously confirmed that the determined minimum value of 2.7 eV was an overestimation due to the insufficient threshold sensitivity of the measurement system (mainly caused by the SID diagnostic, see section 6.3). The direct comparison of the measurements with Mo and stainless steel suggests that the work function reduction of Mo occurs somewhat faster. However, it must be considered that the temporal correlation of the Cs density and work function is subject to an uncertainty of several minutes in the case of drastic work function changes, since the applied interference filters for the work function measurement must be continuously adapted. The increase of the Cs density to $10^{15}\,\mathrm{m}^{-3}$ results in a work function of 1.25 ± 0.10 eV also with the stainless steel substrate, and the A-parameter remains reasonably constant. Hence, it can be concluded that the same caesiation process leads to the same surface work functions of the Mo and stainless steel substrates.

In figure 7.2(b), measured photocurrents for photon energies in the range of $2.04 - 1.45$ eV are depicted during the caesiation of stainless steel, and the dark current is additionally plotted. The work function reduction from 1.95 eV ($t = 5.0$ h) to 1.25 eV ($t \approx 5.6$ h) leads to an increase of the photocurrent for $\langle E_{\mathrm{ph}} \rangle = 2.04$ eV by about two orders of magnitude. This demonstrates that not only the photoelectric threshold is lowered, but also the photoelectric yield is substantially improved. The dark current increases during the transition from the low to the ultra-low work function regime by almost one order of magnitude. Such a large increase of the dark current is not observed during the caesiation shown in figure 6.4, where at even higher Cs densities the work function remains at 1.95 eV. Thus, the dark current increase can predominantly be ascribed to an enhanced thermionic electron emission resulting from the ultra-low work function surfaces within the experiment (Richardson's law).

After the work function of 1.25 eV is reached at $t \approx 5.6$ h, the Cs evaporation is continued for several hours and the Cs evaporation rate is varied to examine the evolution of the photocurrents and the work function. Within the first two hours, the Cs density is gradually increased from about 1.0 to $2.6 \times 10^{15}\,\mathrm{m}^{-3}$ and the evaluated work function remains constant within the error bars. However, the depicted photocurrents for photon energies in the range of $2.04 - 1.45$ eV increase over time. Since also the A-parameter increases slightly, indications for a possibly further reduced work function are given, and photon energies below 1.45 eV would be needed for a more accurate determination of the work function (currently not available due to the limited emission spectrum of the Hg lamp, see figure 6.2). In the inset in figure 7.2(b), photoelectric QE curves in the energy range of $1.45 - 5.04\,\mathrm{eV}$ at $t_1 \approx 6.1\,\mathrm{h}$ and $t_2 \approx 7.6\,\mathrm{h}$ are depicted (calculated after equation (6.12)). The comparison shows that the proceeding Cs evaporation leads to an increase of the QE for photon energies below 3.4 eV and to a decrease for photon energies above 3.4 eV. The change of the QE curve reveals that the electronic properties of the Cs layer change and depend on the applied Cs density, even if the determined work function does not change. The increase of the QE near the photoelectric threshold indicates a higher electron density at the surface, which is expected to be beneficial for the production of negative hydrogen ions, as described in section 2.1.2. The dependence of the QE on the Cs density becomes also evident at $t \approx 7.7\,\mathrm{h}$, where a slight decrease of the Cs density is followed by a small decrease of the photocurrents near the threshold. When the Cs density is increased to $1.3 \times 10^{16}\,\mathrm{m}^{-3}$ (factor of about 5 higher compared to the maximum applied Cs density during the caesiation of Mo in figure 7.1), the photocurrents for $\langle E_{\mathrm{ph}} \rangle = 2.04 - 1.69\,\mathrm{eV}$ reach maximum values and the photocurrent for $\langle E_{\mathrm{ph}} \rangle = 1.45\,\mathrm{eV}$ is slightly reduced. The respective evaluation of the work function results in 1.32 eV with a significantly increased A-parameter, indicating a pronounced uncertainty of the evaluated value.

As described in chapter 4, it is known from literature that surface work functions below the work function of bulk Cs can be generated with Cs submonolayer coverages as well as with Cs oxides under UHV conditions. However, the achievement of ultra-low work functions in a vacuum environment of $10^{-5} - 10^{-6}\,\mathrm{mbar}$ has not been reported so far. The presence of a Cs submonolayer coverage as an explanation for the measured ultra-low work functions can be ruled out due to several reasons. First, work functions even lower than the minima reported for Cs submonolayer coverages on Mo and stainless steel are measured (cf. figure 4.1(b)). Second, the ultra-low work function can be kept stable for several hours with continuous Cs evaporation. An increase of the work function toward the value of bulk Cs is not observed. Third, a color change of the surface is visible by eye after some time during the caesiation process. This can be seen in figure 7.3(a), where a photograph of the Mo surface upon caesiation is shown, taken through the quartz viewport when $\chi = 1.25\,\mathrm{eV}$ is measured. A clear darkening of the Mo surface can easily be recognized because right next to the left clamp, the surface is much brighter and looks the same as before the caesiation (care has been taken that this is not obtained due to optical effects). In this region, the Cs deposition is obstructed: Since the Cs transport is ballistic as described in

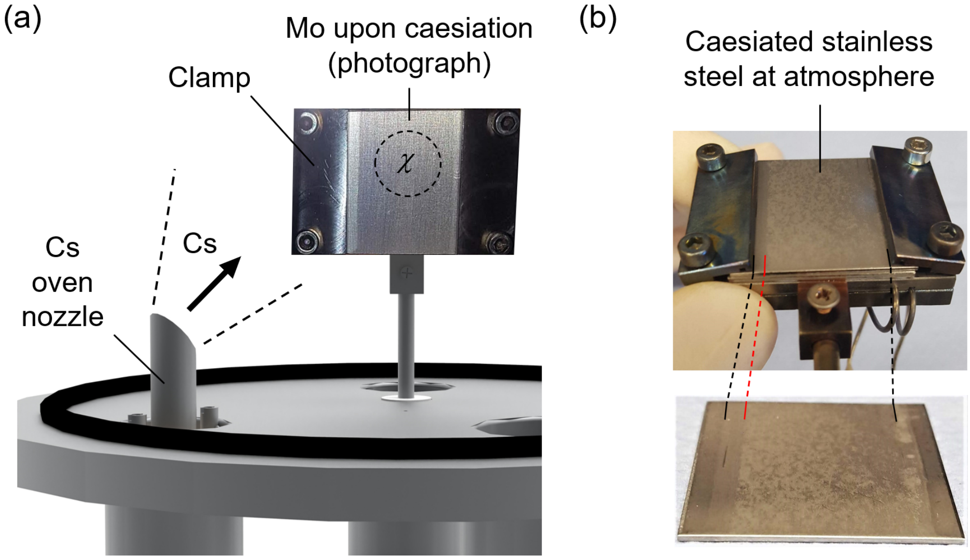

Figure 7.3: *(a) Photograph of the Mo substrate upon caesiation with a measured work function of 1.25 eV, taken through the quartz viewport. The spot for the work function measurement is indicated and the experimental arrangement is illustrated. (b) Caesiated stainless steel substrate exposed to ambient atmosphere.*

section 4.2 and the Cs oven nozzle is located to the left of the sample holder as illustrated, it is shadowed by the clamp to some extent. In consequence, the color change is attributed to an adlayer with a thickness > 1 ML, i. e., a thick Cs coating is present on the Mo substrate where the ultra-low work function is measured.

For an analysis of the chemical composition of the Cs layer, in situ/operando surface analysis techniques would be required. An ex situ analysis of the Cs layer is not meaningful because pronounced surface changes occur as soon as the substrate is exposed to air, which is due to the high reactivity and deliquescence of Cs (compounds). This is demonstrated in figure 7.3(b), where photographs of the caesiated stainless steel substrate exposed to air are shown: After only a few minutes, the surface texture becomes inhomogeneous and dissolves to some extent. Since it is known, however, that work functions down to 1.0 eV can be achieved by the formation of Cs oxides (see section 4.2), the measured ultra-low work functions are expected to be the result of the formation of an oxidized Cs layer. As the residual gas is dominated by water vapor, the growth of an oxidized Cs layer is explained by the inherent coadsorption of Cs and H_2O, where the partial and/or full dissociation of H_2O is promoted, as explained in section 4.2. The interaction of Cs with H_2O becomes also evident from a decreasing background pressure by a factor of $1.5 - 1.8$ during the caesiation process. Furthermore, small amounts of residual O_2 might also contribute to the formation of Cs oxides at the surface. As the Cs compounds have a substantially lower vapor pressure compared to pure Cs, a thick layer can grow on the metal substrate.

In figure 7.4, a compilation of work function data from various caesiation processes of Mo and stainless steel is presented. In the left diagram, the work function is plotted as a function of the applied neutral Cs density, and the corresponding background pressure is depicted. Under consideration that the correlation between the measured work function and Cs density underlies a larger uncertainty during the initial ramp-up phase of the caesiation process, an excellent reproducibility is given: The work function is reduced to ≈ 2 eV with a Cs density in the range of $2-4\times10^{14}\,\mathrm{m}^{-3}$ and to 1.25 ± 0.10 eV with a Cs density $\gtrsim 10^{15}\,\mathrm{m}^{-3}$. The Cs density threshold of $\sim 10^{15}\,\mathrm{m}^{-3}$ must be reached for the achievement of work functions in the range of 1.25 ± 0.10 eV and cannot be compensated by increasing the fluence with a lower Cs density instead (not shown). Since it is expected that the formation and stoichiometry of Cs-O compounds and thus the surface work function are strongly determined by the ratio of the Cs to H_2O flux onto the surface, the compiled work function data are plotted against the flux

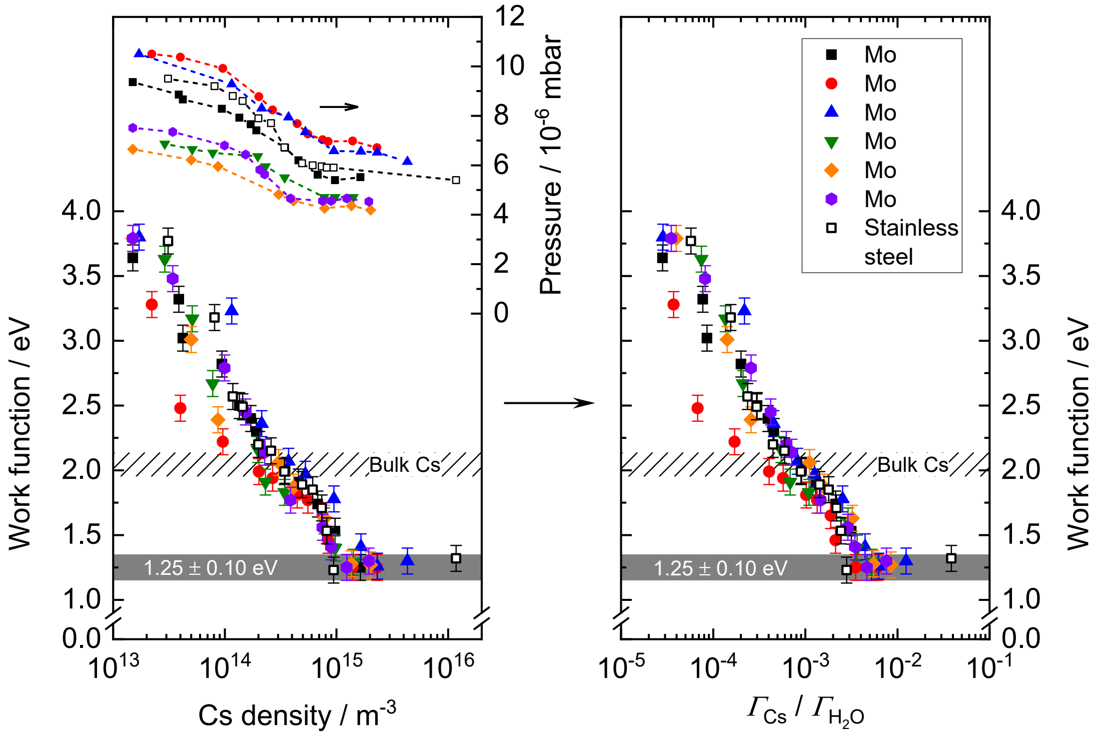

Figure 7.4: *Compilation of work function data from various caesiation processes of Mo and stainless steel. The work function is plotted as a function of the neutral Cs density in the left diagram, and as a function of the flux ratio of neutral Cs atoms to residual water molecules in the right diagram. The corresponding evolution of the background pressure is shown to the top of the left graph.*

ratio of Cs to H_2O in the right diagram of figure 7.4. The fluxes are calculated via equation (3.25), where the H_2O particle density is derived from the measured background pressure and the ideal gas law (the much lower partial pressures of other residual gases are neglected). At a flux ratio of typically $\Gamma_{\mathrm{Cs}}/\Gamma_{\mathrm{H_2O}} \sim 0.005$, the work function of 1.25 eV is reached. For $\Gamma_{\mathrm{Cs}}/\Gamma_{\mathrm{H_2O}} > 0.005$, the evaluated work function remains constant within the error bars. However, the QE curve and the A-parameter change and the work function of 1.25 eV might be an upper limit.

7.2 Degradation and re-caesiation

As described in the previous section, the ultra-low work function is kept stable with a sustained Cs density of $\gtrsim 10^{15}\,\mathrm{m}^{-3}$ in the vacuum chamber. When the Cs density is reduced below $10^{15}\,\mathrm{m}^{-3}$, i. e., $\Gamma_{\mathrm{Cs}}/\Gamma_{\mathrm{H_2O}} \lesssim 0.005$, the work function increases. This is demonstrated in figure 7.5, where the work function behavior during and after the shutdown of the caesiation process shown in figure 7.2 is depicted. As soon as the heating of the Cs oven reservoir is stopped, the Cs density of slightly above $10^{16}\,\mathrm{m}^{-3}$ decreases rapidly (~ one order of magnitude within five minutes). The decrease of the Cs density and thus of the flux ratio of Cs to H_2O onto the surface leads to an almost instant decrease of the photocurrents and to an increase of the work function. At $t = 10\,\mathrm{h}$, the Cs density is $8 \times 10^{13}\,\mathrm{m}^{-3}$ and a work function of about 1.9 eV is measured. Some minutes after the Cs density is below the TDLAS detection limit, the caesiated surface is exposed solely to the residual gas flux and the work function increases from 2.10 to 2.66 eV

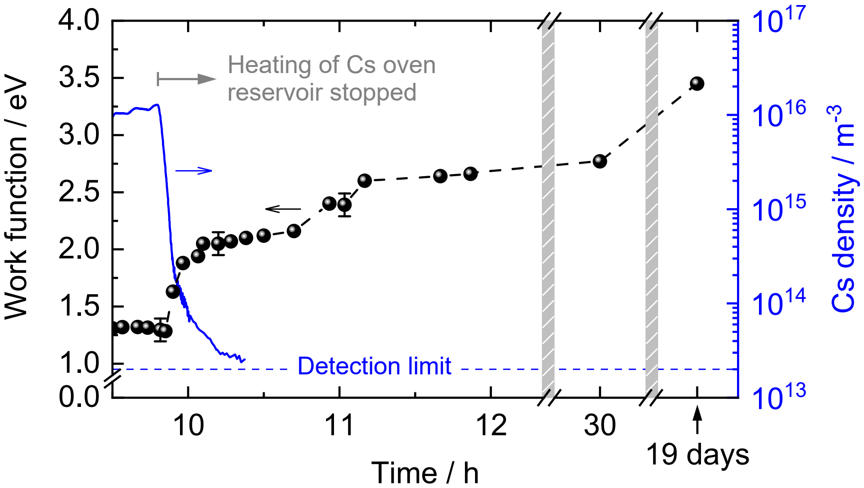

Figure 7.5: *Behavior of the surface work function during and after the shutdown of the caesiation process shown in figure 7.2.*

within 1.5 h, i. e., with a rate of roughly +0.4 eV/h. Afterward, the degradation is slowed down and work functions of 2.77 and 3.45 eV are obtained after 18 h and 19 days, respectively. The background pressure in the vacuum chamber is kept at $6 - 7 \times 10^{-6}$ mbar throughout the whole time. The gradual increase of the work function is explained by the passivation of the Cs layer due to the continuous accumulation of residual gases and the formation of Cs compounds (e. g., CsOH).

In figure 7.6(a), the work function behavior of the stainless steel substrate upon re-caesiation after the 19 days of degradation is compared to the first caesiation (see figure 7.2). The work functions and Cs densities are plotted against the Cs fluence $\varPhi_{\mathrm{Cs}}$, which is a measure of the total amount of Cs atoms to which the sample surface is exposed during the caesiation process. As can be seen, the Cs density vs Cs fluence traces of the first and second caesiation process are almost identical, i. e., similar Cs densities are applied for comparable time periods. Moreover, the background pressures are almost identical during both caesiation processes, which confirms comparable vacuum conditions (not shown). While the work function before the first caesiation is 3.95 eV, it is 0.5 eV lower before the re-caesiation. In both cases, the evaporation of Cs into the vacuum chamber leads to a work function decrease to 2.2 eV at a reached Cs fluence of about $2 \times 10^{19}\,\mathrm{m}^{-2}$, where the Cs density is at $3 \times 10^{14}\,\mathrm{m}^{-3}$. During the first caesiation, the subsequent increase of the Cs density to $\sim 10^{15}\,\mathrm{m}^{-3}$ leads to a drop of the work function into the ultra-low regime, and $\chi = 1.25 \pm 0.10$ eV is obtained at $\varPhi_{\mathrm{Cs}} \gtrsim 2 \times 10^{20}\,\mathrm{m}^{-2}$. During the re-caesiation process, however, the work function remains constant at 2.2 ± 0.1 eV up to $\varPhi_{\mathrm{Cs}} \approx 2 \times 10^{20}\,\mathrm{m}^{-2}$. After keeping the Cs density of the order of $10^{15}\,\mathrm{m}^{-3}$ for some minutes, the work function gradually decreases to $2.0 - 2.1$ eV. Only by the increase of the Cs density up to $\sim 10^{16}\,\mathrm{m}^{-3}$, the work function is reduced further to 1.8 ± 0.1 eV ($\varPhi_{\mathrm{Cs}} > 2 \times 10^{21}\,\mathrm{m}^{-2}$). As shown in figure 7.6(b), the work function decrease from 2.2 to 1.8 eV is accompanied by an increase of the photoelectric QE throughout the accessible spectral range (curves labeled 3 and 4). Also plotted are the QE curves recorded during the first caesiation at $\chi = 2.0$ eV (labeled 1) and 1.3 eV (labeled 2). It can be seen that at a reached work function of 1.8 eV during the re-caesiation, the QEs for $\langle E_{\mathrm{ph}} \rangle \geq 2.0$ eV are still lower compared to the surface with $\chi = 2.0$ eV obtained during the first caesiation. Furthermore, the QE at $\langle E_{\mathrm{ph}} \rangle = 1.9$ eV (close to the threshold) is three orders of magnitude lower compared to the surface with $\chi = 1.3$ eV, which is obtained during the first caesiation with even lower Cs fluxes and fluences. This impressively demonstrates that the photoelectric surface properties generated during the first caesiation are far from being restored upon re-caesiation.

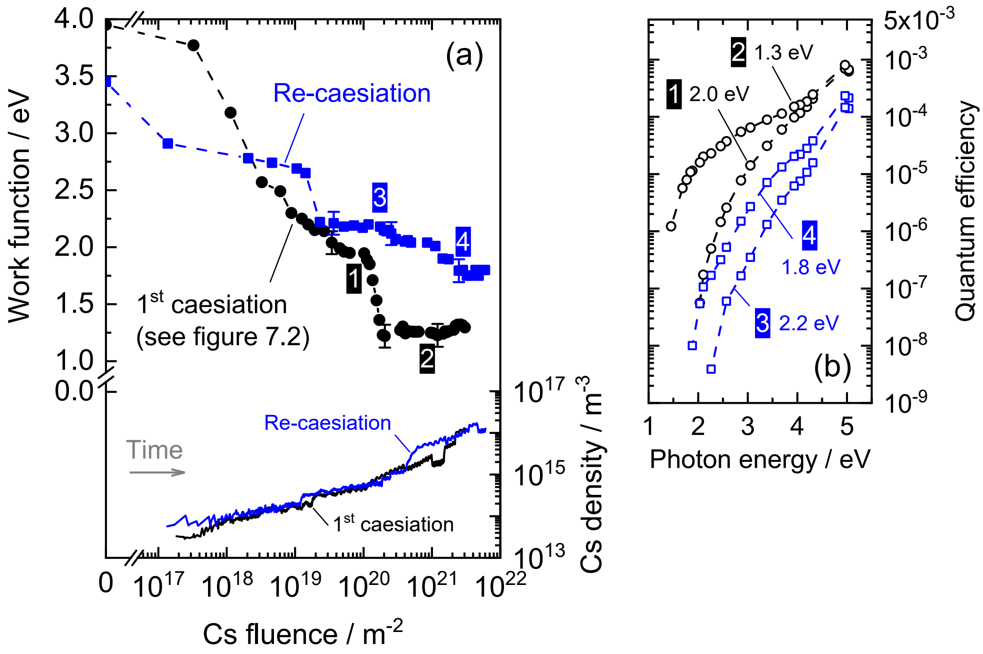

Figure 7.6: *(a) Work function evolution during the first caesiation of the stainless steel substrate and during its re-caesiation after 19 days in vacuum. The work functions as well as the neutral Cs densities are plotted against the calculated Cs fluence applied during the caesiation processes. In (b), QE curves recorded at different times during the first and second caesiation process are shown, and the corresponding work functions are indicated.*

The measurements show that in the absence of Cs evaporation, the residual gases alter the properties of the caesiated surface in a way that prevents the re-establishment of an ultra-low work function coating upon re-caesiation. It is probable that the Cs adsorption on (H_2O covered) Cs compounds leads to much weaker electrostatic dipoles compared to the adsorption on bare metal substrates. Thus, a different surface chemistry is present, and the structural and chemical composition of the Cs layers that grow on the surface are affected (e. g., hampered water dissociation via the electrostatic field-induced effect, see section 4.2). In consequence, different evolutions of the QE and of the Fermi level are plausible.[1]

Various conducted re-caesiations of the Mo substrate after different degradation times (few days up to several weeks) showed a similar behavior of the QE and work function of the surface. It was confirmed that a work function in the ultra-low regime cannot be retrieved upon re-caesiation without any further surface treatment. The actual work function dependence on the Cs density and fluence depends, however, on the experimental history of the substrate (e. g., degradation

---

[1] The reduction of the QE upon re-caesiation is also reported for Cs/O_2 activated photocathodes and is not fully understood up to now [C^{+}14, F^{+}17b].

time and plasma exposure), which underlines the statement that the Cs layer growth is determined by the chemical composition of the layers underneath it. Typically, work functions in the range of 1.9 − 2.1 eV are obtained with applied Cs densities of the order of $10^{15}\,\mathrm{m}^{-3}$ upon re-caesiation.

7.3 Vacuum heat treatment after degradation

First investigations at ACCesS have shown that elevated surface temperatures are beneficial to counteract the degradation of the Cs layer [Fri13, FF15]. Therefore, the influence of heat on a degraded Cs layer is thoroughly investigated with the improved work function diagnostic. In figure 7.7, the result of an annealing process of a degraded caesiated Mo surface from room temperature to close to 900 °C is shown (without Cs evaporation from the oven). Before the annealing process, the Mo substrate was exposed to a Cs fluence of about $7 \times 10^{21}\,\mathrm{m}^{-2}$ and a work function in the range of 1.25 ± 0.10 eV was reached. Afterward, the substrate was left in vacuum for several days, leading to an increase of the work function to 3.3 eV. As can be seen in figure 7.7(a), the heating is performed incrementally in steps of 50 − 100 °C and the sample is kept at each temperature for about 20 − 30 min. The TDLAS system is continuously running to track possibly desorbed Cs atoms from the surface. The corresponding RGA signals for H_2, H_2O, N_2 and O_2 are plotted in figure 7.7(b). The work function is measured at each temperature step and is plotted as a function of the surface temperature in figure 7.7(c). As explained in section 6.3, the heating is switched off during the work function measurement in order not to disturb the photocurrent measurement. Consequently, the surface temperature decreases during the work function measurement, and the decrease is more pronounced the higher the temperature. Up to 400 °C, however, the temperature decrease is only a few degrees during the period of 2 min needed for the work function measurement, and the work function is plotted against the average temperature during the measurement. For temperatures above 500 °C, the dark current increases to above 10^{-7} A due to thermionic electron emission, which is too high to perform reliable work function measurements (see figure 6.5). Therefore, the work function is measured after the sample has cooled down to $\sim$ 400 °C. It is plotted against the applied temperature before the measurement, and the temperature during the measurement is indicated.

The initial temperature increase to 50 °C does not lead to a measurable influence on the work function. However, by further increasing the temperature, the work function is reduced. At 200 °C, the work function is 2.25 ± 0.10 eV and thus more

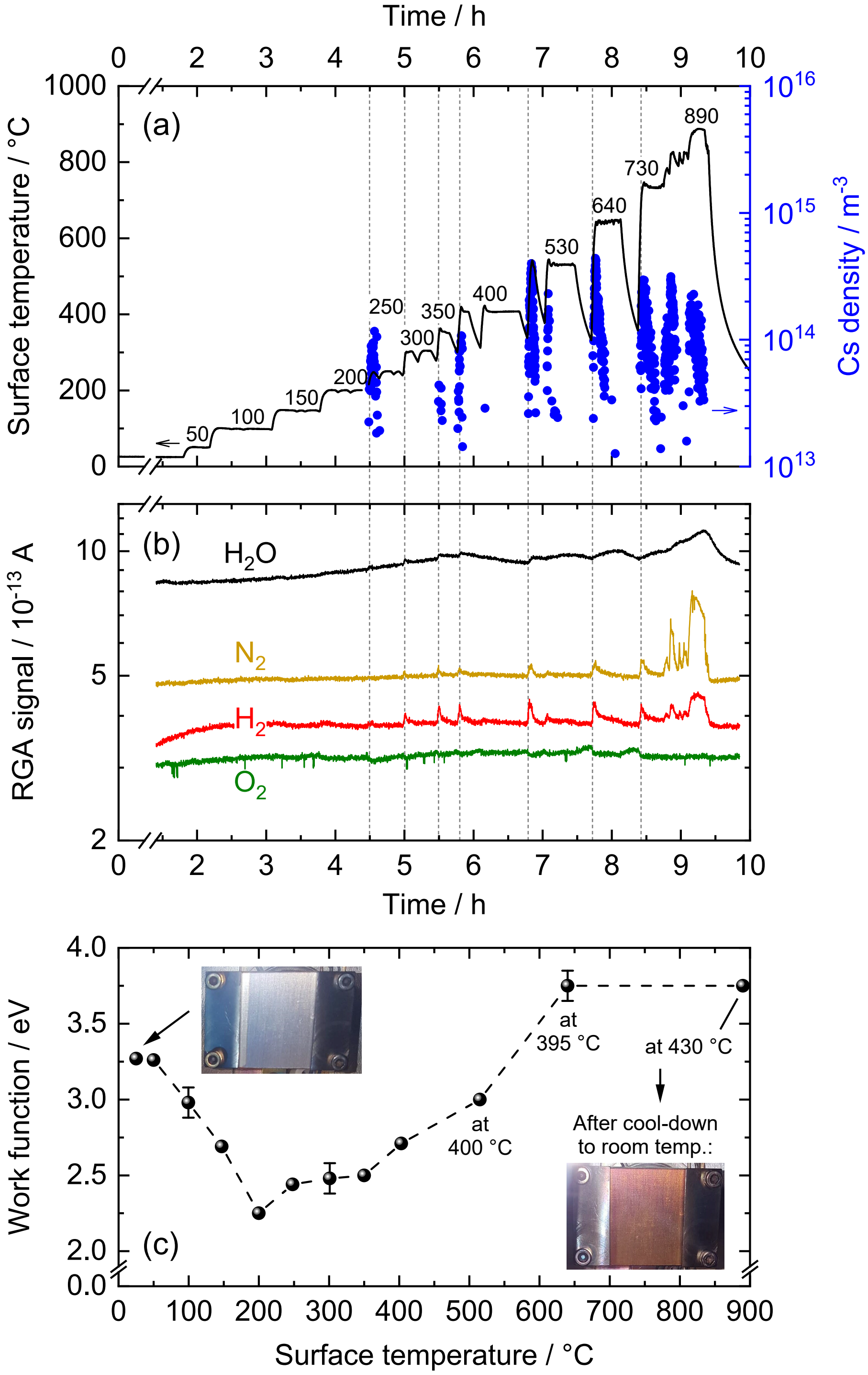

Figure 7.7: *Vacuum heat treatment of a degraded caesiated Mo surface. In (a), the surface temperature and the measured neutral Cs density desorbed from the surface are plotted over time, and in (b), the corresponding RGA signals for selected gases are shown. In (c), the dependence of the work function on the surface temperature is shown. When a temperature above 500 °C is applied, the work function is measured after the sample has cooled down for some minutes, and the temperature during the work function measurement is indicated. The depicted photographs of the sample surface are taken before and after the annealing process.*

than one eV lower than before the heating. Up to this temperature, thermal desorption of Cs is not detected. However, the RGA signal for H_2O increases slightly, indicating thermal desorption of residual gases from the surface. By increasing the temperature to 250 °C, the work function increases by 0.2 eV, and significant desorption of Cs from the surface occurs: The measured Cs density increases to $1.2 \times 10^{14}\,\mathrm{m}^{-3}$ and drops to below $10^{13}\,\mathrm{m}^{-3}$ within a few minutes. Subsequent increases of the temperature lead to further deteriorations of the work function and after a temperature above 600 °C has been applied, the work function is at about 3.75 eV. The temperature elevation leads to recurrent Cs desorption, showing that the Cs atoms have different binding energies at the surface. Each time Cs is desorbed, the background pressure rises (not shown) and the RGA signals for H_2O, N_2 and H_2 increase. In particular, the dominant peaks in the RGA signal for H_2 suggest thermal dissociation of Cs-H bondings (e. g., decomposition of Cs hydride, see section 4.2).[2] The assumption that Cs-H bondings are present and thermally cracked is corroborated by the fact that the H_2 signal remains constant when the bare substrate is heated, while the signals for H_2O and N_2 also increase in this case (not shown). Concerning the RGA signal for O_2, a decrease is occasionally observed during the desorption of Cs, which indicates chemical reactions between Cs and O_2. Moreover, ex situ EDX spectroscopy after the cool-down of the sample revealed a significantly increased amount of oxygen on the surface, which means that the surface is strongly oxidized due to the applied high temperatures. As shown in figure 7.7(c), the Mo surface exhibits a reddish discoloration after the cool-down, which is attributed to the oxidation. Cu from the bulk material beneath the Mo coating could not be detected in the EDX analysis, showing that the Mo coating is not damaged. Furthermore, Cs could not be detected on the surface, which implies that the Cs coating is almost completely desorbed upon the temperature elevation to close to 900 °C.

In summary, the measurements clearly show that an increase of the surface temperature to 200 °C is an effective way to recover a low work function from degraded caesiated surfaces. The reached work function minimum is in the range of 2.25 ± 0.10 eV and is slightly higher than what is typically achieved via re-caesiation (see section 7.2). The thermal stability of Cs coatings with a work function in the range of 1.25 ± 0.10 eV was not investigated explicitly, but measurements presented in [MS91] indicate that Cs oxide coatings are stable for temperatures up to about 200 °C.

---

[2] As a side note, also the heating of the SID wires to their operating temperature (> 900 °C) during a caesiation process leads to a sudden evaporation of Cs from the wires accompanied by a dominant H_2 peak in the RGA recording.

7.4 Influence of gas exposure

Apart from residual gases, the surface upon caesiation is exposed to hydrogen gas at negative hydrogen ion sources. Furthermore, impurity gases such as nitrogen, oxygen or water might leak into the system. In consequence, a clear understanding of the impact of the various gas species on the work function of caesiated surfaces is indispensable.

The issue of impurity gases leaking into the vacuum system becomes evident from figure 7.8, where the inlet of hydrogen gas during a re-caesiation process at ACCesS is shown. Before the hydrogen gas line is opened, the RGA signals for H_2, H_2O, N_2, O_2 and Ar are constant, and the background pressure in the source is 7×10^{-6} mbar. The Cs density is stable at $9 \times 10^{14}\,\mathrm{m^{-3}}$ and a constant surface work function of 2.0 eV is given. At $t = 297$ min, hydrogen gas is introduced and the absolute gas pressure is adjusted to 10 Pa. As can be seen, the Cs density instantly drops below the TDLAS detection limit when the hydrogen gas enters the chamber. Furthermore, the work function increases to 3.1 eV, which is more than 1 eV higher than before the gas inlet. The RGA recording reveals that not only H_2, but also substantial amounts of N_2, O_2, Ar and H_2O enter the chamber. Thus, these gases have accumulated in the gas line and have gradually contaminated the hydrogen gas. The partial pressures of N_2, O_2, Ar and H_2O increase up to 0.636, 0.159, 0.014 and 0.009 Pa, which is estimated by using experimentally determined relative calibration factors for the RGA [Wol22]. Within the next minutes, the RGA signals of the impurity gases gradually decline, showing that the impurity gases are gradually pumped out and the feedgas is composed of high-purity H_2. The Cs density remains, however, below the TDLAS detection limit, even though the temperature of the Cs oven reservoir is the same as before the gas inlet. The temperature of the Cs oven nozzle is decreased from 280 to 265 °C due to convective cooling, but as demonstrated in figure 5.5(b), such a small temperature reduction can be excluded as a reason for the reduced Cs density in the vacuum chamber. Therefore, strong chemical reactions are present that lead to the reduction of the Cs density as well as to the increase of the surface work function: Reactions in the gas phase may lead to chemical vapor deposition of Cs compounds onto the surfaces, reactions at the surfaces can lead to an enhanced Cs gettering and formation of Cs compounds, and reactions at the inner oven surfaces might lead to a reduced diffusion of Cs out of the oven [Fri13].

The amount of accumulated impurities in the gas supply depends on the time period it is not in use, which was one week in the case of the experiment shown

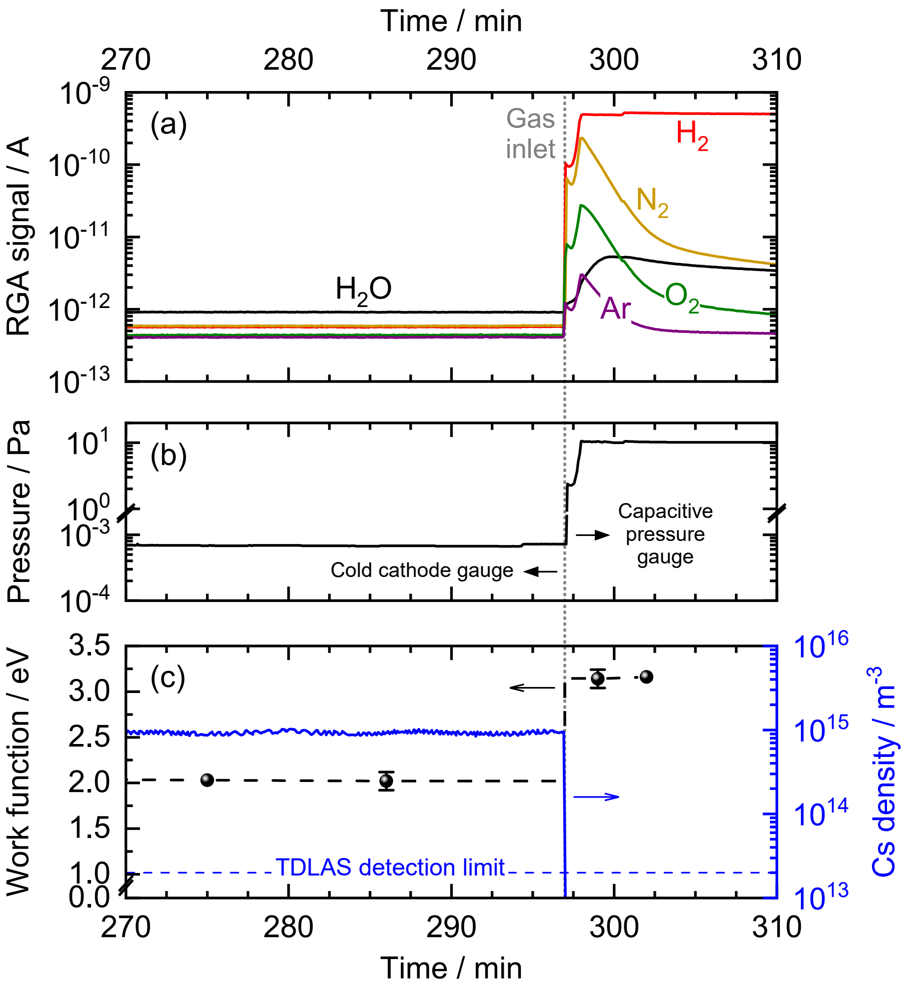

Figure 7.8: *Influence of impure hydrogen gas feeding on the caesiation process. The evolution of the RGA signals for selected masses is shown in (a), the pressure in the vacuum chamber is plotted in (b), and the neutral Cs density and work function of the Mo substrate are depicted in (c).*

in figure 7.8. If the inlet of impurity gases needs to be minimized during the conduction of measurements, the gas supply is opened for ∼ 1 h prior to the experimental campaign. In order to analyze which gases are harmful to the caesiation process, investigations on the influence of selected gases on the work function and Cs content within the vessel are presented in the following.

7.4.1 Hydrogen

Prior to the caesiation process shown in figure 7.9(a), accumulated impurities in the H_2 gas supply were pumped out. When a stable work function of 1.3 eV is reached in the vacuum phase, a H_2 gas pressure of 10 Pa is applied. The corresponding RGA signals for H_2, H_2O, N_2, O_2 and Ar are plotted in figure 7.9(b)

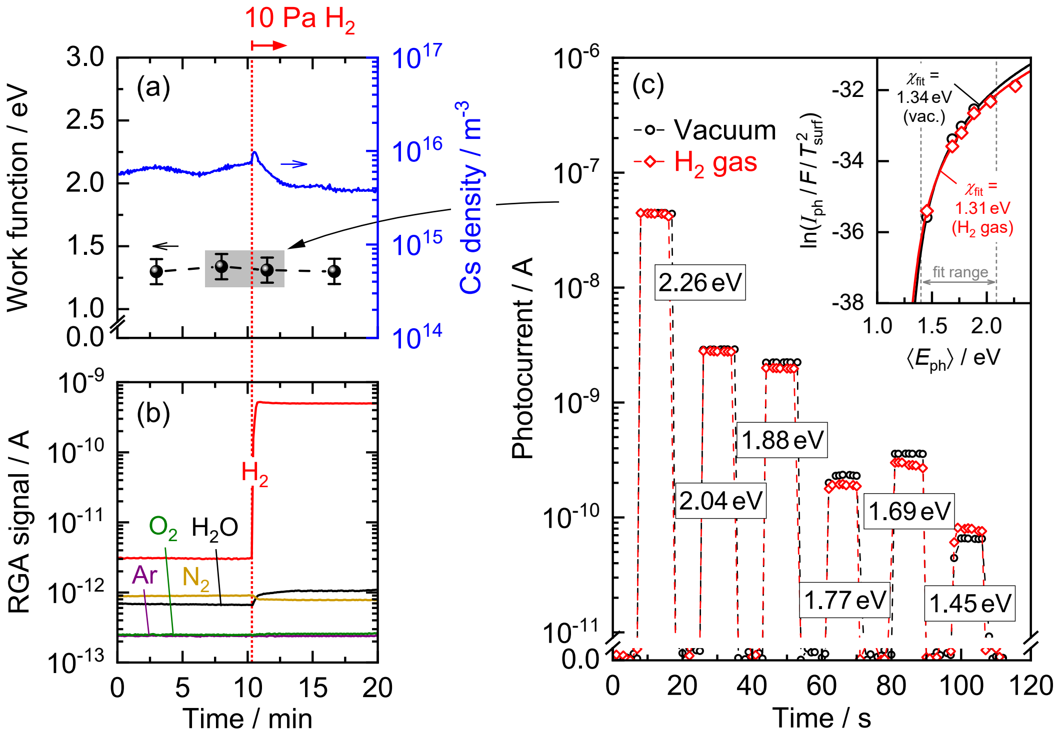

Figure 7.9: *Exposure of a Cs coating with a work function of 1.3 eV to 10 Pa* H_2 *gas. In (a), the evolution of the neutral Cs density and of the work function is depicted and in (b), the RGA recording of selected gases is shown. In (c), photocurrent measurements with photon energies in the range of 2.26 − 1.45 eV before and after the* H_2 *gas exposure are depicted (dark current already substracted), and the corresponding Fowler fits for the work function evaluation are shown in the inset.*

and show that the increase of the RGA signal for H_2 is accompanied only by a slight increase of the RGA signal for H_2O. Consequently, the H_2 gas can be considered as virtually pure.

In the moment H_2 gas is introduced, the Cs density increases by a factor of 1.3. An increase of the Cs density caused by H_2 gas at a pressure of several Pa is already described in [Fri13], where it was only observed in the presence of hot filaments in the vacuum chamber (glowing SID wires). It was speculated that thermally catalyzed chemical reactions of H_2 with Cs compounds might be initiated, leading to an additional Cs source. Here, an increase of the Cs density is given without hot filaments, but it is less pronounced compared to what was observed in [Fri13]. Therefore, it is assumed that the increase of the Cs density in the absence of hot filaments is primarily due to the reduced mean free path of the Cs atoms, leading to a hindered diffusion to the vessel walls and thus to an increased density in the gas phase. The subsequent slight decrease of the Cs density might be due to a hampered Cs diffusion out of the oven. Since such a decrease is, however, only occasionally observed, it is also likely that the increased amount of H_2O that is detected with the RGA plays a role here. In any case, this effect is not severe and could be easily mitigated by a slight increase of the temperature of the Cs oven reservoir.

The measured work function of the caesiated surface is not influenced by the H_2 gas. As shown in figure 7.9(c), the measured photocurrents for photon energies close to the threshold before and after the H_2 gas inlet are comparable, and the respective Fowler plots that are depicted in the inset yield the same work functions within the error of $\pm 0.1\,\mathrm{eV}$. Hence, no influence of the H_2 gas on the surface work function can be identified. The same result is obtained with D_2.

7.4.2 Inert gases

Argon

The impact of noble gases on the caesiation process is of particular interest for negative ion sources for fusion since He that is produced in the fusion reactor might enter the NNBI beamline. Furthermore, the application of non-evaporable getter (NEG) pumps is considered [S$^+$17b, S$^+$19] and already foreseen for the SPIDER test facility [T$^+$21]. NEG pumps provide reactive surfaces for the sorption of gas molecules, but noble gases cannot be trapped as they do not chemically react with the getter material.

To gain insight into the impact of small amounts of noble gases on the caesiation process, investigations with an elevated partial pressure of Ar are conducted. The investigations are performed by the application of a NEG pump from the company SAES group (CapaciTorr® HV 200), which uses the ZAO® getter alloy (composed of Ti, Zr, V and Al) in the shape of porous sintered disks stacked in a cartridge. Active gases like O_2, N_2, H_2O or CO_2 that impinge onto the getter surfaces are dissociated and permanently trapped in the form of stable chemical compounds, while H_2 and its isotopes dissolve in the bulk of the getter material and form a solid solution. In figure 7.10(a), a caesiation process is shown where both the NEG pump and the regular pumping system are attached to the vacuum vessel at ACCesS. The regular pumping system is separated from the vacuum vessel after a stable Cs density of $\sim 10^{15}\,\mathrm{m}^{-3}$ is reached and a work function of $2.1\,\mathrm{eV}$ is given (re-caesiation process). The separation of the regular pumping system is realized via a gate valve installed in between the turbomolecular pump and the vacuum chamber. The NEG pump is able to take over the pumping instantly after the

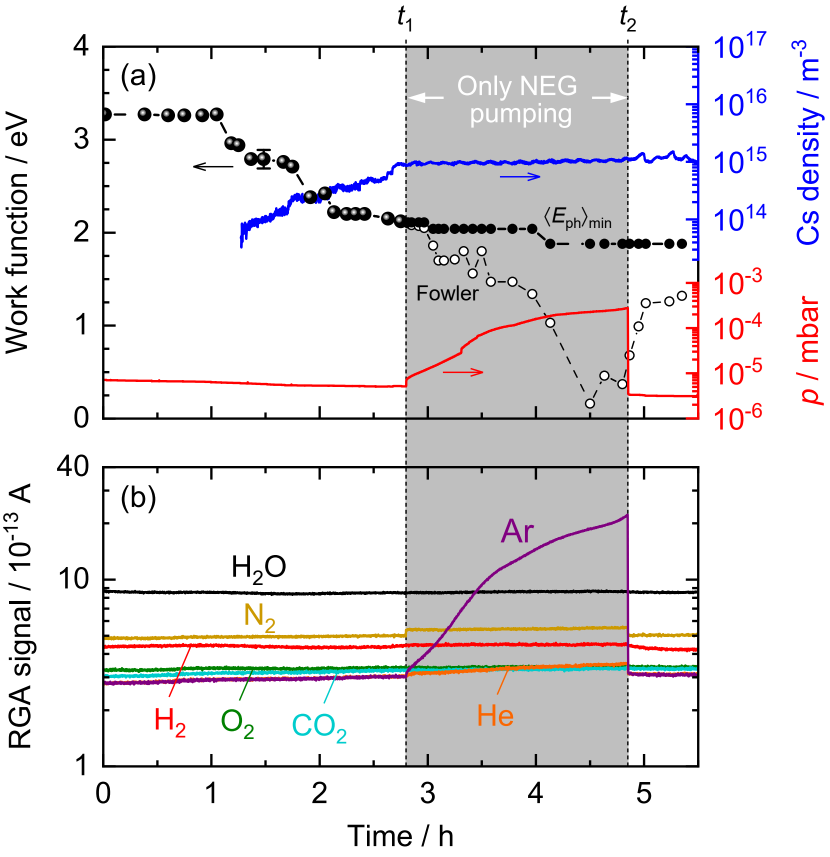

Figure 7.10: *Generation of an Ar dominated background pressure during caesiation by the application of a NEG pump: At $t_1 < t < t_2$, the regular pumping system is separated from the vacuum system and only the NEG pump is used to pump the system. In (a), the work function of the Mo sample together with the neutral Cs density and the background pressure are shown. For $t > t_1$, the work function values obtained via the Fowler method are plotted as open symbols, and the full symbols show the lowest photon energy with which photocurrents are detected. In (b), the RGA monitoring of pertinent gases is depicted.*

gate valve is closed, and only a slight initial increase of the background pressure is observed. The RGA recording in figure 7.10(b) shows that this can be attributed to a small increase of the N_2 content within the vessel due to the reduced total pumping speed. However, the Cs density and work function are not affected.

During the time $t_1 < t < t_2$ when only the NEG pump is attached to the vacuum chamber, the RGA recording reveals that Ar gas permeates through the Viton seals (contained in ambient air at 0.9 %) and is not removed by the NEG pump. After a few minutes, the gradually increasing Ar content in the vessel determines the background pressure. An increase of the RGA signal for He is also observed, but is much less pronounced. During the two hours of “only NEG pumping”, the pressure increases by about two orders of magnitude, from 5×10^{-6} to 3×10^{-4} mbar.

Nonetheless, the Cs density remains constant during the pressure increase. The continuous Cs flux onto the caesiated Mo substrate leads to a further reduction of the work function as the lowest photon energy with which photoelectric response is obtained is decreased from 2.1 to 1.9 eV. However, the work function evaluation via the Fowler method leads to values that are increasingly below the lowest photon energy with which photocurrents are measured. After about 1.5 h, the evaluated work functions are even far below 1 eV, which is considered as physically unreasonable under the given conditions. Therefore, the lowest photon energy $\langle E_{\mathrm{ph}} \rangle_{\mathrm{min}}$ with which photoelectric signal is obtained is taken as an upper limit for the surface work function. As soon as the valve to the turbomolecular pump is opened again ($t = t_2$), the increased Ar content is instantly pumped out. The Cs density and the photoelectric threshold remain unaffected. Afterward, the Fowler evaluation yields increasing work function values approaching the upper limit $\langle E_{\mathrm{ph}} \rangle_{\mathrm{min}}$.

The fact that the Fowler method is not applicable any more with an increased partial pressure of Ar suggests that Ar atoms adsorb on the caesiated surface to some extent and affect the escape probability of electrons from the surface upon photon irradiation. Since the photoelectric threshold is, however, not affected, no indications are given that impairing chemical reactions between Cs and Ar occur, i. e., only physisorption is expected.

In consequence, an elevated Ar content within the vacuum system is not harmful to the caesiation process. This result is in good agreement with literature data, where small to zero work function changes are reported when Cs is exposed to noble gases [CCF84]. Hence, it is a good indicator that also an increased partial pressure of He is not problematic for the caesiation process.

Nitrogen

An elevated partial pressure of N_2 has virtually no influence on the Cs density in the vacuum chamber, as was already reported in [Fri13]. Furthermore, it is observed that an increase of the N_2 partial pressure intrinsically via the gas feed or by the reduction of the pumping rate does not affect the surface work function. Therefore, small amounts of N_2 can be considered as unproblematic as well.

7.4.3 Oxygen

In contrast to H_2 and inert gases, the Cs density in the vacuum chamber and the work function of caesiated surfaces are heavily affected when O_2 leaks into the vacuum system. This is shown in figure 7.11(a), where O_2 is introduced during a caesiation process via the gas supply system. Before O_2 is introduced, the work function is 1.4 eV and the Cs density is $1.5 \times 10^{15}\,\mathrm{m}^{-3}$. By the adjustment of the minimum possible flow rate, the partial pressure of O_2 increases to $\sim 10^{-3}$ mbar in the moment the mass flow controller opens (initial overshoot) and decreases to slightly above 10^{-4} mbar shortly afterward. In the moment O_2 enters the vacuum chamber, the Cs density instantly drops below the TDLAS detection limit of $2 \times 10^{13}\,\mathrm{m}^{-3}$. About half a minute later, a dramatically increased work function of 2.4 eV is measured. During the next 17 min, the partial pressure of O_2 is kept constant and the work function continues to increase, with a gradually decreasing slope. The slope increases again by increasing the O_2 partial pressure, which is demonstrated at $t \approx 32$ min where the partial pressure is elevated to 3.5×10^{-4} mbar. After the O_2 inlet is terminated, the work function is 3.5 eV.

Since the Cs density is diminished by at least two orders of magnitude in less than one second when O_2 enters the vacuum chamber, considerable chemical reaction kinetics are present. The instant increase of the work function by 1 eV reveals a pronounced change of the chemical composition and stoichiometry at the surface, i. e., strong chemical reactions are initiated at the surface due to the high electropositivity of Cs and the high electronegativity of oxygen. Furthermore, surface processes on the minute scale are present because the work function continues to increase with increasing O_2 fluence.

In figure 7.11(b), the work function evolution shown in figure 7.11(a) is depicted as a function of the O_2 fluence to which the caesiated surface is exposed. Furthermore, it is compared to the work function behavior of a degraded caesiated surface with $\chi = 2.7$ eV that is exposed to O_2. After an applied O_2 fluence of $9 \times 10^{22}\,\mathrm{m}^{-2}$, the work function of the surfaces with initially $\chi = 1.4$ and 2.7 eV is increased by 1.3 and 0.3 eV, respectively. Thus, the surface with the ultra-low work function reacts much more sensitive to the O_2 gas. After an applied O_2 fluence of $\sim 5 \times 10^{23}\,\mathrm{m}^{-2}$, the work function is about 3.5 eV in both cases. This fluence is comparable to the fluence of residual H_2O molecules after about 8 h at a base pressure of 5×10^{-6} mbar, after which the work function is typically not higher than 3 eV. Hence, the degradation of caesiated surfaces upon O_2 exposure is more pronounced than upon H_2O exposure. A further substantial increase of the O_2 fluence to $\sim 10^{25}\,\mathrm{m}^{-2}$ leads to a further increase of the work function to about 3.8 eV.

As can be seen in figure 7.11(a), it takes about 6 min for the TDLAS signal to reappear after the O_2 exposure is stopped, and about 18 min until the Cs density

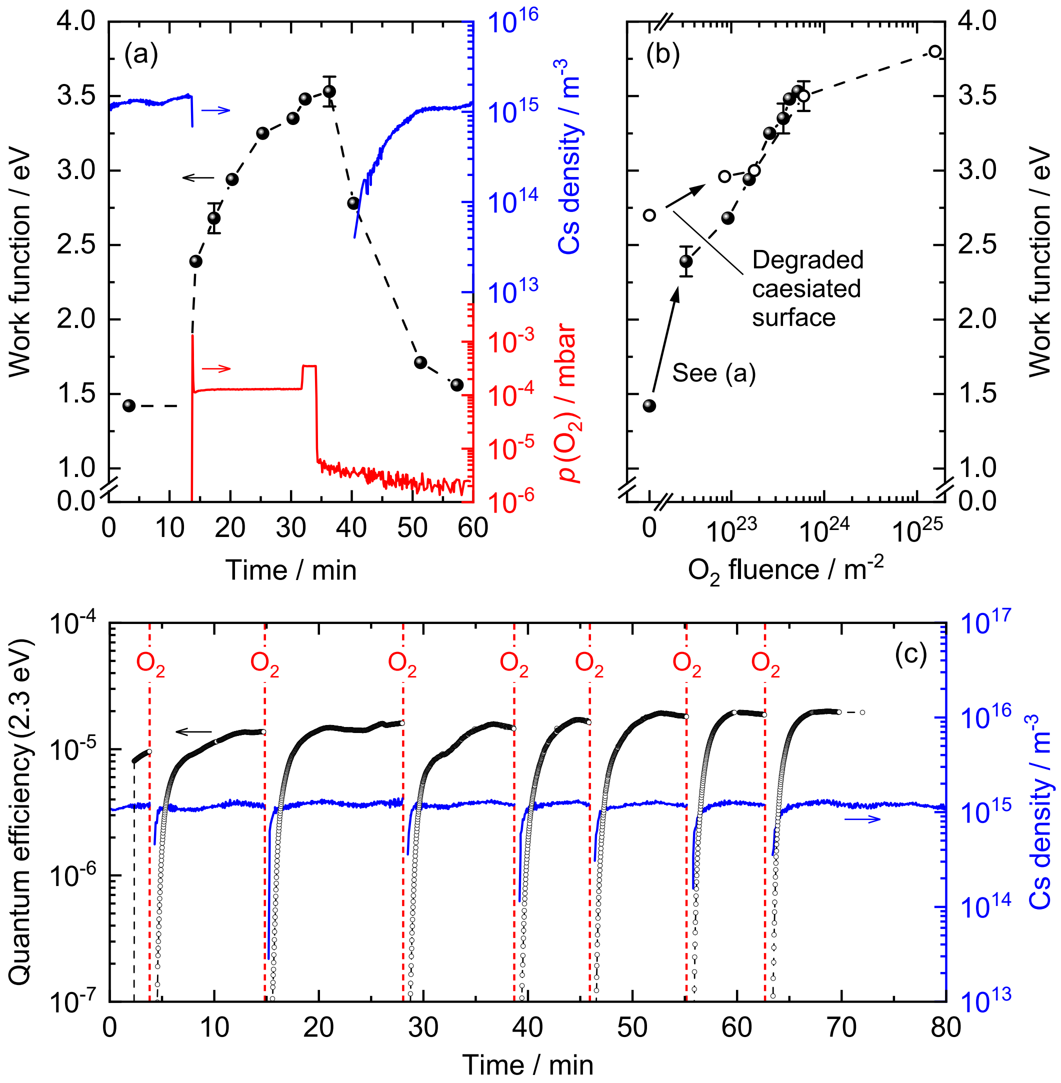

Figure 7.11: *(a) Behavior of the surface work function and neutral Cs density during and after an elevated partial pressure of* O_2 *in the vacuum chamber. (b) Evolution of the work function as a function of the* O_2 *fluence to which caesiated surfaces with different initial work functions are exposed. (c) Evolution of the QE of a caesiated surface with repetitive* O_2 *dosages (estimated fluence per* O_2 *dose:* $\sim 10^{22}$ m^{-2}*).*

is about the same as before the O_2 inlet. The time it takes for the Cs density to reestablish depends on the amount of O_2 that is introduced into the vacuum chamber. In figure 7.11(c), measurements are shown where the O_2 gas feed is opened several times for only a few seconds (pressure increase to $\sim 10^{-3}$ mbar, comparable to the overshoot in figure 7.11(a)) and the times for the TDLAS signal to reappear and the Cs density to fully recover are typically about 30 s and $1-2$ min, respectively.

Before the TDLAS signal reappears in figure 7.11(a), the work function is 3.5 eV and a considerable amount of oxygen is expected to be adsorbed at the sample surface. By the termination of the O_2 flux and the re-establishment of the Cs flux onto the surface, the work function decreases remarkably fast and $\chi = 1.56\,\text{eV}$ is measured after 17 min. When the caesiated surface degrades to $\chi = 3.5\,\text{eV}$ within several days due to H_2O exposure from the background pressure and is subsequently re-caesiated, such a pronounced decrease of the work function is not observed (see section 7.2). The fast recovery after O_2 exposure becomes also evident from figure 7.11(c). Here, the QE at 2.3 eV is continuously monitored with a time resolution of 1 s. An instant drop below the detection limit is given every time O_2 gas is added, and by the subsequent re-establishment of the Cs flux onto the surface the QE is (more than) fully recovered within a couple of minutes. The measured work function after the application of the repetitive O_2 dosages is 1.4 eV. Therefore, it is suggested that the adsorption of O_2 on the caesiated surface facilitates the formation of strong dipoles upon re-caesiation, possibly due to the formation of Cs oxides.

7.4.4 Conclusions

The investigations on the addition of selected gases during the caesiation of a Mo substrate have shown that H_2 (D_2) gas at several Pa as well as small amounts of inert gases (Ar and N_2) with partial pressures of $\sim 10^{-4} - 10^{-3}\,\text{mbar}$ have a negligible influence on the Cs density within the vessel as well as on the work function of the caesiated surface. However, when O_2 leaks into the vacuum system with a partial pressure of $\sim 10^{-4} - 10^{-3}\,\text{mbar}$, an instant reduction of the Cs density by several orders of magnitude and an increase of the work function of the order of 1 eV occur. Therefore, the immediate reduction of the Cs density and increase of the work function from 2.0 to 3.1 eV observed after the impure hydrogen gas feeding in figure 7.8 can primarily be ascribed to the O_2 impurity. Here, the estimated O_2 fluence at the time when $\chi = 3.1\,\text{eV}$ is measured is $3 \times 10^{23}\,\text{m}^{-2}$, which is in good agreement with the measurements shown in figure 7.11(b). The time it takes for the Cs density and work function to recover after the termination of the O_2 inlet is typically of the order of minutes and depends on the totally entered amount of O_2 into the vacuum system. Since the initial equilibrium can be regained, no irreversible effects are identified.

8 Impact of specific hydrogen plasma species on the work function of caesiated surfaces

The caesiated extraction electrode in negative hydrogen ion sources is exposed to a low pressure low temperature hydrogen plasma. The plasma impact leads to a complex interplay of photonic, ionic and atomic interactions with the surface, and a multitude of processes can change the chemical composition and thus the work function of the surface, as described in detail in section 4.3. The evolution of the work function of the caesiated surface under such conditions can hardly be predicted by theoretical models due to a lack of knowledge about the exact chemical composition of the surface as well as the decisive processes influencing the chemical composition of the surface.

It has already been observed at ACCesS that the ignition of a hydrogen plasma in the main chamber decreases the work function of degraded caesiated surfaces [FF17, CFF20a]. In order to identify the mechanisms that are responsible for the decrease of the work function, investigations are conducted where the interactions with the energetic VUV photons, reactive hydrogen atoms and positive hydrogen ions from the hydrogen plasma are decoupled to some extent, and a plasma-induced redistribution of Cs (compounds) within the experimental chamber is suppressed. This is done by the application of the external plasma source that is described in section 5.3. Apart from the examination of how well degraded Cs layers can be "reactivated" upon the exposure to hydrogen plasma species, i. e., how far the work function can be decreased after an increase due to residual gas adsorption, the durability of Cs coatings with a work function in the range of $1.25 \pm 0.10\,\mathrm{eV}$ is studied. For the sake of clarity, an overview of the work function dynamics found in the previous chapter is provided in the bar diagram in figure 8.1 and the aspects that are addressed within the present chapter are indicated as red dotted bars with question mark.

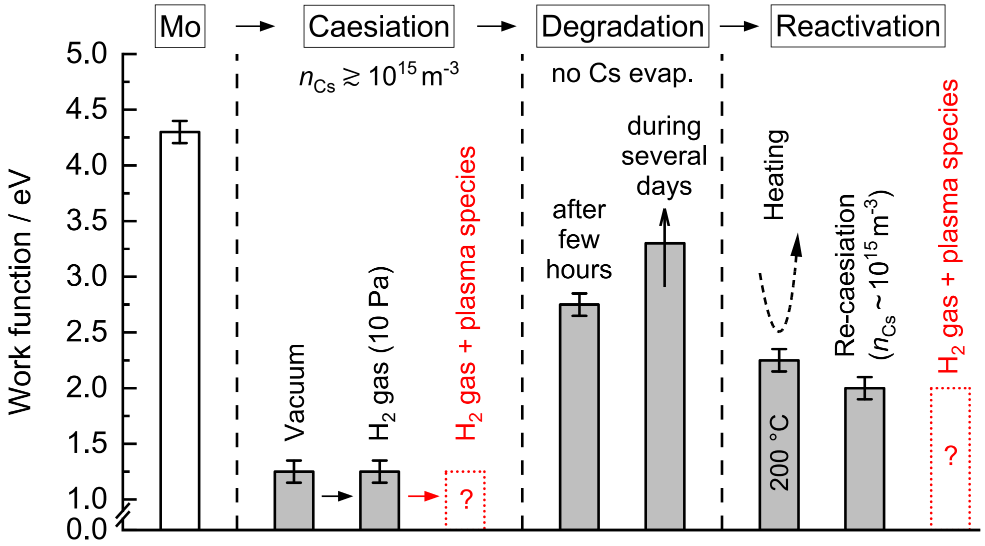

Figure 8.1: *Overview of the work function dynamics of a caesiated Mo surface: The minimum work functions reached in the vacuum and gas phase with active Cs evaporation, the work function increase in the absence of Cs evaporation and the decrease of the work function upon heating and re-caesiation are shown (from left to right, details see chapter 7). The red dotted bars with question mark indicate what is addressed in the present chapter.*

8.1 Quantification and separation of photon and particle fluxes

Plasma characterization

As described in section 5.4, the VUV diode system is applied to quantify the VUV emissivities averaged over the plasma volume of the external plasma source. In figure 8.2(a), the measured emissivities of the Lyman band ($E_{\mathrm{ph}} = 6.6 - 8.4\,\mathrm{eV}$), Lyman-$\alpha$ line ($E_{\mathrm{ph}} = 10.2\,\mathrm{eV}$) and Werner band together with the Lyman series beyond Lyman-α ($E_{\mathrm{ph}} \geq 11.0\,\mathrm{eV}$) are plotted for a variation of the RF power from 100 W to the maximum available RF power of 600 W at a hydrogen gas pressure of 10 Pa. The emissivities of the different energy ranges are comparable within the error bars, highlighting the prominence of the Lyman-α line emission. The emissivities increase with increasing RF power and at 600 W the summed VUV emissivity is about $5 \times 10^{22}\,\mathrm{m}^{-3}\mathrm{s}^{-1}$. However, RF powers in the range of $500 - 600\,\mathrm{W}$ pose the risk of critical temperatures for the elastomer seals of the quartz vessel during steady-state operation so that the plasma source is typically operated with a reduced RF power of 400 W. Since figure 8.2(b) shows that at 400 W the emissivity of the Lyman-α line decreases when the pressure is reduced

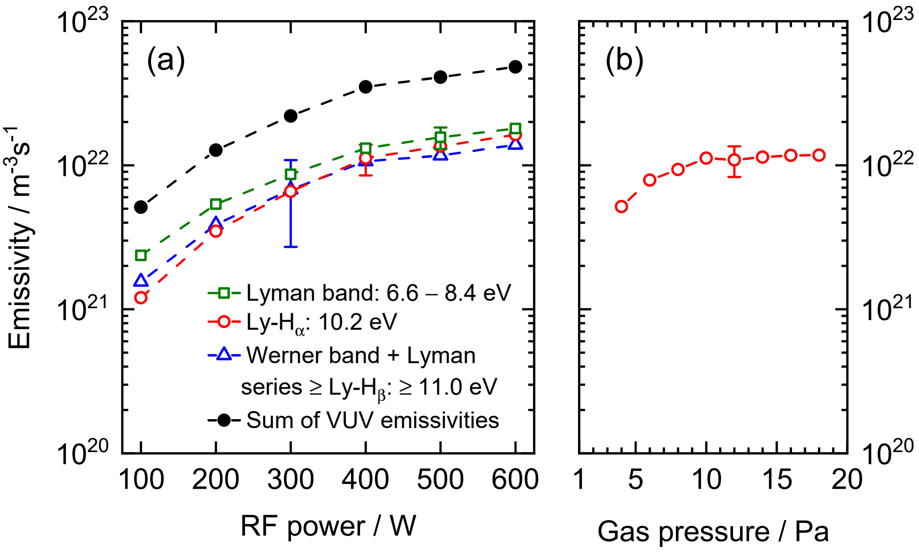

Figure 8.2: *VUV emissivities of hydrogen discharges generated in the external plasma source: (a) RF power scan at 10 Pa gas pressure and (b) pressure scan at 400 W RF power.*

below 10 Pa and remains virtually constant when the pressure is increased (tested up to 18 Pa), 10 Pa gas pressure and 400 W RF power are chosen as standard operational parameters to generate a high steady-state VUV emission. With the volume to surface ratio of the quartz vessel of 0.01 m, a VUV photon flux of $3.4 \times 10^{20}\,\mathrm{m}^{-2}\mathrm{s}^{-1}$ is determined from the sum of the measured emissivities at 10 Pa/400 W.

OES measurements are performed for the evaluation of the gas temperature, electron density, electron temperature and atomic hydrogen density of the discharge. The determined values represent average values along the LOS, which is aligned along the cylinder axis of the quartz vessel to cover the central regime of the discharge (see figure 5.7). The evaluated plasma parameters at 10 Pa/400 W are summarized in table 8.1, together with the calculated H atom flux and positive ion (H_3^+) flux. The ion flux represents the Bohm flux according to equation (3.29). Additionally, the determined VUV flux is listed.

Apart from the operational parameters of 10 Pa/400 W, the source is occasionally operated at a reduced pressure of 4 Pa and an RF power of 600 W. The lower pressure is applied to reduce collisions of H atoms and H_3^+ ions with H_2 molecules on the way toward the caesiated surface in the main vessel, which is discussed in detail in the following subsection. Thus, the measured plasma parameters and corresponding fluxes at 4 Pa/600 W are additionally given in table 8.1. As can be seen, the reduction of the pressure with the simultaneous increase of the RF power leads to a 38 % lower electron density and 3.5 eV higher electron temperature. The substantial increase of the electron temperature can be understood from the ionization balance described in section 3.1.3. While the changed plasma parameters lead to an increase of the VUV flux by a factor of $2-3$, the ion flux is only slightly influenced. The H atom flux is decreased by about 64 % due to a decreasing H atom density with decreasing pressure.

Table 8.1: *Plasma parameters and VUV photon and particle fluxes of hydrogen plasmas generated in the external plasma source at 10 Pa/400 W and 4 Pa/600 W.*

	10 Pa/400 W	4 Pa/600 W
$T_{\mathrm{gas}} = T_{\mathrm{H}}$ / K	662	656
n_{e} / m^{-3}	6.9×10^{16}	4.3×10^{16}
T_{e} / eV	4.4	7.9
n_{H} / m^{-3}	2.8×10^{20}	1.0×10^{20}
$\mathit{\Gamma}_{\mathrm{src,H}}$ / m^{-2}s^{-1}	2.6×10^{23}	9.3×10^{22}
$\mathit{\Gamma}_{\mathrm{src,H_3^+}}$ / m^{-2}s^{-1}	4.1×10^{20}	3.4×10^{20}
$\mathit{\Gamma}_{\mathrm{src,VUV}}$ / m^{-2}s^{-1}	3.4×10^{20}	8.5×10^{20}

Fluxes onto the caesiated surface

The flux $\mathit{\Gamma}_{\mathrm{spl}}$ reaching the caesiated surface in the main vessel is calculated from the determined flux $\mathit{\Gamma}_{\mathrm{src}}$ in the external plasma source under the assumption of ballistic propagation by

$$\mathit{\Gamma}_{\mathrm{spl}} = T_{\mathrm{mesh}} F_{\Omega} \mathit{\Gamma}_{\mathrm{src}}, \tag{8.1}$$

where T_{mesh} is the transmission of the stainless steel mesh installed inside the flange and F_{Ω} is a factor that takes the divergence of the flux into the main vessel into account. The transmission of the mesh is 64 % and is determined with the use of the Ulbricht sphere as radiation source and the survey spectrometer as detector. The geometric constraints for the determination of F_{Ω} are sketched in figure 8.3, where A_{p} represents the open front end surface of the quartz vessel (taken as emitting surface, diameter of 43 mm) and $\mathrm{d}A_{\mathrm{spl}}$ is a surface element positioned on the caesiated sample surface. The normal of A_{p} is parallel to the z-axis of the cylindrical coordinate system given by the quartz tube and the normal of $\mathrm{d}A_{\mathrm{spl}}$ encloses an angle of $\beta = 45°$ with the z-axis. The solid angle of $\mathrm{d}A_{\mathrm{spl}}$ with respect to an arbitrary position $(r, \varphi, z = 0)$ on A_{p} is given by $\mathrm{d}\Omega_{\mathrm{spl}} = \mathrm{d}A_{\mathrm{spl}} \cos(\beta)/s^2$, where s is the distance between $\mathrm{d}A_{\mathrm{spl}}$ and the position

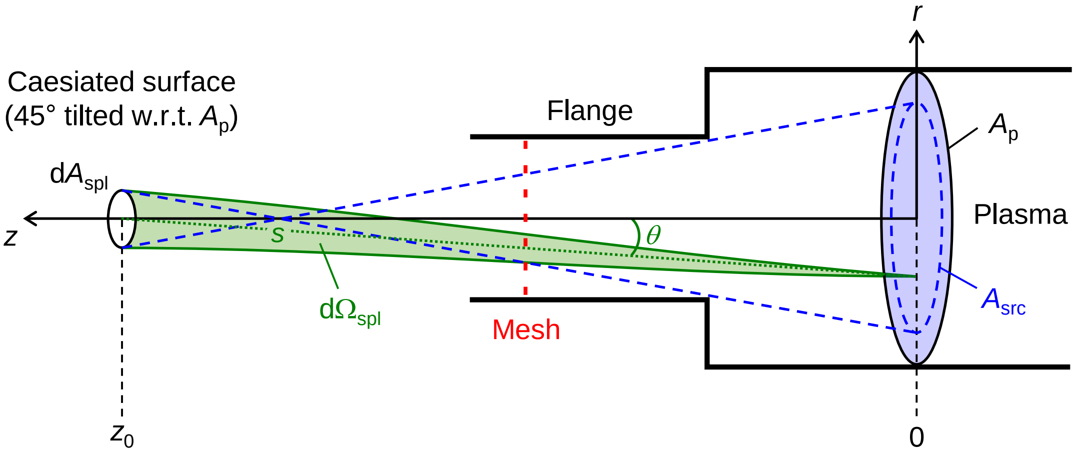

Figure 8.3: *Illustration of the solid angle of a surface element* $\mathrm{d}A_{\mathrm{spl}}$ *on the caesiated surface with respect to positions on the emissive area* A_{p} *of the plasma source. The flange to which the plasma source is connected defines the emitting area* A_{src} *from which plasma species can reach* $\mathrm{d}A_{\mathrm{spl}}$.

on A_{p}. From these considerations, the factor F_Ω is calculated by [Kun09]

$$F_\Omega = \frac{1}{2\pi}\int_{A_{\mathrm{p}}} \cos(\theta)\frac{\cos(\beta)}{s^2}\mathrm{d}A, \tag{8.2}$$

where an isotropic hemispherical release of the species from A_{p} is assumed (factor of $(2\pi)^{-1}$) and θ is the angle between the direction of the emitted species and the normal of A_{p}. In the present case, it must be taken into account that the flange to which the plasma source is connected limits the emitting area from which plasma species can reach $\mathrm{d}A_{\mathrm{spl}}$, which is illustrated in figure 8.3. Hence, the integration in equation (8.2) must be performed over the reduced area A_{src}. The area A_{spl} on the caesiated surface that needs to be considered is the spot where the work function is monitored (diameter $\approx 15\,\mathrm{mm}$), leading to a diameter of about $35\,\mathrm{mm}$ for A_{src}. Since the distance $z_0 = 220\,\mathrm{mm}$ between A_{spl} and A_{src} is much larger than the diameter of A_{src} and A_{spl}, $\cos(\theta) \approx 1$ and $s \approx z_0$ are reasonable approximations. In consequence, the average flux reaching A_{spl} is calculated from equations (8.1) and (8.2) by

$$\mathit{\Gamma}_{\mathrm{spl}} = T_{\mathrm{mesh}}\frac{\sqrt{2}}{4\pi}\frac{A_{\mathrm{scr}}}{z_0^2}\mathit{\Gamma}_{\mathrm{src}}, \tag{8.3}$$

where F_Ω is determined by $\sqrt{2}A_{\mathrm{src}}/(4\pi z_0^2) = 2.3 \times 10^{-3}$.

As the gas pressure in the vacuum system is $10\,\mathrm{Pa}$ ($4\,\mathrm{Pa}$) during the operation of the plasma source, interactions of the plasma species with particles on the way toward the caesiated surface inevitably take place. In the case of photons, reabsorption processes can lead to an attenuation of the photon flux. Reabsorption processes are, however, intrinsically considered in the measurement of $\varGamma_{\mathrm{src,VUV}}$ as the VUV diode system is installed at a distance to the center of the discharge that is comparable to the distance between the center of the discharge and the sample holder. Consequently, the calculation of the VUV flux onto the caesiated surface according to equation (8.3) is a good approximation. In the case of hydrogen atoms and positive hydrogen ions, the usage of equation (8.3) is to be seen as an upper limit since collisional processes with the hydrogen gas are expected to significantly reduce the particle fluxes. Moreover, the evolution of the electrical potential from the plasma source toward the main chamber that is decisive for the resulting ion flux is unknown (note that the mesh inside the flange is on ground potential).

While unfortunately no diagnostic for the detection of the hydrogen atoms propagating toward the sample holder is available at ACCesS, the ions can be measured with the Langmuir probe. Therefore, the Langmuir probe is installed at the flange at the opposite side of the plasma source and is inserted into the main chamber with the sample holder being removed from the experiment. In figure 8.4, the measurement setup is depicted and the measured ion fluxes onto the probe tip are plotted as a function of the distance x from the flange when the source is operated at 10 Pa/400 W and 4 Pa/600 W, respectively. The ion flux is calculated from the measured ion current with an applied bias of −30 V against the grounded vessel walls to ensure that electrons are effectively repelled. The x-error bars indicate the length of the probe tip. As can be seen, the determined ion fluxes gradually decrease with increasing distance to the flange and the decrease is more pronounced at 10 Pa than at 4 Pa. The lower detection limit of the probe system is at about $5 \times 10^{17}\,\mathrm{m^{-2}s^{-1}}$ and is reached at 10 Pa at a distance of about 3 cm and at 4 Pa at a distance of about 1 cm from the sample surface position. As the generated ion fluxes in the plasma source are comparable at 10 Pa and 4 Pa (see table 8.1), the faster decrease of the measured ion flux onto the probe tip at 10 Pa is attributed to a stronger attenuation of the ion flux propagating into the main vessel due to a higher collision rate.

Since the ions are collected from a certain volume around the probe tip due to the bias potential, the ion fluxes determined with the Langmuir probe represent upper limits for the actual ion fluxes. As can be seen in figure 8.4, the measured ion fluxes close to the detection limit are comparable to the calculated ion fluxes after equation (8.3) when the determined Bohm fluxes $\varGamma_{\mathrm{src,H_3^+}}$ from table 8.1 are

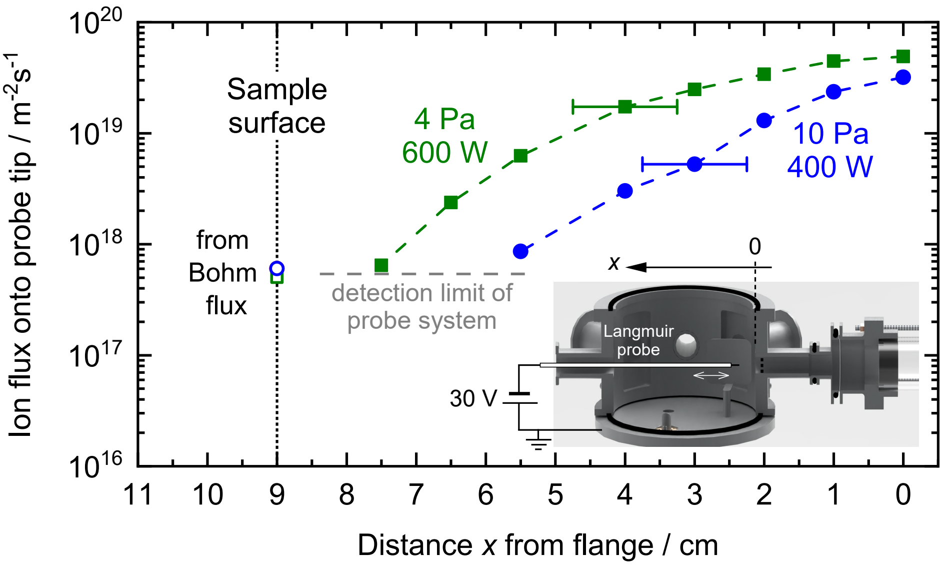

Figure 8.4: *Positive hydrogen ion flux onto the Langmuir probe tip as a function of the distance from the flange to which the external plasma source is connected. The plasma source is operated at 10 Pa/400 W and 4 Pa/600 W. The measurement setup is schematically illustrated in the inset. The calculated ion flux at the sample surface position via equation (8.3) using the determined Bohm flux from the external plasma source (see table 8.1) is additionally depicted.*

used as input parameters. This evidently confirms that the calculated ion fluxes after equation (8.3) are upper limits due to the neglection of particle collisions. The same behavior is expected to be valid for the atomic hydrogen flux.

The bar diagram in figure 8.5 summarizes the calculated VUV photon and particle fluxes onto the caesiated surface after equation (8.3) for the operational parameters of 10 Pa/400 W and 4 Pa/600 W. The facts that the particle fluxes represent upper limits and that the actual particle fluxes are further below the upper limit at 10 Pa than at 4 Pa are indicated by the dashed upper parts of the bars and the vertical arrows, both with different lengths. As will be shown and discussed in chapter 9, the fluxes are orders of magnitude below the typical fluxes impinging onto the plasma grid at the BUG and ELISE test facilities. Therefore, the investigations presented in this chapter serve as a first exploratory approach toward the understanding of the impact of the plasma species on the work function of caesiated surfaces.

Separation of photon and particle fluxes

In order to investigate the impact of photons only and photons together with particles on the work function of caesiated surfaces, the following experimental

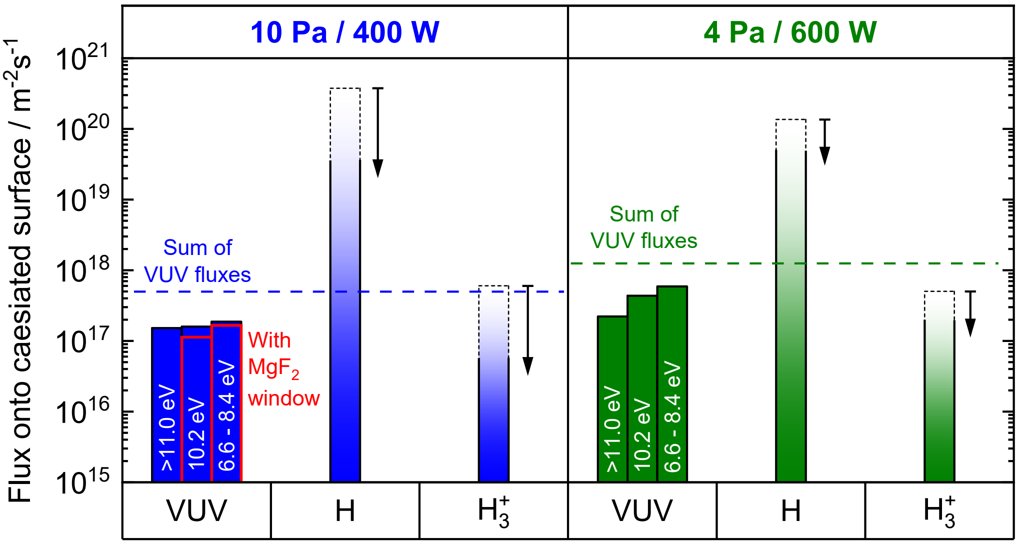

Figure 8.5: *VUV photon and particle fluxes onto the caesiated surface by the generation of hydrogen plasmas in the external plasma source at 10 Pa/400 W and 4 Pa/600 W. As the particle fluxes are calculated under the assumption of ballistic transport, the plotted values represent upper limits and the actual fluxes reaching the surface decrease with increasing pressure, indicated by the dotted upper parts of the bars and the arrows with different lengths. The VUV fluxes reaching the surface at 10 Pa/400 W in the case a* MgF_2 *window is installed are depicted as red bars.*

configurations are applied:

1. *MgF_2 window inside flange (section 8.2)*

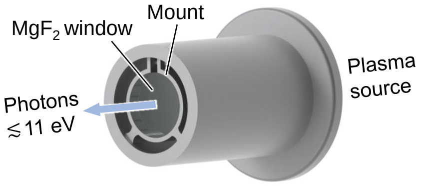

As illustrated in the picture on the right, a MgF_2 window is installed inside the flange (22 mm inner diameter) to separate the photons from the hydrogen atoms and ions. The MgF_2 window (15 mm diameter, 5 mm thickness) serves as a long pass filter with a cut-on wavelength in the VUV. The transmission of the MgF_2 window was determined in the range of 120 − 700 nm by the manufacturer (Korth Kristalle GmbH), showing that the transmission is stable at 93 % and starts to decrease for wavelengths below 200 nm. At 120 nm, the transmission is still 69 %. Therefore, the VUV photons from the intense Lyman-α line and Lyman band can pass through the window. The cut-on wavelength of the MgF_2 window was not determined, but from figure 5.13 it is expected to be roughly at 113 nm (11.0 eV). In this configuration, the plasma source is operated at 10 Pa/400 W and the respective fluxes reaching the sample surface are indicated as red bars in figure 8.5, taking the window transmission into account. The mount of the MgF_2 window is not vacuum tight so that pumping and gas feeding of the plasma source can still be done via the main chamber.

2. No window inside flange and optional application of magnetic filter (section 8.3)

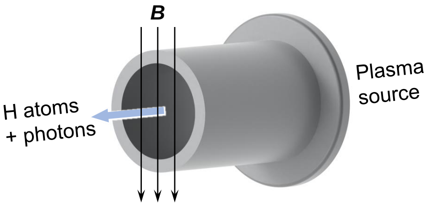

In order to expose the caesiated surface to photons together with hydrogen atoms, no window is installed inside the flange and a magnetic filter field for the positive hydrogen ions is applied, as illustrated in the picture on the right. The magnetic filter field is created by permanent magnets outside the flange, which have a coercivity of 820 kA/m and provide a magnetic flux density of the order of 100 mT inside the flange [Zie22]. With this, the Larmor radius of the ions is of the order of mm and thus much smaller than the experimental dimensions, i. e., the ions are magnetized and cannot reach the sample surface. It should be noted that in this configuration the photon energy is not limited any more, which means that VUV photons with energies up to about 15 eV can reach the surface (see figure 5.13). When the magnets are removed, the surface is exposed to photons together with hydrogen atoms and positive hydrogen ions.

8.2 VUV/UV photons

8.2.1 Impact on degraded Cs layers

For the investigation of the impact of energetic VUV/UV photons on the work function of degraded Cs layers, the MgF_2 window is installed and the Mo sample is prepared as follows: A Cs coating with a work function of 1.25 eV is generated in the vacuum phase by the evaporation of Cs with a density of the order of $10^{15}\,\mathrm{m}^{-3}$. During the caesiation process, the flange to which the external plasma source is attached is covered with the installed shutter (see figure 5.6) to prevent Cs diffusion into the flange and Cs adsorption on the MgF_2 window. After the Cs evaporation is stopped, the sample is left in vacuum where the work function gradually increases.

Figure 8.6(a) presents the influence of the photon irradiation on the work function of Cs layers in different degradation states. The work function is plotted as a function of the cumulative irradiation time, which is the cumulative plasma-on time of the external source operated at 10 Pa/400 W. The corresponding VUV

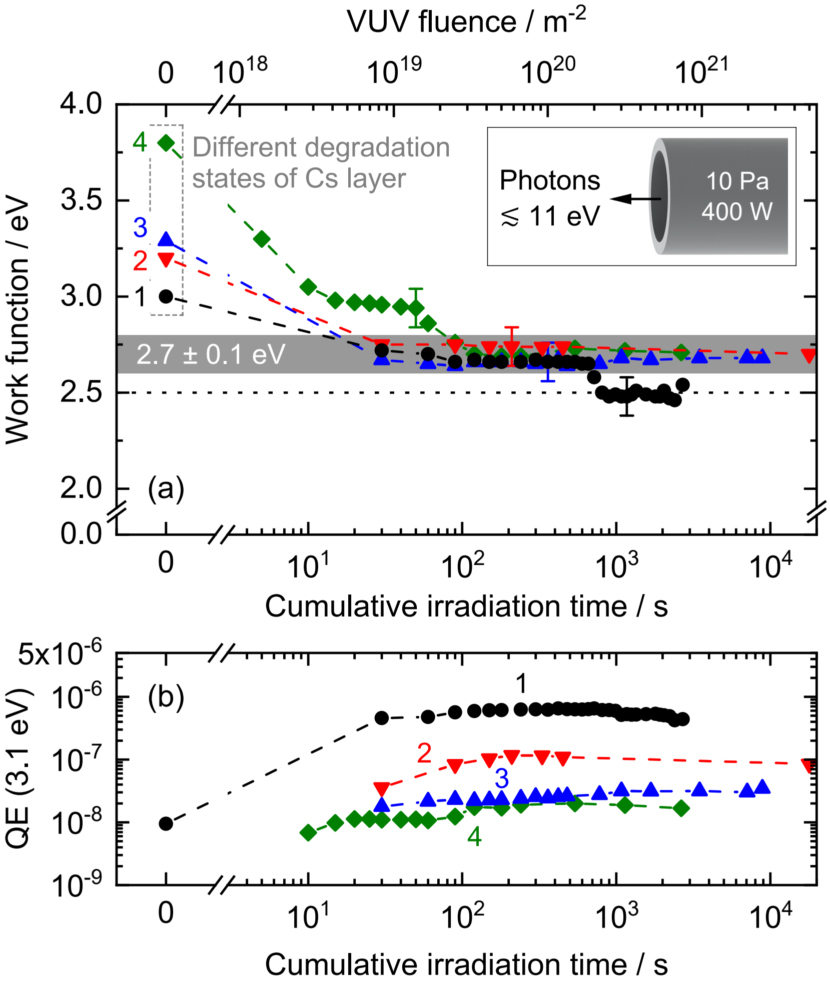

Figure 8.6: *(a) Work function evolution of Cs layers in different degradation states upon the irradiation with photon energies up to 11 eV. (b) Corresponding progressions of the QE at 3.1 eV.*

fluence to which the sample is exposed is shown on the x-axis on the top and is calculated from the sum of the VUV fluxes transmitted by the MgF_2 window, i. e., the Lyman-α line and the Lyman band (indicated in red in figure 8.5). Since during the operation of the source the work function cannot be measured due to RF disturbance of the picoammeter, pulses of several seconds up to several minutes are applied and the work function is measured instantly after each pulse, with the hydrogen gas being maintained in the vacuum system. The curve labeled 1 shows measurements one day after the caesiation process, where the work function of the degraded Cs layer is 2.8 eV (not shown) and is increased to 3.0 eV after impure hydrogen gas (see section 7.4) is introduced into the chamber. An irradiation time of 30 s leads to a reduction of the work function to 2.7 eV, which is lower than the work function of the degraded Cs layer before the impure hydrogen gas feeding.

The work function remains in the range of 2.7 ± 0.1 eV for a cumulative irradiation time of 11 min, and for times $\gtrsim$ 14 min, a work function of ≈ 2.5 eV is obtained. In the cases the initial work functions are 3.2 and 3.3 eV after several days in vacuum, an irradiation time of 30 s leads to a work function of 2.7 eV (curves labeled 2 and 3), and in the case the Cs layer is heavily degraded to $\chi = 3.8$ eV after four weeks, an about three times longer irradiation time is needed to reach the work function of 2.7 eV (curve labeled 4). However, a further reduction of the work function to 2.5 eV is not observed in these three cases: For applied cumulative irradiation times up to 5 h, the work function stays in the range of 2.7 ± 0.1 eV. The temperature of the sample surface remains constant at room temperature during the photon irradiation, i. e., thermal effects can be disregarded.

The progressions of the QE corresponding to the four work function curves are depicted in figure 8.6(b) exemplarily for a photon energy of 3.1 eV. It can be seen that the reached QE depends on the degradation state of the Cs layer: it is systematically lower the higher the initial work function. While in case 1 the work function reduction from 3.0 to 2.7 eV leads to an increase of the QE from $\sim 10^{-8}$ to $\sim 5 \times 10^{-7}$, the QE in case 4 is of the order of 10^{-8} despite the same work function is given within the error bars. This clearly shows that the surface condition after the photon irradiation is still dependent on the previous degradation state, which gets also evident from the fact that only in case 1 a further reduction of the work function to 2.5 eV is obtained.

The QEs plotted in figure 8.6(b) are measured ≈ 90 s after the photon irradiation from the external plasma source is stopped. In figure 8.7(a), the typical temporal behavior of the QE within the first minutes after the termination of the irradiation from the plasma source is demonstrated, with the retrieved work function being 2.7 eV. The depicted QE measurements are performed with 3.9 and 5.0 eV photons by using the Hg lamp with the 313 and 239 nm interference filters. The respective photon fluxes onto the surface are $8 \times 10^{18}\,\mathrm{m^{-2}s^{-1}}$ and $3 \times 10^{18}\,\mathrm{m^{-2}s^{-1}}$ for the 3.9 and 5.0 eV photons, respectively, i. e., the photon fluxes are higher than the VUV flux from the plasma source. The QE measurements are started in both cases about 40 s after the photon irradiation from the plasma source (60 s irradiation time) is stopped. The surface is continuously illuminated with the 3.9 or 5.0 eV photons, and the measured QEs are normalized to the respective values measured right at the beginning of the illumination. In the case of 3.9 eV photons, a continuous decrease of the QE can be observed. The QE is reduced by 50 % after 25 s and by 83 % after about 14 min, showing that the surface is subject to a substantial degradation. The measured work function after the 14 min of

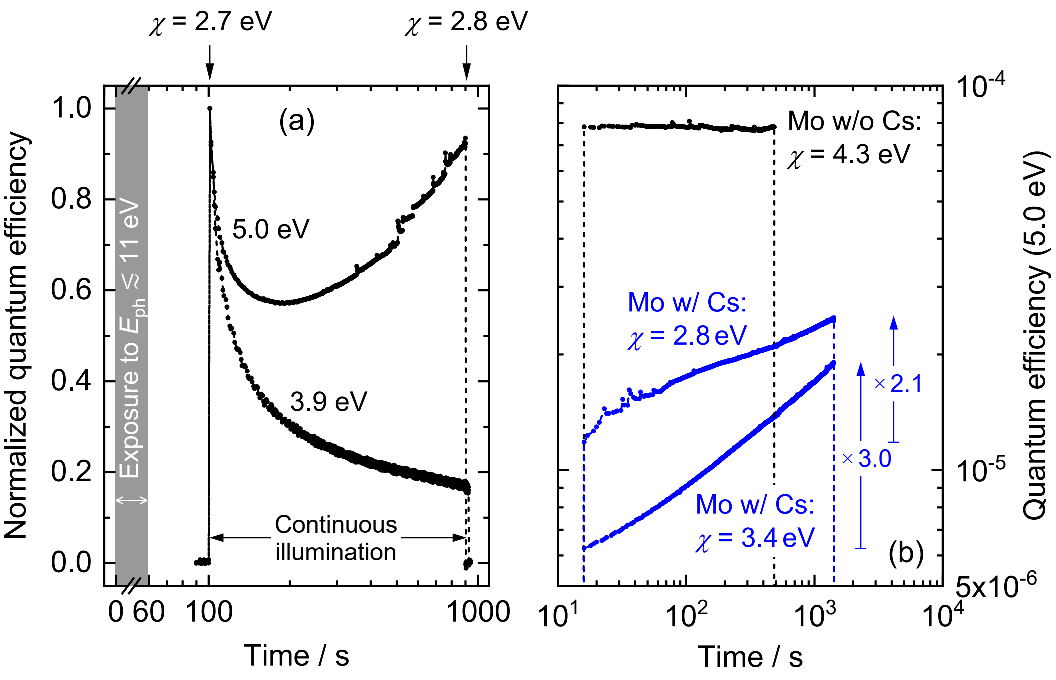

Figure 8.7: *(a) Evolution of the QE for 3.9 and 5.0 eV photons shortly after irradiating the Cs layer with photon energies up to 11 eV. (b) Evolution of the QE at 5.0 eV of an uncaesiated Mo surface and of caesiated Mo surfaces in different degradation states.*

illumination is 2.8 eV, i. e., the work function increases by about 0.1 eV during the illumination period. As the temporal behavior of the QEs for photon energies below 3.9 eV behave comparably (not shown), the QEs plotted in figure 8.6(b) for 3.1 eV must be understood as a “snapshot”, taken ≈ 90 s after the termination of the irradiation from the plasma source as mentioned above. In the case of 5.0 eV photons, the QE decreases within the first seconds of illumination in a similar manner as for 3.9 eV photons. However, the decrease slows down and after about 1.5 min during which the QE is reduced by 43 %, the QE starts to increase again. At the end of the illumination period of 14 min, the QE yields 93 % of the initially measured value. The measured work function afterward is 2.8 eV, i. e., it is the same as after the QE measurement with 3.9 eV photons.

It is generally observed that when degraded caesiated surfaces are irradiated with 5.0 eV photons, the respective QE gradually increases during the period the surface is irradiated. This is demonstrated in figure 8.7(b), where it can be seen that during an irradiation time of 23 min the QE of degraded Cs layers with $\chi = 2.8$ and 3.4 eV increases by a factor of 2.1 and 3.0, respectively (no photon irradiation from the plasma source applied beforehand). Since the additionally plotted QE of an uncaesiated Mo surface remains constant over time as expected, the increase of the QE in the case of degraded Cs layers is attributed to photo-induced changes of the surface. However, a reduction of the work function after the irradiation with 5.0 eV photons is not observed (measured with photon energies in the range of $3.05 - 4.19$ eV). Therefore, the significant work function decrease after the irradiation with photons from the external plasma source shown in figure 8.6 is attributed to the VUV photons with energies higher than 5 eV and up to 11 eV. It is suggested that the VUV photons effectively dissociate Cs compounds and residual gas molecules at the surface, leading to a significant change of the chemical composition of the surface. Moreover, photo-induced desorption processes might play a role. During the VUV irradiation, Cs cannot be detected with the TDLAS system, showing that no significant Cs desorption from the surface is induced. Since RGA measurements are not possible during the operation of the plasma source due to severe RF distortions, the possible desorption of residual gases from the surface cannot be monitored at present.

As can be seen in figure 8.7(b), the QEs of the degraded Cs layers with $\chi = 2.8$ and 3.4 eV are up to an order of magnitude lower than the QE of the uncaesiated Mo surface with $\chi = 4.3$ eV. The lower QE despite the lower work function can be explained by the following reasons [L$^+$17]: First, the electron density at the caesiated surface is expected to be lower compared to the Mo surface because the Fermi energy of Cs is 1.59 eV [Rum21] and the Fermi energy of Mo is 6.77 eV [PV71]. Second, the penetration depth of the 5.0 eV photons is much longer in Cs (~ 100 nm [McW97]) than in Mo (~ 5 nm [KNN71, PDS95]), while the escape depth of the photoelectrons is typically in the range of $1 - 10$ nm [SD79]. This means that in the case of thick Cs layers a significant amount of photoelectrons might not reach the surface. In the case of Cs coatings with a work function of 1.25 eV, however, the QE at 5.0 eV is about one order of magnitude higher compared to the uncaesiated Mo surface (see figure 7.2), which implies that the above mentioned effects are overcompensated by the ultra-low work function.

8.2.2 Impact on ultra-low work function layer

Figure 8.8 presents the impact of the VUV/UV photons from the external plasma source on the work function of a Cs layer with $\chi = 1.25 \pm 0.10$ eV. The Cs layer is generated on the Mo substrate by the application of a neutral Cs density of the order of $10^{15}\,\mathrm{m}^{-3}$ in the vacuum chamber, and the Cs density is sustained during the experiment. The work function is plotted both as a function of the cumulative irradiation time (bottom x-axis) and as a function of the VUV fluence (top x-axis). While for irradiation times up to about 2 min no influence on the work function can be detected, the work function starts to increase for irradiation times of several minutes, i. e., for VUV fluences $\gtrsim 10^{20}\,\mathrm{m}^{-2}$. After an irradiation time of about 1.5 h (VUV fluence $\sim 10^{21}\,\mathrm{m}^{-2}$), a substantially increased work function of about 1.7 eV is obtained. When the Cs layer with a work function of 1.25 eV is exposed to 5.0 eV photons from the Hg lamp with comparable fluences, no influence on the work function can be detected (not shown). Therefore, the increase of the work function is attributed to the photons with energies of 5 to 11 eV. A plausible reason for the work function increase is the damage/dissociation of Cs oxides at the surface.

After the VUV irradiation is stopped, the work function of 1.25 eV can be regained. In the case of the work function increase to 1.7 eV that is shown in figure 8.8, the work function of 1.25 eV is retrieved after about 12 min with the Cs density of $\sim 10^{15}\,\mathrm{m}^{-3}$ in the vacuum chamber. Hence, changes of the chemical composition of the surface upon VUV irradiation are reversible.

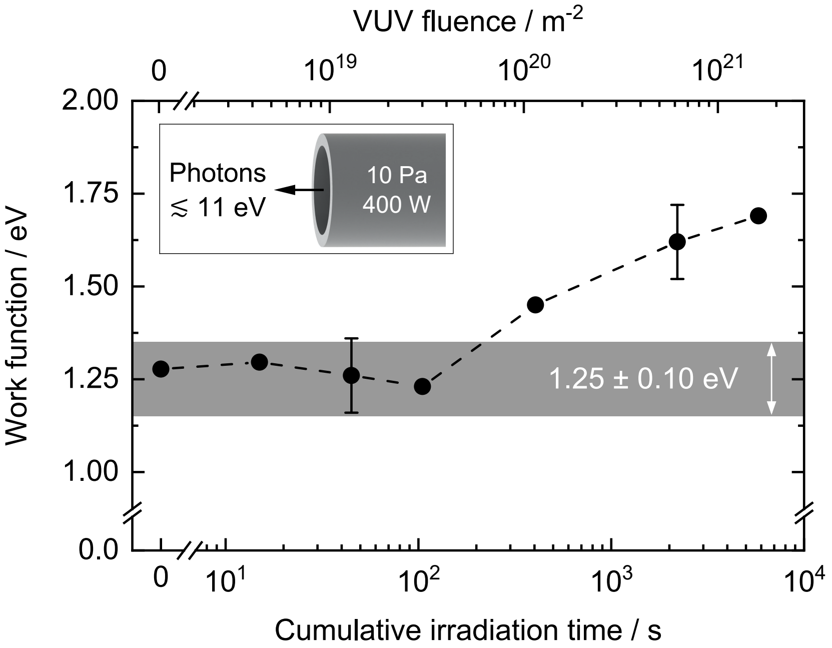

Figure 8.8: *Impact of photons with energies up to 11 eV on the work function of a Cs layer with $\chi \approx 1.25$ eV. The neutral Cs density is of the order of 10^{15} m^{-3} during the experiment.*

8.3 VUV photons + hydrogen atoms and positive hydrogen ions

8.3.1 Impact on degraded Cs layers

The work function change of degraded Cs layers upon the irradiation with VUV photons together with hydrogen atoms and positive hydrogen ions is investigated without the MgF_2 window inside the connection flange. The same experimental procedure as in section 8.2.1 is applied to prepare the Cs layers, and in a first step the plasma source is operated at 10 Pa/400 W. In figure 8.9(a), the resulting evolution of the work function is presented as a function of the cumulative irradiation time. The corresponding VUV fluence is depicted on the top x-axis and is calculated from the fluxes shown in figure 8.5 without the restriction to energies below 11 eV. In the case the initial work function is 3.0 eV (curve labeled 1), a work function reduction to 2.8 eV is already given after an irradiation time of 5 s. Upon further irradiation, the work function decreases further and reaches 2.2 eV after 60 s. Thereafter, the cumulative irradiation time is extended up to 2.5 h and the work function remains constant in the range of 2.2 ± 0.1 eV. The temperature of the sample surface increases only by a few degrees during the irradiation and does not exceed $\approx 30\,°C$. When the work function of the degraded Cs layer is > 3 eV, comparable low work function values are obtained, which is demonstrated by the curves labeled 2 and 3: The work functions of 3.2 and 3.5 eV are lowered to the range of 2.2 ± 0.1 eV for irradiation times ≥ 60 s. However, it can be seen from figure 8.9(b) that the reached QE is systematically lower the higher the initial work function. This behavior was already observed with photon irradiation only (see figure 8.6) and shows that the retrieved surface properties are still dependent on the previous degradation state.

It was shown in figure 8.6 that for a reduction of the work function from 3.0 to 2.5 eV, a VUV fluence of $\sim 2 \times 10^{20}\,\mathrm{m}^{-2}$ is required. Without the MgF_2 window inside the flange, the work function of 2.5 eV is already reached after a VUV fluence of $\sim 7 \times 10^{18}\,\mathrm{m}^{-2}$, and $\chi = 2.2$ eV is obtained after a VUV fluence of $\sim 3 \times 10^{19}\,\mathrm{m}^{-2}$. It has to be noted that without the window, the energy range of the photons striking the surface is extended from 11 eV to about 15 eV due to the emission from the Lyman series beyond Ly-H_α and from the Werner band. However, it is expected that the additional photon energies play a subordinate role as the dissociation energies of Cs compounds and residual gas molecules as well as the typical adsorption energies are below 11 eV. The enhanced work

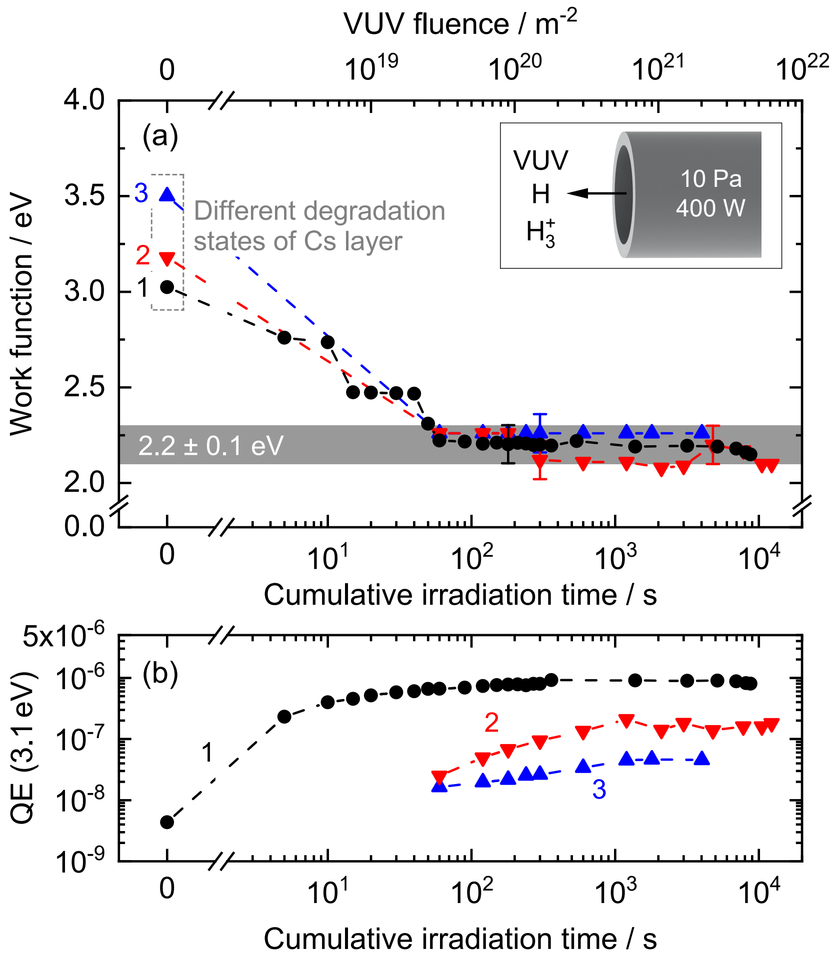

Figure 8.9: *(a) Work function evolution of Cs layers in different degradation states upon the irradiation with VUV photons, H atoms and* H_3^+ *ions from the external plasma source operated at 10 Pa/400 W. (b) Corresponding progressions of the QE at 3.1 eV.*

function reduction is thus attributed to the additional impact of the reactive plasma particles. Since Cs cannot be detected with the TDLAS system during irradiation times on the hour scale, the removal of Cs from the surface is inefficient at the given fluxes.

For a further down-selection of the interacting species with the caesiated surface, the positive hydrogen ions are magnetized by the installation of the permanent magnets outside the flange. With this, the impact of VUV photons together with hydrogen atoms can be studied. Furthermore, investigations are conducted with the plasma source operated at 4 Pa/600 W with and without magnetic filter field in order to increase the fluxes onto the surface (see discussion in section 8.1 and figure 8.4 for ions). The results obtained in the different scenarios are summarized in figure 8.10. It can be seen that at a pressure of 10 Pa, the work function of

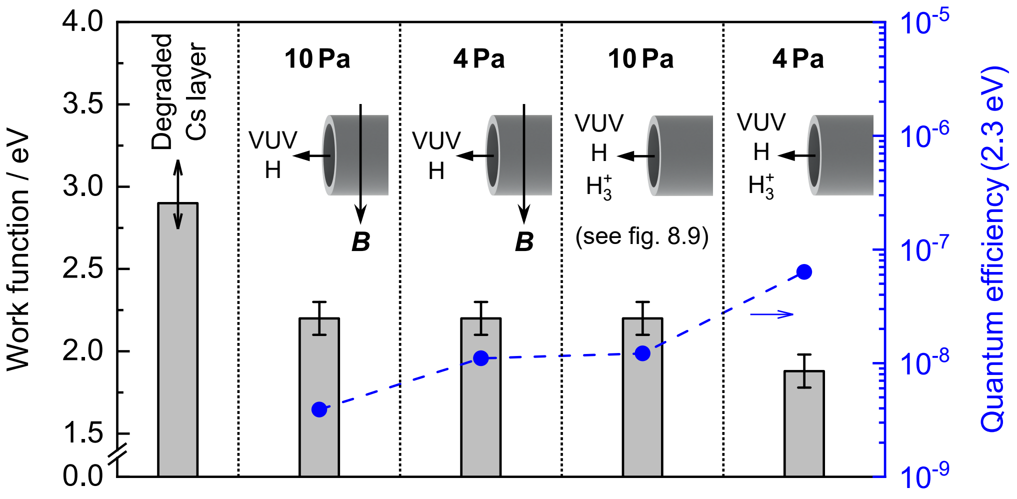

Figure 8.10: *Work function reduction of degraded Cs layers upon the exposure to hydrogen plasma species with and without H_3^+ ions. The external plasma source is operated both at 10 Pa/400 W and 4 Pa/600 W. Typical QEs at 2.3 eV are supplementary depicted.*

degraded Cs layers can be reduced to 2.2 ± 0.1 eV even with the exclusion of positive ions. At the reduced pressure of 4 Pa, the VUV and H fluxes also result in a work function of about 2.2 eV. When the magnetic filter field is removed at 4 Pa, however, a further reduction of the work function to 1.9 eV is achieved.

Additionally depicted in figure 8.10 are the typical QEs at 2.3 eV (i. e., close to the work function). It is observed that the QE increases by about half an order of magnitude when the pressure is reduced from 10 to 4 Pa with magnetic filter field, which is attributed to the higher expected H atom flux and the higher VUV flux by a factor of 2.5 (see figure 8.5). At 10 Pa without magnetic filter, the QE is comparable to the one at 4 Pa with magnetic filter because the lower H and VUV fluxes are compensated by H_3^+ ions striking the surface. At 4 Pa without magnetic filter, the fluxes are expected to be the largest, leading to the highest QE and the lowest work function.

The selective exposure of degraded Cs layers shows that VUV, atom and ion fluxes are beneficial to reactivate the surface. Since the temperature of the surface remains at about room temperature, thermal effects can be neglected. Furthermore, Cs is not detected with the TDLAS system, implying that Cs is not redistributed within the experiment. Consequently, beneficial changes of the chemical composition of the surface are driven by photochemical processes and interactions with hydrogen atoms and ions. A possible desorption of impurity gases from the surface cannot be monitored due to the RF distorted RGA.

8.3.2 Impact on ultra-low work function layer

The impact of VUV photons together with hydrogen atoms and positive hydrogen ions on the work function of a Cs layer with $\chi = 1.25 \pm 0.10\,\mathrm{eV}$ is investigated by the operation of the plasma source at 10 Pa/400 W without the application of the magnetic filter field. In analogy to the investigations presented in section 8.2.2, a Cs density of the order of $10^{15}\,\mathrm{m}^{-3}$ is continuously provided in the vacuum chamber and irradiation from the external source is applied from several seconds up to several minutes. In figure 8.11, the evolution of the work function is plotted as a function of the cumulative irradiation time. Furthermore, the work function evolution is compared to the one resulting from the irradiation with photons only that was shown in figure 8.8. It can be seen that the work function evolutions are quite similar: While for short irradiation times up to $\sim 100\,\mathrm{s}$ the work function remains in the range of $1.25 \pm 0.10\,\mathrm{eV}$, it increases for irradiation times exceeding a few minutes and reaches $\approx 1.7\,\mathrm{eV}$ after about 1.5 h. Consequently, the governing processes that are responsible for the increase of the work function are expected to be photochemical reactions (e. g., photolysis of Cs oxides) with photon energies below 11 eV, and the atomic and ionic particles seem to play a subordinate role here. After the irradiation with the plasma species is stopped, the ultra-low work function is retrieved within 15 min.

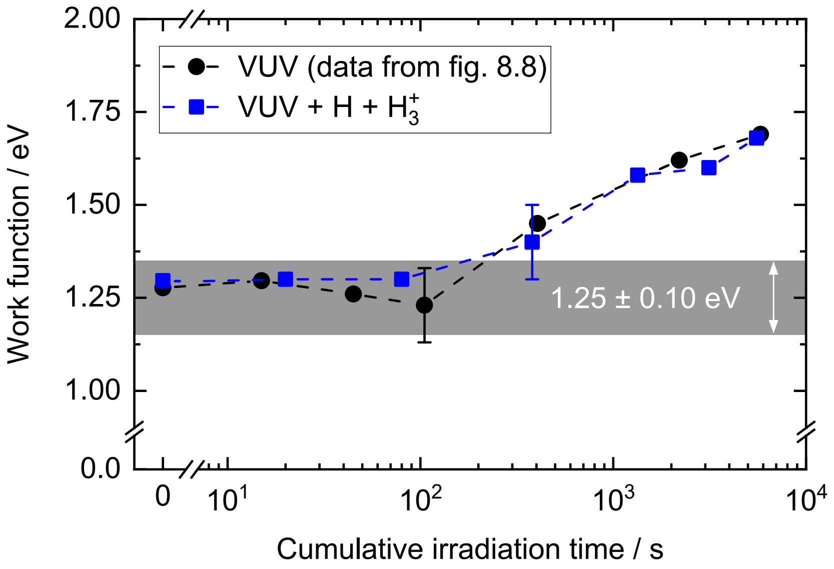

Figure 8.11: *Comparison of the work function evolution of a Cs layer with* $\chi \approx 1.25$ *eV upon VUV irradiation (data from figure 8.8) and upon VUV irradiation together with hydrogen atoms and positive hydrogen ions (external plasma source operated at 10 Pa/400 W). The neutral Cs density is of the order of* $10^{15}\,\mathrm{m}^{-3}$ *during both experiments.*

8.4 Summary

The performed investigations have clearly shown that the work function of caesiated surfaces is strongly affected by the interaction with hydrogen plasma species. A possible influence from the redistribution of Cs (compounds) within the experimental chamber was prevented by the usage of the external plasma source, and thermal effects were negligible as measured at the sample holder. The found work function dynamics are illustrated in figure 8.12 (extending the initial figure 8.1) and are summarized as follows:

- In the case of Cs layers with an ultra-low work function in the range of 1.25 ± 0.10 eV, incident VUV photons with energies up to 11 eV cause a gradual increase of the work function. After the exposure to a VUV fluence of the order of $10^{21}\,\mathrm{m}^{-2}$, an elevated work function of 1.7 eV is obtained. This observation reveals that VUV photons cause photochemical reactions at the surface and shows that the ultra-low work function coating is vulnerable in a hydrogen plasma environment. When the VUV photons are accompanied by hydrogen atoms and positive hydrogen ions, the work function increase is comparable, i. e., an additional influence of the applied atomic and ionic hydrogen fluxes on the ultra-low work function coating is not identified.

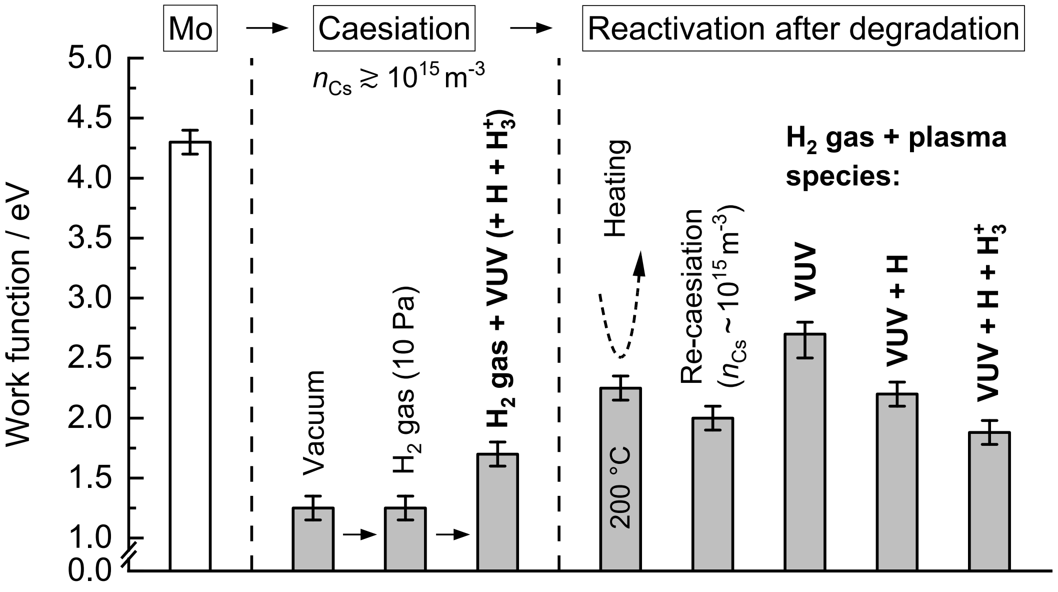

Figure 8.12: *Minimally achieved work functions of the Mo surface upon caesiation and the exposure to plasma species as well as upon heating, re-caesiation and the exposure to plasma species after the degradation due to residual gases. The applied fluxes of the plasma species onto the caesiated Mo surface are provided in figure 8.5.*

- In the case of degraded Cs layers with work functions $\gtrsim 3\,\mathrm{eV}$, the VUV photon irradiation enables an effective reduction of the work function to values in the range of $2.8 - 2.5\,\mathrm{eV}$. When the degraded Cs layers are exposed to VUV photons together with hydrogen atoms, a further reduction of the work function to $2.2 \pm 0.1\,\mathrm{eV}$ is obtained. Therefore, the hydrogen atoms that are used for the production of negative hydrogen ions via the surface conversion process can obviously change the chemical composition of the surface. A further reduction of the work function to $1.9\,\mathrm{eV}$ can be obtained by the additional impact of positive hydrogen ions. This work function is lower than the one achieved by heating to 200 °C and comparable to the one obtained upon re-caesiation with Cs densities of the order of $10^{15}\,\mathrm{m}^{-3}$.

9 Work function of caesiated surfaces upon hydrogen and deuterium plasma exposure

By the generation of hydrogen plasmas in the main vessel at ACCesS, the caesiated Mo surface is exposed to molecular, atomic, ionic and photonic fluxes simultaneously, and Cs (compounds) deposited on the surfaces within the experiment are effectively redistributed. Furthermore, the plasma leads to a considerable thermal load on the surface. For the investigations presented in this chapter, the discharges are generated with a gas pressure of 10 Pa and an RF power of 250 W. With this, the plasma parameters are comparable to those close to the plasma grid at the BUG and ELISE test facilities, i. e., the conditions to which the caesiated plasma grid is exposed in NNBI ion sources are mimicked.

As illustrated in figure 9.1, the work function behavior of caesiated surfaces is studied in various scenarios. Cs coatings with a work function in the range of 1.25 ± 0.10 eV are exposed to plasma pulses with different lengths to investigate their durability in the plasma environment. The reactivation of degraded Cs layers is performed by the application of plasma pulses with and without active Cs evaporation with the aim to identify the scenario resulting in the most effective work function reduction. As NNBI ion sources are required to operate on the hour scale, the work function performance of caesiated surfaces during steady-state plasma operation is explored. The investigations are performed both in hydrogen and deuterium to identify possible isotope effects.

9.1 Quantification of VUV and particle fluxes

The VUV, positive ion and atom fluxes generated by hydrogen discharges in the main vessel at ACCesS are depicted as blue bars in figure 9.2. As described in section 5.4, the VUV fluxes from the Lyman band, the Lyman-α line and the Werner band together with the Lyman series beyond Lyman-α are determined

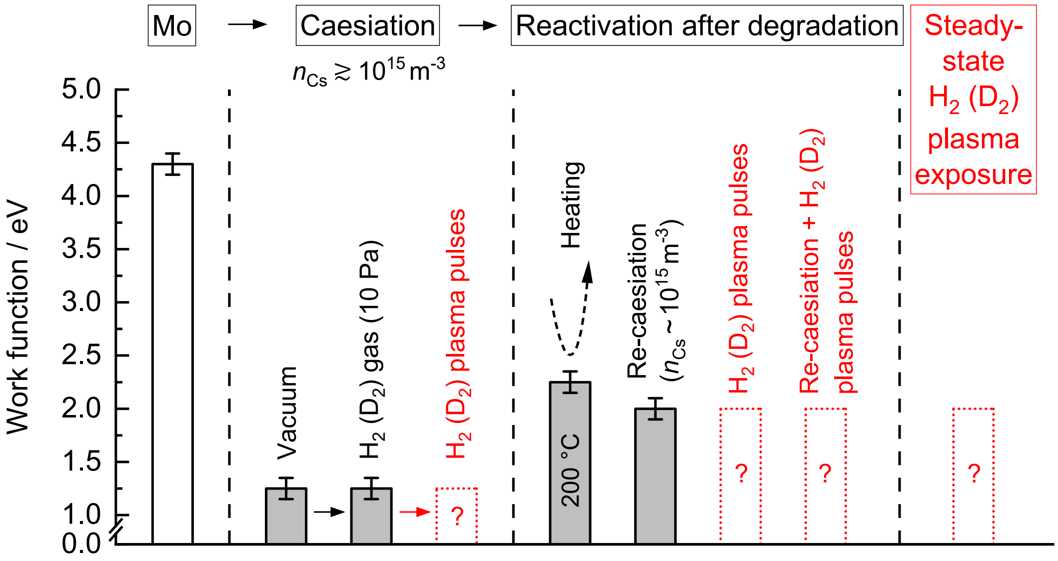

Figure 9.1: *Overview of the work function dynamics of a caesiated Mo surface: The minimum work functions reached in the vacuum and H_2 (D_2) gas phase with active Cs evaporation as well as the decrease of the work function upon heating and re-caesiation are shown (details see chapter 7). The red dotted bars with question mark indicate what is addressed in the present chapter.*

with the VUV diode system. The different contributions are represented by means of a stacked bar, showing that the total VUV flux is about $4 \times 10^{19}\,\mathrm{m^{-2}s^{-1}}$. The flux of positive ions (predominantly H_3^+) is determined from Langmuir probe measurements directly above the Mo surface ($T_\mathrm{e} = 2.1\,\mathrm{eV}$, $n_{\mathrm{i}+} = 1.4 \times 10^{16}\,\mathrm{m^{-3}}$) and is by a factor of 2.8 higher than the VUV flux. The atomic hydrogen flux is determined via OES measurements ($T_\mathrm{gas} = 550\,\mathrm{K}$, $n_\mathrm{H} = 1.7 \times 10^{19}\,\mathrm{m^{-3}}$) and is about $1 \times 10^{22}\,\mathrm{m^{-2}s^{-1}}$, which is significantly higher than the VUV and ion fluxes. While the mean kinetic energy of the hydrogen atoms is, however, only about 0.05 eV, the positive ions strike the surface with energies of about 8 eV in maximum, which is determined from the difference between the plasma potential and the floating potential of the surface. The VUV photons have energies up to about 15 eV and are thus the most energetic species.

It can be seen in figure 9.2 that the fluxes generated in the main vessel are significantly higher than the ones from the external plasma source (EPS) that are applied for the investigations in chapter 8. While the flux of VUV photons is about two orders of magnitude higher, the fluxes of the positive ions and atoms are increased by (more than) two orders of magnitude.

Additionally shown in figure 9.2 are the fluxes onto the plasma grid measured at the BUG test facility for typical operational parameters (0.3 Pa gas pressure, 40 kW RF power). The VUV fluxes are determined from measurements with the

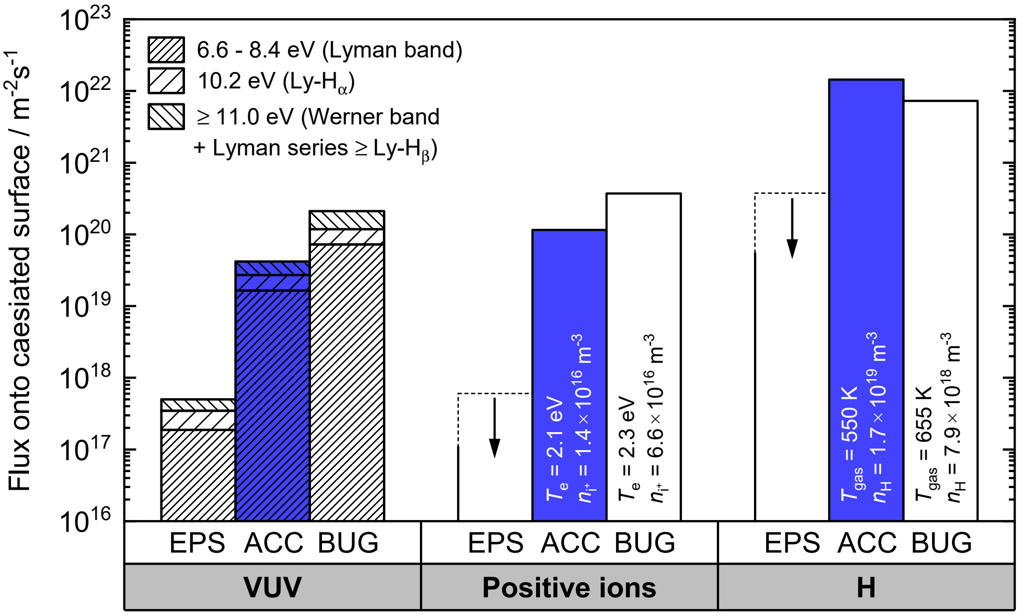

Figure 9.2: *VUV, positive ion and atom fluxes generated by hydrogen plasmas in the main vessel at ACCesS (labeled ACC, plotted in blue). The corresponding plasma parameters determined via Langmuir probe and OES measurements are indicated. The fluxes from the external plasma source applied for the investigations in chapter 8 (labeled EPS, see figure 8.5) as well as the fluxes onto the plasma grid at the BUG test facility together with the corresponding plasma parameters for typical operational parameters [W$^+$21c, BF18, SWF18] are depicted for the sake of comparison. The VUV fluxes are represented as stacked bars, showing the contributions from different energy ranges.*

VUV diode system [FB22, W$^+$21c], the positive ion flux is determined from the indicated electron temperature and positive ion density from Langmuir probe measurements (mean ion mass = 1.8 u) [SWF18], and the H atom flux is calculated from the indicated atomic density and gas temperature, both evaluated from OES measurements [BF18]. The determined VUV flux is by a factor of five higher than at ACCesS, which is mainly due to the intense emission from the driver plasma reaching the plasma grid [FB22]. The determined positive ion density in front of the plasma grid is found to be somewhat higher than in front of the installed sample at ACCesS, resulting in a factor of three higher ion flux. The difference between the plasma potential and the potential of the plasma grid is typically not higher than a few volts so that the maximum kinetic energies of the ions can be considered comparable to ACCesS. The atomic hydrogen flux is found to be slightly higher at ACCesS due to a higher atomic density. As the differences of the evaluated fluxes at BUG and ACCesS are, however, well below one order of magnitude, the plasma-surface interaction can be considered comparable.

Deuterium plasmas are ignited with the same operational parameters as hydrogen plasmas at ACCesS (10 Pa gas pressure, 250 W RF power), and the measured plasma parameters and particle fluxes are compared to hydrogen in table 9.1. As can be seen, the electron density, electron temperature and atomic density are slightly higher in deuterium and the gas temperature is a bit lower, but the calculated fluxes of the atoms and positive ions are almost identical. The difference between the plasma potential and floating potential of the sample is a few volts higher in deuterium, leading to a higher maximum energy of the impinging positive ions. Furthermore, the deuterium particles have twice the mass of the hydrogen particles and the temperature of the sample surface reaches ≈ 270 °C in steady-state operation, which is about 50 °C higher than in hydrogen. VUV fluxes have not yet been measured in deuterium, but since the electron density, electron temperature and atomic density are slightly higher in deuterium, also slightly increased VUV fluxes are expected.

Table 9.1: *Comparison between the plasma parameters and particle fluxes in hydrogen and deuterium plasmas generated at 10 Pa/250 W at ACCesS.*

	H_2 plasma	D_2 plasma
n_{e} / $\mathrm{m^{-3}}$	1.4×10^{16}	2.0×10^{16}
T_{e} / eV	2.1	2.5
$n_{\mathrm{H,D}}$ / $\mathrm{m^{-3}}$	1.7×10^{19}	2.6×10^{19}
$T_{\mathrm{gas}} = T_{\mathrm{H,D}}$ / K	550	530
$\phi_{\mathrm{pl}} - \phi_{\mathrm{fl}}$ / V	8	11
$\mathit{\Gamma}_{\mathrm{H,D}}$ / $\mathrm{m^{-2}s^{-1}}$	1.4×10^{22}	1.5×10^{22}
$\mathit{\Gamma}_{\mathrm{H_3^+,D_3^+}}$ / $\mathrm{m^{-2}s^{-1}}$	1.2×10^{20}	1.3×10^{20}

9.2 Reactivation of degraded Cs layers

The re-conditioning of the caesiated plasma grid at the BUG and ELISE test facilities is performed by the evaporation of fresh Cs into the source together with the application of short repetitive hydrogen (deuterium) plasma pulses of several seconds with vacuum phases of a few minutes in between. To understand the impact of this process on the work function of caesiated surfaces, re-caesiation without the application of plasma pulses, application of plasma pulses without re-caesiation as well as re-caesiation together with the application of plasma pulses need to be studied. Investigations on the re-caesiation without plasma pulses have already been presented in section 7.2 and have shown that work functions in the range of 1.9 – 2.1 eV are typically obtained. In the following section, the impact of repetitive plasma pulses without Cs evaporation is analyzed, and in section 9.2.2, the plasma conditioning with Cs evaporation is investigated.

9.2.1 Short plasma pulses without Cs evaporation

Figure 9.3 presents the results of different experimental campaigns where degraded caesiated surfaces are exposed to repetitive hydrogen plasma pulses with pulse lengths between 5 and 30 s. In (a), the work function is plotted as a function of the cumulative plasma-on time, and in (b), the corresponding QEs at 2.3 eV are depicted. The average neutral Cs densities measured during the applied plasma pulses are shown in (c) (note that ionized Cs atoms as well as Cs compounds are not detected), and in (d), the maximum temperatures of the surface reached during the plasma pulses are plotted.

The data labeled 1 is measured one day after a caesiation process during which a Cs layer with a work function of 1.25 eV was grown on the Mo surface. It can be seen that after a plasma exposure time of 5 s, the work function is reduced from 3.0 to 2.2 eV. During the plasma pulse, the measured Cs density is slightly above $10^{15}\,\mathrm{m}^{-3}$, showing that a considerable Cs redistribution is driven by the interaction of the plasma with the caesiated surfaces within the experiment. The Cs density instantly drops below the TDLAS detection limit ($\leq 2 \times 10^{13}\,\mathrm{m}^{-3}$) when the plasma is switched off. The application of a subsequent 5 s plasma pulse leads to a further reduction of the work function to 2.0 eV. For cumulative plasma-on times $\geq$ 15 s, a stable work function plateau of 1.9 ± 0.1 eV is reached, with the QE remaining virtually constant. The Cs density during the plasma pulses is in the range of $10^{14} - 10^{15}\,\mathrm{m}^{-3}$ and increases again slightly above $10^{15}\,\mathrm{m}^{-3}$ during the last plasma pulse, where the plasma pulse length is extended from 10 to 30 s, i. e., the Cs release from the surfaces is enhanced with longer plasma exposure times. As the temperature of the water-cooled vessel wall is about 22 °C (not shown) and the temperature of the sample surface remains below 50 °C, thermal desorption of Cs from the surfaces can be neglected (cf. figure 7.7) and the Cs release is believed to be mainly the result of chemical sputtering. In the RGA recording, an increase of the signals for H_2O, N_2 and CO_2 is observed during the first plasma pulses, showing that adsorbed residual gases on the (caesiated) surfaces within the experiment are released as well.

As indicated in figure 9.3(a), the reached work function of 1.9 eV is the same as the minimum work function achieved upon the irradiation with photons, hydrogen

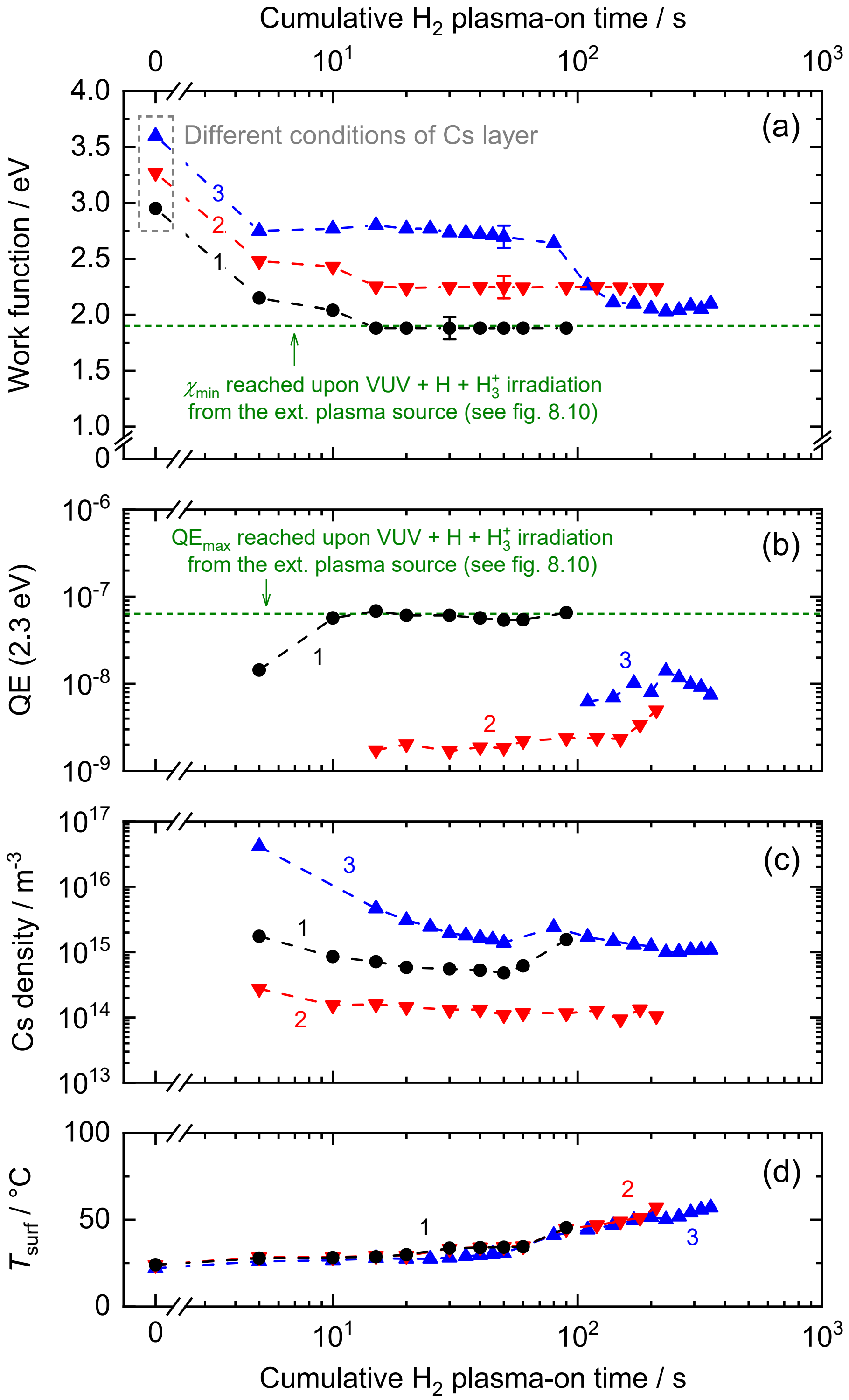

Figure 9.3: *Application of short repetitive hydrogen plasma pulses in different experimental campaigns to reactivate degraded caesiated Mo surfaces without the evaporation of fresh Cs: In (a) and (b), the evolution of the work function and QE at 2.3 eV are shown as a function of the cumulative plasma-on time, and in (c) and (d), the average neutral Cs densities and maximum temperatures of the sample surface during the pulses are depicted.*

atoms and positive hydrogen ions from the external plasma source. Moreover, also the obtained QEs at 2.3 eV shown in figure 9.3(b) are virtually the same, indicating that the obtained surface conditions are very similar. Therefore, it is suggested that the induced chemical reactions at the surface and resulting modifications of the chemical composition of the surface are comparable. A direct comparison of the work function evolution upon the fluences of the plasma species is unfortunately not possible as the exact particle fluxes from the external plasma source reaching the surface are not known. However, it can be stated that the fluences corresponding to the applied total plasma-on time of 90 s are at least one order of magnitude larger compared to what was applied with the external plasma source, i. e., the retrieved work function minimum is 1.9 eV also upon the exposure to increased fluxes and fluences of the hydrogen plasma species.

Further campaigns have shown that the obtained surface conditions (work function and QE) of degraded caesiated surfaces upon the exposure to short plasma pulses without Cs evaporation depend strongly on the experimental history. This is exemplarily demonstrated with the depicted campaigns labeled 2 and 3 in figure 9.3. The measurements labeled 2 are conducted one day after a hydrogen plasma of 4 h was ignited in the main chamber. During the plasma phase of 4 h, Cs was redistributed from Cs reservoirs from a previous caesiation process (measured Cs density of the order of $10^{14}\,\mathrm{m}^{-3}$ during plasma), but no active Cs evaporation was applied. The work function of the degraded caesiated surface is 3.3 eV and is lowered to 2.5 eV after a plasma pulse of 5 s is applied. For plasma-on times ≥ 15 s during which the measured Cs density is of the order of $10^{14}\,\mathrm{m}^{-3}$, a work function plateau of 2.2 ± 0.1 eV is reached. The about 0.3 eV higher work function compared to the reached plateau in campaign 1 is accompanied by an about one order of magnitude lower QE. The measurements labeled 3 in figure 9.3 are conducted after a Cs layer with $\chi = 1.25$ eV was left in vacuum for four weeks. Here, the application of a 5 s plasma pulse leads to the reduction of the work function from 3.6 to 2.8 eV. The Cs density during the plasma phase is higher than $10^{16}\,\mathrm{m}^{-3}$, showing that high amounts of Cs are present in the plasma chamber. During the subsequent plasma pulses, the Cs densities decrease to $\sim 10^{15}\,\mathrm{m}^{-3}$ and are still higher compared to the campaigns 1 and 2. Nonetheless, the work function remains in the range of $2.7 - 2.8$ eV for cumulative plasma-on times up to 50 s, and decreases into the range of $2.0 - 2.1$ eV after a plasma-on time of $\gtrsim 2$ min. The reached QE is higher than the one of campaign 2 and lower than the one of campaign 1.

In consequence, it can be stated that a distinct memory effect is given that prevents the reproducible conditioning of degraded caesiated surfaces by the application of short plasma pulses without Cs evaporation. Comparable results are obtained with deuterium.

9.2.2 Short plasma pulses with Cs evaporation

Figure 9.4(a) presents an experimental campaign where the ion source conditioning scenario is mimicked, i. e., short repetitive hydrogen plasma pulses together with continuous Cs evaporation are applied. The length of the plasma pulses (indicated by the vertical red lines) is 5 s and the vacuum phases in between the plasma pulses last $3-5$ min during which the work function is measured. At the beginning, a degraded Cs layer with a work function of 3.1 eV is present, resulting from the degradation of a Cs coating with a work function of 1.25 eV due to residual gas adsorption. During the first plasma pulse, the measured neutral Cs density is slightly above $10^{15}\,\mathrm{m}^{-3}$ and a work function of 2.2 eV is obtained afterward, comparable to campaign 1 in figure 9.3. After the subsequent plasma pulse, the work function is 2.1 eV and the Cs evaporation is started. The evaporation rate is gradually increased such that a Cs density of $\sim 5\times10^{14}\,\mathrm{m}^{-3}$ is given during the vacuum phases (reached after the fifth plasma pulse). During the plasma phases, the Cs density is each time $\sim 2\times10^{15}\,\mathrm{m}^{-3}$. The work function decreases further and reaches a stable value of 1.75 ± 0.10 eV after 12 pulses, i. e., after a plasma-on time of 60 s. This work function is lower than the minimally achieved value of 1.9 eV by the application of plasma pulses without Cs evaporation. The decrease of the work function is accompanied by a significant enhancement of the QE, which is exemplarily shown for 2.3 eV: The decrease from $\chi = 2.2$ eV after the first plasma pulse to $\chi = 1.75$ eV after the twelfth pulse is accompanied by an increase of the QE from 7×10^{-8} to 9×10^{-7}. Furthermore, the QE measured after the subsequent plasma pulses continues to increase slightly and reaches 2×10^{-6} after the last (25th) pulse, which is more than one order of magnitude higher than the maximally reached QE by the application of plasma pulses without Cs evaporation. The surface temperature increases only by a few degrees during the plasma pulses and remains below 50 °C.

After the application of the 25 plasma pulses, the Cs density is maintained in the vacuum vessel. The measured work function after about 50 min ($t \approx 3.6$ h) is 1.72 eV, showing that the work function is sustained in the absence of plasma pulses. However, the QE is slightly reduced. The Cs density is then gradually increased and comparable to the known behavior from the first caesiation of the

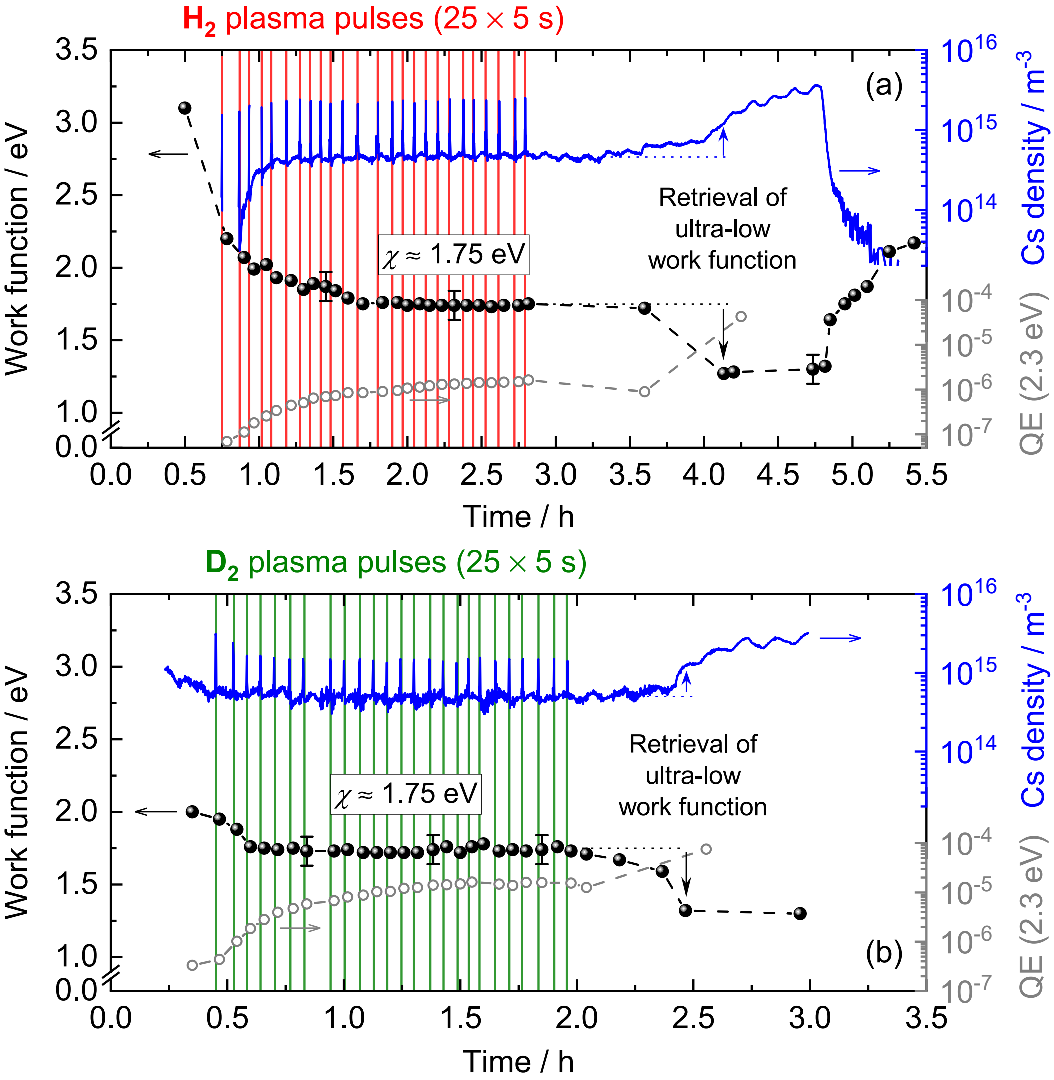

Figure 9.4: *Evolution of the surface work function of a degraded Cs layer upon caesiation in vacuum together with the exposure to repetitive 5 s plasma pulses (indicated by the vertical lines). In (a), the plasma pulses are performed in hydrogen and in (b) in deuterium. The continuously monitored neutral Cs density as well as the progression of the QE at 2.3 eV from pulse to pulse are additionally depicted.*

Mo surface (see figure 7.4), the work function decreases to ultra-low values of 1.3 eV for Cs densities $\gtrsim 10^{15}\,\mathrm{m}^{-3}$, accompanied by an increase of the QE by about one and a half orders of magnitude. The work function of 1.3 eV is kept constant as long as the Cs density is $\gtrsim 10^{15}\,\mathrm{m}^{-3}$. When the Cs evaporation is decreased and eventually shut down, the rapid work function increase already described in section 7.2 is observed.

In analogy to figure 9.4(a), the work function behavior upon the exposure to $25 \times 5\,\mathrm{s}$ deuterium plasma pulses with a Cs density of $\sim 5 \times 10^{14}\,\mathrm{m}^{-3}$ during the vacuum phases is shown in figure 9.4(b). In this case, the Cs evaporation is already running before the first plasma pulse, leading to an initial work function of 2 eV and a QE of 3×10^{-7} at 2.3 eV. Comparable to the conditioning with hydrogen plasma pulses, a work function plateau of 1.75 ± 0.10 eV is reached with deuterium. However, the work function of 1.75 eV is reached after the application of only three plasma pulses, which is probably due to the fact that the Cs evaporation is already running and the work function is already at a low value of 2 eV before the first pulse. The QE is 2×10^{-6} after the first three pulses, which is the same as after the 25 pulses with hydrogen in figure 9.4(a). By the application of the subsequent deuterium plasma pulses, the QE increases further and saturates at 2×10^{-5}, while the work function stays at about 1.75 eV. The surface temperature remains below 50 °C and is only a few degrees higher than after the hydrogen plasma pulses (not shown). By increasing the Cs density afterward, the work function decreases and ultra-low values of 1.3 eV are obtained for Cs densities $\gtrsim 10^{15}\,\mathrm{m}^{-3}$. The reached QE is by a factor of 1.8 higher compared to the one after the hydrogen plasma pulses.

Further investigations have shown that the exposure of degraded Cs layers to a series of H_2 (D_2) plasma pulses of a few seconds in combination with stable Cs densities of the order of $10^{15}\,\mathrm{m}^{-3}$ in the vacuum phases leads to a reliable retrieval of work functions in the range of 1.25 ± 0.10 eV. It is generally observed that the ultra-low work function is retrieved faster the weaker the degradation, but for a detailed evaluation of the dependence of the temporal work function (and QE) evolution on the initial degradation state and number of required plasma pulses further studies would be required.

Since both re-caesiation without plasma pulses and plasma pulses without re-caesiation lead to work functions of typically $1.9 - 2.1$ eV (see section 7.2 and 9.2.1, respectively), it is unveiled that a beneficial synergistic effect is given by the combination of both. This is also impressively demonstrated in figure 9.5, where typical QE curves are plotted: While the reactivation via re-caesiation without H_2 plasma pulses ($\chi = 2.0$ eV) and via H_2 plasma pulses without re-caesiation ($\chi = 1.9$ eV, from campaign 1 in figure 9.3) lead to comparable QEs in the energy range of $2.1 - 2.6$ eV, a $2 - 3$ orders of magnitude higher QE is achieved in this energy range after the re-caesiation together with H_2 plasma pulses, where the photoelectric response is extended to the near IR and the evaluated work function is 1.3 eV. As $\chi = 1.3$ eV is only achieved when the Cs density is $\gtrsim 10^{15}\,\mathrm{m}^{-3}$ during the vacuum phases, the flux ratio $\mathit{\Gamma}_{\mathrm{Cs}}/\mathit{\Gamma}_{\mathrm{H_2O}}$ still seems to be the decisive parameter to reach the ultra-low work function values (cf. figure 7.4). However, it is demonstrated in figure 9.5 that the QEs achieved near the photoelectric

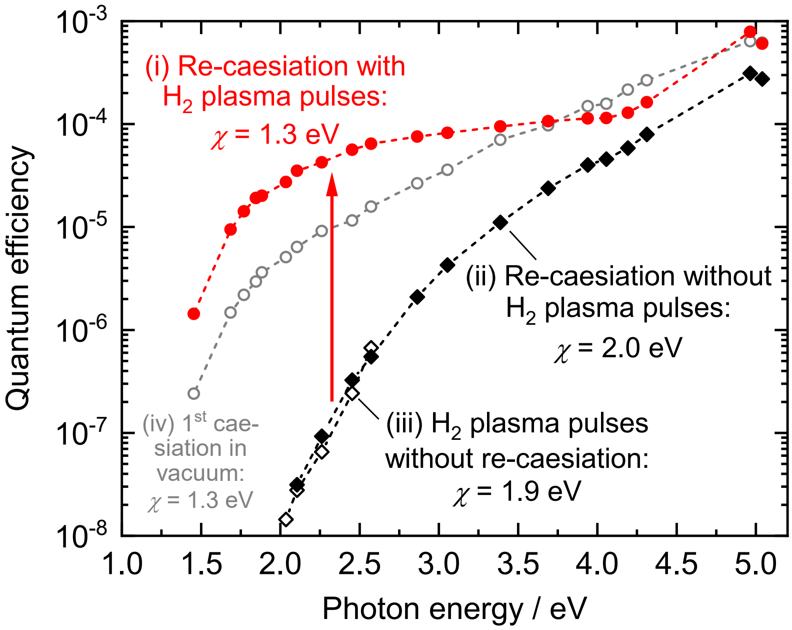

Figure 9.5: *Typical QE curves of caesiated Mo surfaces measured (i) after the reactivation of degraded Cs layers with short hydrogen plasma pulses together with a Cs density of* $\sim 10^{15}\,\mathrm{m}^{-3}$ *in the vacuum phase, (ii) upon re-caesiation with a Cs density of* $\sim 10^{15}\,\mathrm{m}^{-3}$ *without the application of hydrogen plasma pulses, (iii) after short hydrogen plasma pulses without evaporation of fresh Cs (from campaign 1 in figure 9.3), and (iv) upon first caesiation with a Cs density of* $\sim 10^{15}\,\mathrm{m}^{-3}$*. Evaluated work functions from the measured QEs are indicated.*

threshold are higher than those obtained by the first caesiation of the Mo surface in vacuum. This suggests that the chemical composition of the surface is positively affected by the impinging plasma species, as the higher QE indicates a higher electron density at the surface, which is expected to be favorable for the generation of negative ions. With increasing photon energies, the relative differences between the QE curves generally decrease.

9.3 Durability of ultra-low work function layer

To investigate the durability of Cs layers with a work function of $1.25 \pm 0.10\,\mathrm{eV}$ upon H_2 and D_2 plasma exposure, plasma pulses with different lengths are applied and the work function is measured directly afterward. The neutral Cs density is kept on the order of $10^{15}\,\mathrm{m}^{-3}$ during the vacuum phases and is in the range of $5 \times 10^{15} - 1 \times 10^{16}\,\mathrm{m}^{-3}$ during the plasma phases due to the plasma-induced Cs redistribution within the vessel. The bar diagram in figure 9.6 presents the resulting work functions as a function of H_2 and D_2 plasma pulse lengths between

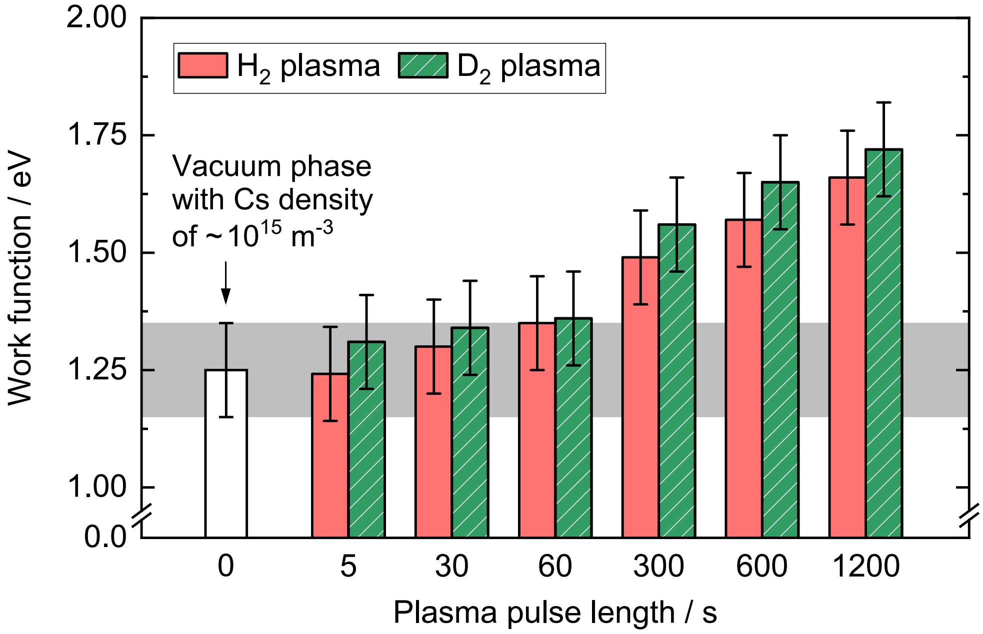

Figure 9.6: *Surface work function after the exposure of Cs layers with a work function of* 1.25 ± 0.10 *eV to hydrogen and deuterium plasma pulses with different lengths. The neutral Cs density is of the order of* 10^{15} m^{-3} *during the vacuum phases and in the range of* $5 \times 10^{15} - 1 \times 10^{16}$ m^{-3} *during the plasma phases.*

5 s and 20 min. It can be seen that for plasma pulse lengths up to 30 s, the work function remains in the range of 1.25 ± 0.10 eV. This result is remarkable as a plasma pulse of 30 s leads to a VUV fluence of the order of $10^{21}\,\mathrm{m}^{-2}$ onto the caesiated surface, where in chapter 8 an increase of the work function was observed (cf. figure 8.8). Possible reasons for the enhanced durability of the ultra-low work function layer might be the elevated Cs density during the plasma phase and/or the redistribution of Cs compounds (e. g., Cs oxides) within the vessel, which might lead to a beneficial effect regarding the chemical composition of the surface.

After plasma pulses with a length of $\gtrsim$ 1 min, work functions above the range of 1.25 ± 0.10 eV are measured. The work function increase seems to be systematically higher in deuterium than in hydrogen, however, the values still agree within the error bars so that no difference is stated here. After plasma pulse lengths of 20 min, the work function is about 1.7 eV. The surface temperature after the 20 min H_2 and D_2 plasma pulses is 182 °C and 209 °C, respectively. As mentioned in section 7.3, temperatures up to about 200 °C are not expected to be harmful for Cs oxide coatings so that it is suggested that thermal effects play a subordinate role here and the increase of the work function is mainly driven by chemical reactions with the impinging plasma species. From these results, it can be concluded that the ultra-low work function coating is not stable during long plasma pulses at ion source relevant conditions.

After the plasma exposure is stopped, the increased work function decreases again in the vacuum phase and ultra-low values in the range of $1.25 \pm 0.10\,\text{eV}$ are regained. The time it takes for the retrieval of the ultra-low values is shorter the less the work function has increased during the plasma phase, i. e., the recovery time depends on the applied plasma pulse length. In general, the retrieval of $1.25 \pm 0.10\,\text{eV}$ occurs on a time scale comparable to the plasma pulse length.

9.4 Work function performance during steady-state plasma operation

As described in section 2.3, the NNBI systems for ITER must deliver stable negative ion beams for a duration of 1000 s in hydrogen and 3600 s in deuterium. In view of the demonstration power plant DEMO (currently in a pre-conceptual design phase [F$^+$19b, F$^+$21b]) and a potential commercial fusion power plant, the operation of NNBI systems on the hour scale would be generally necessary. Therefore, it is of utmost importance that a stable ion source performance is guaranteed, for which a stable low work function of the plasma grid surface is necessary. As it was already shown in the previous section that Cs layers with an ultra-low work function of 1.3 eV are not stable upon plasma exposure times $\gtrsim 1\,\text{min}$, the lowest work function that can be maintained during steady-state plasma operation needs to be identified. To do so, the work function behavior of the caesiated Mo surface is analyzed after the application of several $30 - 60\,\text{min}$ plasma pulses during which different Cs fluxes onto the surface are provided.

Hydrogen plasma operation

Figure 9.7(a) shows an exemplary campaign where the work function of the caesiated Mo surface is measured after the application of 60 min hydrogen plasma pulses. The initial work function is 1.9 eV and is prepared by the exposure of a degraded Cs layer to a couple of short hydrogen plasma pulses (cf. campaign 1 in figure 9.3). The Cs oven is not activated during this experiment, i. e., the Cs flux during plasma operation results solely from the plasma-induced release of Cs from the caesiated surfaces within the vessel. When the first 60 min plasma pulse is started, the measured neutral Cs density is instantly at $2 \times 10^{14}\,\text{m}^{-3}$ and increases to $6 \times 10^{14}\,\text{m}^{-3}$ within 15 min. The Cs density of $6 \times 10^{14}\,\text{m}^{-3}$ is maintained for a

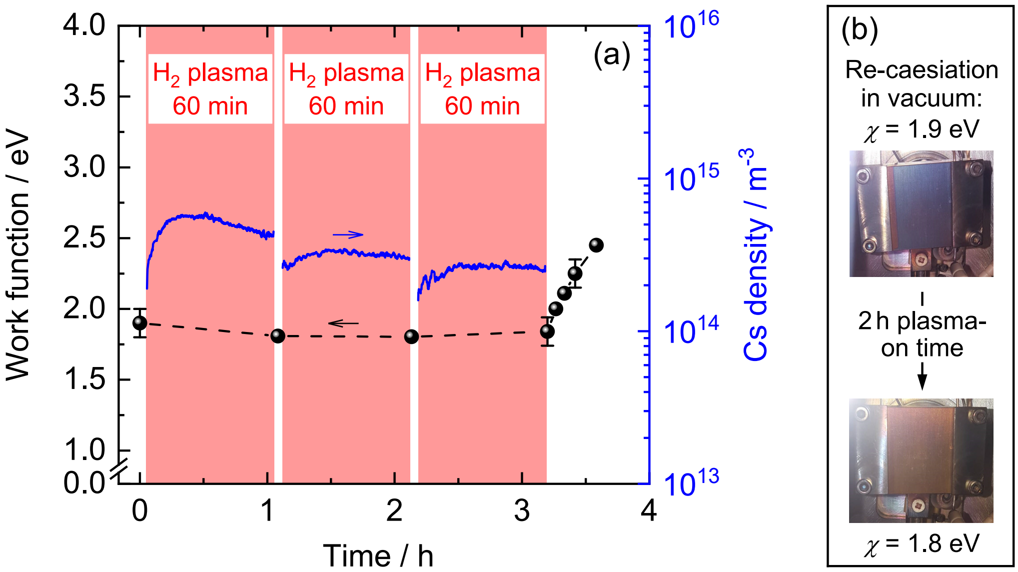

Figure 9.7: *(a) Work function behavior of a caesiated Mo surface after the application of 60 min hydrogen plasma pulses. The plasma phases are indicated by the red shaded areas and the measured neutral Cs density is additionally depicted (no active Cs evaporation applied). (b) Photographs of a re-caesiated Mo surface in vacuum and after a subsequently applied hydrogen plasma-on time of two hours. The reddish discoloration of the Mo surface results from a previously performed annealing process (see figure 7.7).*

couple of minutes and decreases slowly afterward, showing that the Cs reservoirs within the vessel are gradually depleted and Cs diffuses to regions where it is lost for the experiment. At the end of the 60 min plasma pulse, the Cs density is $4 \times 10^{14}\,\mathrm{m^{-3}}$. While the temperature of the water-cooled vessel wall does not exceed ≈ 40 °C during plasma operation, the temperature of the sample surface reaches about 220 °C in maximum. As soon as the plasma is switched off, the Cs density drops below the TDLAS detection limit. The work function measured right after the plasma is switched off is 1.8 eV, i. e., it is 0.1 eV lower than what was achieved by the previous reactivation of the degraded Cs layer with short plasma pulses.

The plasma-on time is extended by two subsequent 60 min plasma pulses during which the mean neutral Cs density is about $3 \times 10^{14}\,\mathrm{m^{-3}}$. After each plasma pulse, the work function is 1.8 eV, demonstrating that the work function remains at a constant value. Furthermore, it is shown that a pronounced work function increase is given without further plasma exposure: 25 min after the last plasma pulse, the work function is 2.5 eV, i. e., the degradation rate after the plasma is switched off and no Cs flux is given is in the range of $0.02 - 0.03\,\mathrm{eV/min}$.

In a different campaign, the reddish discolored Mo surface obtained after the annealing process shown in figure 7.7 was re-caesiated in vacuum and subsequently exposed to long hydrogen plasma pulses. The upper photograph in figure 9.7(b) shows the sample surface after the re-caesiation process, with the work function being 1.9 eV. The deposited Cs layer is clearly visible as a silvery coating, i. e., a thick Cs layer is created on the substrate (right next to the left clamp, the surface still has the reddish color since this region is shadowed by the clamp, as described in section 7.1). After a plasma-on time of about two hours with a measured Cs density of $\sim 5 \times 10^{14}\,\mathrm{m}^{-3}$ during the plasma phase, the work function is 1.8 eV and the lower photograph in figure 9.7(b) shows that the silvery layer is no more visible. Hence, it can be concluded that a substantial amount of Cs is removed from the surface by the long-term plasma impact, leading to a strongly reduced Cs layer thickness.

Extensive investigations regarding the temporal stability of the work function during long hydrogen plasma pulses are compiled in figure 9.8. The work functions depicted as open symbols are measured after pulse lengths of 30 min and those depicted as full symbols are measured after 60 min plasma pulses. The work functions are plotted against the neutral Cs flux during the plasma phases, which is calculated from the average neutral Cs density and the temperature of the Cs atoms ($\approx 550\,\mathrm{K}$) from TDLAS measurements. The x-error bars result from the standard deviation of the averaged Cs density. The Cs flux is provided either solely by the plasma-induced Cs redistribution as in figure 9.7(a) (Cs oven not active) or with the additional evaporation of Cs from the oven (Cs oven active). It is observed that for Cs fluxes $\gtrsim 2 \times 10^{16}\,\mathrm{m}^{-2}\mathrm{s}^{-1}$ ($n_{\mathrm{Cs}} \gtrsim 3 \times 10^{14}\,\mathrm{m}^{-3}$) a work function of 1.8 eV is given each time within the error bar of ± 0.1 eV. Moreover, this work function is maintained for cumulative plasma-on times of several hours (cf. figure 9.7(a)) so that $\chi = 1.8 \pm 0.1\,\mathrm{eV}$ is identified as a stable work function plateau during steady-state plasma operation. Work functions below the range of $1.8 \pm 0.1\,\mathrm{eV}$ are not measured after the long plasma pulses, which was tested for neutral Cs fluxes up to $\sim 2 \times 10^{17}\,\mathrm{m}^{-2}\mathrm{s}^{-1}$ ($n_{\mathrm{Cs}} \sim 2 \times 10^{15}\,\mathrm{m}^{-3}$) during the plasma phase. Furthermore, it can be stated that the equilibrium work function of 1.8 eV is independent of the work function at the beginning of the pulse, which was varied between 1.3 and 3 eV (indicated by the blue arrows). Therefore, it is concluded that the temporal work function evolution of the caesiated surface during long-term plasma exposure is determined only during the first minutes by the work function generated in the vacuum phase: In the case the initial work function is in the ultra-low regime, the work function gradually increases (cf. figure 9.6) and in the case of a degraded Cs layer, the work function gradually

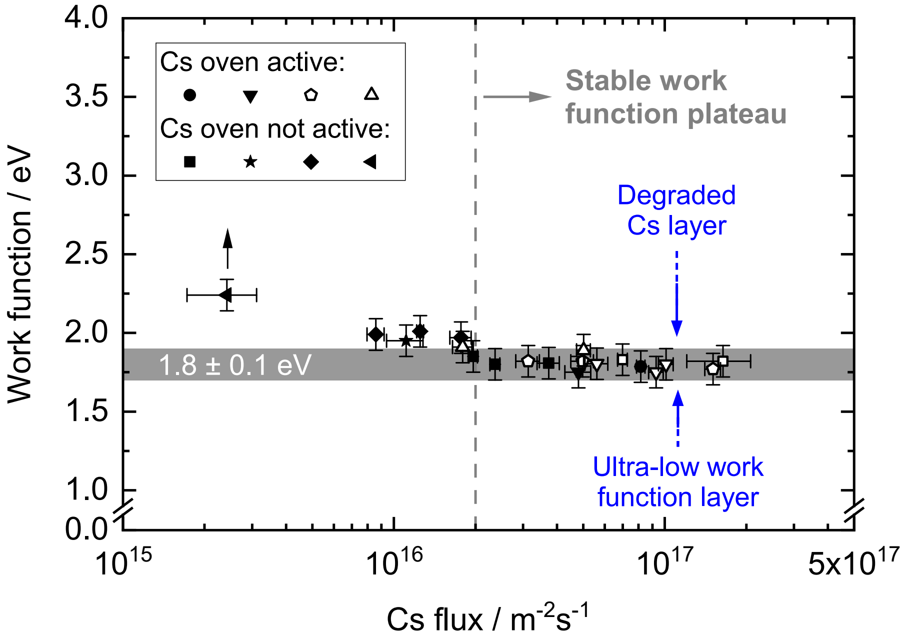

Figure 9.8: *Compilation of measured surface work functions after the application of hydrogen plasma pulses with a length of 30 min (open symbols) and 60 min (full symbols) as a function of the average neutral Cs flux during the plasma pulse.*

decreases (cf. figure 9.3).

When the Cs flux is $\lesssim 2 \times 10^{16}\,\mathrm{m^{-2}s^{-1}}$ during the plasma pulse, a work function > 1.8 eV is typically measured after a plasma exposure time of $30-60$ min. With a Cs flux of only $2.4 \times 10^{15}\,\mathrm{m^{-2}s^{-1}}$, an elevated work function of 2.25 eV is obtained. Moreover, it is known from [CFF20a] that the work function gradually increases further for plasma exposure times of several hours, which means that the Cs layer exhibiting the work function of 1.8 eV is gradually removed from the surface.

Deuterium plasma operation

As explained in section 2.3, a deterioration of the ion source performance is observed when the operational gas is changed from hydrogen to deuterium. In order to directly compare the work function performance in hydrogen and deuterium, experiments with alternating H_2 and D_2 plasma pulses are performed at ACCesS. Figure 9.9 presents an experimental run where 30 and 60 min plasma pulses are performed and the isotope is changed a few times. The measured surface work functions and neutral Cs densities are shown in the upper diagram and the temperature of the sample surface T_{surf} as well as the temperature of the Cs oven reservoir $T_{\mathrm{oven}}^{\mathrm{res.}}$ are plotted in the lower diagram. Before the first plasma pulse, the Cs evaporation is already running and a Cs density of $6 \times 10^{14}\,\mathrm{m^{-3}}$ is given in the

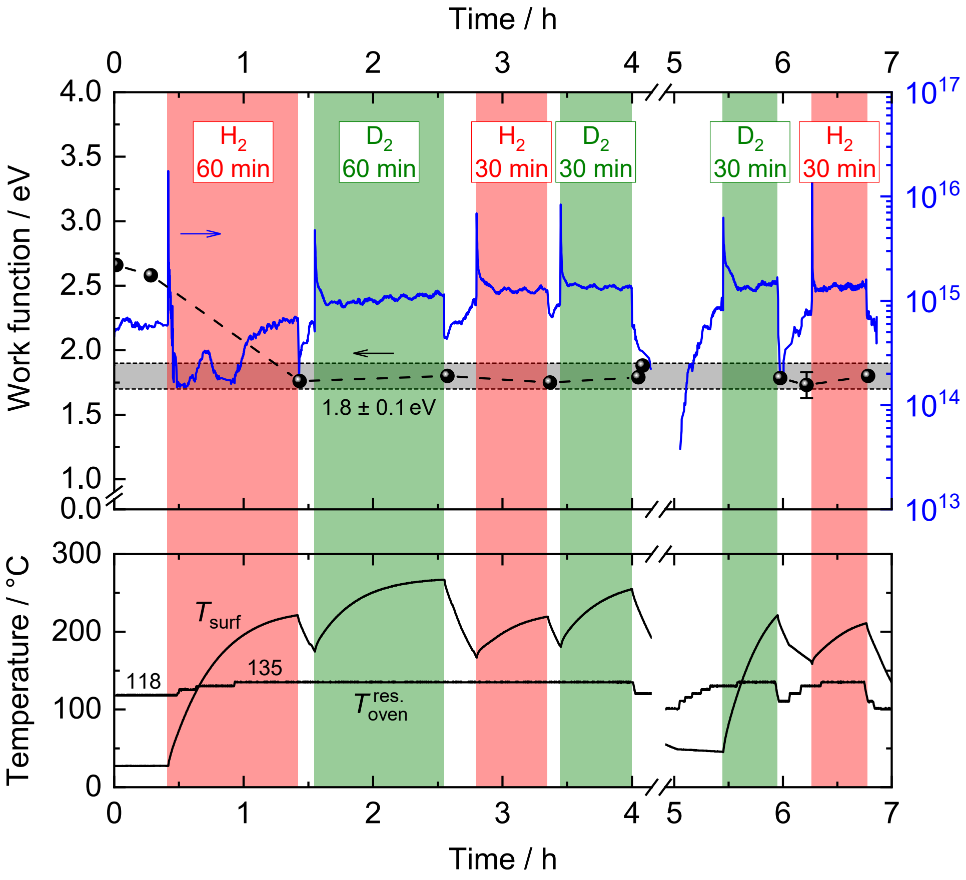

Figure 9.9: *Work function of a caesiated Mo surface after 30 and 60 min hydrogen and deuterium plasma pulses with continuous Cs evaporation. The hydrogen and deuterium plasma pulses are indicated by the red and green shaded areas, respectively. The applied Cs oven reservoir temperature* $T_{\text{oven}}^{\text{res.}}$ *and the temperature of the caesiated Mo surface* T_{surf} *are plotted in the lower diagram.*

vacuum phase with $T_{\text{oven}}^{\text{res.}} = 118\,°\text{C}$. The first plasma pulse is performed in hydrogen for a duration of 60 min. As can be seen, a strong Cs redistribution is driven within the first few seconds as the Cs density increases to values higher than $10^{16}\,\text{m}^{-3}$. After about 4 min, however, the Cs density has decreased to $\sim 10^{14}\,\text{m}^{-3}$, showing that the Cs reservoirs within the source are rather small and the Cs evaporation out of the oven is reduced in the plasma environment. To reach the same neutral Cs density as in the vacuum phase before plasma ignition, $T_{\text{oven}}^{\text{res.}}$ must be increased to 135 °C. During the 60 min H_2 plasma pulse, the caesiated Mo surface reaches a temperature of about 220 °C in maximum. Right after the plasma is switched off, a work function of 1.8 eV is measured, in accordance with figure 9.8. Subsequently, a 60 min D_2 plasma pulse is performed, followed by 30 min H_2 and D_2 plasma pulses. The series of plasma pulses shows that the Cs density in the first few seconds after plasma ignition is comparably high and virtually the same Cs density is reached in steady-state ($\sim 10^{15}\,\mathrm{m^{-3}}$). Hence, the Cs evaporation from the oven is not affected by changing the isotope and comparable Cs redistribution dynamics are present. In D_2 plasmas, the temperature increase of the caesiated Mo surface is more pronounced than in H_2 plasmas and a maximum temperature of about 270 °C is reached after the 60 min D_2 plasma pulse. Nevertheless, comparable work functions of about 1.8 eV are measured after each pulse, showing that the work function remains at a constant level and is independent of the isotope.

The compilation of work functions measured after 30 and 60 min hydrogen plasma pulses as a function of the neutral Cs flux during the plasma pulse in figure 9.8 is complemented in figure 9.10(a) by the corresponding results obtained

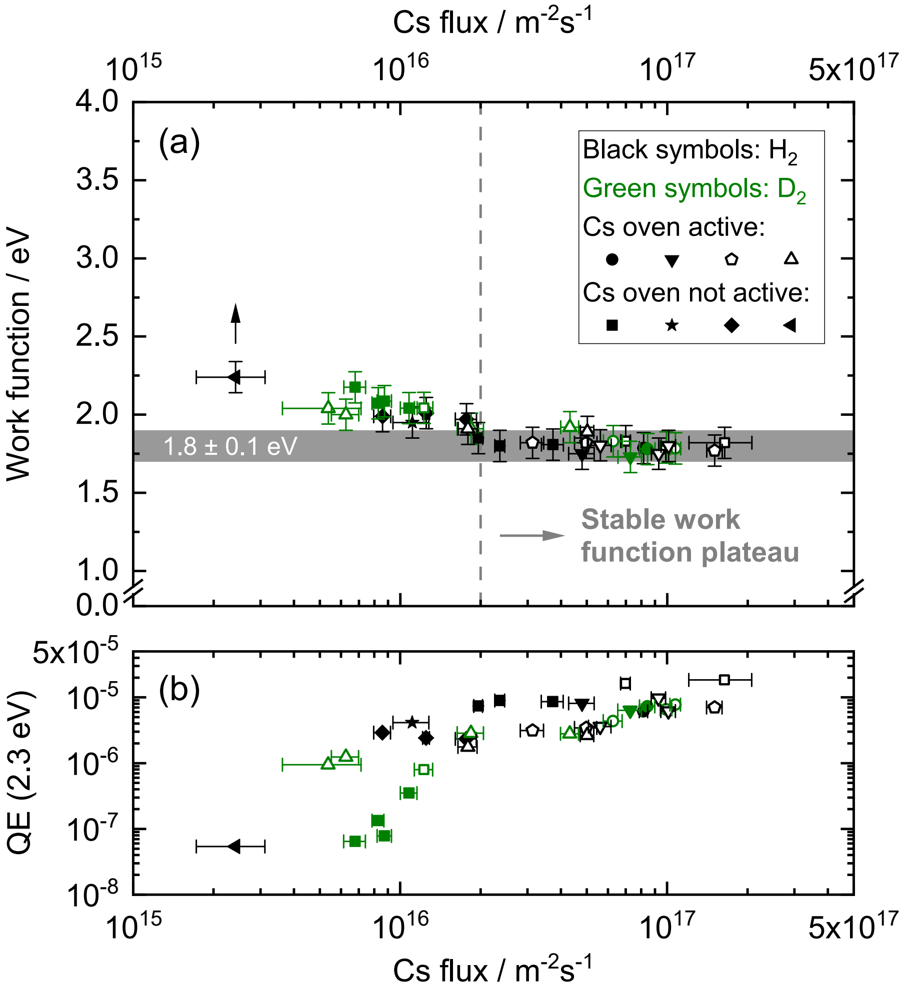

Figure 9.10: *(a) Compilation of measured surface work functions after the application of hydrogen and deuterium plasma pulses with a length of 30 min (open symbols) and 60 min (full symbols) as a function of the average neutral Cs flux during the plasma pulse. The corresponding QEs measured at 2.3 eV are depicted in (b).*

in deuterium. As can be seen, a work function in the range of $1.8 \pm 0.1\,\mathrm{eV}$ is reliably reached after deuterium plasma pulses for Cs fluxes $\gtrsim 2 \times 10^{16}\,\mathrm{m}^{-2}\mathrm{s}^{-1}$ ($n_{\mathrm{Cs}} \gtrsim 3 \times 10^{14}\,\mathrm{m}^{-3}$), which is in agreement with the results obtained in hydrogen. In figure 9.10(b), the corresponding QEs measured at 2.3 eV are supplementary depicted, showing that also comparable QE values are reached in hydrogen and deuterium. For Cs fluxes $\lesssim 2 \times 10^{16}\,\mathrm{m}^{-2}\mathrm{s}^{-1}$, a work function above the range of $1.8 \pm 0.1\,\mathrm{eV}$ is obtained, which is also in agreement with the results obtained in hydrogen. The increase of the work function with the reduced Cs fluxes is accompanied by a reduction of the QE.

9.5 Summary

The work function behavior of caesiated surfaces exposed to hydrogen and deuterium plasma pulses is generally found to be comparable, i. e., no isotopic differences are identified. The observed work function dynamics are illustrated in figure 9.11 (extending the initial figure 9.1) and are summarized as follows:

- Cs layers with work functions in the range of $1.25 \pm 0.10\,\mathrm{eV}$ are sustained upon plasma exposure times $\lesssim 1\,\mathrm{min}$. For longer plasma exposure times, the work function gradually increases above the range of $1.25 \pm 0.10\,\mathrm{eV}$, and a work function of about 1.7 eV is reached after 20 min. Hence, the chemical composition of the ultra-low work function surface undergoes considerable changes in a typical ion source plasma environment. As work functions in the range of $1.25 \pm 0.10\,\mathrm{eV}$ can be retrieved in the vacuum phase with sufficiently high Cs densities ($\sim 10^{15}\,\mathrm{m}^{-3}$), the plasma impact does not lead to irreversible effects.

- Concerning the reactivation of degraded Cs layers, a beneficial synergistic effect is identified by the application of short repetitive plasma pulses of the order of seconds in combination with continuous Cs evaporation. When the Cs density during the vacuum phases is sufficiently high ($\gtrsim 10^{15}\,\mathrm{m}^{-3}$), a work function of $1.25 \pm 0.10\,\mathrm{eV}$ is reliably retrieved. The reduction of the work function to the ultra-low regime is not observed upon re-caesiation without the application of plasma pulses nor by the application of plasma pulses without re-caesiation (minimum work function in both cases typically in the range of $1.9 - 2.1\,\mathrm{eV}$).

- For long plasma pulses $\geq 30\,\mathrm{min}$, a stable work function plateau of $1.8 \pm 0.1\,\mathrm{eV}$ is achieved when the neutral Cs density during the plasma phase is $\gtrsim 3 \times 10^{14}\,\mathrm{m}^{-3}$ (corresponding to a Cs flux of $\gtrsim 2 \times 10^{16}\,\mathrm{m}^{-2}\mathrm{s}^{-1}$). The equilibrium work function of 1.8 eV is independent of the initial work function in the vacuum phase, i. e., the work function gradually increases during long plasma pulses in the case the initial work function is in the ultra-low regime and gradually decreases in the case the Cs layer is degraded before the plasma exposure. For Cs densities (fluxes) $\lesssim 3\times10^{14}\,\mathrm{m}^{-3}$ ($\lesssim 2\times10^{16}\,\mathrm{m}^{-2}\mathrm{s}^{-1}$) during the plasma phase, the work function gets unstable and gradually increases.

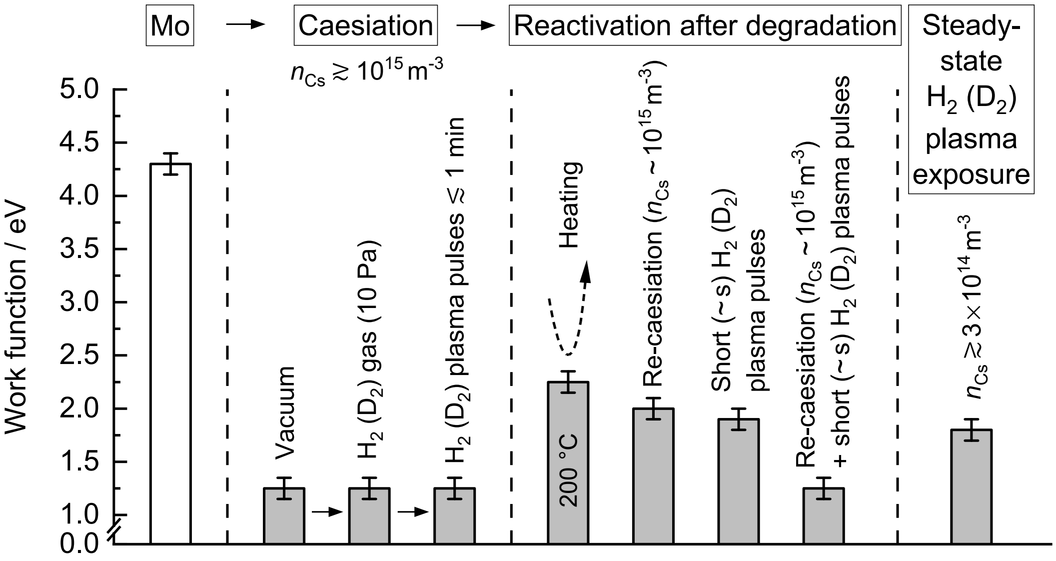

Figure 9.11: *Minimally achieved work functions of a Mo surface upon caesiation and the exposure to hydrogen (deuterium) plasma pulses, upon various reactivation scenarios for degraded Cs layers, and upon steady-state hydrogen (deuterium) plasma exposure.*

10 Conclusions for negative hydrogen ion sources

The conducted investigations on the work function dynamics of caesiated metal surfaces under non-UHV conditions and upon the exposure to particle and photon fluxes of hydrogen (deuterium) plasmas allow to draw valuable conclusions for Cs seeded negative hydrogen ion sources. The studies were in particular carried out with regard to negative hydrogen ion sources currently developed for NNBI systems for nuclear fusion, where the optimization of the Cs management is one of the most urgent and demanding tasks to achieve a temporally stable and reliable ion source performance.

Cs layer growth in the vacuum phase

The non-UHV conditions under which ion sources commonly operate were previously considered unfavorable for the caesiation of surfaces since the minimum achievable work function in the vacuum phase was determined to be 2.7 eV [FF17]. With the improved work function measurement setup, it has been unveiled that non-UHV conditions with H_2O being the dominant residual gas are highly beneficial for the caesiation process because Cs coatings with ultra-low work functions in the range of $1.25 \pm 0.10\,\mathrm{eV}$ can be generated. The work function of significantly below the one of bulk Cs ($2.0 - 2.1\,\mathrm{eV}$) is attributed to the formation of Cs oxides at the surface due to reactions between Cs and H_2O. The flux ratio $\Gamma_{\mathrm{Cs}}/\Gamma_{\mathrm{H_2O}}$ onto the surface is thus proposed as the figure of merit and must be $\gtrsim 0.005$ to achieve 1.25 eV. At the ion sources of the BUG and ELISE test facilities where operational scenarios for the ITER NNBI systems are developed, the flux ratio $\Gamma_{\mathrm{Cs}}/\Gamma_{\mathrm{H_2O}}$ is typically in the range of $0.003 - 0.009$ during the vacuum phases (Cs density $\sim 5 \times 10^{13}\,\mathrm{m}^{-3}$, base pressure $\sim 1 - 4 \times 10^{-7}\,\mathrm{mbar}$), which implies that the growth of ultra-low work function coatings can be expected on the extraction electrode (plasma grid).

Under UHV conditions, it is known from literature that the reachable work functions are in the range of $1.5 - 1.6\,\mathrm{eV}$ in the case of submonolayer coverages

($\sim 0.5 - 0.7$ ML) and in the range of $2.0 - 2.1$ eV for coverages $\gtrsim 1$ ML. Apart from the fact that the minimum work function lies above the range of 1.25 ± 0.10 eV, a Cs submonolayer coverage has the disadvantage that the work function is very sensitive to the surface condition of the substrate and that maintaining the optimum Cs coverage upon plasma exposure is challenging. With the presence of water vapor, Cs coatings with a work function of 1.25 eV can become several MLs in thickness because Cs compounds have a substantially lower vapor pressure than pure Cs, and the quality of the coating seems to be widely independent of the composition of the metal substrate. The possibility to prepare thick coatings in the vacuum phase is a valuable countermeasure for the plasma-induced removal of Cs (compounds) from the surface, especially with regard to long pulse operation of the ion sources.

Impact of impurity gases

As Cs exhibits a high chemical reactivity, it is important to understand which impact impurity gases that might leak into the vacuum system can have on the caesiation process and the work function of caesiated surfaces. The performed investigations have shown that elevated partial pressures of the inert gases Ar and N_2 do not have an adverse effect on the Cs content and the work function of caesiated surfaces, indicating that also He, which is formed in the fusion plasma and might enter the NNBI beamline, is not harmful to the caesiation process. Based on these results, the application of NEG pumps that are not able to pump noble gases is considered unproblematic for NNBI beamlines. However, it should be considered that ionized impurity gases with masses higher than hydrogen (deuterium) can strike the surface in the plasma phase with several eV so that higher Cs removal rates might be given due to an enhanced sputtering yield.

In contrast to inert gases, additional amounts of O_2 have a substantial impact on the caesiation process: Even small partial pressures of $\gtrsim 10^{-4}$ mbar lead to an instant depletion of the Cs density in the gas phase by several orders of magnitude, to a hindered Cs evaporation out of the oven and to an increase of the work function of the order of 1 eV, showing that strong chemical reactions between Cs and O_2 occur. The initial equilibrium can be regained after the O_2 inlet is terminated and the elevated O_2 content is pumped out (recovery time dependent on the totally entered amount of oxygen into the vacuum system), but an undesirable increase of the Cs consumption and a prolonged conditioning time of the ion source would be the result. Therefore, the leakage of O_2 into the ion source (e. g., via the gas supply system) must be avoided.

In the absence of Cs evaporation, the H_2O flux from the background pressure causes a gradual increase of the work function. At a pressure of $\sim 10^{-6}$ mbar, work functions in the range of $2.7 - 2.8$ eV are reached after one day and values higher than 3 eV are obtained after a few days. Hence, a severe passivation of the Cs layer occurs during operational breaks due to the non-UHV conditions. However, the passivation can fully be reversed by the application of an appropriate Cs conditioning procedure (see below).

Impact of elevated temperatures

Elevated surface temperatures are beneficial to counteract the degradation due to residual gases, and an optimum temperature of about 200 °C is identified to retrieve work functions in the range of $2.2 - 2.3$ eV in the vacuum phase without the evaporation of fresh Cs. For temperatures above 200 °C, a significant thermal desorption of Cs is observed, accompanied by an increase of the work function. At the test facilities BUG and ELISE, the optimum temperature of the plasma grid was determined empirically and comprises a rather broad range of $130 - 200$ °C. Recent experiments with plasma grid temperatures of up to 450 °C at BUG have shown that the source performance is strongly reduced for temperatures exceeding ~ 250 °C, i. e., a strong increase of co-extracted electrons and significant decrease of extracted negative ions is given [W$^+$22]. Even if the temperature dependence of the work function changes upon plasma exposure, the deterioration of the source performance for temperatures $\gtrsim 250$ °C is most probably attributed to an enhanced Cs desorption from the surface and an increase of the work function as observed at ACCesS in the vacuum phase. Since the plasma impact would lead to an increase of the plasma grid temperature to above 250 °C during long pulses, a temperature stabilized plasma grid is required so that a thermally induced work function increase is prevented and an enhanced Cs desorption that would increase the Cs consumption is suppressed.

Impact of hydrogen plasma species

An understanding of how hydrogen plasma species can affect the work function of caesiated surfaces is essential in the context of ion sources. While the work function is not affected in a hydrogen gas environment (tested up to 10 Pa), the selective exposure to VUV photons, hydrogen atoms and positive hydrogen ions has shown that the generated species in the plasma phase influence the work function considerably. In the case of degraded Cs layers with work functions

$\gtrsim 3\,\mathrm{eV}$, each plasma species can contribute to the reduction of the work function, and a minimum value of about 1.9 eV is retrieved. In contrast, an increase of the work function by some 0.1 eV is given when Cs layers with work functions in the range of $1.25 \pm 0.10\,\mathrm{eV}$ are exposed to VUV photons with energies up to 11 eV, indicating that Cs oxides at the surface are damaged. These results impressively demonstrate that impinging photons, atoms and ions can cause strong changes of the work function of caesiated surfaces so that photonic, atomic as well as ionic interactions must be considered in the plasma-surface interaction.

Cs conditioning procedure

Due to the passivation of caesiated surfaces in the absence of Cs evaporation, a Cs conditioning procedure is required after operational breaks to reduce the work function of the extraction electrode surface and to approach the optimum source performance. At present, the conditioning procedure at BUG and ELISE is performed by the application of repetitive plasma pulses of several seconds with continuous Cs evaporation into the source. In this work, it has been revealed that such a conditioning procedure leads to a reliable retrieval of work functions in the range of $1.25 \pm 0.10\,\mathrm{eV}$, provided that the surface is exposed to a flux ratio of $\Gamma_{\mathrm{Cs}}/\Gamma_{\mathrm{H_2O}} \gtrsim 0.005$ during the vacuum phases. Since the generation of such low work functions is not observed via re-caesiation without the application of plasma pulses nor via the application of plasma pulses without Cs evaporation (minimum work functions typically in the range of $1.9 - 2.1\,\mathrm{eV}$), the currently applied conditioning procedure is well suited to reliably optimize the work function of the plasma grid. As the flux ratio $\Gamma_{\mathrm{Cs}}/\Gamma_{\mathrm{H_2O}}$ is typically in the range of $0.003 - 0.009$ during the vacuum phases at BUG and ELISE, the generation of ultra-low work function layers can be expected during the Cs conditioning procedure. The achievable work function is thus significantly lower than the previously assumed value of 2.1 eV at optimum source performance.

Work function dynamics during long plasma pulses

Cs layers with a work function in the range of $1.25 \pm 0.10\,\mathrm{eV}$ withstand plasma pulse lengths of $\lesssim 1\,\mathrm{min}$. For longer plasma exposure times, however, a gradual increase of the work function is given and a value of about 1.7 eV is reached after 20 min. As it is expected that the work function of the plasma grid at BUG and ELISE is in the range of $1.25 \pm 0.10\,\mathrm{eV}$ at optimum source performance after the conditioning procedure, the ultra-low work function would explain the good performance during short pulses (several seconds) and at the beginning of long pulses [K+18]. The application of long pulses (several minutes up to one hour) is typically accompanied by a deterioration of the source performance over time, which shows up first by an increase of the co-extracted electron current before ultimately also the extracted negative ion current decreases [K+18, W+19a]. This temporal behavior could consequently be explained by the gradual increase of the work function above the ultra-low regime.

After the application of long pulses, the ion source performance is typically recovered within vacuum breaks of several minutes during which Cs is continuously evaporated [W+19a]. Since the plasma impact does not lead to irreversible effects and ultra-low work functions are retrieved during vacuum phases of several minutes provided that $\Gamma_{\mathrm{Cs}}/\Gamma_{\mathrm{H_2O}} \gtrsim 0.005$, the recovery of the ion source performance can be explained by the re-establishment of an ultra-low work function coating on the plasma grid. Consequently, the continuous evaporation of Cs onto the plasma grid during vacuum phases is highly beneficial for the preparation of long pulses.

Since Cs coatings with ultra-low work functions are not stable in the hydrogen plasma environment, a temporal increase of the plasma grid work function and the associated deterioration of the optimum source performance seem to be unavoidable during long plasma pulses. For plasma pulse lengths $\gtrsim 30\,\mathrm{min}$, a minimum work function of $1.8 \pm 0.1\,\mathrm{eV}$ is measured. This work function is reached independently of the initial work function in the vacuum phase, i. e., the work function gradually increases in the case the work function is in the ultra-low regime and gradually decreases in the case the Cs layer is degraded before the plasma exposure. In order to prevent an increase of the work function above 1.8 eV during steady-state plasma operation, a continuous Cs flux onto the surface is required. At ACCesS, the neutral Cs flux must be $\gtrsim 2 \times 10^{16}\,\mathrm{m^{-2}s^{-1}}$. At BUG and ELISE, the neutral Cs flux is typically a few $10^{16}\,\mathrm{m^{-2}s^{-1}}$ during the plasma phases [W+18a, M+18], but the threshold Cs flux to reach a temporally stable work function might be different from ACCesS. Possible reasons are different Cs redistribution dynamics (note that most of the Cs is ionized during plasma phases [M+18] so that effective Cs self-sputtering can occur [Wad18]) and the presence of higher fluxes of positive ions and VUV photons (see figure 9.2), which might lead to an enhanced removal of Cs (compounds) from the surface. Therefore, a transfer of quantitative work function values is not straightforward and work function measurements are required at the ion sources to determine the threshold Cs flux that is needed to provide a temporally stable work function of the plasma grid surface during long pulses.

Comparison between hydrogen and deuterium operation

When the operational gas is changed from hydrogen to deuterium at the ion sources, the co-extracted electron current is generally higher and rises more quickly than in hydrogen [W$^+$19b, F$^+$21a]. The reasons behind this isotope effect are not well understood yet, but a higher electron density in front of the plasma grid [WFN16], a different evolution of the electrostatic potential at the extraction apertures (investigated by particle-in-cell code modeling [M$^+$19, W$^+$21b]) and a changed work function behavior of the caesiated plasma grid might play a role. In order to investigate the latter, hydrogen and deuterium plasmas were alternately applied at ACCesS. However, no differences in the work function dynamics were found between hydrogen and deuterium operation, leading to the conclusion that there is no intrinsic isotope effect that prevents the generation of comparably low work function values.

Apart from the work function dynamics, also the Cs redistribution dynamics in hydrogen and deuterium plasmas are comparable at ACCesS. At the ion sources, however, a substantially higher neutral Cs density is measured in front of the plasma grid when the operational gas is changed from hydrogen to deuterium, with the Cs flux evaporated from the ovens remaining constant [W$^+$19b]. This shows that an enhanced plasma-induced Cs redistribution is driven in deuterium at the ion sources. The reason why an increased Cs redistribution in deuterium is not observed at ACCesS remains to be resolved, but changes in the evolution of the electrostatic potentials at the ion sources in combination with the higher mass of deuterium particles might lead to higher sputtering yields. Therefore, it is expected that a more effective removal of Cs (compounds) from the plasma grid is given, which would result in a faster increase of the work function beyond the ultra-low regime. Furthermore, it is expected that the Cs flux onto the plasma grid is insufficient to provide a temporally stable work function during long pulses, which means that measures for an enhancement of the Cs flux toward the plasma grid need to be identified.

Alternatives to Cs

As described in section 2.2, one of the most promising Cs-free alternatives for H^- (D^-) converter surfaces is the air-stable, mechanically robust and machinable C12A7 electride. The usage of a bulk material would facilitate the ion source operation considerably since the complex redistribution dynamics of Cs in the plasma phase is a major challenge for providing a homogeneous and temporally stable Cs layer on the large plasma grid. The investigations performed within the framework of this work have shown that the C12A7 electride is resilient to long-term plasma exposure and exhibits a temporally stable work function of $2.75 \pm 0.10\,\mathrm{eV}$ [H+21]. However, the work function of the C12A7 electride is about $1\,\mathrm{eV}$ higher than the minimum work function that is reached during steady-state plasma operation with caesiated surfaces. Consequently, the negative ion conversion yield via direct electron transfer from the surface is expected to be much smaller with the C12A7 electride than with caesiated surfaces. For a final conclusion on the C12A7 electride as potential Cs-free alternative, however, an implementation at a test facility with extraction system is required in order to investigate the behavior of the extracted ion and co-extracted electron currents.

Outlook

Based on the achieved results within this work, further investigations are proposed that would extend the understanding of the properties of caesiated surfaces under ion source conditions and would thus support the optimization of the Cs management:

- The background pressure in present-day ion sources ranges from about 10^{-10} to $10^{-6}\,\mathrm{mbar}$ depending on the application. In the case of the ITER ion sources, the envisaged background pressure is $\sim 10^{-8}\,\mathrm{mbar}$. Therefore, systematic investigations on the Cs layer growth in a vacuum environment ranging from $10^{-6}\,\mathrm{mbar}$ to the UHV regime ($\lesssim 10^{-9}\,\mathrm{mbar}$) are required and the consequences on the Cs conditioning procedure and the temporal work function dynamics upon plasma exposure need to be identified. A lower background pressure might be beneficial regarding the Cs consumption and degradation dynamics, but could also prevent the growth of thick Cs layers with work functions in the ultra-low regime.

- The investigations on the influence of VUV photons, hydrogen atoms and positive hydrogen ions on caesiated surfaces were performed with fluxes significantly lower than the ones impinging onto the plasma grid at the ion sources. The undesired removal of Cs from the surface (and the associated increase of the work function at some point) was not observed with the applied fluxes. Hence, investigations with increased fluxes should be performed with the aim to identify the driving mechanisms leading to the Cs removal, which is necessary for the identification of possible countermeasures.

- The application of in situ/operando surface analysis techniques is advisable in order to gain insights into the chemical composition and stoichiometry of caesiated surfaces. An investigation of the chemical composition of the Cs layer in the vacuum phase (with different background pressures) and upon hydrogen (deuterium) plasma exposure would significantly advance the understanding of the occurring surface chemistry. Suitable diagnostics would be thermal desorption spectroscopy, Auger electron spectroscopy and X-ray photoelectron spectroscopy.

- To correlate the work function of the extraction electrode with extracted negative ion and co-extracted electron currents, work function measurements should be performed directly at the ion sources. Triggered by the results obtained within this work, a photoelectric work function measurement system for ion sources has been developed and recently installed at BUG, and first preliminary measurements have confirmed that work functions in the ultra-low regime are reached during the Cs conditioning procedure. Further systematic investigations during the caesiation process in vacuum and with short and long plasma pulses both in hydrogen and deuterium are required to assess the work function performance of the caesiated plasma grid in more detail.

- Depending on the operational scenario, the QE of caesiated surfaces can be orders of magnitude different, even for comparable work functions. Since the QE is expected to be correlated with the electron density of the surface, it might be a decisive parameter for the surface production yield of negative hydrogen ions. In addition, the QE determines the amount of photoelectrically released electrons upon irradiation with photons from the plasma. Therefore, it should be analyzed in future studies to what extent the QE has an impact on the extracted negative ion and co-extracted electron currents.

Bibliography

[ABZ14] M. Akbi, A. Bouchou, and N. Zouache, *Effects of vacuum heat treatment on the photoelectric work function and surface morphology of multilayered silver–metal electrical contacts*, Appl. Surf. Sci. **303** (2014), 131.

[Alt86] G. D. Alton, *Semi-empirical mathematical relationships for electropositive adsorbate induced work function changes*, Surf. Sci. **175** (1986), 226.

[AM89] T. Aruga and Y. Murata, *Alkali-metal adsorption on metals*, Prog. Surf. Sci. **31** (1989), 61.

[B$^+$04] A. Band et al., *Characterization of Oxides of Cesium*, J. Phys. Chem. B **108** (2004), 12360.

[B$^+$21] M. Boldrin et al., *1 MV power supplies integration issues in MITICA experiment, the ITER Heating Neutral Beam Injector prototype*, Fus. Eng. Des. **164** (2021), 112170.

[BČS20] T. Bučko, I. Černušák, and H. Said, *Final Report on Deliverable Computational Modelling of Cs-Mo interactions in NBI sources*, 2020, EUROfusion.

[BDD74] Y. I. Belchenko, G. I. Dimov, and V. G. Dudnikov, *A powerful injector of neutrals with a surface-plasma source of negative ions*, Nucl. Fusion **14** (1974), 113.

[Beh91] K. Behringer, *Diagnostics and modelling of ECRH microwave discharges*, Plasma Phys. Control. Fusion **33** (1991), 997.

[BF94] K. Behringer and U. Fantz, *Spectroscopic diagnostics of glow discharge plasmas with non-Maxwellian electron energy distributions*, J. Phys. D: Appl. Phys. **27** (1994), 2128.

[BF18] S. Briefi and U. Fantz, *Spectroscopic investigations of the ion source at BATMAN upgrade*, AIP Conf. Proc. **2052** (2018), 040005.

[BF20] ———, *A revised comprehensive approach for determining the H_2 and D_2 rovibrational population from the Fulcher-α emission in low temperature plasmas*, Plasma Sources Sci. Technol. **29** (2020), 125019.

[BN81] R. Brako and D. M. Newns, *Charge exchange in atom-surface scattering: Thermal versus quantum mechanical non-adiabaticity*, Surf. Sci. **108** (1981), 253.

[BNH76] A. Blandin, A. Nourtier, and D. W. Hone, *Localized time-dependent perturbations in metals : formalism and simple examples*, J. Phys. **37** (1976), 369.

[Boh80] J. Bohdansky, *Important sputtering yield data for tokamaks: A comparison of measurements and estimates*, J. Nucl. Mater. **93-94** (1980), 44.

[Bon88] H. P. Bonzel, *Alkali-metal-affected adsorption of molecules on metal surfaces*, Surf. Sci. Rep. **8** (1988), 43.

[BPR91] H. P. Bonzel, G. Pirug, and C. Ritke, *Adsorption of H_2O on Alkali-Metal-Covered Pt(111) and Ru(001): A Systematic Comparison*, Langmuir **7** (1991), 3006.

[BPS75] K. H. Berkner, R. V. Pyle, and J. W. Stearns, *Intense, mixed-energy hydrogen beams for CTR injection*, Nucl. Fusion **15** (1975), 249.

[Bra78] G. Brauer, *Handbuch der Präparativen Anorganischen Chemie*, 3rd ed., Vol. 2, F. Enke Verlag, Stuttgart, Germany, 1978.

[BS64] C. N. Berglund and W. E. Spicer, *Photoemission Studies of Copper and Silver: Experiment*, Phys. Rev. **136** (1964), A1044.

[BS66] A. J. Blodgett and W. E. Spicer, *Experimental Determination of the Density of States in Nickel*, Phys. Rev. **146** (1966), 390.

[BS77] T. R. Briere and A. H. Sommer, *Low-work-function surfaces produced by cesium carbonate decomposition*, J. Appl. Phys. **48** (1977), 3547.

[BW15] M. Bacal and M. Wada, *Negative hydrogen ion production mechanisms*, Appl. Phys. Rev. **2** (2015), 021305.

[BW20] ———, *Negative ion source operation with deuterium*, Plasma Sources Sci. Technol. **29** (2020), 033001.

[C⁺01] R. Celiberto et al., *Cross section data for electron-impact inelastic processes of vibrationally excited molecules of hydrogen and its isotopes*, At. Data Nucl. Data Tables **77** (2001), 161.

[C⁺10] A. Chakraborty et al., *Diagnostic Neutral Beam for ITER-Concept to Engineering*, IEEE Trans. Plasma Sci. **38** (2010), 248.

[C⁺12] S. H. Chou et al., *An orbital-overlap model for minimal work functions of cesiated metal surfaces*, J. Phys.: Condens. Matter **24** (2012), 445007.

[C⁺14] X. Chen et al., *Effect of Cs adsorption on the photoemission performance of GaAlAs photocathode*, Appl. Opt. **53** (2014), 7709.

[C⁺19] S. Cristofaro et al., *Design and comparison of the Cs ovens for the test facilities ELISE and SPIDER*, Rev. Sci. Instrum. **90** (2019), 113504.

[CB11] P. Chabert and N. Braithwaite, *Physics of Radio-Frequency Plasma*, Cambridge University Press, Cambridge, 2011.

[CC03] F. F. Chen and J. P. Chang, *Lecture Notes on Principles of Plasma Processing*, Springer, New York, 2003.

[CCF84] Y. C. Chen, J. E. Cunningham, and C. P. Flynn, *Dependence of rare-gas-adsorbate dipole moment on substrate work function*, Phys. Rev. B **30** (1984), 7317.

[CF72] R. P. Clow and J. H. Futrell, *Ion-molecule reactions in isotopic hydrogen by ion cyclotron resonance*, Int. J. Mass Spectrom. Ion Phys. **8** (1972), 119.

[CFF17] S. Cristofaro, R. Friedl, and U. Fantz, *Simultaneous measurements of work function and* H^- *density including caesiation of a converter surface*, AIP Conf. Proc. **1869** (2017), 030036.

[CFF20a] ———, *Correlation of Cs flux and work function of a converter surface during long plasma exposure for negative ion sources in view of ITER*, Plasma Res. Express **2** (2020), 035009.

[CFF20b] ______, *Effect of a low pressure low temperature hydrogen plasma on the work function of europium*, J. Vac. Sci. Technol. A. **38** (2020), 063002.

[CFF21] ______, *Negative Hydrogen and Deuterium Ion Density in a Low Pressure Plasma in Front of a Converter Surface at Different Work Functions*, Plasma **4** (2021), 94.

[Che01] F. F. Chen, *Langmuir probe analysis for high density plasmas*, Phys. Plasmas **8** (2001), 3029.

[Cri18] S. Cristofaro, *Work function of caesiated surfaces in H_2/D_2 low temperature plasmas correlated with negative ion formation*, Ph.D. thesis, University of Augsburg, 2018.

[Dan81] L. R. Danielson, *Coadsorption of cesium and oxygen on iridium and lanthanum hexaboride*, J. Appl. Phys. **52** (1981), 300.

[Dav57] J. E. Davey, *Thermionic and Semiconducting Properties of [Ag]-Cs_2O, Ag, Cs*, J. Appl. Phys. **28** (1957), 1031.

[Des83] J.-L. Desplat, *Work function of Mo(110) in mixed cesium and cesium monoxide vapors*, J. Appl. Phys. **54** (1983), 5494.

[Die72] G. H. Dieke, *The Hydrogen Molecule Wavelength Tables of Gerhard Heinrich Dieke*, Crosswhite, H. M.Wiley-Interscience, New York, 1972.

[DM96] R. D. Diehl and R McGrath, *Structural studies of alkali metal adsorption and coadsorption on metal surfaces*, Surf. Sci. Rep. **23** (1996), 43.

[DM97] R. D. Diehl and R. McGrath, *Current progress in understanding alkali metal adsorption on metal surfaces*, J. Phys.: Condens. Matter **9** (1997), 951.

[DP80] J.-L. Desplat and C. A. Papageorgopoulos, *Interaction of cesium and oxygen on W(110): I. Cesium adsorption on oxygenated and oxidized W(110)*, Surf. Sci. **92** (1980), 97.

[DR32] L. A. DuBridge and W. W. Roehr, *Photoelectric and Thermionic Properties of Palladium*, Phys. Rev. **39** (1932), 99.

[Dru30] M. J. Druyvesteyn, *Der Niedervoltbogen*, Z. Phys. **64** (1930), 781.

[DuB32] L. A. DuBridge, *A Further Experimental Test of Fowler's Theory of Photoelectric Emission*, Phys. Rev. **39** (1932), 108.

[DuB48] ———, *Electron Emission from Metal Surfaces*, Am. J. Phys. **16** (1948), 191.

[Dud72] V. Dudnikov, 1972, SU Patent No. 411542, Application C1.H013/04.

[Ebe60] A. Eberhagen, *Die Änderung der Austrittsarbeit von Metallen durch eine Gasadsorption*, Fortschr. Phys. **8** (1960), 245.

[ES79] G. Ebbinghaus and A. Simon, *Electronic structure of Rb, Cs and some of their metallic oxides studied by photoelectron spectroscopy*, Chem. Phys. **43** (1979), 117.

[EVKP87] M.-L. Ernst-Vidalis, M. Kamaratos, and C. Papageorgopoulos, *The effects of Cs on the adsorption of H_2 on Mo(110)*, Surf. Sci. **189-190** (1987), 276.

[F^+96] U. Flender et al., *RF harmonic suppression in Langmuir probe measurements in RF discharges*, Plasma Sources Sci. Technol. **5** (1996), 61.

[F^+17a] U. Fantz et al., *Towards powerful negative ion beams at the test facility ELISE for the ITER and DEMO NBI systems*, Nucl. Fusion **57** (2017), 116007.

[F^+17b] C. Feng et al., *Comparison of degradation and recaesiation between GaAs and AlGaAs photocathodes in an unbaked vacuum system*, Appl. Opt. **56** (2017), 2568.

[F^+18] U. Fantz et al., *Technology developments for a beam source of an NNBI system for DEMO*, Fusion Eng. Des. **136** (2018), 340.

[F^+19a] ———, *Advanced NBI beam characterization capabilities at the recently improved test facility BATMAN Upgrade*, Fusion Eng. Des. **146** (2019), 212.

[F^+19b] G. Federici et al., *Overview of the DEMO staged design approach in Europe*, Nucl. Fusion **59** (2019), 066013.

[F^+20] U. Fantz et al., *Achievement of the ITER NBI ion source parameters for hydrogen at the test facility ELISE and present status for deuterium*, Fusion Eng. Des. **156** (2020), 111609.

[F^+21a] ———, *Negative Hydrogen Ion Sources for Fusion: From Plasma Generation to Beam Properties*, Front. Phys. **9** (2021), 709651.

[F^+21b] G. Federici et al., *The EU DEMO staged design approach in the Pre-Concept Design Phase*, Fus. Eng. Des. **173** (2021), 112959.

[F^+22] U. Fantz et al., *Ion source developments at IPP: On the road towards achieving the ITER-NBI targets and preparing concepts for DEMO*, J. Phys.: Conf. Ser. **2244** (2022), 012049.

[Fan06] U. Fantz, *Basics of plasma spectroscopy*, Plasma Sources Sci. Technol. **15** (2006), S137.

[FB^+21] C. Fröhler-Bachus et al., *Absolute radiometric calibration of a VUV spectrometer in the wavelength range 46–300 nm*, J. Quant. Spectrosc. Radiat. Transfer **259** (2021), 107427.

[FB22] C. Fröhler-Bachus, *A portable diagnostic tool for the absolute determination of photon fluxes in low pressure plasmas down to the VUV region*, Ph.D. thesis, University of Augsburg, 2022.

[FCF18] R. Friedl, S. Cristofaro, and U. Fantz, *Work function of Cs-free materials for enhanced H^- surface production*, AIP Conf. Proc. **2011** (2018), 050009.

[FF15] R. Friedl and U. Fantz, *Temperature dependence of the work function of caesiated materials under ion source conditions*, AIP Conf. Proc. **1655** (2015), 020004.

[FF17] ———, *Influence of H_2 and D_2 plasmas on the work function of caesiated materials*, J. Appl. Phys. **122** (2017), 083304.

[FFBF22] R. Friedl, C. Fröhler-Bachus, and U. Fantz, *A portable diagnostic system for the quantification of VUV fluxes emitted from low-temperature plasmas*, 2022, in press `https://doi.org/10.1088/1361-6501/acab23`.

[FGW10] U. Fantz, R. Gutser, and C. Wimmer, *Fundamental experiments on evaporation of cesium in ion sources*, Rev. Sci. Instrum. **81** (2010), 02B102.

[FL18a] D. Faircloth and S. Lawrie, *An overview of negative hydrogen ion sources for accelerators*, New J. Phys. **20** (2018), 025007.

[FL18b] U. Fantz and J. Lettry, *Focus on sources of negatively charged ions*, New J. Phys. **20** (2018), 060201.

[FO72] T. A. Flaim and P. D. Ownby, *Adsorbate-induced work function changes*, Surf. Sci. **32** (1972), 519.

[Fow31] R. H. Fowler, *The Analysis of Photoelectric Sensitivity Curves for Clean Metals at Various Temperatures*, Phys. Rev. **38** (1931), 45.

[Fri13] R. Friedl, *Experimental investigations on the caesium dynamics in H_2/D_2 low temperature plasmas*, Ph.D. thesis, University of Augsburg, 2013.

[Fri16] ———, *Enhancing the accuracy of the Fowler method for monitoring non-constant work functions*, Rev. Sci. Instrum. **87** (2016), 043901.

[FSC85] R. S. Freund, J. A. Schiavone, and H. M. Crosswhite, *The Electronic Spectrum and Energy Levels of the Deuterium Molecule*, J. Phys. Chem. Ref. Data **14** (1985), 235.

[FW06] U. Fantz and D. Wünderlich, *Franck-Condon factors, transition probabilities, and radiative lifetimes for hydrogen molecules and their isotopomeres*, At. Data Nucl. Data Tables **92** (2006), 853.

[FW11] U. Fantz and C. Wimmer, *Optimizing the laser absorption technique for quantification of caesium densities in negative hydrogen ion sources*, J. Phys. D: Appl. Phys. **44** (2011), 335202.

[FW12] ———, *Cesium dynamics in long pulse operation of negative hydrogen ion sources for fusion*, Rev. Sci. Instrum. **83** (2012), 02B110.

[G^+59] M. Green et al., *Recombination of atoms at surfaces. Part 7.-Hydrogen atoms at silica and other similar surfaces*, Trans. Faraday Soc. **55** (1959), 2152.

[G$^+$75] P. E. Gregory et al., *The oxidation of Cs-uv photoemission studies*, J. Appl. Phys. **46** (1975), 3525.

[GD11] V. A. Godyak and V. I. Demidov, *Probe measurements of electron-energy distributions in plasmas: what can we measure and how can we achieve reliable results?*, J. Phys. D: Appl. Phys. **44** (2011), 233001.

[GM18] R. Gross and A. Marx, *Festkörperphysik*, 3rd ed., De Gruyter, Berlin, Boston, 2018.

[GMS95] V. A. Godyak, V. P. Meytlis, and H. R. Strauss, *Tonks-Langmuir problem for a bi-Maxwellian plasma*, IEEE Trans. Plasma Sci. **23** (1995), 728.

[GWF11] R. Gutser, C. Wimmer, and U. Fantz, *Work function measurements during plasma exposition at conditions relevant in negative ion sources for the ITER neutral beam injection*, Rev. Sci. Instrum. **82** (2011), 023506.

[H$^+$09] B. Heinemann et al., *Design of the "half-size" ITER neutral beam source for the test facility ELISE*, Fusion Eng. Des. **84** (2009), 915.

[H$^+$15] H. Hosono et al., *Superconductivity in room-temperature stable electride and high-pressure phases of alkali metals*, Phil. Trans. R. Soc. A **373** (2015), 20140450.

[H$^+$17a] B. Heinemann et al., *Towards large and powerful radio frequency driven negative ion sources for fusion*, New J. Phys. **19** (2017), 015001.

[H$^+$17b] R. S. Hemsworth et al., *Overview of the design of the ITER heating neutral beam injectors*, New J. Phys. **19** (2017), 025005.

[H$^+$21] A. Heiler et al., *Work function performance of a C12A7 electride surface exposed to low pressure low temperature hydrogen plasmas*, J. Vac. Sci. Technol. A **39** (2021), 013002.

[Hen02] M. A. Henderson, *The interaction of water with solid surfaces: fundamental aspects revisited*, Surf. Sci. Rep. **46** (2002), 1.

[Her50] G. Herzberg, *Molecular Spectra and Molecular Structure, I. Spectra of Diatomic Molecules*, 2nd ed., D. Van Nostrand Company, New York, 1950.

[HFF20] A. Heiler, R. Friedl, and U. Fantz, *Application of a Langmuir probe AC technique for reliable access to the low energy range of electron energy distribution functions in low pressure plasmas*, J. Appl. Phys. **127** (2020), 113302.

[HFF22] ———, *Impact of the photoelectric threshold sensitivity on the work function determination—Revealing ultra-low work functions of caesiated surfaces*, AIP Adv. **12** (2022), 035339.

[Hos04] H. Hosono, *Functioning of traditional ceramics $12CaO{\cdot}7Al_2O_3$ utilizing built-in nano-porous structure*, Sci. Technol. Adv. Mater. **5** (2004), 409.

[I$^+$20] E. J. Iglesias et al., *Ultraviolet/vacuum-ultraviolet emission from a high power magnetron sputtering plasma with an aluminum target*, J. Phys. D: Appl. Phys. **53** (2020), 055202.

[IAE02] IAEA, *ITER Technical Basis*, ITER EDA documentation series 24, International Atomic Energy Agency, Vienna, 2002.

[IKS92] J. D. Isenberg, H. J. Kwon, and M. Seidl, *Surface production of H^- ions by backscattering of H^+ and H_2^+ ions in the $3-50$ eV ion energy range*, AIP Conf. Proc. **287** (1992), 38.

[Ish18] H. Ishii, *Photoelectron Yield Spectroscopy, In: Compendium of Surface and Interface Analysis*, p. 457, Springer, Singapore, 2018.

[ITE22] ITER website, `https://www.iter.org`, accessed on August, 2022.

[JRS03] R. K. Janev, D. Reiter, and U. Samm, *Collision Processes in Low-Temperature Hydrogen Plasmas*, Berichte des Forschungszentrums Jülich JUEL-4105, Forschungszentrum Jülich, 2003.

[K$^+$05] Y. Kudriavtsev et al., *Calculation of the surface binding energy for ion sputtered particles*, Appl. Surf. Sci. **239** (2005), 273.

[K$^+$07a] K.-B. Kim et al., *Photoelectron Spectroscopic Study of C12A7:e^- and Alq_3 Interface: The Formation of a Low Electron-Injection Barrier*, J. Phys. Chem. C **111** (2007), 8403.

[K$^+$07b] S.-W. Kim et al., *Fabrication of room temperature-stable $12CaO{\cdot}7Al_2O_3$ electride: a review*, J. Mater. Sci. Mater. Electron. **18** (2007), 5.

[K+07c] S. W. Kim et al., *Metallic State in a Lime-Alumina Compound with Nanoporous Structure*, Nano Lett. **7** (2007), 1138.

[K+17] D. Kuwahara et al., *Study of negative hydrogen ion production at low work function material surface using a hydrogen atom source*, AIP Conf. Proc. **1869** (2017), 020009.

[K+18] W. Kraus et al., *Deuterium results at the negative ion source test facility ELISE*, Rev. Sci. Instrum. **89** (2018), 052102.

[K+22] A. Kramida et al., *NIST Atomic Spectra Database (ver. 5.9)*, National Institute of Standards and Technology, Gaithersburg, MD., `https://physics.nist.gov/asd`, 2022.

[KB91] Y. C. Kim and M. Boudart, *Recombination of oxygen, nitrogen, and hydrogen atoms on silica: kinetics and mechanism*, Langmuir **7** (1991), 2999.

[KFF17] U. Kurutz, R. Friedl, and U. Fantz, *Investigations on Cs-free alternatives for negative ion formation in a low pressure hydrogen discharge at ion source relevant parameters*, Plasma Phys. Control. Fusion **59** (2017), 075008.

[KH06] A. Krylov and R. S. Hemsworth, *Gas flow and related beam losses in the ITER neutral beam injector*, Fusion Eng. Des. **81** (2006), 2239.

[KH12] S. W. Kim and H. Hosono, *Synthesis and properties of* $12CaO\cdot 7Al_2O_3$ *electride: review of single crystal and thin film growth*, Philos. Mag. **92** (2012), 2596.

[KNN71] M. M. Kirillova, L. V. Nomerovannaya, and M. M. Noskov, *Optical properties of molybdenum single crystals*, Sov. Phys. JETP **33** (1971), 1210.

[Kun09] H.-J. Kunze, *Introduction to Plasma Spectroscopy*, Springer, Berlin, Heidelberg, 2009.

[L+89] D. Lackey et al., *Water adsorption on clean and caesium covered Cu{110}*, J. Chem. Phys. **91** (1989), 1365.

[L+17] J. Laulainen et al., *Hydrogen plasma induced photoelectron emission from low work function cesium covered metal surfaces*, Phys. Plasmas **24** (2017), 103502.

[Lin17] M. Lindauer, *Laserabsorptionsspektroskopie zur Quantifizierung der Caesiumdichte in Gasphase und im Plasma*, Fachpraktikumsarbeit, University of Augsburg, 2017.

[LL05] M. A. Lieberman and A. J. Lichtenberg, *Principles of Plasma Discharges and Materials Processing*, 2nd ed., John Wiley & Sons, Hoboken, NJ, 2005.

[LM22] P. J. Linstrom and W. G. Mallard (eds.), *NIST Chemistry WebBook, NIST Standard Reference Database Number 69*, National Institute of Standards and Technology, Gaithersburg MD, 20899, `https://doi.org/10.18434/T4D303`, 2022.

[M^+03] S. Matsuishi et al., *High-Density Electron Anions in a Nanoporous Single Crystal: $[Ca_{24}Al_{28}O_{64}]^{4+}(4e^-)$*, Science **301** (2003), 626.

[M^+06] I. Méndez et al., *Atom and Ion Chemistry in Low Pressure Hydrogen DC Plasmas*, J. Phys. Chem. A **110** (2006), 6060.

[M^+09] P. McNeely et al., *A Langmuir probe system for high power RF-driven negative ion sources on high potential*, Plasma Sources Sci. Technol. **18** (2009), 014011.

[M^+11] A. Masiello et al., *The European contribution to the development of the ITER NB injector*, Fus. Eng. Des. **86** (2011), 860.

[M^+17] A. Mimo et al., *Modelling of caesium dynamics in the negative ion sources at BATMAN and ELISE*, AIP Conf. Proc. **1869** (2017), 030019.

[M^+18] ———, *Studies of Cs dynamics in large ion sources using the CsFlow3D code*, AIP Conf. Proc. **2052** (2018), 040009.

[M^+19] I. M. Montellano et al., *3D-PIC modelling of a low temperature plasma sheath with wall emission of negative particles and its application to NBI sources*, J. Phys. D: Appl. Phys. **52** (2019), 235202.

[McW97] J. D. McWhirter, *Extinction coefficient and skin depth of alkali metals from 10 to 1000 nm*, Opt. Lasers Eng. **28** (1997), 305.

[MDZ99] M. Mozetič, M. Drobnič, and A. Zalar, *Recombination of neutral hydrogen atoms on AISI 304 stainless steel surface*, Appl. Surf. Sci. **144-145** (1999), 399.

[Mic77] H. B. Michaelson, *The work function of the elements and its periodicity*, J. Appl. Phys. **48** (1977), 4729.

[Mim18] A. Mimo, *Optimization of Caesium Dynamics in Large and Powerful RF Sources for Negative Hydrogen Ions*, Ph.D. thesis, University of Augsburg, 2018.

[MM71] G. A. Melin and R. J. Madix, *Energy accommodation during hydrogen atom recombination on metal surfaces*, Trans. Faraday Soc. **67** (1971), 2711.

[Möl93] W. Möller, *Plasma and Surface Modeling of the Deposition of Hydrogenated Carbon Films from Low-Pressure Methane Plasmas*, Appl. Phys. A **56** (1993), 527.

[MS91] S. T. Melnychuk and M. Seidl, *Reflection of hydrogen atoms from alkali and alkaline earth oxide surfaces*, J. Vac. Sci. Technol. A **9** (1991), 1650.

[MS10] P. McNeely and L. Schiesko, *Investigation of fringe plasma parameters on a high power rf driven ion source*, Rev. Sci. Instrum. **81** (2010), 02B111.

[MSL26] H. M. Mott-Smith and I. Langmuir, *The Theory of Collectors in Gaseous Discharges*, Phys. Rev. **28** (1926), 727.

[NK07] S. Nunomura and M. Kondo, *Characterization of high-pressure capacitively coupled hydrogen plasmas*, J. Appl. Phys. **102** (2007), 093306.

[NL79] J. K. Nørskov and B. I. Lundqvist, *Secondary-ion emission probability in sputtering*, Phys. Rev. B **19** (1979), 5661.

[OHS19] P.-V. Ong, H. Hosono, and P. V. Sushko, *Structure and Electronic Properties of* $[Ca_{24}Al_{28}O_{64}]^{4+}\cdot 4e^{-}$ *Surfaces: Opportunities for Termination-Controlled Electron Transfer*, J. Phys. Chem. C **123** (2019), 6030.

[Oka10] H. Okamoto, *Cs-O (Cesium-Oxygen)*, J. Phase Equilib. Diffus. **31** (2010), 86.

[Pap82] C. A. Papageorgopoulos, *Studies of separate adsorption and coadsorption of Cs and* O_2 *on Cu(100)*, Phys. Rev. B **25** (1982), 3740.

[PC73] C. A. Papageorgopoulos and J. M. Chen, *Coadsorption of electropositive and electronegative elements: II. Cs and O_2 on W (100)*, Surf. Sci. **39** (1973), 313.

[PDS95] S. Preuss, A. Demchuk, and M. Stuke, *Sub-picosecond UV laser ablation of metals*, Appl. Phys. A **61** (1995), 33.

[Phe22] Phelps database, `https://www.lxcat.net`, retrieved on February 28, 2022.

[PRB91] G. Pirug, C. Ritke, and H. P. Bonzel, *Adsorption of H_2O on Ru(001): II. Effect of coadsorbed alkali metals (Na, K, Cs)*, Surf. Sci. **257** (1991), 50.

[PV71] I. Petroff and C. R. Viswanathan, *Calculation of Density of States in W, Ta, and Mo*, Nat. Bur. Stand. (U.S.), Spec. Publ. **323** (1971), 53.

[Rau18] D. Rauner, *Efficiency of RF plasma generation for fusion relevant ion sources*, Ph.D. thesis, University of Augsburg, 2018.

[RG65] B. S. Rump and B. L. Gehman, *Work Function Measurements of Nickel, Molybdenum, and Tungsten in a Cesium-Hydrogen Atmosphere*, J. Appl. Phys. **36** (1965), 2347.

[Rum21] J. R. Rumble (ed.), *CRC Handbook of Chemistry and Physics, 102nd Edition*, CRC Press/Taylor & Francis, Boca Raton, FL, 2021.

[RvWL82] B. Rasser, J. N. M. van Wunnik, and J. Los, *Theoretical models of the negative ionization of hydrogen on clean tungsten, cesiated tungsten and cesium surfaces at low energies*, Surf. Sci. **118** (1982), 697.

[S^+81] P. J. Schneider et al., *H^- and D^- production by backscattering from alkali-metal targets*, Phys. Rev. B **23** (1981), 941.

[S^+96] M. Seidl et al., *Negative surface ionization of hydrogen atoms and molecules*, J. Appl. Phys. **79** (1996), 2896.

[S^+00] F. Stienkemeier et al., *Langmuir-Taylor surface ionization of alkali (Li, Na, K) and alkaline earth (Ca, Sr, Ba) atoms attached to helium droplets*, Rev. Sci. Instrum. **71** (2000), 3480.

[S^+01] P. Scheubert et al., *Experimental and theoretical characterization of an inductively coupled plasma source*, J. Appl. Phys. **90** (2001), 587.

[S$^+$03] P. V. Sushko et al., *Electron Localization and a Confined Electron Gas in Nanoporous Inorganic Electrides*, Phys. Rev. Lett. **91** (2003), 126401.

[S$^+$06] E. Speth et al., *Overview of the RF source development programme at IPP Garching*, Nucl. Fusion **46** (2006), S220.

[S$^+$07] P. V. Sushko et al., *From Insulator to Electride: A Theoretical Model of Nanoporous Oxide* $12CaO{\cdot}7Al_2O_3$, J. Am. Chem. Soc. **129** (2007), 942.

[S$^+$15] L. Schiesko et al., *First experiments with Cs doped Mo as surface converter for negative hydrogen ion sources*, J. Appl. Phys. **118** (2015), 073303.

[S$^+$17a] M. J. Singh et al., *Heating neutral beams for ITER: negative ion sources to tune fusion plasmas*, New J. Phys. **19** (2017), 055004.

[S$^+$17b] P. Sonato et al., *Conceptual design of the DEMO neutral beam injectors: main developments and R&D achievements*, Nucl. Fusion **57** (2017), 056026.

[S$^+$18] M. Sasao et al., *Negative-hydrogen-ion production from a nanoporous* $12CaO{\cdot}7Al_2O_3$ *electride surface*, Appl. Phys. Express **11** (2018), 066201.

[S$^+$19] M. Siragusa et al., *Conceptual design of scalable vacuum pump to validate sintered getter technology for future NBI application*, Fus. Eng. Des. **146** (2019), 87.

[S$^+$20] G. Serianni et al., *First operation in SPIDER and the path to complete MITICA*, Rev. Sci. Instrum. **91** (2020), 023510.

[S$^+$21a] H. Said et al., *Ab initio molecular dynamics investigation of Cs adsorption on Mo(0 0 1): Beyond a single monolayer coverage*, Appl. Surf. Sci. **559** (2021), 149822.

[S$^+$21b] L. Schiesko et al., *Surface and sub-surface investigations of the plasma influence on Cs doped Mo as surface converter for negative hydrogen ion sources for fusion*, EPL **134** (2021), 18002.

[S$^+$22] E. Sartori et al., *First operations with caesium of the negative ion source SPIDER*, Nucl. Fusion **62** (2022), 086022.

[SCČ14] M. Sudolská, L. Cantrel, and I. Černušák, *Microhydration of caesium compounds: Cs, CsOH, CsI and Cs_2I_2 complexes with one to three H_2O molecules of nuclear safety interest*, J. Mol. Model. **20** (2014), 2218.

[SD79] M. P. Seah and W. A. Dench, *Quantitative electron spectroscopy of surfaces: A standard data base for electron inelastic mean free paths in solids*, Surf. Interface Anal. **1** (1979), 2.

[Sha70] T. E. Sharp, *Potential-energy curves for molecular hydrogen and its ions*, At. Data Nucl. Data Tables **2** (1970), 119.

[Sha71] ______, *Erratum: Potential-energy curves for molecular hydrogen and its ions*, At. Data Nucl. Data Tables **3** (1971), 299.

[SJ94] H. Shi and K. Jacobi, *Reaction between H_2O and Cs on the Ru(001) surface*, Surf. Sci. **317** (1994), 45.

[SL49] K. E. Shuler and K. J. Laidler, *The Kinetics of Heterogeneous Atom and Radical Reactions. I. The Recombination of Hydrogen Atoms on Surfaces*, J. Chem. Phys. **17** (1949), 1212.

[SP94] J. Songster and A. D. Pelton, *The H-Cs (Hydrogen-Cesium) System*, J. Phase Equilibria **15** (1994), 84.

[SR17] J. R. Salasin and C. Rawn, *Structure Property Relationships and Cationic Doping in $[Ca_{24}Al_{28}O_{64}]^{4+}$ Framework: A Review*, Crystals **7** (2017), 143.

[SS68] L. W. Swanson and R. W. Strayer, *Field-Electron-Microscopy Studies of Cesium Layers on Various Refractory Metals: Work Function Change*, J. Chem. Phys. **48** (1968), 2421.

[SS00] M. Scheffler and C. Stampfl, *Theory of Adsorption on Metal Substrates*, in: Handbook of Surface Science, vol. 2 (K. Horn and M. Scheffler, eds.), Elsevier, Amsterdam, 2000, p. 285.

[Ste19] D. A. Steck, *Cesium D Line Data*, 2019, available online at `http://steck.us/alkalidata/` (revision 2.2.1, 21 November 2019).

[SVY95] I. I. Sobel'man, L. A. Vainshtein, and E. A. Yukov, *Excitation of Atoms and Broadening of Spectral Lines*, 2nd ed., Springer, Berlin, Heidelberg, 1995.

[SWF18] L. Schiesko, C. Wimmer, and U. Fantz, *Langmuir probe investigations of different magnetic filter field configurations at BATMAN upgrade*, AIP Conf. Proc. **2052** (2018), 040006.

[T+97] K. Tsumori et al., *Large ion yields in hydrogen scattering from a graphite surface*, J. Appl. Phys. **81** (1997), 6390.

[T+07] Y. Toda et al., *Work Function of a Room-Temperature, Stable Electride* $Ca_{24}Al_{28}O_{64}]^{4+}(e^-)_4$, Adv. Mater. **19** (2007), 3564.

[T+11] ———, *Surface of Room-Temperature-Stable Electride* $[Ca_{24}Al_{28}O_{64}]^{4+}(e^-)_4$*: Preparation and Its Characterization by Atomic-Resolution Scanning Tunneling Microscopy*, ACS Nano **5** (2011), 1907.

[T+12] K. Tsumori et al., *Spatial distribution of the charged particles and potentials during beam extraction in a negative-ion source*, Rev. Sci. Instrum. **83** (2012), 02B116.

[T+17] V. Toigo et al., *The PRIMA Test Facility: SPIDER and MITICA test-beds for ITER neutral beam injectors*, New J. Phys. **19** (2017), 085004.

[T+21] ———, *On the road to ITER NBIs: SPIDER improvement after first operation and MITICA construction progress*, Fusion Eng. Des. **168** (2021), 112622.

[TL33] J. B. Taylor and I. Langmuir, *The Evaporation of Atoms, Ions and Electrons from Caesium Films on Tungsten*, Phys. Rev. **44** (1933), 423.

[TL37] ———, *Vapor Pressure of Caesium by the Positive Ion Method*, Phys. Rev. **51** (1937), 753.

[TLJ99] A. Thorne, U. Litzén, and S. Johansson, *Spectrophysics: Principles and Applications*, Springer, Berlin, Heidelberg, 1999.

[TM87] P. A. Thiel and T. E. Madey, *The interaction of water with solid surfaces: Fundamental aspects*, Surf. Sci. Rep. **7** (1987), 211.

[UJ70] J. J. Uebbing and L. W. James, *Behavior of Cesium Oxide as a Low Work-Function Coating*, J. Appl. Phys. **41** (1970), 4505.

[vA+86] P. W. van Amersfoort et al., *Formation of negative hydrogen ions on a coadsorbed layer of cesium and hydrogen on W(110)*, J. Appl. Phys. **59** (1986), 241.

[vATG85] P. W. van Amersfoort, Y. C. Tong, and E. H. A. Granneman, *A model for the stationary cesium coverage on a converter surface in a cesium seeded hydrogen discharge*, J. Appl. Phys. **58** (1985), 2317.

[VGK14] D. Vlachos, E. Giotopoulou, and M. Kamaratos, *Adsorption of Water on a Cesium Covered $SrTiO_3$ (100) Surface*, Proc. NAP **3** (2014), 01NTF15.

[vOvAL88] C. F. A. van Os, P. W. van Amersfoort, and J. Los, *Negative ion formation at a barium surface exposed to an intense positive-hydrogen ion beam*, J. Appl. Phys. **64** (1988), 3863.

[VSE04] P. Vankan, D. C. Schram, and R. Engeln, *High rotational excitation of molecular hydrogen in plasmas*, Chem. Phys. Lett. **400** (2004), 196.

[W+87] B. Woratschek et al., *The interaction of cesium with oxygen*, J. Chem. Phys. **86** (1987), 2411.

[W+18a] C. Wimmer et al., *Improved understanding of the Cs dynamics in large H^- sources by combining TDLAS measurements and modeling*, AIP Conf. Proc. **2011** (2018), 060001.

[W+18b] D. Wünderlich et al., *Initial caesium conditioning in deuterium of the ELISE negative ion source*, Plasma Phys. Control. Fusion **60** (2018), 085007.

[W+18c] ———, *Long pulse operation at ELISE: Approaching the ITER parameters*, AIP Conf. Proc. **2052** (2018), 040001.

[W+19a] ———, *Achievement of ITER-relevant accelerated negative hydrogen ion current densities over 1000 s at the ELISE test facility*, Nucl. Fusion **59** (2019), 084001.

[W+19b] ———, *Formation of large negative deuterium ion beams at ELISE*, Rev. Sci. Instrum. **90** (2019), 113304.

[W+21a] ———, *Application of molecular convergent close-coupling cross sections in a collisional radiative model for the triplet system of molecular hydrogen*, J. Phys. D: Appl. Phys. **54** (2021), 115201.

[W⁺21b] ———, *Effects of the magnetic field topology on the co-extracted electron current in a negative ion source for fusion*, J. Appl. Phys. **130** (2021), 053303.

[W⁺21c] ———, *Emission spectroscopy of negative hydrogen ion sources: From VUV to IR*, Rev. Sci. Instrum. **92** (2021), 123510.

[W⁺21d] ———, *NNBI for ITER: status of long pulses in deuterium at the test facilities BATMAN Upgrade and ELISE*, Nucl. Fusion **61** (2021), 096023.

[W⁺22] C. Wimmer et al., *Overview of recent and upcoming activities at the BATMAN Upgrade test facility*, J. Phys.: Conf. Ser. **2244** (2022), 012051.

[Wad18] M. Wada, *Plasma-surface interaction in negative hydrogen ion sources*, Rev. Sci. Instrum. **89** (2018), 052103.

[WC92] H. F. Winters and J. W. Coburn, *Surface science aspects of etching reactions*, Surf. Sci. Rep. **14** (1992), 162.

[WE33] H. E. White and A. Y. Eliason, *Relative Intensity Tables for Spectrum Lines*, Phys. Rev. **44** (1933), 753.

[WF16] D. Wünderlich and U. Fantz, *Evaluation of State-Resolved Reaction Probabilities and Their Application in Population Models for He, H, and H_2*, Atoms **4** (2016), 26.

[WFN16] C. Wimmer, U. Fantz, and NNBI-Team, *Extraction of negative charges from an ion source: Transition from an electron repelling to an electron attracting plasma close to the extraction surface*, J. Appl. Phys. **120** (2016), 073301.

[Wil66a] R. G. Wilson, *Electron and Ion Emission from Polycrystalline Surfaces of Be, Ti, Cr, Ni, Cu, Pt, and Type-304 Stainless Steel in Cesium Vapor*, J. Appl. Phys. **37** (1966), 3161.

[Wil66b] ———, *Electron and Ion Emission from Polycrystalline Surfaces of Nb, Mo, Ta, W, Re, Os, and Ir in Cesium Vapor*, J. Appl. Phys. **37** (1966), 4125.

[WLK89] S. R. Walther, K. N. Leung, and W. B. Kunkel, *H^- production in a small multicusp ion source with addition of barium*, Appl. Phys. Lett. **54** (1989), 210.

[Wol22] V. Wolf, *Private communication*, University of Augsburg, AG Experimental Plasma Physics, 2022.

[WPL73] G. A. Woolsey, I. C. Plumb, and D. B. Lewis, *Langmuir probe characteristics in a positive-ion/negative-ion plasma*, J. Phys. D: Appl. Phys. **6** (1973), 1883.

[WW62] B. J. Wood and H. Wise, *The kinetics of hydrogen atom recombination on pyrex glass and fused quartz*, J. Phys. Chem. **66** (1962), 1049.

[Y+12] H. Yanagi et al., *Electron injection barriers between air-stable electride with low work function, C12A7:e^-, and pentacene, C_{60} and copper phthalocyanine*, J. Mater. Chem. **22** (2012), 4278.

[YB80] S.-J. Yang and C. W. Bates, *The role of cesium suboxides in low-work-function surface layers studied by x-ray photoelectron spectroscopy: Ag-O-Cs*, Appl. Phys. Lett. **36** (1980), 675.

[Z+17] W. Zou et al., *Direct fabrication of C12A7 electride target and room temperature deposition of thin films with low work function*, Mater. Res. Express **4** (2017), 036408.

[Zie22] D. Zielke, *Private communication*, Max-Planck-Institut für Plasmaphysik, Garching, 2022.

List of publications

- **A. Heiler**, R. Friedl, and U. Fantz, *Impact of the photoelectric threshold sensitivity on the work function determination—Revealing ultra-low work functions of caesiated surfaces*, AIP Adv. **12** (2022), 035339.
- **A. Heiler**, K. Waetzig, M. Tajmar, R. Friedl, R. Nocentini, and U. Fantz, *Work function performance of a C12A7 electride surface exposed to low pressure low temperature hydrogen plasmas*, J. Vac. Sci. Technol. A **39** (2021), 013002.
- **A. Heiler**, R. Friedl, U. Fantz, R. Nocentini, and M. Sasao, *Work function behavior of a biased C12A7 electride in low temperature hydrogen plasmas*, AIP Conf. Proc. **2373** (2021), 020004.
- U. Fantz, S. Briefi, **A. Heiler**, C. Wimmer, and D. Wünderlich, *Negative Hydrogen Ion Sources for Fusion: From Plasma Generation to Beam Properties*, Front. Phys. **9** (2021), 709651.
- **A. Heiler**, R. Friedl, and U. Fantz, *Application of a Langmuir probe AC technique for reliable access to the low energy range of electron energy distribution functions in low pressure plasmas*, J. Appl. Phys. **127** (2020), 113302.
- R. Friedl, D. Rauner, **A. Heiler**, and U. Fantz, *Dissociative recombination and its impact on the line profile of the hydrogen Balmer series*, Plasma Sources Sci. Technol. **29** (2020), 015014.

Acknowledgments

I would like to express my sincere gratitude to everyone who supported me during my PhD. In particular, I would like to thank:

- Prof. Dr.-Ing. Ursel Fantz for giving me the opportunity to do my PhD and to join the ITED group at the Max Planck Institute for Plasma Physics and the EPP group at the University of Augsburg. I am very grateful for the excellent supervision, the frequent and encouraging discussions, and the continuous support during my time as a PhD student.
- Priv.-Doz. Dr. Hans-Albrecht Krug von Nidda for being the second reviewer of my PhD thesis.
- Dr. Roland Friedl for always having an open door, giving me the right hint in the right moment, and helping me to realize this work. I benefited greatly from your expertise and the numerous scientific discussions we had. I am also very thankful for the careful proofreading of this work.
- Dr. Sofia Cristofaro for introducing me to the ACCesS experiment and explaining the various diagnostic methods and evaluation techniques to me.
- Dr. David Rauner and Caecilia Fröhler-Bachus for supporting me with the experimental setup and the conduction of measurements with the VUV diode system, and for the many fruitful discussions from which I could benefit a lot.
- All my other (current and former) colleagues of the ITED and EPP group for the pleasant working atmosphere and good collaboration. In particular, I would like to thank Dr. Riccardo Nocentini, Dr. Stefan Briefi, Dr. Dirk Wünderlich, Dr. Christian Wimmer, Dr. Dominikus Zielke, Dr. Alessandro Mimo, Markus Fröschle, Christoph Haindl, Jacob Berner, Vinzenz Wolf and Marina Huber.
- Prof. Dr. Martin Tajmar and Dr. Katja Wätzig for providing the C12A7 electride material.

I could not have undertaken this journey without the support from my parents throughout my whole academic career. I am also deeply grateful to my girlfriend Katharina. Your understanding, moral support and unconditional love mean everything to me.